Effects of Black Carbon on Climate: Advances in Measurement and Modeling

Yutaka Kondo

Department of Earth and Planetary Science, Graduate School of Science, The University of Tokyo, Hongo 7-3-1, Bunkyo-ku, Tokyo, 113-0033, Japan
e-mail: kondo@eps.s.u-tokyo.ac.jp; kondo.yutaka@nipr.ac.jp

Received June 30, 2014; **Revised** November 14, 2014; **Accepted** November 17, 2014; **Online published** April 30, 2015.

Citation: Kondo, Y. (2015), Effects of black carbon on climate: Advances in measurement and modeling, *Monogr. Environ. Earth Planets*, *3*, 1–85, doi:10.5047/meep.2015.00301.0001.

Abstract Black carbon (BC) particles are non-spherical agglomerates consisting of hundreds or thousands of graphitic carbon spherules the diameters of which are about 15–50 nm. The spherules are graphitic in their molecular states and are, thus, strongly light-absorbing. BC particles are emitted by the incomplete combustion of carbon-based fossil fuels and biomass. BC mass in the atmosphere resides in agglomerates typically between 100 and 600 nm in diameter. They influence the global radiation budget by strongly absorbing solar radiation in the visible wavelengths and by changing the albedo of snow through deposition. Radiative forcing (RF) of BC is defined as the change in net radiative flux at the top of the atmosphere in W m^{-2} due to a change of BC between the pre-industrial time and present-day periods. The instantaneous direct radiative forcing of airborne BC particles (BC DRF), which does not include climate feedbacks, is determined by their absorption cross sections and spatial distributions. The distributions of BC are, in turn, controlled by its emission, dynamical transport, and loss during transport. The absorption cross section of BC is controlled by its optical properties (i.e., refractive index) and microphysical properties (size distribution, morphology, and mixing state). Because it is crucial to characterize these parameters, we first developed techniques to measure them accurately. Newly-developed BC measurement technologies constitute the firm basis of our studies. The techniques were applied to laboratory experiments and field observations of BC particles in air and rainwater. We also developed regional scale three-dimensional (3D) models to quantitatively interpret the observational results. One of the models calculates BC aging and optical/radiative processes explicitly without parameterizations. The reliable field measurements and model calculations of BC has enabled an improved understanding of the physical and chemical processes that control the microphysical properties of BC. We also quantitatively analyzed the emission rate, transport, and wet removal processes of BC in Asia by comparing the observed, and model-calculated, BC distributions. Through aircraft measurements in the Arctic, we characterized emissions of BC from biomass burning and the strong seasonal variations of the efficiency of transport of BC from different regions in the northern hemisphere to the Arctic. A number of findings, brought about by the observational and modeling efforts, demonstrate the strength of our innovative methodologies for improving the estimate of BC DRF, which has been highly uncertain thus far.

Keywords: Black carbon, Aerosols, Absorption, Scattering, Radiative forcing, Observations, Modelling, Emission, Transport, Wet depositon.

1. Introduction

Aerosol particles interact with solar radiation in the visible wavelength region (direct effect), as shown schematically in Fig. 1(a) (modified version of FAQ 7.2 figure 1 of IPCC (2013)). Light scattering particles (LSP), mainly composed of inorganic and organic compounds, scatter solar radiation and cool the surface and atmosphere. Light absorbing particles, such as black carbon (BC) and dust particles, absorb solar radiation and thus heat the atmosphere. These particles also act as cloud condensation nuclei (CCN) at the supersaturation of water vapor (H_2O), depending on their size and chemical composition, as shown in Fig. 1(b) (modified version of FAQ 7.2 figure 2 of IPCC (2013)). They alter the microphysical properties of cloud droplets, leading to changes in cloud albedo (indirect effect), especially of warm clouds. BC can also act as ice nuclei (IN), influencing the phases of clouds (e.g., DeMott *et al*., 2010; Murray *et al*., 2012).

BC particles are agglomerates of spherical graphitic carbon with primary diameters of 15–50 nm. The spherules are graphitic in their molecular states and thus are strongly light absorbing. The BC mass in the atmosphere is found in agglomerates typically between 100 and 600 nm in diameter. BC particles are non-spherical as observed from electron microscope images, as shown, for example, in figure 2 of Bond *et al*. (2013). Predominant sources of BC are fossil fuels used for transportation, solid fuels for industrial and residen-

doi:10.5047/meep.2015.00301.0001 ISSN: 2186-4853

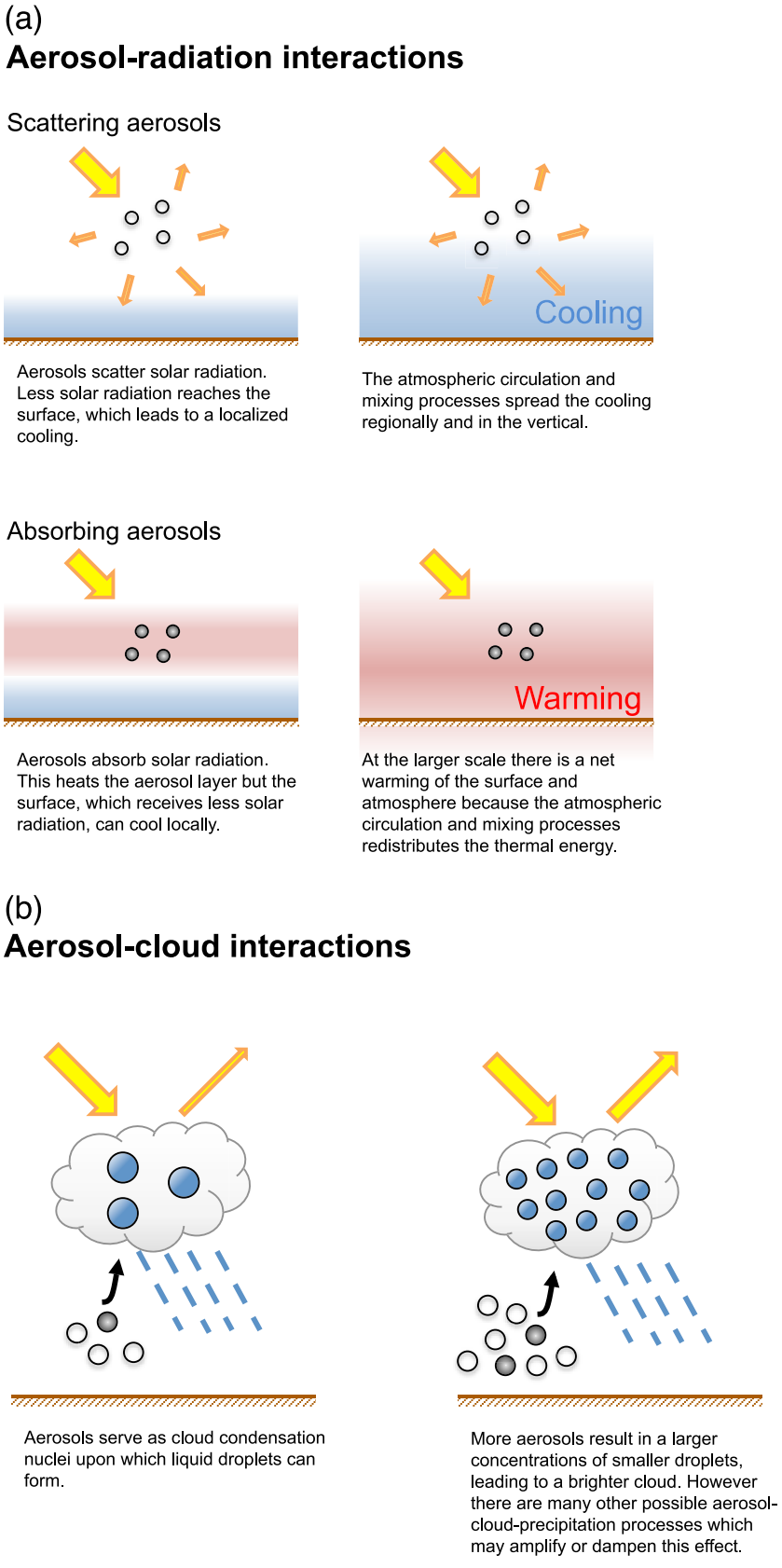

Fig. 1. (a) Overview of interactions between aerosols and solar radiation and their impact on climate. The left panels show the instantaneous radiative effects of aerosols, while the right panels show their overall impact after the climate system has responded to their radiative effects. Adapted from FAQ 7.2 figure 1 of IPCC (2013). (b) Overview of aerosol-cloud interactions and their impact on climate. Left and right panels represent a clean and a polluted low-level cloud, respectively. Adapted from FAQ 7.2 figure 2 of IPCC (2013).

doi:10.5047/meep.2015.00301.0001

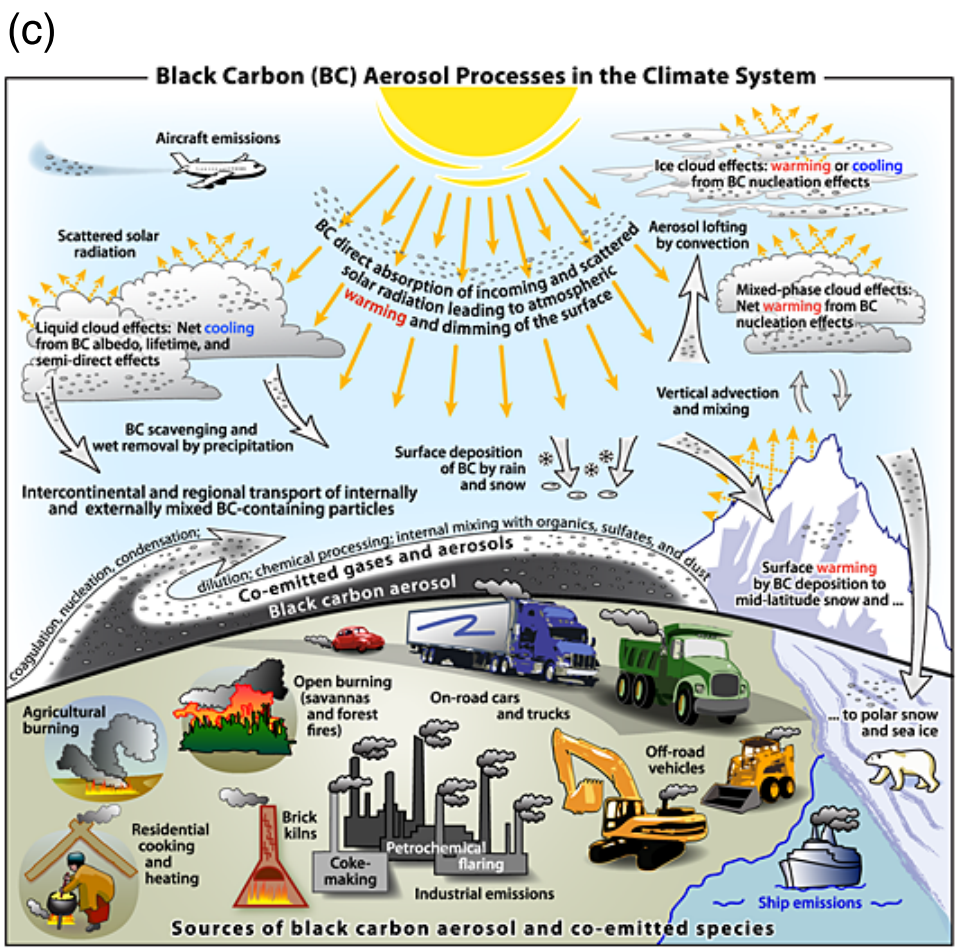

Fig. 1. (c) Schematic overview of the primary black-carbon emission sources and the processes that control the distribution of black carbon in the atmosphere and determine its role in the climate system. From figure 1 of Bond *et al*. (2013).

tial uses, and the open burning of biomass (e.g., Streets *et al*., 2003; Bond *et al*., 2004, 2013).

Bond *et al*. (2013) made the first comprehensive assessment of BC in the climate system. Figure 1(c) (figure 1 of Bond *et al*. (2013)) shows the diverse BC sources and the processes that control BC distribution in the atmosphere and determine its role in the climate system. The assessment included all known and relevant processes and provided best estimates and uncertainties of the main forcing terms: direct solar absorption; influence on liquid, mixed phase, and ice clouds; and deposition on snow and ice. These effects were calculated with climate models. The major findings provided in the assessment are (1) BC properties, (2) BC emissions and abundance, (3) synthesis of BC climate forcing terms, (4) BC direct radiative forcing, (5) BC cloud effects, (6) BC snow and ice effects, (7) impacts of BC climate forcing, (8) net climate forcing by BC-rich source categories, (9) perspective on mitigation options for BC emissions, and (10) policy implications. Our results, described in this monograph, have contributed to the assessment, especially in the research areas (1), (2), (3), and (4), providing support to their methodologies and conclusions. Further discussion is made below based on this assessment.

The radiative effects of BC on the global mean surface temperature are represented by radiative forcing (RF). RF is defined as the change in net (down minus up) radiative flux in W m^{-2} due to an imposed change between pre-industrial time (typically ca. 1750) and the present-day (IPCC, 2013). In the case of aerosols and BC, the imposed changes are the changes of aerosol and BC concentrations, respectively. The instantaneous RF is usually defined in terms of flux changes at the top of the atmosphere (TOA) or at the climatological tropopause, without including climate feedbacks. The assumed relation of a sustained RF and equilibrium global mean surface temperature change (ΔT) is $\Delta T = \lambda \times \mathrm{RF}$, where λ is the climate sensitivity parameter. This means that the steady-state global mean climate response to a given forcing is determined both by the forcing and the responses of the climate system inherent in λ. Direct radiative forcing of BC (BC DRF) is the instantaneous RF caused by the changes in absorption and scattering of sunlight by airborne BC particles associated with the changes in the emissions of BC (Schulz *et al*., 2006). Estimates of BC DRF are based on the difference between radiative transfer calculations for the atmosphere with present-day BC and with a background level of BC corresponding to the BC emissions typically for the year 1750 (Bond *et al*., 2013).

In addition to the radiative effects of airborne BC particles

doi:10.5047/meep.2015.00301.0001

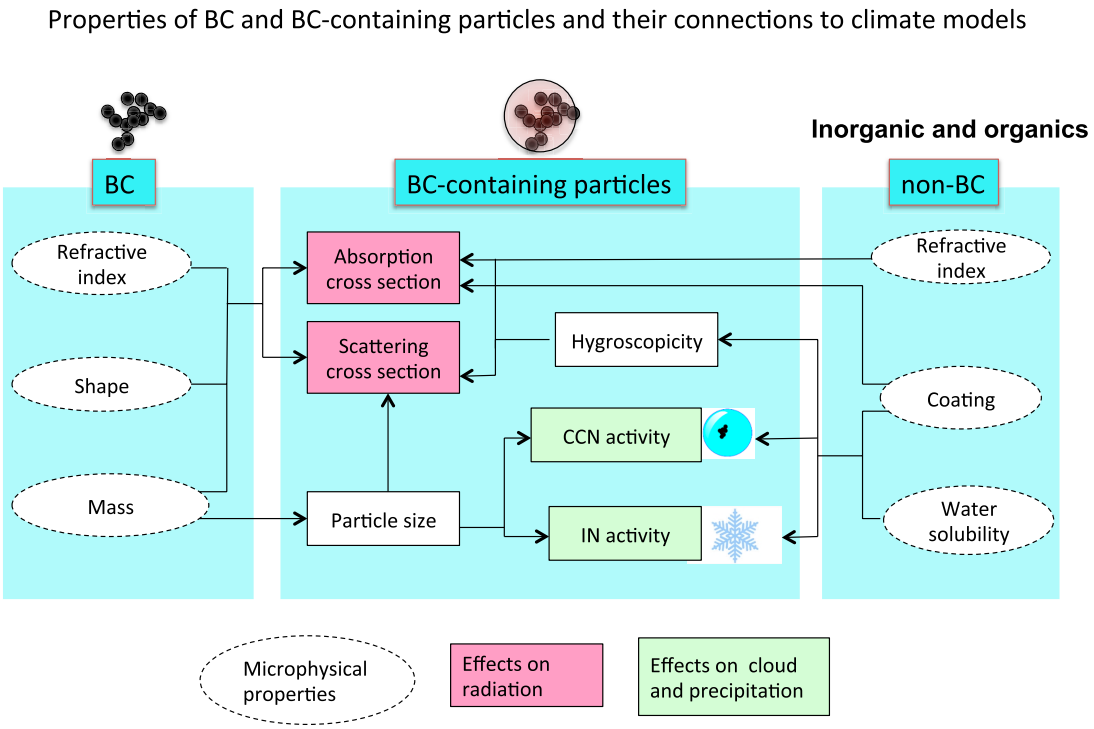

Fig. 2. Schematic of the connections between the properties of BC and BC-containing particles. A combination of these properties determines the contribution of BC and BC-containing particles to climate forcing. The properties depend on those of other substances produced in the atmosphere or co-emitted with BC, and on atmospheric processes such as nucleation and condensation. The mass and number of BC and BC-containing particles depend, in part, on particle properties that affect the lifecycle of BC. CCN and IN stand for cloud condensation nuclei and ice nuclei, respectively. Adapted from figure 3 of Bond *et al.* (2013) and provided by courtesy of N. Moteki.

(Jacobson, 2001; Ramanathan *et al.*, 2001, 2007; Bond *et al.*, 2013; IPCC, 2013), BC particles deposited in the polar regions change the snow albedo (Hansen and Nazarenko, 2004), leading to a heating of the climate system. It is critically important to estimate or assess reliably the impacts of BC on climate, considering the predicted large magnitudes of the effects. BC DRF is determined by the microphysical properties and spatial distributions of BC, as discussed in detail in Chapter 20.

The properties of BC and non-BC particles, important in estimating the climate effects of BC by climate models, are schematically shown in Fig. 2 (modified version of figure 20 of Bond *et al.* (2013)). The absorption cross section is controlled by the optical properties (i.e., refractive index) and microphysical properties (size distribution, morphology, and mixing state) of BC. As an example, Fig. 3 shows the size dependence of the mass absorption cross section of BC calculated by Mie theory, although the uncertainty associated with the application of Mie theory to the non-spherical BC particle is not quantified. It is qualitatively seen that the light absorption of BC is efficient in the sub-micron range and, therefore, accurate estimates of the BC size distribution are needed in this range.

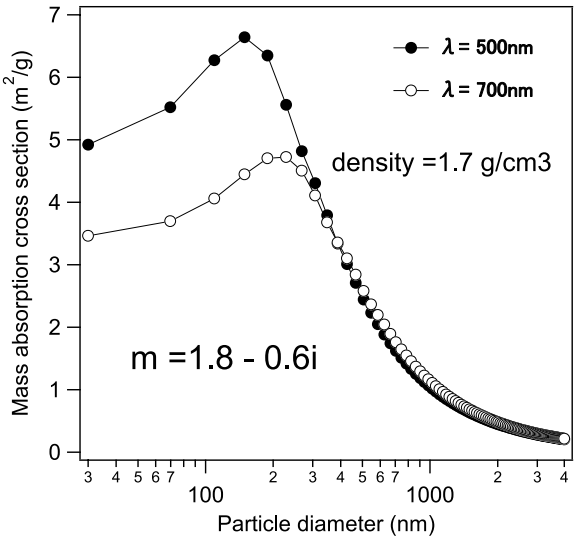

Fig. 3. Mass absorption cross section of BC with a refractive index of $m = 1.8 - 0.6i$ and a density of 1.7 g cm^{-3} at wavelengths of 500 and 700 nm calculated by Mie theory assuming a spherical shape. This figure was provided by courtesy N. Moteki.

The microphysical properties of BC are controlled by collisions between aerosol particles, condensation of low volatility compounds on BC, and cloud processing, as schematically illustrated by Fig. 4. Changes in the microphysical properties, in turn, alter the rate of loss of BC by precipitation. The abundance of BC is controlled by its emission, dynamical transport, and loss during transport.

The product of BC the mass concentration M_{BC} (g m^{-3}) and the mass absorption cross section σ_{abs} (m^2 g^{-1}) (absorption cross section per unit BC mass) is the absorption co-

doi:10.5047/meep.2015.00301.0001

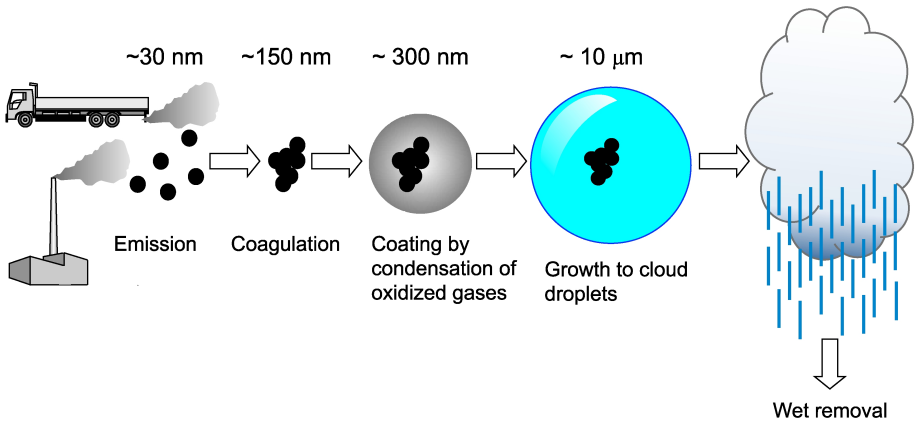

Fig. 4. Schematic showing the evolution of BC particles from emission to growth to cloud droplets. BC and non-BC particles grow in size by coagulation and condensation. BC particles are mixed with non-BC compounds (internal mixing) through these processes. Internal mixing of BC enhances light absorption by BC (lens effect). CCN activities of BC particles also increase by internal mixing. Aerosol concentration, composition, diameter, and mixing state are determined by these processes. This figure was provided by courtesy N. Takegawa.

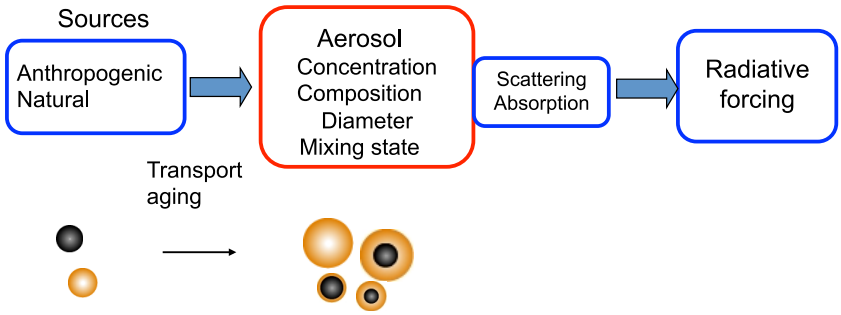

Fig. 5. Schematic showing the parameters and microphysical processes of BC and non-BC particles, which are key in accurate calculations of aerosol radiative forcing. This figure was provided by courtesy of H. Matsui.

efficient b_{abs} (m^{-1}). Namely, $b_{abs} = \sigma_{abs} M_{BC}$. Vertically integrating the b_{abs} results in the BC absorption aerosol optical depth (BC AAOD) (dimensionless). The BC AAOD is closely related to the BC column abundance and is a very useful diagnostic that can be compared with atmospheric measurements. There is about a factor of 3 difference between model-calculated and observed BC AAOD (Bond *et al.*, 2013). The large discrepancy points to the lack of quantitative understanding of some of the key parameters and processes controlling BC DRF, mentioned above.

One of the most important causes of the uncertainties in estimating BC DRF arises from the fact that BC particles are non-spherical. This non-spherical nature introduces large complexities and difficulties in reliably estimating the microphysical properties of BC (e.g., the absorption cross section, hygroscopicity, and mixing states). In order to overcome these difficulties, we have developed innovative techniques to measure the microphysical properties of BC, closely related to its climatic impacts, as presented in Chapters 2, 3, and 4. Our efforts began with studies to define the "masses of individual BC particles", which were poorly defined for more than two decades. We needed a consistent definition of BC, upon which a sound understanding of the effects of BC on climate could be constructed.

From a modelling point of view, large uncertainties in estimates of the BC DRF can arise from oversimplification in representing the key parameters and processes. Previously, bulk properties of aerosol, typically the total mass concentration of BC, were used for modeling studies. This simplification includes using prescribed microphysical properties (the shapes of the aerosol size distribution and the mixing state). It will be shown later that the magnitude of BC DRF is sensitive to these parameters. The accurate prediction of the BC DRF must be based on appropriate representations of aerosol as an ensemble of individual particles, and not based solely on its bulk properties, as is schematically shown in Fig. 5.

It should be stressed that innovative instrument development followed by field measurements strongly activated modeling studies. The field data have been critical in validating model calculations. In turn, advanced models, combined with meteorological analyses, have enabled the quantitative interpretation of field data. In this way, close collaboration between measurement and modeling efforts has been an important driving force of BC studies, as shown in the following chapters.

In this monograph, first of all, new techniques to measure the microphysical properties of BC are described. Second, the results of laboratory and field experiments are presented. The field measurements were made mostly in East Asia,

doi:10.5047/meep.2015.00301.0001

Table 1. Acronyms and abbreviations.

Acronym	Definition
AAOD	aerosol absorption optical depth
AERONET	Aerosol Robotic NETwork
A-FORCE	Aerosol Radiative Forcing in East Asia
AMS	Aerodyne aerosol mass spectrometer
AOD	aerosol optical depth
APM	aerosol particle mass analyzer
APT	accumulated precipitation along a trajectory
ARCTAS	Arctic Research of the Composition of the Troposphere from Aircraft and Satellite
B_{abs}	absorption coefficient for airborne particles
B_{scat}	scattering coefficient for airborne particles
b_{abs}	absorption coefficient
BB	biomass burning
BC	black carbon
BC-DRF	black-carbon direct radiative forcing
C_{abs}	absorption cross section
C_{BC}	BC mass concentrations in rainwater
CCN	cloud condensation nuclei
CN	condensation nuclei
CMAQ model	Community Multiscale Air Quality model
CMD	count median diameter
COSMOS	continuous soot monitoring system
CPC	condensation particle counter
CTM	chemical transport model
D_{BC}	mass equivalent diameter of BC
D_C	core diameter of BC = mass equivalent diameter of BC
DEP_{BC}	total BC mass deposited per unit area during a specified period
DMA	differential mobility analyzer
D_p	particle diameter
DRF	direct radiative forcing
DRH	deliquescence relative humidity
EC	elemental carbon
FF	fossil fuel
f_{fil}	correction factor of the magnitude of BC photo-absorption by multiple scattering in the filter media
FT	free troposphere
GPCP	global precipitation climatology project
HTDMA	humidified tandem differential mobility analyzer
HTDT	heavy-duty diesel truck
HULIS	humic-like substance
IN	ice nuclei
IPCC	Intergovernmental Panel on Climate Change
lidar	light detection and ranging
LII	laser induced incandescence
LSP	light scattering particle
LT	lower troposphere
MAAP	multi-angle absorption photometer
MAC	mass absorption cross section
M_{BC}	mass concentration of BC
MBL	marine boundary layer
MCE	modified combustion efficiency
MMD	mass median diameter
MS-resolved	Mixing-state-resolved
NASA	National Aeronautics and Space Administration
NC	north china
OA	organic aerosols
OC	organic carbon
PASS or PAS	photo-acoustic absorption spectrometer

doi:10.5047/meep.2015.00301.0001

Table 1. (continued.)

Acronym	Definition
PASCAL	Process, Age, and Source region Chasing Algorithm
PBL	planetary boundary layer
PILS	particle-into-liquid sampler
PM	particulate matter
PM_1	total mass concentration of particles with diameters smaller than 1 μm
$PM_{2.5}$	total mass concentration of particles with diameters smaller than 2.5 μm
PM_{10}	total mass concentration of particles with diameters smaller than 10 μm
PMF	positive matrix factorization
POA	primary organic aerosol
PSAP	Particle Soot Absorption Photometer
PSL	polystyrene latex
RF	radiative forcing
RT	residence time
SC	south China
SC ratio	shell-to BC core diameter ratio
SEA	Southeast Asia
SKYNET	Sky Radiometer Network
SOA	secondary organic aerosol
SP2	Single Particle Soot Photometer
SSA	single scattering albedo
SS_c	critical supersaturation
TE	transport efficiency
TOA	top of the atmosphere
TOT	thermal optical transmittance
TRACE-P	Transport and Chemical Evolution over the Pacific
UHSAS	ultra-high sensitivity aerosol spectrometer
UB	ultrasonic bath
USN	ultrasonic nebulizer
UT	upper troposphere
VTAPM	volatility tandem aerosol particle mass analyzer
VTDMA	volatility tandem differential mobility analyzer
WCB	warm conveyor belt
WRF	Weather Research and Forecasting model
WSOC	water soluble organic carbon
σ_{abs}	mass absorption cross section

where the emission of BC is very high from a global perspective. The data are interpreted by our 3D models, which incorporate detailed representations of the key processes. The optical properties of BC are also discussed in relation with the uncertainties in the BC DRF. Third, the emissions and transport of BC in anthropogenic source regions in Asia are analyzed based on our field measurements.

The results we have published in peer-reviewed journals are used extensively in this monograph. The descriptions of individual studies start with introductions, which refer to relevant previous studies. Individual studies are placed so that the relationships between them can be understood in a straightforward way. The symbols and acronyms used in this monograph are summarized in Table 1.

2. Laser Induced Incandescence Technique for Ambient BC Measurement

2.1 BC mass

BC particles are non-spherical agglomerates comprising hundreds, or thousands, of graphitic carbon spherules having diameters of about 15–50 nm. Usually, BC particles are coated by organic compounds upon emission (e.g., Park *et al*., 2004a, b; Seinfeld and Pandis, 2006). They are further coated with various non-refractory compounds (inorganic and organic) by condensation and coagulation as they age in the atmosphere (e.g., Riemer *et al*., 2004). This complicated the operational definition of BC for many years. This difficulty has been largely overcome by the laser-induced incandescence (LII) technique, as detailed below.

Measurements of the mass of individual BC particles are based on the LII technique using a continuum laser (Stephens *et al*., 2003; Baumgardner *et al*., 2004; Schwarz *et al*., 2006). The Single Particle Soot Photometer (SP2) (Droplet Measurement Technologies (DMT), Boulder, CO) was designed for this measurement. We have made a few modifications to the original system to enhance its capabilities, as discussed later in this chapter.

The descriptions of this section and Section 2.2 are based on the study of Moteki and Kondo (2007). The operational principle of the SP2 has been described in previous studies

doi:10.5047/meep.2015.00301.0001

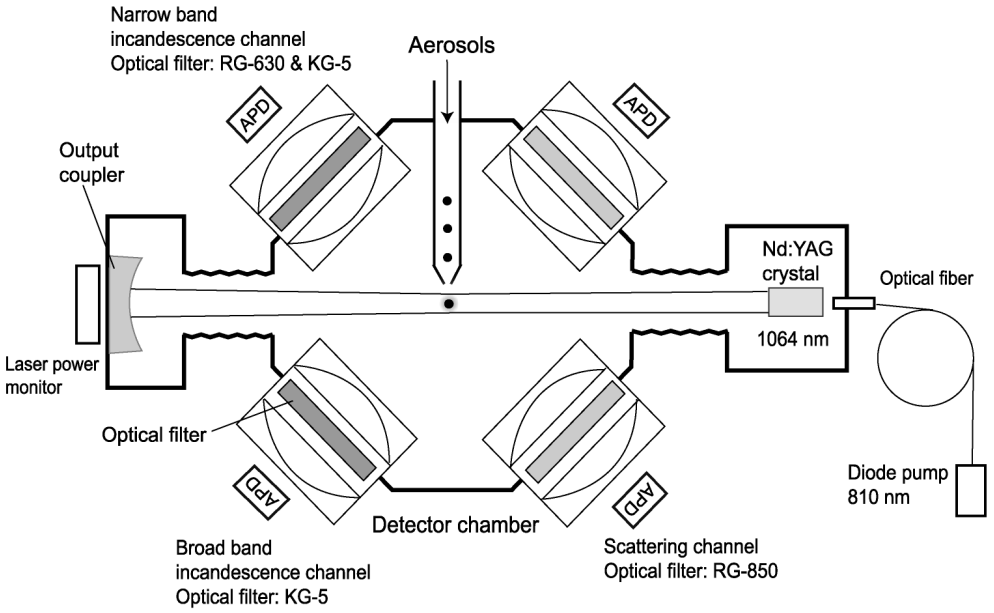

Fig. 6. Schematic of the single-particle soot photometer (SP2) (Moteki and Kondo, 2007). Although the axis of the aerosol jet is perpendicular to the plane containing the avalanche photo-diodes (APDs) and the beam of the YAG laser, it is drawn in the plane for simplicity. The components shown in this figure are explained in detail in Moteki and Kondo (2007). (*Aerosol Sci. Technol.*: Effects of mixing state on black carbon measurements by laser-induced incandescence. (41): 398–417. Copyright 2007. Reston, VA. Reprinted with permission.)

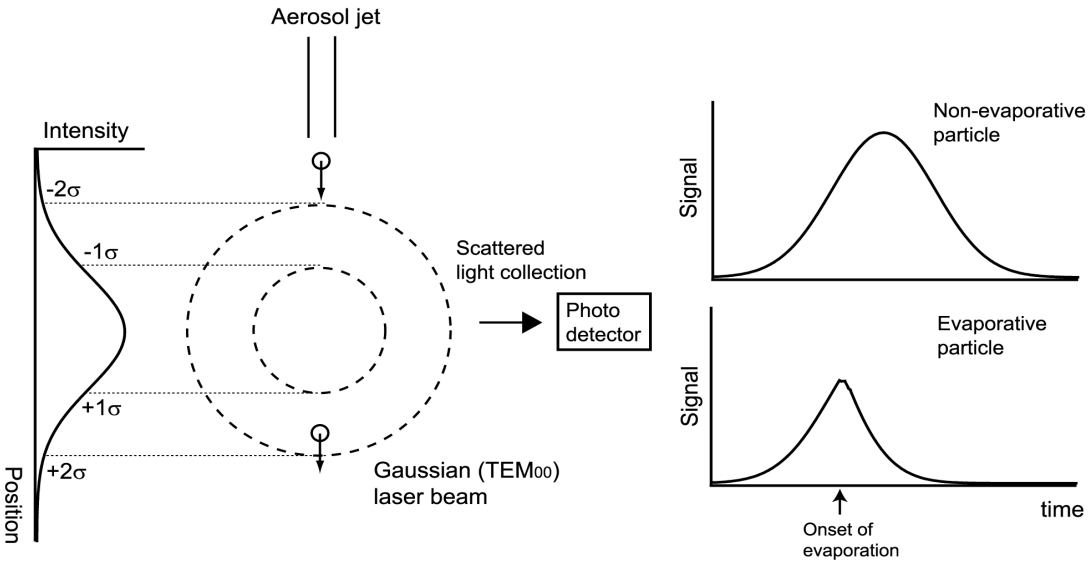

Fig. 7. General schematic of the scattering probe for sizing individual flowing particles using a continuous-wave Gaussian laser beam (Moteki and Kondo, 2008). The aerosol particles intersect with the laser beam at right angles with constant velocity. Conceptual waveforms of the scattering signal of a particle with, and without, evaporation are also shown on the right hand side of the figure. The waveform of the scattering signal for non-evaporative particles is Gaussian in shape, which is equal to the cross-sectional profile of the Gaussian (TEM_{00} mode) laser beam. In contrast, the corresponding waveform for the evaporative particle is distorted from the Gaussian function because of evaporation of the particle during transit in the laser beam. (Reprinted from *J. Aerosol Sci.*, *39*, Moteki, N., and Y. Kondo, Method to measure time-dependent scattering cross-section of particles evaporating in a laser beam, 348–364, Copyright 2008, with permission from Elsevier.)

(Stephens *et al.*, 2003; Baumgarder *et al.*, 2004; Schwarz *et al.*, 2006; Gao *et al.*, 2007; Slowik *et al.*, 2007). The schematic of the SP2 is depicted in Fig. 6. An air jet containing sample aerosols intersects an intense ($\sim$1 MW cm^{-2}), Nd:YAG, intra-cavity, continuous laser beam ($\lambda = 1064$ nm) pumped by a diode laser. The laser is in a TEM_{00} mode, with a Gaussian intensity distribution (Fig. 7) (Stephens *et al.*, 2003; Schwarz *et al.*, 2006). Aerosol particles elastically scatter light in the laser beam and, if they contain light-absorbing material at the wavelength of the incident light, such as BC, they are also heated as they absorb the laser radiation and eventually incandesce and vaporize due to evaporation at high temperatures. The mass of BC with diameters between about 70–900 nm is derived by measuring the in-

doi:10.5047/meep.2015.00301.0001

tensity of the LII signal from individual particles. Non-light absorbing aerosols, e.g., sulfate, nitrate, and organics, elastically scatter laser light without evaporation during laser irradiation. The size of a non-light absorbing aerosol with a diameter of 200–1000 nm can be measured by the intensity of scattering. BC particles coated by non-light-absorbing material scatter laser light more efficiently than uncoated BC due to the larger scattering cross section (Slowik *et al.*, 2007). We can constrain the chemical composition of an incandescing particle based on the temperature at the point of the peak LII intensity because it is a proxy of the boiling point of the composition (Stephens *et al.*, 2003; Baumgardner *et al.*, 2004; Schwarz *et al.*, 2006). Scattering signals, in comparison with the LII signals, are also used for estimating the mixing state of BC particles, as discussed in Sections 2.5 and 2.6.

The laser beam power is monitored by a detector that measures a small fraction of the light that passes through the output coupler. The light detection system consists of four detectors: one for scattered light, two for LII, and one for redundancy. Each detector system consists of an avalanche photo-diode (APD) (Perkin Elmer C30916E), a complex lens to focus light onto the APD, and optical filters. The broadband and narrowband LII channels are equipped with band pass filters for wavelength regions of $\lambda = 350$–800 nm (Schott KG5) and $\lambda = 630$–800 nm (Schott KG5 and RG630), respectively. The scattering channel uses a low pass filter that rejects light at $\lambda < 850$ nm (Schott RG850). The solid angle $\Delta\Omega$ (str) of light collection for the lens system is determined by the configuration of the optical system.

The amplified voltage signal is digitized by an A-D converter at a sampling rate of 5 MHz (i.e., a time resolution of 0.2 μs) for each channel. The duration of the light pulse is equal to the transit time of a particle in the laser beam, which is typically about 10 μs. The time resolution of 0.2 μs for sampling is adequate for recording the temporal evolution of LII and scattering intensities of single particles.

Laboratory experiments and theoretical calculations were carried out to characterize the performance of the SP2. For this study, graphite was used as a surrogate of BC. Graphite particles with mass equivalent diameters of 110–200 nm were layered with organic liquids (glycerol and oleic acid) to produce coated graphite with diameters up to 650–800 nm. These were sampled by the SP2 to measure the waveforms (i.e., time development) of the LII and scattering signals. The peak temperature and the peak LII signal of graphite particles were independent of the coating thickness or the coating material to within experimental errors, as shown in Fig. 8. These results indicate that the mass of BC can be measured by using the peak LII signal without interference by the coating conditions.

LII and scattering waveforms were calculated using a theoretical model that takes into account the physical processes controlling the temperature and evaporation rate of the coated graphite particle in the laser beam. The calculations reproduced the general features of observed waveforms of LII and scattering signals, providing a firm theoretical basis for the interpretation of the SP2 data. In conclusion, we have first demonstrated that the measurement of BC by SP2 is not affected by the co-existence of non-refractory compounds.

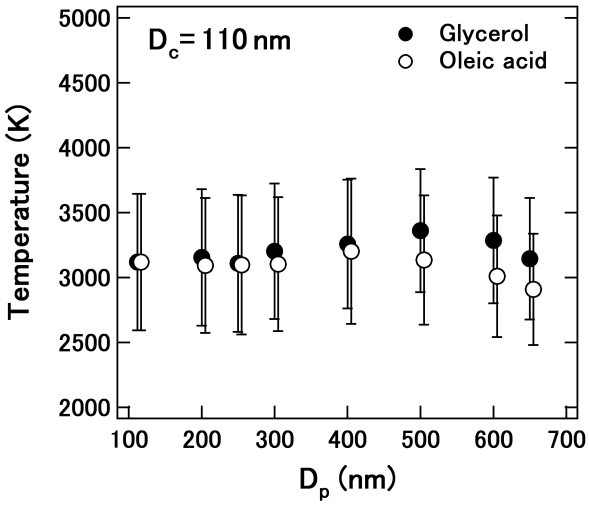

Fig. 8. D_p dependence of peak intensity of LII signal of organic-coated graphite particles with a core diameter (D_c) = 110 nm (from Moteki and Kondo, 2007). (*Aerosol Sci. Technol.*: Effects of mixing state on black carbon measurements by laser-induced incandescence. (41): 398–417. Copyright 2007. Reston, VA. Reprinted with permission.)

2.2 Selective detection of BC particles

LII signals of the SP2 from broadband (S_{bb}) and narrow band (S_{nb}) channels represent radiances at wavelengths $\lambda = 350$–800 nm and $\lambda = 630$–800 nm, respectively. Assuming that the emissivity (ε) of BC is independent of wavelength within the range of $\lambda = 350$–800 nm, the S_{bb}/S_{nb} ratio at time t when light-absorbing particles are in the laser beam, can be expressed approximately as:

$$S_{bb}/S_{nb}(t) \sim C\,[a + b \times T(t)] \tag{1}$$

where, a, b, and C are constants, determined from the optical characteristics of the photo detectors. By using Eq. (1), the particle temperature $T(t)$ can be determined independent of the absolute value of ε, if ε is independent of λ. The particle temperature T at the peak of the LII signal (T^{peak}) was used to estimate the chemical composition of the particle (e.g., metals, BC) (Stephens *et al.*, 2003; Baumgardner *et al.*, 2004; Schwarz *et al.*, 2006). In a strict sense, ε depends on the particle diameter, and the error in estimating T becomes significant for particles with diameters smaller than about 150 nm.

Schwarz *et al.* (2006) measured the T^{peak} (or the vaporization temperature) for different types of light-absorbing particles, including, nickel, chromium, chromium (III) oxide, vanadium, vanadium (V) oxide, iron, iron oxide, and aluminum, and BC. The T^{peak} of atmospheric BC ranged between 3700–4300 K and does not overlap significantly with the peak temperature of any other material tested. These tests indicate that the SP2 is selective of BC. Our T^{peak} data for the ambient BC at a number of locations in East Asia show the same T^{peak}, confirming the selective measurements of BC by the SP2.

doi:10.5047/meep.2015.00301.0001

2.3 Physical properties of BC and the calibration of the SP2

The SP2 quantifies the mass of BC inside individual particles by LII without interference from internally mixed semivolatile materials, as discussed above. To derive the absolute BC mass per particle for ambient aerosols, the SP2 has to be calibrated with appropriate calibration standards. Thus, we need to evaluate and select appropriate BC standards for this purpose. Intensities of incandescence were measured as a function of particle mass for various kinds of BC samples (Slowik *et al*., 2007; Shiraiwa *et al*., 2008). However, we need a theoretical framework for the interpretation of the relationship between the intensity of the incandescence signal and the microphysical properties of BC. We provide the physical basis for the interpretation of the relationship based on the descriptions given by Moteki and Kondo (2010).

In our previous studies, the range of the measured BC mass was limited to less than ∼60 fg, corresponding to a mass equivalent diameter (D_{BC}) of about 400 nm. The upper limit of the measured BC size corresponded to a saturation threshold of signal intensity for the data-acquisition system then available for the SP2, even though ambient BC particles are typically distributed in size ranges that exceed 400 nm. Since then, we have extended the upper limit of the detectable BC size to ∼900 nm by modifying the SP2's electronics and the data-acquisition system. We measured the characteristics of incandescence of various types of BC samples in the extended size range, combined with the theoretical interpretation of the results based on the general theory of thermal emission.

The vaporization temperatures of eight commercial BC samples and the ambient BC were found to differ by less than 2.2%, from the analysis of the time evolutions of the color ratio of incandescence in the SP2 laser beam. In the $x < \sim 1$ regime, the measured peak amplitude of incandescence was linearly proportional to the particle mass, as shown in Fig. 9. The size parameter x is defined as $x = kD_{\mathrm{BC}}/2$, where k is the wavenumber ($= 2\pi/\lambda$). D_{BC} is the mass equivalent diameter, i.e., BC mass $= \rho(\pi/6){D_{\mathrm{BC}}}^3$, where ρ is the density of BC, which is about 2 g cm^{-3}. The wavelength region of LII detected by the SP2 is unchanged and the emissivity of BC particles is not highly dependent on the wavelength (Moteki and Kondo, 2007). Therefore, the change in x is dominated by that of D_{BC}. The mass of the ambient BC was measured by removing non-BC compounds by heating BC-containing particles to about 400°C. The evaluation of the effects of heating is given in Section 2.4. The slopes of such correlations were positively correlated with the $|(m^2-1)/(m^2+2)|$ values, which were measured independently from the analysis of light scattering data (Moteki and Kondo, 2010). This correlation is consistent with the emissivity predicted by the Rayleigh-Gans theory, considering that $|(m^2-1)/(m^2+2)|$ was positively correlated with $\mathrm{Im}((m^2-1)/(m^2+2))$ (the imaginary part of $(m^2-1)/(m^2+2)$) for the range of measured $|(m^2-1)/(m^2+2)|$ values.

In the $x > \sim 1$ regime, the peak amplitude of incandescence is predicted to be proportional to the particle mass (volume) for an extremely non-compact shape, whereas it should be proportional to the 2/3 (= 0.667) power of particle mass (volume) for extremely compact shapes. Consistent with the theoretical prediction, the rates of the increase in the peak amplitude with the increase in the particle mass were negatively correlated with the effective density. The present measurements combined with the theoretical calculations clearly demonstrate the importance of taking into ac-

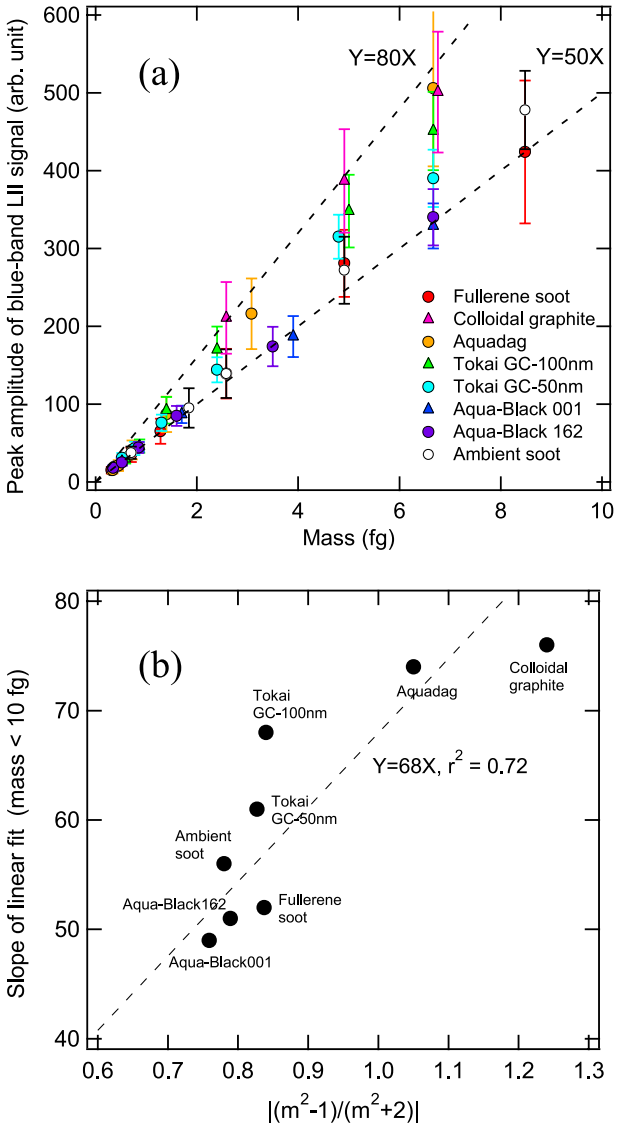

Fig. 9. (a) Measured relationship between peak amplitude of the blue-band incandescence signal and particle mass for particle masses up to 800 fg. Each data point and error bar indicates the average and standard deviation for ∼10^3 particles. The reference lines with approximately maximum and minimum slope values are shown as broken lines. (b) Relationship between the exponent of the power fit for the data in the upper panel (a) and the average effective density of BC samples for mobility diameters in the range of 400–900 nm. The theoretical limits according to the Rayleigh-Gans approximation and the geometrical optics approximation are also shown as dashed lines. The figures are from Moteki and Kondo (2010). (*Aerosol Sci. Technol.*: Dependence of laser-induced incandescence on physical properties of black carbon aerosols: Measurements and theoretical interpretation. (44): 663–675. Copyright 2010. Reston, VA. Reprinted with permission.)

doi:10.5047/meep.2015.00301.0001

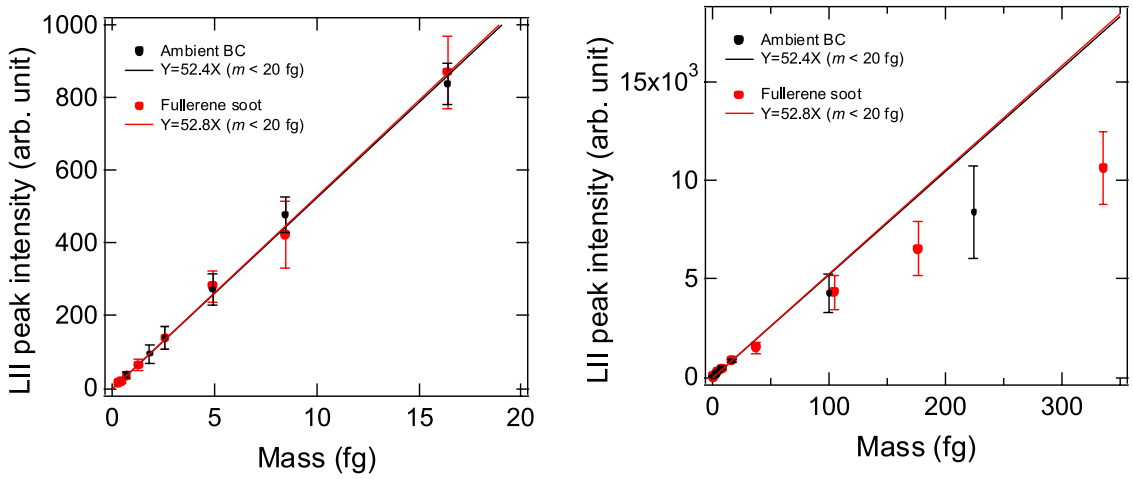

Fig. 10. Relationship between the LII peak intensity measured by the SP2 and the BC masses of ambient BC and fullerene soot (from Kondo *et al*., 2011b). (*Aerosol Sci. Technol*.: Consistency and traceability of black carbon measurements made by laser-induced incandescence, thermal-optical transmittance, and filter-based photo-absorption techniques. (45): 295–312. Copyright 2011. Reston, VA. Reprinted with permission.)

count the refractive index in the $x < \sim 1$ regime and the particle shape in the $x > \sim 1$ regime when selecting appropriate BC calibration standards for ambient BC measurements by the SP2.

Figure 10 shows plots of the LII peak intensity versus mass of ambient BC and fullerene soot (Kondo *et al*., 2011b). Of all the types of BC, we selected only ambient BC and fullerene soot for this plot in order to demonstrate clearly their similarity in the relationships between LII peak intensity and ambient BC mass. The masses of ambient BC and fullerene soot ranged up to 230 fg and 350 fg, respectively. The LII peak intensity increased linearly with mass up to about 20 fg. At higher masses, the relationship deviated from linearity. We attributed the similarity of the LII response of fullerene soot and ambient BC to the similarity in their microphysical properties: namely, their refractive indices and particle shapes. Although further investigations are needed on the refractive indices and particle shapes of other laboratory BC samples and ambient BC in other environments, these results support, for the first time, the use of fullerene soot as a calibration standard for the SP2.

2.4 Heated inlet for the calibration of the SP2

It is necessary to extract BC core in various aspects of BC measurements, including the calibration of the SP2 and accurate BC measurements by filter-based instruments. Evaluation of the heated inlet is discussed in this section, based on the descriptions by Irwin *et al*. (2013).

2.4.1 Necessity of heating inlet Calibration of the SP2 system is typically achieved using commercially available size- or mass-selected BC particles of known density, having a similar refractive index and particle shape to that of ambient BC. For studies monitoring atmospheric BC, the SP2 calibration should ideally be performed with ambient BC. However, ambient BC calibration particles cannot always be easily obtained in sufficient quantities and, consequently, a commercially available standard reference material is generally used as a proxy for ambient BC in the SP2 calibrations. The preferred calibration standard amongst the SP2 community is fullerene soot (Schwarz *et al*., 2006; Moteki and Kondo, 2007, 2010; McMeeking *et al*., 2010; Gysel *et al*., 2011; Kondo *et al*., 2011b; Spackman *et al*., 2011; Baumgardner *et al*., 2012), which has shown good agreement with ambient BC in Tokyo for SP2 calibration to within 10% for particle masses of up to 10 fg (Moteki and Kondo, 2010), and is insensitive to aerosol generation procedures (Gysel *et al*., 2011).

SP2 calibrations have been performed using ambient BC passed through a thermal-denuder set to 400°C to remove non-refractory, semi-volatile components (Kondo *et al*., 2011b). Gysel *et al*. (2011) and Laborde *et al*. (2012) investigated the SP2 sensitivity to fullerene soot downstream of a 400°C thermal-denuder and concluded that, despite the presence of non-BC components in the aerosol, fullerene soot should be used in an unheated form due to observed changes in the response of the SP2. Gysel *et al*. (2011) and Laborde *et al*. (2012) interpreted an increase in the incandescence intensity caused by heating BC standards to be a direct result of an increase in the BC mass fraction due to the removal of the presence of non-BC material coexistent in the calibration particles after thermal treatment at 400°C for a few seconds, prior to mass-selection. Thickly-coated BC particles have been efficiently treated by denuders operating at temperatures as low as 200°C (e.g. Ghazi and Olfert, 2013); however, it is common to find such use of thermal-denuders reported without explicitly stating the particle residence time (RT) in the heated section.

2.4.2 Laboratory experiments We have evaluated the performance of a thermal-denuder during fullerene soot and ambient BC calibrations of the SP2 by testing a range of denuder materials (stainless steel and glass), temperatures, and residence times. The impact of each of these parameters was determined by measuring the changes in BC mass, LII and scattering intensity. Unlike previous studies, we have measured changes in the mass of fullerene soot particles, after thermal treatment, using a tandem aerosol particle mass analyzer (APM) system.

doi:10.5047/meep.2015.00301.0001

The mass of monodisperse fullerene soot particles of initial mass 1.4 and 10.7 fg decreased by 9 and 11% respectively, for a denuder temperature of 500°C. Above 500°C, the particle number distribution became bimodal with a mode populated by a non-BC aerosol of lower mass, and the total number concentration was reduced significantly. This implies that an appropriate upper limit denuder temperature for achieving reliable BC calibration without distorting or losing the BC mass is around 400°C (mass losses $\leq 7\%$).

The SP2-derived LII intensity of fullerene soot particles with a mass of 1.4 fg increased by around 1% and 6% when passed through a denuder at 300°C and 400°C respectively, for a particle RT of about 2.5 s. The increase in the LII intensity was considerably larger for a denuder with a particle residence time of ~6 s (17% at 300°C and 400°C). Some increase in LII intensity is expected due to a higher relative BC mass in the aerosol particle, though this does not explain the simultaneous increase in the scattering intensity observed with denuder temperatures of 400°C and above. These results suggest that the microphysical or optical properties of BC (e.g. its refractive index) may have changed.

Ambient BC is typically internally mixed with non-refractory compounds. It is necessary to use denuders for calibration using ambient BC, which should be regarded as the primary standard. The increase in the LII intensity of ambient BC particles with a mass of 1.1 fg was about 4% between denuder temperatures of 200°C and 400°C, similar to the results for fullerene soot. In the light of these results, we recommend a denuder temperature of 300±50°C, with a corresponding particle RT of ≤2.5 s for calibration of the SP2 for BC measurements. With these parameters constrained, the uncertainty in the changes in LII intensity by heating should be less than 8%.

2.5 Coating thickness

Accurate measurement of the coating thickness of BC particles is critically important in estimating the light absorption by BC, as discussed in Chapter 5. In this section, a reliable method of determining BC coating thickness is presented based on the descriptions by Moteki and Kondo (2008).

An SP2 measures the differential scattering cross section integrated over angular ranges (ΔC_{sca}) of scattered light collection for individual particles. The size of flowing individual particles can be determined by the peak amplitude of the scattering signal $S(t)$, which is proportional to ΔC_{sca} of the particle (e.g., Pinnick *et al*., 2000), if ΔC_{sca} remains unchanged during the measurement. If the particle shrinks in the laser beam by evaporation due to heating, the ΔC_{sca} determined from the peak amplitude of the scattering signal is underestimated. The ΔC_{sca} of BC particles internally mixed with evaporative compounds (e.g., sulfate, organics) cannot be measured because of the particle evaporation problem mentioned above (Schwarz *et al*., 2006). Gao *et al*. (2007) proposed a method to estimate the ΔC_{sca} of BC-containing particles prior to evaporation by adding a position-sensitive detector to the SP2 for scattered light detection.

We have developed a new method to measure the time-dependent ΔC_{sca} of individual particles flowing across a Gaussian laser beam. This method is based on the principle that the normalized derivative of the scattering signal (S'/S) measured by the SP2 can be decomposed into the normalized derivative of the incident irradiance (I'/I) and that of the scattering cross section ($\Delta C'_{\mathrm{sca}}/\Delta C_{\mathrm{sca}}$). For evaporative particles, $S'/S = I'/I$ holds true until evaporation starts at a certain position in the laser beam. The $I(t)$ for individual particles is determined from I'/I, which is extracted from S'/S. $\Delta C_{\mathrm{sca}}(t)$ is derived from $I(t)$ and $S(t)$. We apply the method to particles with, and without, evaporation using the SP2. More detailed descriptions are given below.

2.5.1 Measurement system Figure 7 shows the schematic of the scattering probe of the SP2. A Gaussian continuous-wave laser beam (TEM_{00} mode) is used as a light source for particle irradiation. The aerosol flow intersects with the laser beam at right angles. The light elastically scattered by a transiting particle is assumed to be collected with constant efficiency over all angles where the particle is irradiated by the laser beam. The width of the laser beam is much wider than that of the aerosol flow such that particles always pass through the cross-sectional center of the laser beam. The particle transit velocity only depends on the flow rate of the carrier gas in the aerosol jet and does not depend on any other factors (e.g., particle size, effects of laser irradiation).

The incident irradiance $I(t)$ of the laser beam for individual particles is described by a Gaussian function with respect to elapsed time t:

$$I(t) = I_0 \exp\left(-\frac{(t-\tau)^2}{2\sigma^2}\right), \tag{2}$$

where I_0, τ, and σ denote the incident irradiance at the cross-sectional center of the beam, the center time, and 1-standard deviation (width) of the Gaussian function, respectively. The measured signal $S(t)$ of elastically scattered light by individual aerosols is proportional to the product of $I(t)$ and the $\Delta C_{\mathrm{sca}}(t)$ of the particle:

$$S(t) = sI(t)\int_{\Delta\Omega}\left(\frac{dC_{\mathrm{sca}}}{d\Omega}\right)d\Omega = sI(t)\Delta C_{\mathrm{sca}}(t), \tag{3}$$

where s denotes a proportionality constant that depends on the instrument, and $\Delta\Omega$ denotes the solid angle of light collection. As schematically shown in Fig. 7, for non-evaporative (i.e., non-light-absorbing) particles, $S(t)$ becomes a Gaussian function because ΔC_{sca} does not change with time during laser irradiation. In contrast, for evaporative (i.e., light-absorbing) particles, ΔC_{sca} changes due to evaporation of the particle inside the laser beam, and $S(t)$ deviates from the Gaussian function after the onset of evaporation. From Eqs. (2) and (3), the time-dependent scattering cross section $\Delta C_{\mathrm{sca}}(t)$ of the particle can be written as:

$$\Delta C_{\mathrm{sca}}(t) = \frac{1}{s}\cdot\frac{S(t)}{I(t)} = \frac{1}{sI_0}\cdot S(t)\cdot\exp\left\{\frac{(t-\tau)^2}{2\sigma^2}\right\}, \tag{4}$$

where $1/sI_0$ is an instrument-dependent constant that is calibrated by measuring the peak amplitude of the scattering signal (i.e., $S(t=\tau)$) of non-evaporative particles with known ΔC_{sca}. For evaporative particles, $\Delta C_{\mathrm{sca}}(t)$ can be determined

doi:10.5047/meep.2015.00301.0001

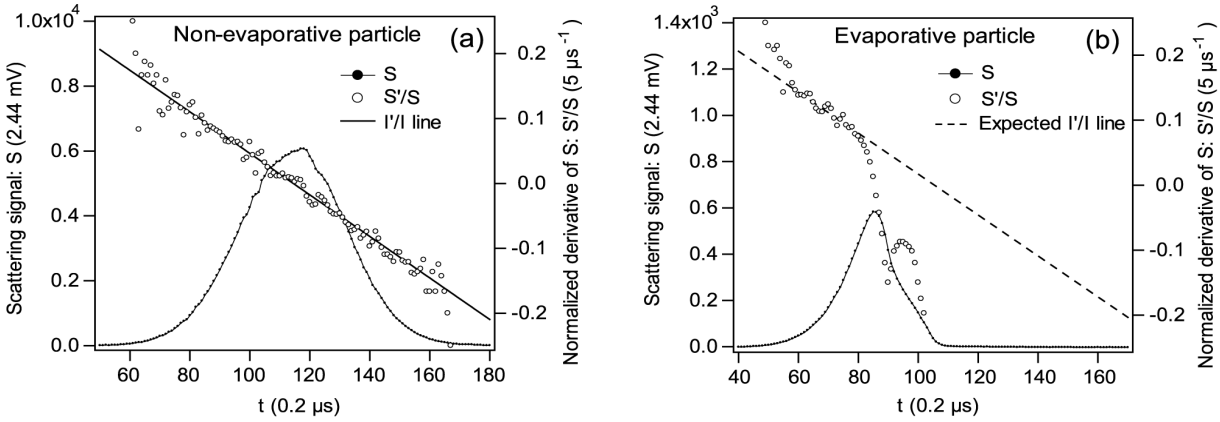

Fig. 11. Scattering signal (S) and normalized derivative of scattering (S'/S) observed for individual particles with, and without, evaporation. (a) Non-evaporative particle: polystyrene latex (PSL). (b) Evaporative particle: oil-coated graphite. The solid line in (a) indicates the I'/I function whose intercept and slope were determined by direct Gaussian function fitting of the $S(t)$ data. The solid line in (b) is the tentatively fitted I'/I line for the S'/S data segment at the leading edge ($60 < t < 80$). (Reprinted from *J. Aerosol Sci.*, *39*, Moteki, N., and Y. Kondo, Method to measure time-dependent scattering cross-section of particles evaporating in a laser beam, 348–364, Copyright 2008, with permission from Elsevier.)

from the measured $S(t)$ by Eq. (4) if both the center (τ) and width (σ) of the Gaussian function are known.

The $S(t)$ is digitized with 12-bit resolution ranging from -5 to $+5$ V (2.44-mV resolution). Hereafter, we denote t and $S(t)$ in units of 0.2 μs and 2.44 mV, respectively. Scattered light is collected over a solid angle of $\sim\pi/2$ sr around scattering angles of 45° and 135°. The $1/e^2$ power diameter of the laser beam is about 1 mm. The detectable range of particle diameters (D_p) for the SP2 is approximately 200–1000 nm for particles with optical properties equivalent to those of polystyrene latex. The width of the Gaussian function (σ) is about 3–4 μs, which depends on the ratio of the beam diameter to the flow rate of the carrier gas in the aerosol jet. In addition to the scattering signal, the laser-induced incandescence signal in the visible band (λ = 350–800 nm) is simultaneously measured by the SP2.

2.5.2 Theoretical framework The two unknown parameters τ and σ in the Gaussian function (Eq. (2)) need to be determined in order to estimate the $\Delta C_\mathrm{sca}(t)$ of evaporative particles. From Eq. (3), the normalized derivative of $S(t)$ (i.e., S'/S) can be decomposed into the normalized derivative of $I(t)$ (i.e., I'/I) and the normalized derivative of ΔC_sca (i.e., $\Delta C'_\mathrm{sca}/\Delta C_\mathrm{sca}$) as follows:

$$\frac{S'}{S}(t) = \frac{I' \cdot \Delta C_\mathrm{sca} + I \cdot \Delta C_\mathrm{sca}{}'}{I \cdot \Delta C_\mathrm{sca}} = \frac{I'}{I}(t) + \frac{\Delta C_\mathrm{sca}{}'}{\Delta C_\mathrm{sca}}(t). \quad (5)$$

If ΔC_sca is not changed by evaporation, or any other laser-induced change of the optical properties of the particle, S'/S is equal to I'/I. The I'/I of the Gaussian beam is derived from Eq. (2) as:

$$\frac{I'}{I}(t) = -\frac{1}{\sigma^2}(t - \tau). \quad (6)$$

This equation shows that I'/I is a linear function of t, whose slope and intercept are related to the center (τ) and width (σ) of the Gaussian function. The I'/I ratio equals 0 at the center of the Gaussian ($t = \tau$).

Figure 11(a) shows an $S(t)$ waveform measured by the SP2 for a non-evaporative particle (polystyrene latex) and the calculated S'/S. The solid line in Fig. 11(a) represents Eq. (6), with the τ and σ determined by direct nonlinear fitting of a Gaussian function onto the $S(t)$ data. Good agreement between the S'/S data points and Eq. (6) over the entire t-region is consistent with Eqs. (5) and (6).

Even strongly evaporative particles do not necessarily begin shrinking just after entering the laser beam. Figure 11(b) shows $S(t)$ and S'/S for an evaporative particle (oil-coated graphite). From this figure, it is expected that $\Delta C_\mathrm{sca}{}' = 0$ (i.e., $S'/S = I'/I$) at the leading edge ($60 < t < 80$), considering that the data points of S'/S linearly correlate with t very tightly in the t-region. The dashed line in Fig. 11(b) is a tentative fit to S'/S at $60 < t < 80$. The slope of the dashed line agrees well with that of the I'/I line in Fig. 11(a), supporting the expectation that $\Delta C_\mathrm{sca}{}' = 0$ at the leading edge of $S(t)$.

For evaporative particles, if the I'/I line is correctly determined from a S'/S data set in a t-region where $\Delta C_\mathrm{sca}{}' = 0$ holds, the center (τ) and width (σ) of the Gaussian function can be determined from the intercept and slope of the I'/I line. $\Delta C_\mathrm{sca}(t)$ can be calculated from these parameters using Eq. (4).

2.5.3 Measurements of evaporative particles Figure 12 shows typical examples of SP2 measurements for (a) glycerol-, and (b) oleic acid-coated graphite particles with (D_BC, D_p) = (110 nm, 500 nm). These figures show the time developments of the scattering signal and the LII signal (top), the normalized derivative of scattering (S'/S) and the statistical distance (d^2) (middle), and the normalized incident irradiance (I/I_0) and ΔC_sca (bottom). d^2 is the statistical distance between an S'/S data set and the I'/I line and is a quantitative measure to judge whether the S'/S data represent the I'/I line or not (Moteki and Kondo, 2008). The $\Delta C_\mathrm{sca}(t)$ value was calculated by Eq. (4) with the measured scattering intensity $S(t)$ and the determined Gaussian parameters (τ and σ). For the glycerol-coated graphite par-

doi:10.5047/meep.2015.00301.0001

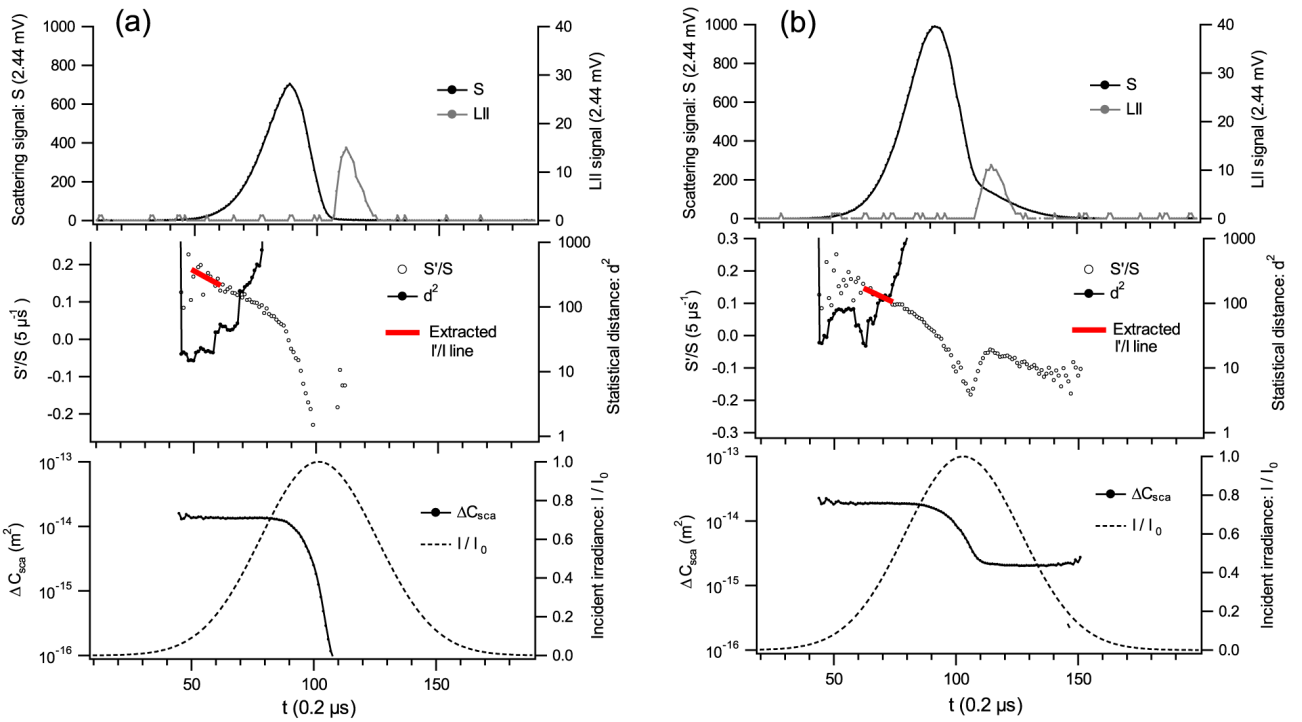

Fig. 12. Examples of the time development of important parameters for (a) glycerol- and (b) oleic acid-coated graphite particles with (D_{BC}, D_p) = (110 nm, 500 nm) (Moteki and Kondo, 2008). The important parameters shown in these figures are: the waveforms of scattering and LII signals (top); the rate of change of scattering (S'/S) and the statistical distance d^2 (middle); the Gaussian function of the incident irradiance (normalized by I_0) and the scattering cross section ΔC_{sca} (bottom). Red line segments appended on the middle figures denote the extracted I'/I functions with the smallest d^2 value. The length of the line segment indicates the length of the sub-array of S'/S data used for the statistical analysis. (Reprinted from *J. Aerosol Sci.*, *39*, Moteki, N., and Y. Kondo, Method to measure time-dependent scattering cross-section of particles evaporating in a laser beam, 348–364, Copyright 2008, with permission from Elsevier.)

ticle, the order of the timing of scattering and the LII signal shown in the top part of Fig. 12(a) indicate that the coating material has completely evaporated by $t \sim 105$ followed by heating of the graphite particle to its incandescent point ($T = 3000 \sim 4000$ K; Moteki and Kondo, 2007) at $t > 105$. In Fig. 12(a), the statistical distance d^2 continues to be about 10 at the leading edge ($45 < t < 60$) of the $S(t)$ waveform, indicating that the evaporation does not occur in this t-range. A change in ΔC_{sca} (i.e., $\Delta C_{sca}{}' \neq 0$) accounts for a dramatic increase in d^2 at $t > 75$.

The red line depicted in the middle part of Fig. 12(a) indicates the I'/I function extracted from a S'/S data set with the smallest d^2. The bottom part of Fig. 12(a) shows the normalized Gaussian function of $I(t)/I_0$ and $\Delta C_{sca}(t)$ derived from τ and σ estimated from the extracted I'/I line. The $\Delta C_{sca}(t)$ value does not change significantly at the leading edge ($t < 80$), followed by a rapid decrease at $t > 90$ due to evaporation. Using the relationship between particle size (D_{BC}, D_p) and $\Delta C_{sca}(t)$ the approximate time-dependent size of the particle in the laser beam can be estimated.

Figure 12(b) shows the results for oleic acid-coated graphite particles. In contrast to Fig. 12(a) (i.e., glycerol), the high intensity of $S(t)$ lasts even after the emission of the LII signal, indicating that a different evaporation phenomena occurs for this type of particle. The stepwise decrease of ΔC_{sca} around $t = 100$ followed by the second plateau of ΔC_{sca} in $t > 110$ indicates that the break up of the oleic acid-coated graphite occurs at $t \sim 100$–110.

2.5.4 Comparison with Mie theory Theoretical ${\Delta C_{sca}}^0$ values were calculated by Mie scattering theory for internally mixed particles. Mie calculations were made with various combinations of refractive indices of graphite and coating materials, to examine the uncertainty caused by assumed optical constants for these compounds. The Mie scattering codes of BHCOAT and BHMIE (Bohren and Huffman, 1983) were used for calculations with the shell-core model. Figure 13 shows measured and theoretical ${\Delta C_{sca}}^0$ of oleic acid-coated graphite particles with (a) $D_{BC} = 110$ and (b) 240 nm (D_{BC} is denoted as D_c in the figure). This figure shows that systematic deviations of the theoretical curves from the measurements are moderately small (i.e., within 30%) in the case of the graphite refractive indices of 2.0–0.8i or 1.8–0.6i and 1.46–0i or 1.35–0i for oleic acid. Further analysis shows that particles with a small D_p/D_{BC} ratio tend to evaporate rapidly inside the laser beam, and particles with large D_p/D_{BC} ratios evaporate very little. The systematic deviations of the theoretical curves from the measurements are moderately small (i.e., within 50%) in the case of graphite refractive indices of 2.0–0.8i or 1.8–0.6i and 1.35–0i for glycerol.

2.6 Attachment type of BC

In Section 2.5, a method of determining coating thickness was discussed. A more detailed measurement of the BC mixing state has become possible. This section discusses the

doi:10.5047/meep.2015.00301.0001

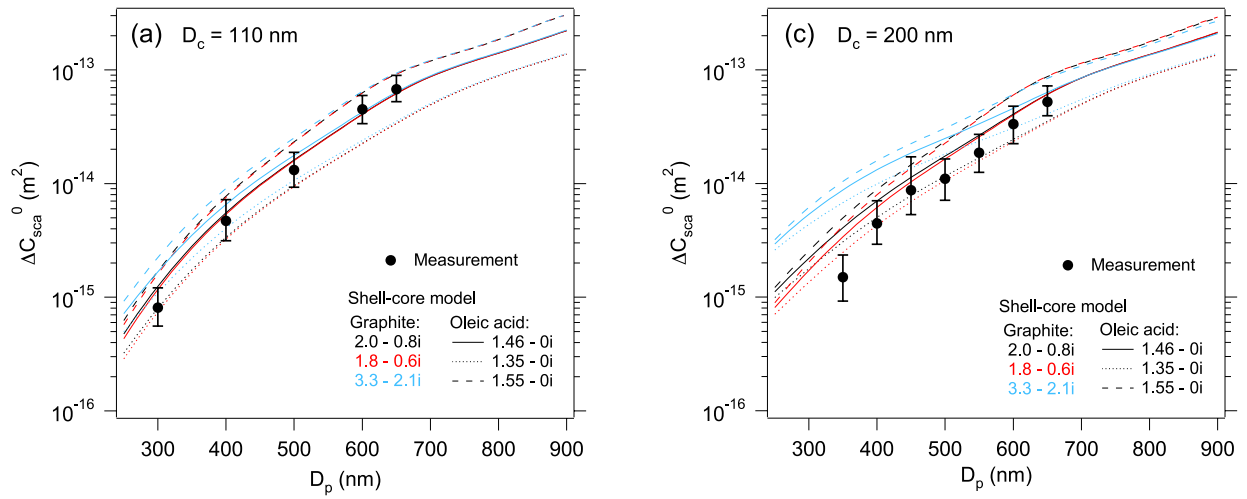

Fig. 13. Comparisons between measurement and theory for $\Delta C_{sca}(t)$ before the onset of evaporation ($\Delta C_{sca}{}^0$) for oleic acid-coated graphite particles with (a) a BC core diameter (D_c) = 110 nm, and (b) D_c = 240 nm (Moteki and Kondo, 2008). The filled circles denote the median values of each measurement for $\sim 10^3$ particles. The vertical bars indicate the ranges of the 25th–75th percentile values for each measurement. Theoretical prediction curves for $\Delta C_{sca}{}^0$ are shown for the shell-core model with various refractive indices of graphite and oleic acid. (Reprinted from *J. Aerosol Sci.*, *39*, Moteki, N., and Y. Kondo, Method to measure time-dependent scattering cross-section of particles evaporating in a laser beam, 348–364, Copyright 2008, with permission from Elsevier.)

method of quantifying the "attachment type" of the BC mixing state based on the descriptions by Moteki *et al.* (2014).

BC particles exist as bare BC or as internal mixtures of BC with non-BC compounds (mixed BC-containing particles). Mixed BC-containing particles can be broadly classified into two morphological types: bare BC on the surface of non-BC particles ("attached type"), or BC embedded within or coated by non-BC compounds ("coated type"). For the same amount of mixed non-BC compounds, enhancements of the mass absorption cross section of BC by the coated type are much larger than those of the attached type. Consequently, identification of the two morphological types in mixed BC-containing particles is important for understanding the impact of BC on climate.

Several studies have reported qualitatively on the relationship between the morphology of BC-containing particles and the signals observed by the SP2. Moteki and Kondo (2007) found that when the total particle size exceeds a certain limit, an oil-coated graphite particle can be fragmented during evaporation in a laser beam to form an uncoated graphite particle and a graphite-free oil droplet, possibly owing to the higher likelihood of eccentric positioning of graphite cores inside the particle volumes of larger droplets. An example of a time-dependent scattering cross section of a fragmenting oleic-acid-coated graphite particle (figure 7(b) of Moteki and Kondo (2008)) shows that the graphite-free oleic-acid droplet fragments from the graphite core before the onset of incandescence of the graphite, and the fragmented graphite-free droplet does not evaporate further in a laser beam. Sedlacek *et al.* (2012) found ambient BC-containing particles fragmented in a laser beam during a ground-based observation. They used the "negative lag-time"—the time lag of the peak of the scattering signal after the peak of the incandescence signal—as an indication of the fragmentation of BC-containing particles in a laser beam. They interpreted the morphology of such fragmenting particles to be the "near-surface type", in which the BC component is located near the surface of the particle.

In a quantitative study, Dahlkötter *et al.* (2013) identified fragmenting BC-containing particles in long-range transported forest-fire plumes from the scattering cross section of a BC-free fragment at the trailing edge of the laser beam. They also showed that the negative lag-time of Sedlacek *et al.* (2012) is a sufficient, but not necessary, condition for fragmentation: fragmentation does not guarantee a negative lag-time. Although fragmentation implies an eccentric location of the BC component in an internally mixed BC-containing particle, it does not indicate whether the BC component is embedded under the surface of the particle (a special case of the coated type) or attached on the surface of the non-BC particle (the attached type). Among mixed BC-containing particles of the near-surface type, the distinction between the coated and attached types is of critical importance for the accurate prediction of the mass absorption cross section (MAC) of BC.

Moteki *et al.* (2014) developed a new algorithm to classify mixed BC-containing particles into attached and coated types by using the SP2. This method identifies BC attached to the surface of non-absorbing particles and discriminates them from BC particles coated by non-absorbing compounds on the basis of time-dependent scattering cross-sections $C_s(t)$ measured by the SP2, as schematically shown in Fig. 14. $C_s(t)$ is the same as $\Delta C_{sca}(t)$ and "Scat." shown in Fig. 14 is the scattering signal $S(t)$ defined in the previous section. We verified our method by analyzing laboratory-generated BC-containing particles of two distinct morphological types: two-particle clusters consisting of fullerene soot and ammonium sulfate (attached type), and fullerene soot coated by oleic acid (coated type). Our algorithm uses the ratios of three scattering cross-sections: the total scatter-

doi:10.5047/meep.2015.00301.0001

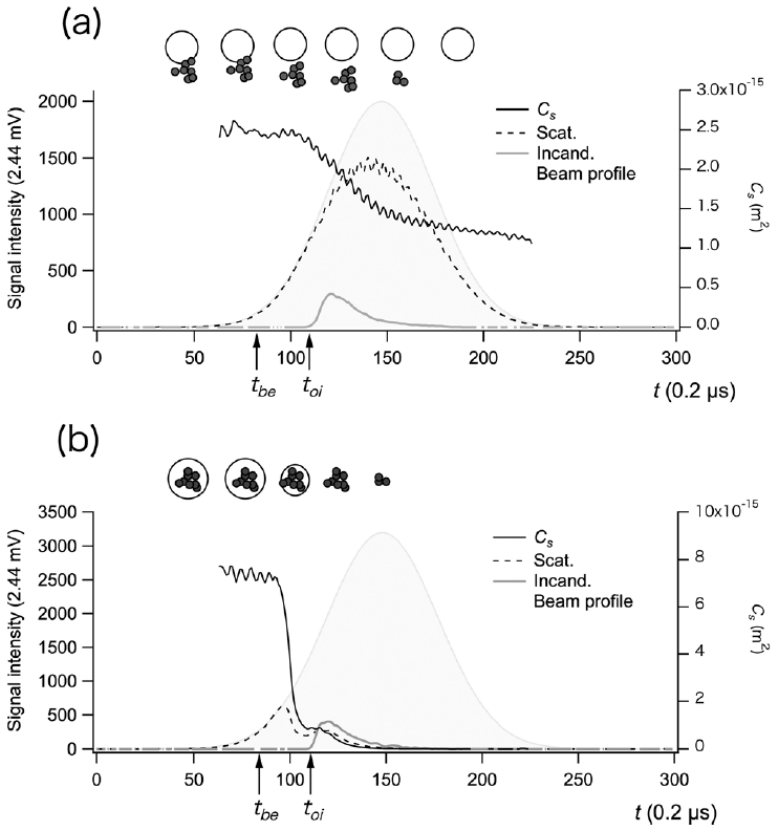

Fig. 14. Examples of waveforms of scattering and incandescence signals and $C_s(t)$ (time-dependent scattering cross section of particle estimated from scattering waveform) for (a) fullerene soot (FS) + ammonium sulfate (AS) two-particle cluster containing 25.3 fg AS and (b) oleic-acid-coated FS particle containing 25.9 fg oleic acid. Expected structural changes of the particles in a laser beam are shown schematically (from Moteki *et al*., 2014). FS mass was 8.0 fg in both cases. Time of onset of incandescence t_{oi} and time before evaporation t_{be} ($t = -2.5\sigma$) are also shown.

ing cross-section before evaporation $C_{s\text{-}be}$, the total scattering cross section at the onset of incandescence $C_{s\text{-}oi}$, and the scattering cross section of pure BC $C_{s\text{-}bc}$. For the ambient BC, $C_{s\text{-}bc}$ was determined from the BC mass M_{BC} using an empirical $C_{s\text{-}bc}$ (M_{BC}) function, obtained from the observation data.

We used the algorithm (Moteki *et al*., 2014) to identify the morphology of mixed BC-containing particles with a BC mass of ∼8.0 fg in ambient air in Tokyo. The observed number fractions of attached-type particles among morphologically identified BC-containing particles were generally less than 0.1. Further observations are needed of BC particles processed in different ways, to investigate the regional and global abundance of the attached type among mixed BC-containing particles.

2.7 Refractive index of BC

This section describes the methodology of determining the refractive index of BC and is based on the study of Moteki *et al*. (2010b).

According to Bond and Bergstrom (2006), primary estimates of the refractive index of BC were limited to less than 20 published papers in 2006. Among these papers, reported refractive indices for BC particles were quite diverse, possibly depending on the experimental approach and the method of sample preparation. The refractive indices of bulk matter can be determined by fitting Fresnel's formula onto reflectance and transmittance data of an optically flat surface (e.g., Bohren and Huffman, 1983). For this method, careful preparation of an optically flat surface is critically important to satisfy the applicability condition of Fresnel's formula. The refractive index of fine particulate matter can differ from bulk matter when its production process is gas-to-particle conversion rather than fracturing of parent bulk materials because of structural differences at the nanometer scale (e.g., degree of crystallization). Therefore, a direct knowledge of the refractive indices of small particles, rather than assuming the value of bulk matter, is desirable for accurate electromagnetic calculations of scattering and absorption by small particles.

Measurements of the refractive indices of small particles have been made via three distinct approaches: (1) fitting Fresnel's formula to reflectance and transmittance data measured for compressed pellets, (2) fitting Mie theory onto light-scattering data for individual spherical particles, and (3) fitting either Mie theory, or some approximation formulas, onto scattering and extinction data for particle ensembles. Approach (1) has been used widely to estimate the refractive indices of solid aerosols such as combustion-generated soot (Mullins and Williams, 1987). However, direct evidence of the optical flatness of pellet surfaces, which

doi:10.5047/meep.2015.00301.0001

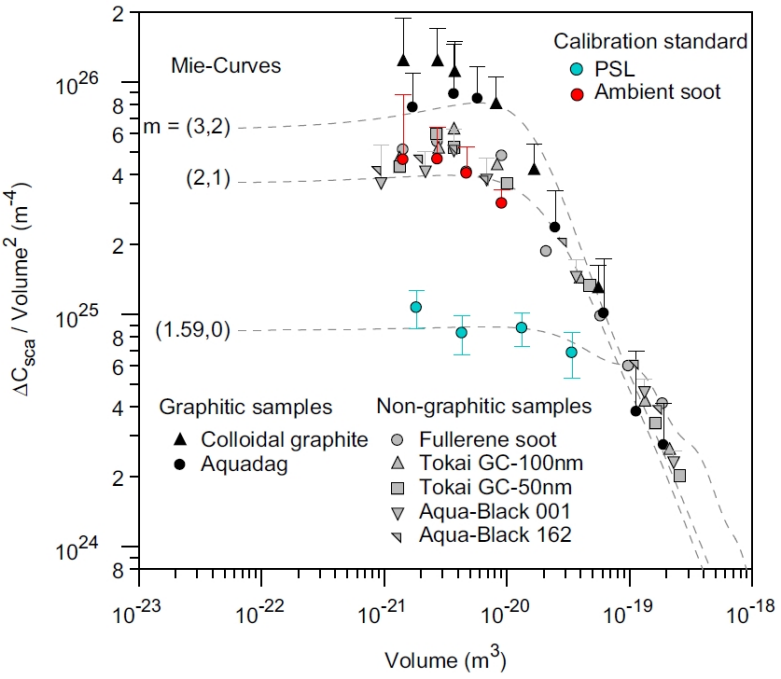

Fig. 15. Measured relationships between the partial scattering cross section divided by the square of the particle volume ($\Delta C_{\rm sca}/v^2$) vs. the particle volume (v) (Moteki *et al*., 2010b). Error bars are shown only for several selected species for graphical convenience. Theoretical curves determined with Mie theory for various complex refractive indices $m = (n, k)$ are also shown. (Reprinted from *J. Aerosol Sci*., *41*, Moteki, N., Y. Kondo, and S. Nakamura, Method to measure refractive indices of small nonspherical particles: Application to black carbon particles, 513–521, Copyright 2010, with permission from Elsevier.)

is necessary for the application of Fresnel's formula, has never been shown for wavelengths shorter than the infrared (Janzen, 1979). Therefore, it is difficult to confirm the reliability and reproducibility of the refractive indices derived by approach (1) for visible-to-near infrared wavelengths. In approach (2), measurements of resonance structures in Mie scattering can determine the refractive index with an accuracy of 10^{-5} (Chylek *et al*., 1983). However, this approach is limited only to spherical particles like liquid droplets. In approach (3), the refractive index and size distribution function are simultaneously inferred from extinction or scattering data for an ensemble of particles. Solving this inversion problem requires a theory to connect microphysical and light-scattering properties: the Mie theory has been used for spherical particles (Lack *et al*., 2009), and the Mie theory or the Rayleigh-Gans approximation have been used for nonspherical particles (Charalampopoulos *et al*., 1989; Van-Hulle *et al*., 2002). For polydisperse or nonspherical particles, the inversion results might depend on a simplification of the theories (e.g., constraints on the size distribution function, particle-to-particle variation in shape) that have never been a significant concern in previous studies.

Moteki *et al*. (2010b) introduced a new method to infer the refractive indices m of small particles by measuring the relationship between the scattering cross section ($\Delta C_{\rm sca}$) and the particle volume (v). For particles sufficiently smaller than the wavelength, the Rayleigh-Gans approximation holds and $\Delta C_{\rm sca}/v^2$ becomes proportional to $|(m^2-1)/(m^2+2)|^2$, as has been shown by laboratory experiments (Fig. 15). We determined the $|(m^2-1)/(m^2+2)|$ value from the average value of measured $\Delta C_{\rm sca}/v^2$ in $v < 4\times10^{-21}$ m^3 domain. The real and imaginary parts of m were determined from the measured $|(m^2-1)/(m^2+2)|$ value using an empirical model, as described in detail by Moteki *et al*. (2010b).

Because this method is insensitive to particle shape it can be applied to infer refractive indices of highly non-spherical BC particles. Particle volumes were estimated from measurements of mass by APM and assumed density. We have inferred the refractive indices of eight different BC samples (fullerene soot, colloidal graphite, Aquadag, glassy carbon-100 nm, glassy carbon-50 nm, Aqua-black 001, Aqua-black 002, and ambient BC) at 1064 nm wavelength and demonstrated the consistency between the inferred refractive indices and the microphysical structure observed by transmission electron microscope.

The values of $m(n, k)$ (n and k are the real and imaginary parts of the refractive index m, respectively) of the BC sampled derived by this method is summarized in table 1 of Moteki *et al*. (2010b). The refractive index of atmospheric BC sampled in Tokyo was determined to be (2.26±0.13, 1.26±0.13). This value is within the range of the m values of five commercial non-graphitic carbon samples as seen from table 1 of Moteki *et al*. and Fig. 15. This is a plausible value for the refractive index of ambient BC in urban areas and is useful for a quantitative improvement in the calculations of the climate effects of BC.

doi:10.5047/meep.2015.00301.0001

3. Filter-Based Photo-Absorption Technique for BC Mass Concentration

In this chapter, we discuss the filter-based measurement technology of BC mass concentration based mainly on the studies by Kondo *et al.* (2009, 2011b), Nakayama *et al.* (2010), and Moteki *et al.* (2010a). The consistency of different BC measurement technologies is also discussed, leading to an improved operational definition of BC.

3.1 Filter-based absorption photometers

The number and mass size distribution of BC can be measured accurately with an SP2, as discussed above. The mass concentration of BC (M_{BC}) can be derived by integrating the BC mass in each size bin:

$$M_{\mathrm{BC}} = \int \rho_{\mathrm{BC}} \left(\pi {D_{\mathrm{BC}}}^3/6\right) (dN_{\mathrm{BC}}/d\log D_{\mathrm{BC}})\, d\log D_{\mathrm{BC}}, \tag{7}$$

where ρ_{BC} is the density and $dN_{\mathrm{BC}}/d\log D_{\mathrm{BC}}$ is the number size distribution of BC, respectively, as a function of the BC core diameter (D_{BC}). However, it is often difficult to maintain high-quality BC measurements on a long-term basis using this method, especially at remote sites.

Filter-based photometers have been used to derive M_{BC} routinely from the measurement of the attenuation of light through filter media. Widely used filter-based photometers include the particle soot absorption photometer (PSAP; Radiance Research, Seattle, WA) (Bond *et al.*, 1999; Virkkula *et al.*, 2005), the continuous soot monitoring system (COSMOS; Kanomax, Osaka, Japan) (Miyazaki *et al.*, 2008; Kondo *et al.*, 2009), the aethalometer (Magee Scientific, Berkeley, CA) (Weingartner *et al.*, 2003; Arnott *et al.*, 2005), and the multi-angle absorption photometer (MAAP; Thermo Scientific, Franklin, MA) (Petzold *et al.*, 2002, 2005b; Petzold and Schönlinner, 2004; Kanaya *et al.*, 2013).

The absorption coefficient of airborne BC particles is defined from the Beer-Lambert law and is expressed as:

$$B_{\mathrm{abs}}(\lambda) = \int C_{\mathrm{abs}}(D_{\mathrm{BC}},\lambda)(dN_{\mathrm{BC}}/d\log D_{\mathrm{BC}})\, d\log D_{\mathrm{BC}} \quad [\mathrm{m}^{-1}], \tag{8}$$

where C_{abs} (D_{BC}, λ) [m^2] is the absorption cross section per particle and depends not only on D_{BC}, but also on other parameters, especially the mixing states of BC. The mass absorption cross section (MAC) for a given BC size distribution is defined as:

$$\sigma_{\mathrm{abs}} = B_{\mathrm{abs}}(SD)/M_{\mathrm{BC}} \quad [\mathrm{m}^2\ \mathrm{g}^{-1}], \tag{9}$$

Here, the dependence of B_{abs} on the size distribution (SD) of BC is explicitly denoted as B_{abs} (SD). The wavelength λ is omitted from now on because a single wavelength of 565 nm is used for COSMOS.

Absorption by aerosols in filter media is strongly enhanced by the multiple scattering of photons emitted from the light source, and this results in the high sensitivity of absorption photometers. However, as a result of multiple scattering, the Beer-Lambert law does not hold, as discussed quantitatively by Moteki *et al.* (2010a). Optical parameters derived from measurements by absorption photometers are different from those for airborne particles, including B_{abs} (SD). Not recognizing this often leads to the incorrect interpretation of the parameters derived by absorption photometers. Below, we clarify the principle and basis of the reliability of BC measurements by COSMOS.

3.2 Difficulties in estimating B_{abs}

Filter-based absorption photometers quantify the absorption of aerosols by measuring the reduction of irradiance through a filter loaded with aerosols, except for MAAP, which measures both transmittance and reflectance. In addition to absorption, scattering by aerosol particles loaded on the filter reduces the transmitted light. Operationally, the attenuation of light at a given wavelength is determined for filter-based absorption photometers by the following equation:

$$b_0 = (A/V)\ln[I_{t-\Delta t}/I_t], \tag{10}$$

where A is the area of the sample spot, V is the air sample volume during a given time period Δt (between $t - \Delta t$ and t), and $I_{t-\Delta t}$ and I_t are the average transmittances (Bond *et al.*, 1999). b_0 does not follow the Beer-Lambert law from the definition. The value of b_0 does not account for the magnification of absorption by the filter media, and nonlinearities in the response of the photometer as the filter is loaded. Correction factors have been introduced to convert b_0 to b_{abs}, to compensate for these effects:

$$b_{\mathrm{abs}} = f_{\mathrm{fil}} f_{\mathrm{amp}} b_0 - f_{\mathrm{sca}} B_{\mathrm{sca}}, \tag{11}$$

where f_{amp} represents the amplification of light absorption of BC and includes the effect of coating by non-absorbing compounds and the co-existence of non-absorbing particles, which are all embedded in the filter media (Schnaiter *et al.*, 2005; Mikhailov *et al.*, 2006; Bond *et al.*, 2006; Bond and Bergstrom, 2006; Cappa *et al.*, 2008; Shiraiwa *et al.*, 2010, and references therein). By using mono-disperse nigrosine ($C_{48}N_9H_{51}$) particles, Kondo *et al.* (2009) showed that the penetration depth of BC depends on its size, leading to the dependence of f_{fil} on BC size, which is unknown unless measured. In addition, the absolute uncertainties f_{fil} also arise associated with parameters involved in filtration (Moteki *et al.*, 2010a). f_{sca} is a correction factor for aerosol scattering. B_{sca} is the scattering coefficient of airborne aerosols, which needs to be measured independently of absorption photometers. Considering the uncertainties of the parameters that need to be measured simultaneously, it is difficult to reliably derive B_{abs} from b_0 measured by absorption photometers.

3.3 BC mass concentration by COSMOS

We now show that M_{BC} can be estimated reliably without being influenced by the uncertainties encountered in estimating B_{abs} from b_0. We first remove the effects of non-BC particles in Eq. (11) by vaporizing the volatile compounds (e.g., organics, sulfate, and nitrate) by heating the sampling inlet to 300–400°C, as discussed in Section 2.4. For nigrosine particles, $f_{\mathrm{sca}} B_{\mathrm{sca}}$ contributes less than about 2% to b_{abs} (Nakayama *et al.*, 2010). The same is true for BC particles passed through the heater and which can thus be neglected

doi:10.5047/meep.2015.00301.0001

hereafter. Hence, f_{amp} becomes close to 1 and

$$b_{abs} = f_{fil} b_0 \quad (12)$$

holds for a good approximation.

Bond *et al*. (1999) obtained f_{fil} for PSAP in the following form.

$$f_{fil}(Tr) = [1/(1.0796Tr + 0.71)]/B, \quad (13)$$

where Tr ($= I_t/I_{t=0}$) is the filter transmission and B is a constant scaling factor. This equation was derived using polydisperse nigrosine particles in the fine mode. According to Bond *et al*. (1999), $B = 1.22$, which was corrected to be $B = 1.397$ by Sheridan *et al*. (2005), although the value of B does not influence M_{BC} at all, as shown below.

f_{fil} (Tr) depends on aerosol size, as discussed above. We have determined particle size-dependent correction factors, f_{fil} (Tr, D_p), where D_p is the particle diameter, for two filter-based photometers, PSAP and COSMOS, using nigrosine particles (Nakayama *et al*., 2010). The size-dependent f_{fil} (Tr, D_p) corresponding to Eq. (9) was derived as:

$$f_{fil}(Tr, D_p) = [1/(1.0796Tr + 0.71)]/(B \times E(D_p)) = h(Tr)/B \times E(D_p), \quad (14)$$

$$E(D_p) = (0.594 \pm 0.032) + (155.3 \pm 6.5)/D_p, \quad (15)$$

$$h(Tr) = 1/(1.0796Tr + 0.71). \quad (16)$$

Recently, we obtained the form of h (Tr) for ambient BC in Tokyo (Irwin *et al*., 2015), which is slightly different from that given by Eq. (16). We do not discuss it here because the main point of this chapter is unchanged by this difference. The correction factor f_{fil} (Tr, SD) averaged over the entire BC size range, is expressed as follows by assuming lognormal BC size distributions with mass median diameters (MMDs) and σ:

$$f_{fil}(Tr, SD) = \frac{[h(Tr)]}{B \times E(SD)}, \quad (17)$$

$$E(SD) = \frac{\int_0^\infty E(D_p)\left(dM/d\log D_p\right) d\log D_p}{\int_0^\infty \left(dM/d\log D_p\right) d\log D_p}. \quad (18)$$

Now, we estimate the MAC of BC (σ_{abs}) from simultaneous measurements of b_0 by COSMOS (Eq. (10)) and the mass concentration of BC by the SP2 (M_{BC} (SP2)) for a given size distribution of BC. These measurements were made in Tokyo for about a month in 2009 (Kondo *et al*., 2011c). σ_{abs} is given as the average slope of the b_{abs}-M_{BC} (SP2) or f_{fil} (Tr, SD) b_0-M_{BC} (SP2) correlation for this period. Using Eq. (17):

$$\sigma_{abs}(\text{COSMOS, SP2}) = [b_{abs}/M_{BC}(\text{SP2})]_{av} = [f_{fil}(Tr, SD)b_0/M_{BC}(\text{SP2})]_{av} = [h(Tr)b_0/(B{\times}E(SD)M_{BC}(\text{SP2}))]_{av}, \quad (19)$$

where the subscript "av" denotes the average value of the quantity in the brackets. Here, we assume that σ_{abs} (COSMOS, SP2) does not depend on time and location. M_{BC} can then be determined from b_0 measured by COSMOS at any time and location by:

$$M_{BC}(\text{COSMOS}) = b_{abs}/\sigma_{abs}(\text{COSMOS, SP2}) = f_{fil}(Tr, SD)b_0/[f_{fil}(Tr, SD)b_0/M_{BC}(\text{SP2})]_{av} = [h(Tr)b_0/E(SD)]/[h(Tr)b_0/E(SD)M_{BC}(\text{SP2})]_{av}. \quad (20)$$

It should be noted here the constant B in Eq. (13) is cancelled out. If we further assume that E (SD) is also constant, it is also cancelled out and M_{BC} (COSMOS) is then expressed as:

$$M_{BC}(\text{COSMOS}) = [h(Tr)b_0]/[h(Tr)b_0/M_{BC}(\text{SP2})]_{av}. \quad (21)$$

The absolute accuracy of M_{BC} (COSMOS) depends also on the accuracy of M_{BC} (SP2) and b_0. The accuracy of M_{BC} (SP2) is estimated to be about 10% (Kondo *et al*., 2011b). The accuracy of b_0 depends on the uncertainties of A and V in Eq. (10) and is estimated to be about 5% (Miyazaki *et al*., 2008; Kondo *et al*., 2009). h (Tr) varies only by 20% for the Tr range between 0.7 and 1.0, set for COSMOS and does not lead to a significant uncertainty in M_{BC} (COSMOS). Assuming a constant σ_{abs} (COSMOS, SP2) is nearly equivalent to assuming a constant E (SD) and the validity of this assumption is shown below.

3.4 Stability of E (SD) and σ_{abs}

The M_{BC} (COSMOS)/M_{BC} (SP2) ratio is approximately proportional to $1/E$ (SD) as seen from Eq. (20). These values were obtained for the data obtained in Tokyo in 2009, which was used to determine σ_{abs} (COSMOS, SP2). The typical size distributions of BC measured by the SP2 are shown in Fig. 16. The mean MMD was 146±12 nm, with a mean geometrical standard deviation (σ_{gm}) of 1.82±0.14. The M_{BC} (COSMOS)/M_{BC} (SP2) ratio decreased by only 7% as MMD increased from 130 to 180 nm and changed little with aging as shown in Fig. 17. This suggests that E (SD) actually decreased by 7% and M_{BC} (COSMOS) was underestimated by not considering this change.

Nakayama *et al*. (2010) derived E (SD) as a function of MMD assuming $\sigma_{gm} = 1.6$ using E (D_p) given by Eq. (18) for nigrosine as shown in figure 6 of Nakawama *et al*. (2010). The calculated E (SD) decreased by about 20% for the same increase in MMD. It should be noted that the $E(D_p)$ data is for nigrosine and not for ambient BC. It is likely that differences in microphysical properties, including morphology, between the ambient of BC and nigrosine particles caused this difference. There is a need to measure $E(D_p)$ for BC to confirm this point. The field data indicates that the dependence of E (SD) on SD is small for BC and the assumption that E (SD) is constant holds to a good approximation.

In order to further evaluate the stability of the E (SD) or σ_{abs}, we made simultaneous measurements of b_0 by PSAP and COSMOS with heated inlets together with the BC mass concentrations by an EC-OC thermal optical transmittance (TOT) analyzer (M_{BC} (TOT)) to determine σ_{abs} (COSMOS, TOT) at 6 locations in Asia (Japan, Korea, China, and Thailand). We denote σ_{abs} (COSMOS, TOT) even for σ_{abs} (PSAP,

doi:10.5047/meep.2015.00301.0001

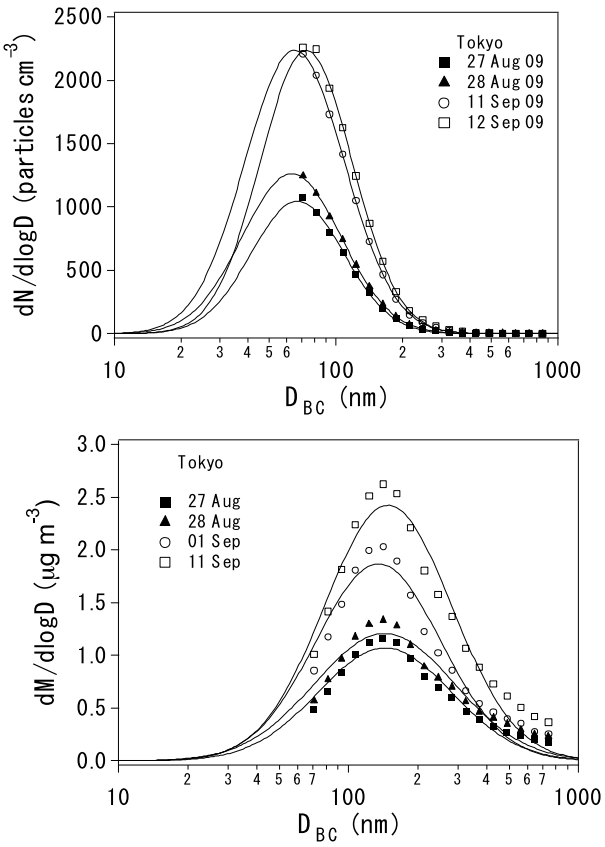

Fig. 16. Daily averaged number and mass size distributions of BC measured by the SP2 in Tokyo in August and September 2009 (Kondo *et al.*, 2011b). (*Aerosol Sci. Technol.*: Consistency and traceability of black carbon measurements made by laser-induced incandescence, thermal-optical transmittance, and filter-based photo-absorption techniques. (45): 295–312. Copyright 2011. Reston, VA. Reprinted with permission.)

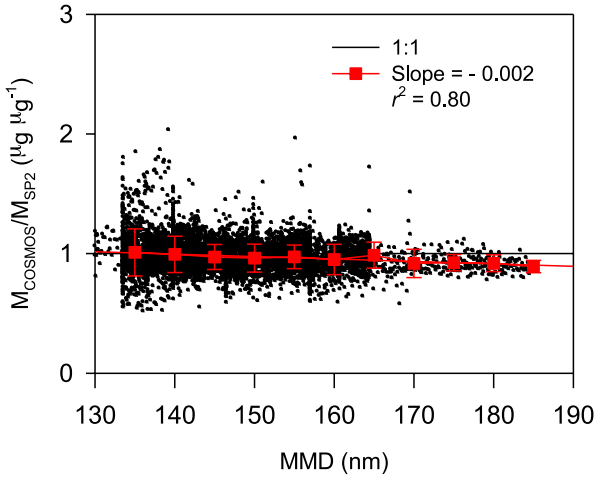

Fig. 17. M_{COSMOS} (BC mass concentration measured by COSMOS)/M_{SP2} (BC mass concentration measured by an SP2) ratio versus the MMD of BC. The solid black line is the least squares fitted line, and the red squares denote the mean $M_{\mathrm{COSMOS}}/M_{\mathrm{SP2}}$ ratios for 10-nm MMD bins (from Kondo *et al.*, 2011b). (*Aerosol Sci. Technol.*: Consistency and traceability of black carbon measurements made by laser-induced incandescence, thermal-optical transmittance, and filter-based photo-absorption techniques. (45): 295–312. Copyright 2011. Reston, VA. Reprinted with permission.)

TOT) for simplicity, because they should be the same for the same type of filters (PALLFLEX quartz filter E70-2075W) used (Irwin *et al.*, 2015). σ_{abs} (COSMOS, TOT) is defined by replacing M_{BC} (SP2) with M_{BC} (TOT) in Eq. (19). σ_{abs} (COSMOS, TOT) was stable to within 7% for BC strongly impacted by emissions from vehicles and biomass burning. The stable σ_{abs} (COSMOS, TOT) value provides a firm basis for the stability of the factor E (*SD*) independent of the location in Asia.

3.5 Effects of mineral dust and light-absorbing organic aerosol on BC measurements

The effect of mineral dust on the BC measurements was negligibly small on average in previous measurements in Asia (Kondo *et al.*, 2009). We confirmed this by using the observed mass concentrations of coarse particles, as detailed below. Mass concentrations of the particulate matter with size cutoffs at 2.5 μm ($PM_{2.5}$) and 10 μm (PM_{10}) were also measured at the Hedo observation site using a Tapered Element Oscillating MicroBalance (TEOM, RP1400) with an accuracy of 7% and Beta X-ray Absorption (Thermo-FH62-C14) with an accuracy of 10%, respectively. The Hedo observations are discussed in detail in Chapter 13. For this analysis, we have used $PM_{2.5}$ and PM_{10} observed during winter and spring, as lidar backscattering coefficients at 532 nm and 1064 nm and the depolarization ratio at 532 nm at Hedo suggested that the dust storms originating over the continent were expected to influence BC measurements at Hedo during these seasons (Yumimoto *et al.*, 2008; Sugimoto *et al.*, 2011).

The observed BC concentrations were highly correlated ($r^2 = 0.78$) with $PM_{2.5}$ for $\Delta PM < 50$ μg m^{-3} (not shown). Because of the high correlation, we assumed that BC can be approximately expressed as a function of $PM_{2.5}$, namely, $[BC^*] = (0.0295 \times [PM_{2.5}]) - 0.098$. BC_{ART} was estimated by subtracting $[BC^*]$ from the observed BC concentrations ($[BC_{\mathrm{obs}}]$). Namely, $[BC_{\mathrm{ART}}] = [BC_{\mathrm{obs}}] - [BC^*]$.

No correlation ($r^2 = 0.00$) was observed between BC_{ART} and ΔPM (Verma *et al.*, 2011). The average and median values also remained close to zero for the entire range of ΔPM. Thus, the effect of coarse particles on the BC measured by the COSMOS was assessed to be negligible.

The coexistence of organic aerosol (OA) causes significant uncertainties in BC measurements, depending on the techniques used. In order to assess the effects of OA, we measured the volatilities of 13 organic species with different molecular weights (MW) through a heated inlet, as described in detail in Kondo *et al.* (2011b). Four humic-like substances (HULIS) tested belong to high-MW organics. The low-MW organics were evaporated almost completely. Only about 10–30% and 20–60% of the volumes of the HULIS were lost at 300°C and 400°C, respectively. Because HULIS is light absorbing, the response of COSMOS gives us a measure of the interference of light-absorbing OA on BC measurements by COSMOS.

The laboratory experiments showed that the HULIS underwent partial charring, causing additional absorption in the COSMOS. Only about 5–12% of the carbon atoms contained in HULIS contributed to the equivalent BC mass concentra-

doi:10.5047/meep.2015.00301.0001

tion measured by COSMOS (equivalent M_{COSMOS}) with an inlet heated at 400°C. This interference is reduced by about a factor of 3 at 300°C. The charred carbon mass was found to be directly related with the signal of organic carbon that is resistant to volatilization in the He mode of EC-OC TOT analysis, defined as OC5. The [equivalent M_{COSMOS}]/[OC5] ratios were about 0.17 and 0.05, respectively, for the inlet temperatures of 400°C and 300°C.

The OC5 values measured by the TOT technique at the 6 locations in Asia were used to quantify the interference of OA to the M_{COSMOS}. The average errors on M_{COSMOS} due to the charring of refractory organics were estimated to be smaller than 5% in Asia. We recommend setting the inlet temperature at 300°C for COSMOS measurements.

3.6 Consistency and traceability of BC measurements

Figure 18 shows the correlation between M_{BC} (COSMOS) using σ_{abs} (COSMOS, TOT) and M_{BC} (SP2) measured in Tokyo in 2009. The M_{BC} (COSMOS) values were highly correlated ($r^2 = 0.97$) with M_{BC} (SP2). The derived σ_{abs} (COSMOS, SP2) agreed with σ_{abs} (COSMOS, TOT) to within 2%. This means that the masses of refractory aerosols in fine mode that incandesce were very close to M_{BC} (TOT). These results demonstrate that M_{BC} (SP2), M_{BC} (TOT), and M_{BC} (COSMOS) are nearly identical to a first approximation in Asia in the absence of pronounced effects of forest fires and dust particles. Throughout these studies, the COSMOS measurements were stable and traceable to the calibrated SP2 measurements to within about 10%. As discussed above, the first thorough intercomparisons of COSMOS, SP2, and TOT instruments established the analytical validity of BC measurements. This formed a firm basis for our aircraft and ground-based field studies of BC using SP2 and COSMOS.

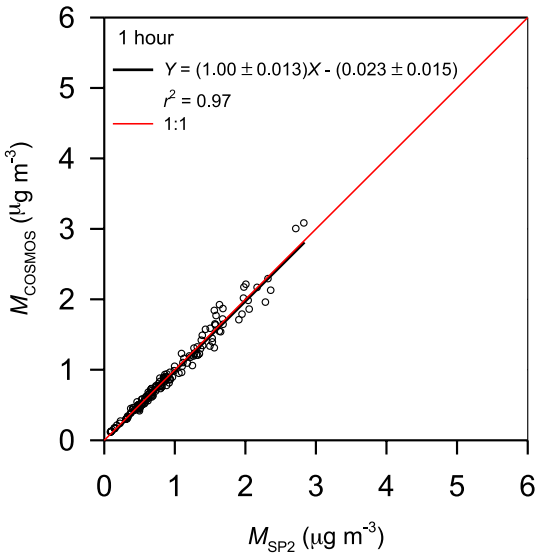

Fig. 18. Correlation plots of BC mass concentrations measured by an SP2 and those measured by COSMOS in 2009 using 1-hour average data. The least squares fitted line is denoted as the solid line (from Kondo *et al.*, 2011b). (*Aerosol Sci. Technol.*: Consistency and traceability of black carbon measurements made by laser-induced incandescence, thermal-optical transmittance, and filter-based photo-absorption techniques. (45): 295–312. Copyright 2011. Reston, VA. Reprinted with permission.)

4. Methods of the Measurement of BC in Rainwater and Snow

In this chapter, we describe the techniques to measure size distributions of BC suspended in water based on the studies by Ohata *et al.* (2011, 2013). The applications of the methods to field measurements are discussed in Chapter 13.

4.1 Methodology

Spatial and temporal variations of the wet deposition flux of BC are controlled by a series of complex processes. Freshly-emitted BC particles from fossil fuel sources are hydrophobic. However, they become active as cloud condensation nuclei (CCN) by their coating with hygroscopic materials (e.g., Dusek *et al.*, 2006; Kuwata *et al.*, 2007, 2009). The CCN activity of BC particles is controlled by their size and mixing state. Under supersaturation conditions of water vapor, aged BC particles are activated into cloud droplets. Depending on the liquid water content available, the formed droplets grow into raindrops followed by precipitation. The transport efficiency of BC has been observed to decrease with the amount of precipitation that air masses experience during transport from the planetary boundary layer (PBL) to the free troposphere (FT) (Matsui *et al.*, 2011b; Oshima *et al.*, 2012). Below-cloud scavenging of aerosols with diameters of 0.05–1 μm by falling raindrops is not efficient (Slinn, 1983; Seinfeld and Pandis, 2006), the so-called Greenfield gap. However, these complex processes are not fully understood, due to a lack of appropriate observations.

BC particles deposited in or on snow can reduce the snow albedo and may accelerate snow melting (Warren and Wiscombe, 1980; Clarke and Noone, 1985). The concentration of BC in surface snow can be important for determining the extent of these effects (Schwarz *et al.*, 2013).

The concentration of BC in rainwater and snow is a useful parameter regarding a detailed understanding of the wet deposition of BC. Three principal methods are currently used for quantifying the mass concentration of BC in liquid water samples. The first method utilizes the thermal optical transmittance (TOT) technique (Ogren *et al.*, 1983; Hadley *et al.*, 2008; Wang *et al.*, 2011). In this method, the liquid water sample is filtered, and the BC particles retained on the filter are thermally converted into CO_2. This method can also provide the mass concentration of organic carbon (OC) suspended in water samples. The major uncertainty of the method derives from the collection efficiency of the filter and the separation of the BC/OC contributions in the analysis. Different protocols of the analytical procedures may introduce additional uncertainties. Wang *et al.* (2011) also reported the effect of dust on the quantification of BC.

The second method, which also uses a filter to collect particulate matter suspended in liquid samples, utilizes the Integrating Sphere/Integrating Sandwich Spectrometer (ISSW) (Doherty *et al.*, 2010; Granfell *et al.*, 2011). The ISSW uses a multiple-wavelength light emitting diode and measures the attenuation of the light passing through the filter as a function of wavelength. Absorption by BC and non-BC material

doi:10.5047/meep.2015.00301.0001

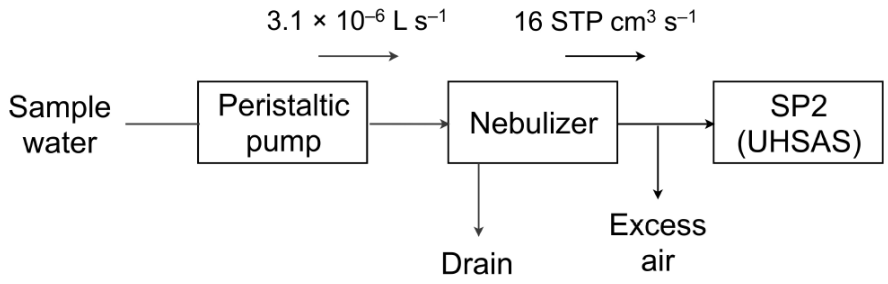

Fig. 19. Schematic of experimental setup for measuring BC particles or PSL (polystyrene latex) spheres in water samples (from Ohata *et al*., 2013). For the measurement of BC, only the SP2 was used; for measurement of the PSL spheres, either the SP2 or the UHSAS was used. (*Aerosol Sci. Technol*.: Evaluation of a method to measure black carbon particles suspended in rainwater and snow samples. (47): 1073–1082. Copyright 2013. Reston, VA. Reprinted with permission.)

is differentiated by assuming the absorption angstrom exponent of the non-BC material. The mass concentration of BC is quantified from the BC absorption, via the assumption of a mass absorption coefficient of BC. The major uncertainties in this method derive from the collection efficiency of the filter used and the assumed optical properties.

The third method, which we evaluate in this study, consists of an ultrasonic nebulizer (USN) and an SP2 (McConnell *et al*., 2007; Kaspari *et al*., 2011; Ohata *et al*., 2011; Schwarz *et al*., 2012), as shown in Fig. 19. The USN disperses a liquid sample into micron-size droplets and then dries them to release BC particles into the air. The extracted particles are transferred to the SP2, which measures the masses of the individual BC particles. The advantage of this method is that it typically requires less than 5 mL of sample water for analysis, substantially less than that required for the filter-based techniques. In addition, the SP2 is little affected by dust. The main uncertainty of this method derives from determining the efficiency of the USN in releasing BC particles in liquid water to air. In most of the aforementioned studies, the efficiency is considered to be a constant independent of the properties of the particles in the liquid samples. However, Schwarz *et al*. (2012) showed that the efficiency depends strongly on particle size, and the size dependence was different for the USN and the Collison-type nebulizer (CTN) used in the study.

Despite the increasing use of the USN-SP2 method for measuring BC particles in rainwater, snow, and ice samples, an in-depth evaluation of the method has not been carried out. A systematic evaluation of this method is described below.

4.2 Experimental setup

The experimental setup shown in Fig. 19 consists of a peristaltic pump (REGRO Analog, ISMATEC SA., Feldeggstrasse, Glattbrugg, Switzerland), an USN (U-5000AT, Cetac Technologies Inc., Omaha, NE, USA), and an SP2 (Ohata *et al*., 2011). The pump feeds sample water to the USN at a constant flow rate of 3.1×10^{-6} L s^{-1}, and the USN converts a fraction of the sample water into micron-sized ($\sim$10 μm) droplets. The droplets evaporate while passing through a tube heated to 140°C, and the nonvolatile particles in the droplets are released into the air. A cooling stage at 3°C then removes the water vapor from the air. The extracted particles are transferred to the SP2 at a constant gas flow rate of 16 cm^3 s^{-1} (STP). The masses of individual BC particles with mass-equivalent diameters of between 70 and 850 nm are measured without interference from non-absorbing particles, using an SP2. The SP2 also has two avalanche photodiodes (APDs) for detecting scattering signals, which allow quantification of scattering particles with sizes between around 170 and 850 nm.

The Ultra-High Sensitivity Aerosol Spectrometer (UHSAS) is an optical particle counter covering a wide range of scattering particles with sizes between about 60 and 1500 nm. Characterization of the UHSAS can be seen in Cai *et al*. (2008). The UHSAS utilizes an intra-cavity Nd^{3+}:YLF laser with a wavelength of 1054 nm and detects scattering signals by two pairs of Mangin mirrors and APDs. In the present study, we used the SP2 and the UHSAS to measure polystyrene latex (PSL) spheres with sizes of 202–771 nm and 107–1025 nm, respectively, to determine the size-dependent extraction efficiency of the USN. PSL spheres with diameters of 202, 309, and 402 nm were used to check the instrumental performance. PSL concentrations in air measured by the SP2 and UHSAS were in agreement within 10%.

The extraction efficiency (ε) of the USN was determined as a function of the PSL diameter (D_{PSL}) by the following equation:

$$\varepsilon(D_{\mathrm{PSL}}) = \frac{N_{\mathrm{SP2/UHSAS}} \cdot F_{\mathrm{neb}}}{n_{\mathrm{samp}}(D_{\mathrm{PSL}}) \cdot V_{\mathrm{pump}}}. \quad (22)$$

Here, $N_{\mathrm{SP2/UHSAS}}$ is the number concentration of PSL spheres in air measured by the SP2 or UHSAS (cm^{-3}), F_{neb} is the nebulizer gas flow rate (cm^3 s^{-1}), n_{samp} (D_{PSL}) is the size-resolved number concentration of PSLs in water (L^{-1}), and V_{pump} is the liquid flow rate of the pump (L s^{-1}). n_{samp} was determined by an extinction measurement, as detailed below. The values of the constants F_{neb} and V_{pump} are 16 STP cm^3 s^{-1} and 3.1×10^{-6} L s^{-1}, respectively. We assumed:

$$\varepsilon(D_{\mathrm{PSL}}) = \varepsilon(D_{\mathrm{BC}}), \quad (23)$$

where D_{BC} is the volume-equivalent diameter of the BC particles. Then the BC mass concentration in sample water,

doi:10.5047/meep.2015.00301.0001

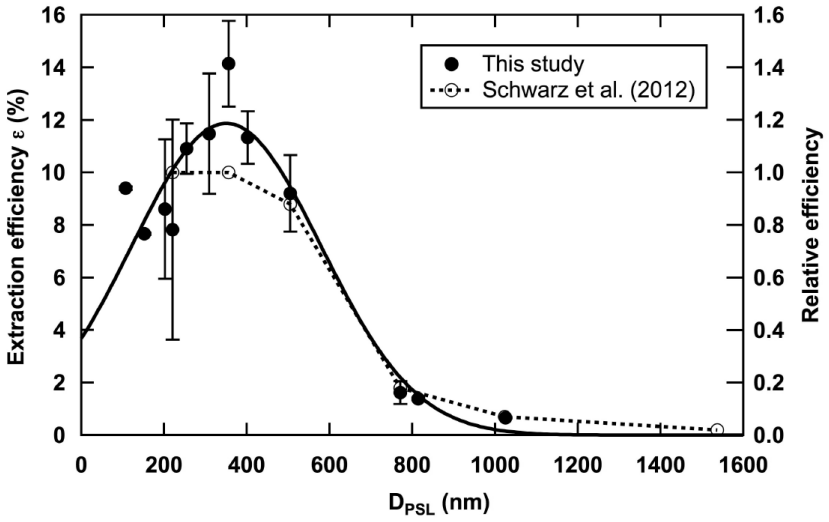

Fig. 20. Size-dependent extraction efficiency of the USN (from Ohata *et al*., 2013). Bars show 1σ values derived from repeated measurements over 6 months. For PSL spheres with diameters of 107, 152, 814, and 1025 nm, two PSL suspensions of known concentration were measured for each diameter within 1 day, and therefore their 1σ values were much smaller than those of the other data. The solid curve indicates Gaussian fitting to the data. The relative extraction efficiency of the USN reported in Schwarz *et al*. (2012) is also shown. The efficiencies for PSL spheres with diameters of 220 and 350 nm were similar and therefore set to be 1, and the efficiencies for the other sizes are relative to them. (*Aerosol Sci. Technol*.: Evaluation of a method to measure black carbon particles suspended in rainwater and snow samples. (47): 1073–1082. Copyright 2013. Reston, VA. Reprinted with permission.)

m_{samp} (μg L^{-1}), was determined by:

$$m_{\mathrm{samp}} = \int_{70}^{850} \frac{dm_{\mathrm{samp}}}{d\log D_{\mathrm{BC}}} d\log D_{\mathrm{BC}} = \int_{70}^{850} \frac{F_{\mathrm{neb}} \cdot \frac{dM_{\mathrm{SP2}}}{d\log D_{\mathrm{BC}}}}{V_{\mathrm{pump}} \cdot \varepsilon(D_{\mathrm{BC}})} d\log D_{\mathrm{BC}}. \quad (24)$$

Here, $dm_{\mathrm{samp}}/d\log D_{\mathrm{BC}}$ is the mass size distribution of BC in the sample water (μg L^{-1}), and $dM_{\mathrm{SP2}}/d\log D_{\mathrm{BC}}$ is the mass size distribution of BC in air measured by the SP2 (μg cm^{-3}). Only the mass concentration in the size range of detection of the SP2 (70–850 nm) was calculated.

4.3 PSL number concentration in water

The diameters of the PSL spheres used in this study ranged between 107 and 1025 nm. n_{samp} (D_{PSL}) was determined for each PSL suspension by placing the PSL suspension in a rectangular acrylic cell and measuring the attenuation of a 532-nm laser beam (GSHG-3020F, KTG Co. Ltd., Kochi, Japan). $n_{\mathrm{samp}}(D_{\mathrm{PSL}})$ was determined by using the Beer-Lambert law (e.g. Hinds, 1999) with an uncertainty of 8%:

$$n_{\mathrm{samp}}(D_{\mathrm{PSL}}) = \frac{4}{\pi \cdot D_{\mathrm{PSL}}^2 \cdot Q_{\mathrm{PSL}} \cdot L} \ln\left(\frac{I}{I_{\mathrm{ref}}}\right). \quad (25)$$

Here, Q_{PSL} is the extinction efficiency of the PSL calculated by Mie theory (Bohren and Huffman, 1983). We assumed an ideal monodisperse size distribution of the PSL with a refractive index of $1.59 + 0i$. L is the length of the acrylic cell (30.0 cm). I and I_{ref} (W cm^{-2}) are the intensities of the laser passing through the PSL suspensions and pure water, respectively.

4.4 Laboratory BC samples

Three kinds of laboratory BC samples were tested: two fullerene soot samples (Alpha Aeser, Inc., Wardhill, MA, USA, Stock No. 40971, Lots F12S011 and G25N20), which are dry powders; and AquaBlack 162 (Tokai Carbon Co. Ltd., Tokyo, Japan), a carbon black liquid ink. The procedure for generating known concentrations of fullerene soot in water is described in Schwarz *et al*. (2012). The BC particles in AquaBlack 162 were stably dispersed in water without sedimentation or coagulation, due to the manufacturer's treatment of the surface of individual BC particles by carboxyl groups.

The measured mass size distributions of BC in the laboratory-generated BC samples are shown in figure 3 of Ohata *et al*. (2011). The size distributions were determined by taking the size-dependent extraction efficiency of the USN into consideration.

4.5 Size-dependent nebulizer efficiency

A large fraction of the BC particles in the water samples is lost during nebulization and transport in the USN tubing. Using Eq. (22) and the size-resolved PSL suspensions detailed above, we determined the size-dependent extraction efficiency of the USN, as shown in Fig. 20. The number concentration of PSL spheres in air detected by the SP2 during each measurement was stable to within 10%. For these measurements, we counted each PSL sphere only within the appropriate size range. The fraction of doublets, which consist of two coagulated PSL spheres, was <9% from the SP2 and UHSAS data and was excluded from our analysis. The efficiency showed a broad maximum of about 10% in the diameter range 200–500 nm and decreased substantially at larger sizes. The overall uncertainty of the measured BC concentration in water (m_{samp}) was calculated to be $\pm$25% for this size range of BC and under the assumption that Eq. (23) is valid.

doi:10.5047/meep.2015.00301.0001

4.6 Reproducibility

Rainwater was collected in glass beakers in Tokyo to test the reproducibility of the measured BC size distributions and BC mass concentrations in samples after long-term storage. Immediately (<2 h) after sampling, the sample water was transferred to a glass bottle and analyzed. After analysis, the sample was kept in a refrigerator and reanalyzed about 1 month later and again 12 months later. The rainwater sample was agitated by an ultrasonic bath (UB) for 15 minutes just before analysis to disperse BC particles and detach them from the wall of the container. The change in the measured total mass concentration of BC during storage was within 35%.

Reproducibility of the measured mass concentration after long-term storage was also determined for another rainwater sample collected in Okinawa in Japan over the East China Sea. Although this sample was not analyzed on the day of sampling, the BC mass concentrations measured after 2 and 9 months were higher by 33% and lower by 10% than that of the first measurement, respectively. Therefore, reproducibility of the measured mass concentration for this sample was also within 35%.

4.7 Loss of BC to the walls of containers

To assess the loss of BC particles due to their attachment to the walls of the glass container during storage, five rainwater samples collected in Tokyo were analyzed after storage for 9 months in the refrigerator, with and without agitation by an UB for 15 min just before analysis. We found that when the samples were simply shaken by hand (i.e., no UB agitation), the mass concentrations of BC in all five samples were lower by (18±13)% on average, than the concentrations measured after UB agitation. The systematic underestimation indicates that the UB agitation just before analysis and transfer of sample water to other bottles is required for an improved analytical accuracy.

4.8 Overall uncertainty

In summary, the reproducibility of the measured mass concentration in rainwater after refrigerated storage in glass containers for 12 months was ±35%. Agitation of the sample water by an UB reduced the effect of the attachment of BC particles to the wall of the container. This provides the basis in constraining the uncertainty of the measurement of BC concentrations in water. One of the largest uncertainties in measuring the size distributions of BC in water is the relatively large size dependence and variability in the extraction efficiency of BC. In addition, BC size distribution can extend beyond the upper limit of the current SP2 (Schwarz *et al*., 2012), indicating the necessity of extending the upper limit of the BC size that can be measured by the SP2.

5. Amplification of the Light Absorption of BC

Internal mixing between BC and other compounds increases the absorption of visible light, in part, because the non-absorbing material can refract light toward the absorbing particle (Ackerman and Toon, 1981; Bond *et al*., 2013). Recent results on this effect by laboratory experiments are reviewed by Bond *et al*. (2013). In short, the absorption increase is low for very thin coatings (Slowik *et al*., 2007) and increases by a factor up to about 2 for thicker coatings (Schnaiter *et al*., 2005; Khalizov *et al*., 2009; Cross *et al*., 2010; Shiraiwa *et al*., 2010; Bueno *et al*., 2011). In this chapter, the evaluation of this effect by laboratory experiments is presented based on the descriptions by Shiraiwa *et al*. (2010).

5.1 Laboratory measurements

Direct measurements of the amplification of BC by internal mixing are still limited. Previous studies focused on the optical properties of coated BC with ozonolysis products of α-pinene (Schnaiter *et al*., 2005), water (Mikhailov *et al*., 2006), oleic acid (Slowik *et al*., 2007), wax (Gangl *et al*., 2008), and sulfate (Zhang *et al*., 2008; Khalizov *et al*., 2009). In most of these studies, the photo-absorption coefficients were measured by taking the difference between the extinction and scattering coefficients. Photo-absorption was shown to be amplified by a BC coating. However, we still need to characterize the amplification of the photo-absorption of coated BC as a function of coating thickness along with a comparison with Mie theory in detail.

We measured the amplification of the photo-absorption by BC as a function of shell/core diameter ratio (i.e. coating thickness). Graphite particles were used as a surrogate for BC. The physical properties (i.e., refractive index, density) of graphite are similar to those of ambient BC (Bond and Bergstrom, 2006). The absorption was measured directly using the photoacoustic technique (Arnott *et al*., 2003), which can provide non-destructive, airborne measurements. BC particles with known core diameters are coated with organic compounds using a tandem differential mobility analyzer (TDMA) system (Moteki and Kondo, 2007). The coating thickness and size distribution of the coated particles are measured using an SP2. The amplification of absorption is measured as a function of the coating thickness and compared with model calculations based on Mie theory.

Graphite particles (Alfa Aesar, Inc., Ward Hill, MA, USA) used in this study were observed to be non-aggregates by transmittance electron microscopy (TEM) (figure 2, Moteki and Kondo, 2007), suggesting that their shapes changed very little by the condensation of organics (Moteki and Kondo, 2007). The mass-equivalent diameters (D_{BC}) of graphite particles with given mobility diameters were measured using a differential mobility analyzer (DMA)-APM system (McMurry *et al*., 2002). D_{BC} is calculated as $D_{\mathrm{BC}} = (6M/\pi\rho)^{1/3}$, where M is the particle mass and ρ is a graphite particle density of 2.28 g cm^{-3} (Michelsen, 2003). D_{BC} with mobility diameters of 150, 200, 250, and 300 nm were measured to be 123, 185, 234, and 281 nm, respectively. The dynamic shape factors were calculated to be ∼1.2, indicating that they were non-spherical.

The refractive index (m) of graphite was reported to be $m_{\mathrm{graphite}} = 2.65 - 1.39i$ at a wavelength (λ) of 533 nm (Stagg and Charalampopoulos, 1993). The real and imaginary parts of the refractive index given by Bond and Bergstrom (2006) are in the range of 2.0–3.3 and 0.7–2.1, respectively.

For the interpretation of the measurements, the absorption cross section (C_{abs}) of graphite was calculated by Mie theory assuming that the particles were dense and spheri-

doi:10.5047/meep.2015.00301.0001

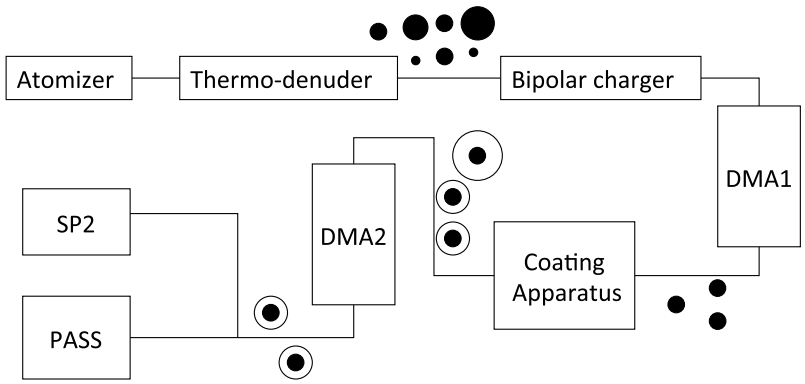

Fig. 21. Schematic of the laboratory experiment for measuring the absorption of organic-coated graphite particles (from Shiraiwa *et al*., 2010). The system uses differential mobility analyzers (DMA1 and DMA2), an SP2, and a photo-acoustic absorption spectrometer (PASS). (*Aerosol Sci. Technol*.: Amplification of light absorption of black carbon by organic coating. (44): 46–54. Copyright 2010. Reston, VA. Reprinted with permission.)

cal. To evaluate the uncertainties due to this assumption, graphite particles were also assumed not to be dense but mixed with air voids in the particle mobility diameter (Bond *et al*., 2006). The volume fraction of air was calculated to be 20–45% for diameters of 150–300 nm. The refractive index of air-included graphite ($m_{\text{graphite-air}}$) was computed using the Maxwell-Garnett theory of volume mixing model (Bohren and Huffman, 1983), assuming an m_{air} of $1.0 - 0.0i$, resulting in an $m_{\text{graphite-air}}$ of $2.0 - 0.9i$. To estimate the maximum uncertainty, a volume fraction of air of 45% was assumed. This value is in the range of values reported by Bond and Bergstrom (2006). In calculating C_{abs}, we used both m_{graphite} and $m_{\text{graphite-air}}$ to give a measure of the uncertainties of m and the non-sphericity.

Photo-absorption of uncoated and coated graphite particles at given BC diameters and coating thicknesses was investigated using the experimental setup depicted in Fig. 21. The system consists of an atomizer, a tandem differential mobility analyzer (TDMA) with a vapor condensing system (coating apparatus) (Moteki and Kondo, 2007), photo-acoustic absorption spectrometer (PASS), and SP2. Particles generated by the atomizer were heated to 400°C to remove non-refractory compounds by the thermo-denuder. The coating apparatus was bypassed for the production of uncoated graphite particles. DMAs were used to select the size of both the core and shell mobility diameters, and the APM was not used in this experiment. The coating thickness was changed by controlling the temperature of the oil bath of the coating apparatus. The overall uncertainty of the shell/core mobility diameter ratio was estimated to be 34%. Coated graphite particles with D_{BC} of 185, 234, and 281 nm and coating thicknesses of 0–300 nm were produced. The $D_{\text{p}}/D_{\text{BC}}$ ratios of particles were in the range of 1–2.5, which covers the ratios observed in the tropical atmosphere (Schwarz *et al*., 2008b) and East Asia (Shiraiwa *et al*., 2008). The absorption coefficients (B_{abs}) of coated graphite particles were measured by PASS. Core and shell diameters (D_{BC} and D_{p}) were determined by SP2 and these values were used in the analysis of absorption amplification.

Glycerol and oleic acid were used as coating materials. The refractive indices of coatings of glycerol and oleic acid at $\lambda = 589$ nm have been reported to be $1.47 - 0i$ (The Chemical Society of Japan, 1993) and $1.46 - 0i$ (Japan Oil Chemist's Society, 2001), respectively. The refractive index of organics at $\lambda = 550$ nm was reported to be $1.45 - 0i$ (Jacobson, 2005), suggesting that the optical properties of glycerol and oleic acid are similar to that of organics in general.

Graphite particles that passed through DMA1 (Fig. 21) were not purely monodisperse but polydisperse to some extent due to multiple charging. Therefore, the size distribution of the graphite particles after passing through DMA2 was also not purely monodisperse, as measured by the SP2 downstream of DMA2 (Fig. 21).

The normalized size distribution of D_{BC} depended little on the shell mobility diameter selection by DMA2. The average number ratios of singly-, doubly-, and triply-charged particles ($D_{\text{BC}} = 185$ nm) were 68–74, 21–25, and 5–7%, respectively. The number fractions of the singly-charged particles were larger than 85% for the graphite particles with 250 and 300 nm core mobility diameters selected by DMA1. The sampling of multiply-charged particles influences the absorption measurements, which is further discussed below. The effects of multiply-charged particles on the number size distribution of graphite are discussed in Shiraiwa *et al*. (2010).

The mass absorption cross section σ_{abs} was derived by dividing B_{abs} by the mass concentrations of graphite particles. For example, σ_{abs} of uncoated graphite particles was 5.1 ($\pm$0.9) m^2 g^{-1} at $D_{\text{BC}} = 185$ nm. σ_{abs} increased with $D_{\text{p}}/D_{\text{BC}}$, becoming $\sim$10 ($\pm$1.9) m^2 g^{-1} at $D_{\text{p}}/D_{\text{BC}} = 2$. The absorption measurements were influenced by multiply-charged particles, and the uncertainty in σ_{abs} was estimated as discussed in detail in Shiraiwa *et al*. (2010).

The absorption amplification factor (γ) was calculated by the ratios of σ_{abs} (D_{BC}) for coated and uncoated graphite particles. The derived γ is plotted in Fig. 22 for $D_{\text{BC}} = 185$ nm as functions of $D_{\text{p}}/D_{\text{BC}}$ ratio and coating thickness ($(D_{\text{p}} - D_{\text{BC}})/2$). D_{BC} is denoted as D_{c} in this figure. The error of γ was estimated to be $\sim$25%, caused by the propagation of the error of σ_{abs}. The bottom axis is the median $D_{\text{p}}/D_{\text{BC}}$ ratio of singly-charged particles. The horizontal

doi:10.5047/meep.2015.00301.0001

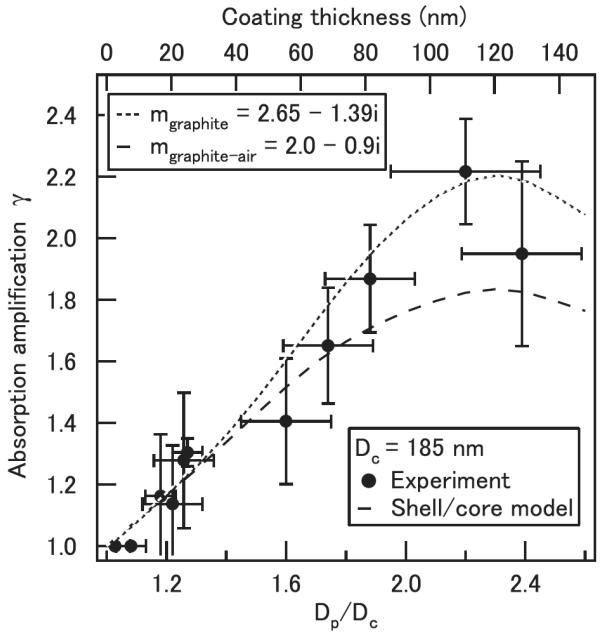

Fig. 22. Observed absorption amplification factor (γ) for organic-coated graphite particles with a D_c of 185 nm (from Shiraiwa *et al*., 2010). The bottom axis shows the median of the shell/core diameter ratio (D_p/D_c) and the top axis shows the coating thickness (nm). Shell/core model calculations are also shown for $m_{graphite}$ (refractive index of graphite) and $m_{graphite\text{-}air}$ (refractive index of air-included graphite). (*Aerosol Sci. Technol*.: Amplification of light absorption of black carbon by organic coating. (44): 46–54. Copyright 2010. Reston, VA. Reprinted with permission.)

bars of the median D_p/D_{BC} represent the uncertainty caused by the distribution of D_p/D_{BC}, as discussed above.

The absorption increased by about 30% even with a thin coating of $D_p/D_{BC} \approx 1.2$. Much larger enhancements were observed at larger D_p/D_{BC} ratios. The maximum γ was about 2.2 when D_p/D_{BC} reached about 2.2. This is a clear demonstration of the effect of the amplification of photo-absorption by the coating of BC particles. The maximum γ of 2.0 was also observed by soot coated with secondary organic aerosols (Schnaiter *et al*., 2005). The photo-absorption increased monotonically with the increase in the D_p/D_{BC} ratios for graphite particles. However, BC particles in the atmosphere have fractal structures in general. The collapse of aggregates due to the capillary force of coatings can lead to a reduction in the absorption, because some spherules that make up aggregates become screened by other spherules in compact forms (Schnaiter *et al*., 2005; Bond *et al*., 2006). Indeed, no significant amplification was observed for flame-generated soot aggregates coated with 10–50-nm thick oleic acid (Slowik *et al*., 2007). Therefore, for a more realistic assessment of photo-absorption by ambient BC, this factor has to be taken into account at small D_p/D_{BC} ratios.

5.2 Comparison with Mie theory

We compared the model calculations based on Mie theory with the laboratory measurements. The σ_{abs} and γ were calculated using the shell/core model of Mie theory (Bohren and Huffman, 1983), which was reported to be a good proxy for internally mixed BC with arbitrary eccentricity (Schnaiter *et al*., 2005).

Figure 22 shows the calculated γ using the shell/core model with $m_{graphite\text{-}air}$ and $m_{graphite}$ for $D_{BC} = 185$ nm. The calculated γ for $m_{graphite\text{-}air}$ is ~15% smaller than that for $m_{graphite}$ in both models. At $D_{BC} = 185$ nm, the model agreed with the observed γ reasonably well. At $D_{BC} = 234$ and 281 nm, the shell/core model reproduced well the observed γ (not shown). Overall, the γ calculated by the shell/core model agreed with that observed within the uncertainties of the observed γ (y-axis) and the median of D_p/D_{BC} (x-axis). The demonstration of the validity of the lens effect is among the first performed by laboratory experiments.

BC particles in the atmosphere have fractal structures and have different compositions from graphite. In order to obtain a more precise assessment of photo-absorption by ambient BC, this factor has to be taken into account.

5.3 Considerations for field studies

It is more difficult to measure γ values in ambient air because of the complexities in comparing σ_{abs} for uncoated and coated BC particles. Knox *et al*. (2009) found γ values of 1.2 to 1.6 near source regions as reviewed by Bond *et al*. (2013). However, Cappa *et al*. (2012) observed γ as small as 1.06 in large urban centers. It was hypothesized that the low γ values were caused by BC inclusions at the edge of the sampled BC particles. This hypothesis can now be tested by the new analytical method using SP2 as described in Section 2.6. There is a strong need for new experimental and theoretical methodologies to measure and interpret absorption cross sections of BC in ambient air.

6. Hygroscopicity of BC

In this chapter, a method to measure the CCN activity of BC is described, mainly based on Kuwata *et al*. (2007, 2008, 2009). The technique is applied to the BC measurements in Tokyo.

6.1 Previous studies

BC particles are hydrophobic and insoluble in water soon after emission because of their graphitic structure. However, it has been shown that BC becomes hydrophilic by surface oxidation (e.g., Zuberi *et al*., 2005), and hygroscopic by the condensation of secondary aerosol components (e.g., Saathoff *et al*., 2003; Sellegri *et al*., 2003) and coagulation with pre-existing particles (Matsui *et al*., 2013a). Coated BC particles act as cloud condensation nuclei (CCN), based on laboratory experiments (e.g., Lammel and Novakov, 1995; Petzold *et al*., 2005a; Dusek *et al*., 2006). These laboratory studies have shown that some portion of BC particles is activated as CCN when water-soluble compounds condense on BC.

However, direct measurements of the hygroscopicity of BC in the atmosphere are still very limited. One of the difficulties is to separate out co-existing non-BC particles in the measurements of hygroscopicity. The volatility tandem differential mobility analyzer (VTDMA) technique was used to isolate the less volatile aerosol components, which were considered to be mainly composed of BC in urban areas (Kuwata *et al*., 2007; Rose *et al*., 2011). However, the estimate of

doi:10.5047/meep.2015.00301.0001

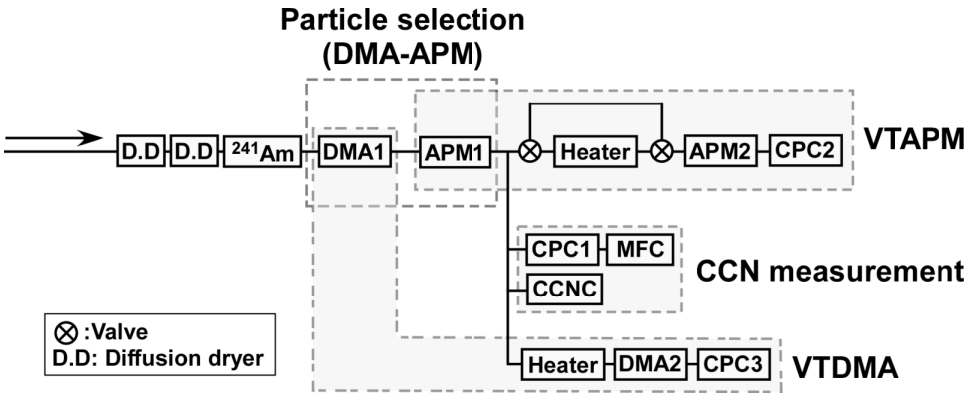

Fig. 23. Experimental setup used for the measurements of hygroscopicity of BC (from Kuwata *et al*., 2009). The system comprises a volatility tandem differential mobility analyzer (VTDMA), volatility tandem aerosol particle mass analyzer (VTAPM), and cloud condensation nuclei counter (CCNC). Differential mobility analyzers (DMAs) and aerosol particle mass analyzers (APMs) are used for particle selection by the mobility and mass of the particles, respectively, and condensation particle counters (CPCs) are used for particle detection. MFC stands for a mass flow controller.

the CCN activity of BC was not fully quantitative, as the DMA cannot quantitatively measure non-spherical particles such as BC (Park *et al*., 2004a). Kuwata *et al*. (2009) developed a volatility tandem aerosol particle mass analyzer (VTAPM) to determine the critical mass of condensed compounds separating the two types of BC quantitatively. Recent studies have used an SP2, combined with the humidified tandem differential mobility analyzer (HTDMA) (McMeeking *et al*., 2011; Laborde *et al*., 2013), to directly measure the hygroscopicity of BC. Below, we describe the results of the measurements made in Tokyo (Kuwata *et al*., 2009).

6.2 Hygroscopicity of BC in Tokyo

We have shown that particles containing large BC cores are basically CCN inactive (Kuwata *et al*., 2007; Kuwata and Kondo, 2008) and that the number fraction of CCN-active BC particles $(\mathrm{CCN/CN})_{\mathrm{BC}}$ can be estimated using the following equation :

$$\left(\frac{\mathrm{CCN}}{\mathrm{CN}}\right)_{\mathrm{BC}} = \frac{F_{\mathrm{BC}} - \left(1 - \frac{\mathrm{CCN}}{\mathrm{CN}}\right)}{F_{\mathrm{BC}}}, \tag{26}$$

where (CCN/CN) and F_{BC} represent the number fractions of CCN-active particles and particles containing large BC cores, respectively. The number concentration of CCN is measured with a cloud condensation nuclei counter (CCNC). CN (condensation nuclei) denotes the number concentration of all particles, which is measured with a condensation particle counter (CPC). The value of F_{BC} is determined using a VTDMA (Rose *et al*., 2006; Kuwata *et al*., 2007; Kuwata and Kondo, 2008). In deriving Eq. (26), we assumed that CCN-inactive non-BC particles (e.g., primary organic aerosol particles) do not exist. According to Köhler theory, the CCN activity of BC can be determined from the mass (Δm) and chemical composition of condensed compounds on the BC particle (Kuwata *et al*., 2007).

The experimental setup is shown schematically in Fig. 23 (Kuwata *et al*., 2009). The key feature of the setup is the use of two aerosol particle mass analyzers (APMs) in tandem. Particles mass-selected by APM1 were introduced to a heater operated at 400°C to extract the BC cores. The mass distributions of the BC cores were measured by means of APM2 and CPC2.

The tandem APM system was operated downstream of a DMA. The combination of DMA1 and APM1 selected the particle type according to the effective density (ρ_{eff}), which is defined by the following equation:

$$m_{\mathrm{p}} = \frac{\pi}{6}\rho_{\mathrm{eff}}{d_{\mathrm{m}}}^3, \tag{27}$$

where m_{p} is the particle mass selected by APM1, and d_{m} is the particle mobility diameter selected by DMA1. In general, ρ_{eff} of BC particles is relatively small ($\rho_{\mathrm{eff}} < 1$ g cm^{-3}), owing to their non-spherical shape (Park *et al*., 2004b). We found that relatively light (0.6 g cm^{-3} $< \rho_{\mathrm{eff}} <$ 1.1 g cm^{-3}) particles contained large BC cores. Thus, we focused on these particles in this study. During the observation period (8 days in April 2007), we set DMA1 to classify 100-nm particles because the number concentration of fresh BC particles is highest at around this size (Rose *et al*., 2006). Particles selected by DMA1 and APM1 were also introduced to a CCNC (Roberts and Nenes, 2005) and CPC1 (Zhang and Liu, 1991) to measure the number fraction of CCN-active particles (CCN/CN). Supersaturation (S) inside the CCNC was set at 0.9% and 1.3%. In addition, we introduced the selected particles to the VTDMA system to measure F_{BC} (Kuwata *et al*., 2007; Kuwata and Kondo, 2008).

When Δm was small (∼0.05 fg), the ratio of the number fraction of CCN inactive particles (1 − CCN/CN) to F_{BC} was almost equal to unity. This result demonstrates the validity of the assumption employed in Eq. (26). Then, we analyzed the present result using Eq. (26). $(\mathrm{CCN/CN})_{\mathrm{BC}}$ is plotted against Δm in Fig. 24. $(\mathrm{CCN/CN})_{\mathrm{BC}}$ clearly increased with increasing Δm, which indicates that hydrophilic BC and hydrophobic BC were effectively separated according to the mass of the condensed compounds. At $S = 0.9\%$, $(\mathrm{CCN/CN})_{\mathrm{BC}}$ was 0.5 at $\Delta m = 0.18$ fg. This Δm value corresponds to critical mass separating hydrophilic BC and hydrophobic BC (Δm_{crit}). Δm_{crit} was 0.08 fg at $S = 1.3\%$.

We have made an indirect estimate of the chemical composition of condensed compounds on BC particles. For a

doi:10.5047/meep.2015.00301.0001

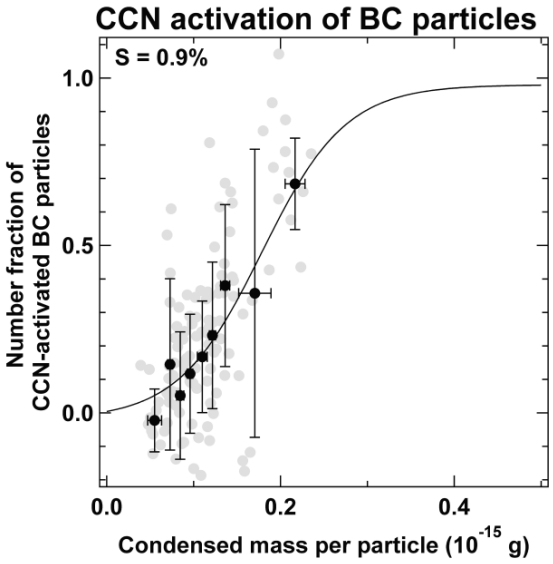

Fig. 24. The number fraction of CCN-active BC particles versus the mass of the coating material for a supersaturation of 0.9%. The data represent the response of 100 nm BC particles sampled in Tokyo in April 2007. The filled black circles with 1σ error bars are averages of the individual runs shown as gray data points. The solid curve is a sigmoidal fit to the averaged data points. A sigmoidal function is used because the ordinate should fall in the region between 0 and 1 by definition, although some deviations are apparent and are likely due to measurement errors as well as some deviations from the assumptions made for the calculation. Adapted from Kuwata *et al.* (2009, figure 11).

more quantitative interpretation of the hygroscopicity of BC, more direct measurements of the chemical composition of the condensed compounds are needed.

7. Aging of BC

The change of BC from hydrophobic to hydrophilic occurs through aging processes, as mentioned above. The e-folding time of the change is assumed or estimated to be about 1 day in a number of global models (Bond *et al.*, 2013 and references therein). However, direct evidence based on observations of the mixing states of BC is limited. Therefore, it is critically important to understand the evolution of the mixing state of freshly-emitted BC. The mixing states of BC near emission sources and remote areas have been investigated by indirect methods without using an SP2 in a number of studies (Clarke *et al.*, 2004, and references therein). However, the time scale of the changes in the mixing state has not been investigated thus far. We have carried out field measurements in urban areas (Moteki *et al.*, 2007; Shiraiwa *et al.*, 2007) and at a remote location (Shiraiwa *et al.*, 2008) in Japan. In this chapter, important findings from these studies are presented.

7.1 Outflow from urban areas

7.1.1 Aircraft observations Aircraft measurements of urban plumes over the ocean is suited for studies of aging processes without interference from additional emissions once air parcels leave land areas. We carried out aircraft observations of aerosols and trace gases in the marine boundary layer (MBL) over the Pacific Ocean offshore of the Nagoya Urban Area, Japan (∼35°N, 137°E) during the Pacific Exploration of Asian Continental Emission-C (PEACE-C) aircraft observation campaign from March 22 to 27, 2004. The flight routes were designed to enable studies of the chemical evolution of air parcels in Lagrangian coordinates. BC was measured by an SP2. Water soluble organic carbon (WSOC) was measured by a system combining the Particle-Into-Liquid Sampler with a total organic carbon (TOC) analyzer (PILS-WSOC) (Sullivan *et al.*, 2004) with an integration time of 6 minutes. Water soluble inorganic ions were measured by PILS with Ion Chromatography analysis (PILS-IC) (Weber *et al.*, 2001) with an integration time of 5 minutes. Mixing ratios of non-methane hydrocarbons (NMHCs) were measured by a whole air sampling technique (Colman *et al.*, 2001), with sampling intervals of 3–4 minutes. The ethene (C_2H_4) and ethyne (C_2H_2) data were used in estimating the chemical ages (t_{age}) of air parcels measured on board the aircraft.

The time delay (Δt) between the scattering peak and LII peak measured by the SP2 was used as a measure of the thickness of the BC coating (Schwarz *et al.*, 2006). The D_p/D_{BC} ratio larger than about 2 (threshold) was defined as thickly-coated BC for this experiment. For $D_p/D_{BC} = 2$, the uncertainty of the D_p/D_{BC} ratio was ± 0.5, significantly larger than that determined by the method described in Section 2.5. Figure 25 shows the changes of the number fraction of thickly-coated BC as a function of t_{age}. The average ($\pm\sigma$) fraction of thickly-coated BC increased from 0.35 (± 0.05) to 0.63 (± 0.09) within 12 hours (h). The rate of the increase in the thickly-coated number fraction (R_{coat}) averaged 2.3% h^{-1}. This increase of thickly-coated BC is likely due to the oxidation of the precursor gases, followed by the condensation of non-refractory compounds, including sulfate and or-

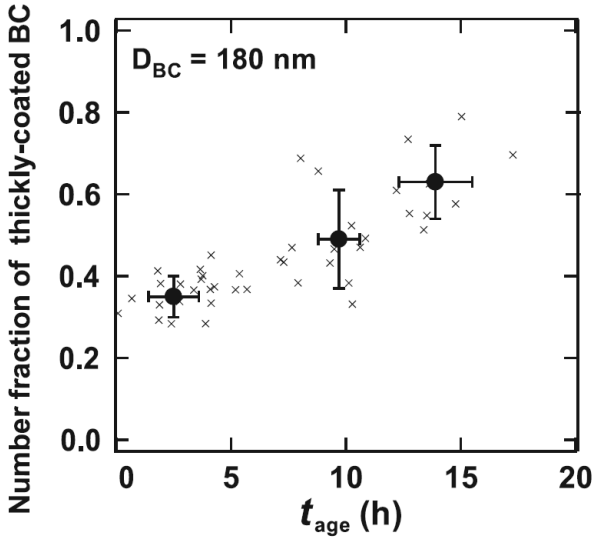

Fig. 25. The number fraction of thickly-coated BC particles versus t_{age} (photochemical age of air parcels) (from Moteki *et al.*, 2007). The small crosses indicate data merged with the integration time for the whole air samplings. The filled circles with bars indicate the data averaged over each category of t_{age}. Vertical and horizontal bars indicate the 1σ values.

doi:10.5047/meep.2015.00301.0001

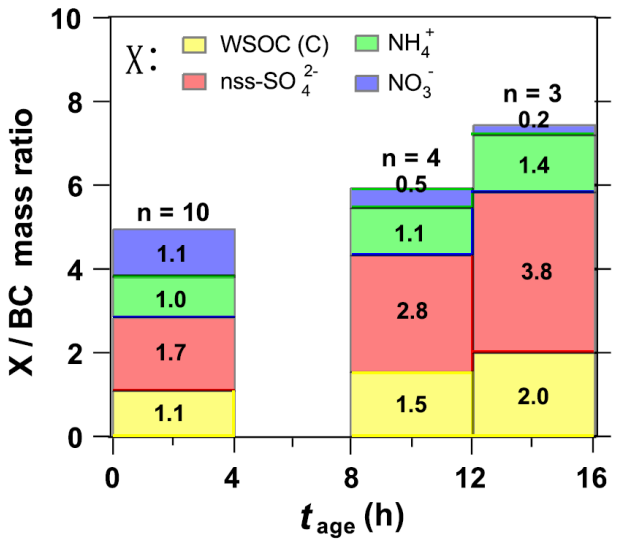

Fig. 26. BC-normalized mass concentration of aerosol chemical compositions for three categories of the photochemical age (t_{age}): t_{age} = 0–4, 8–12, and 12–16 h (from Moteki *et al*., 2007). The WSOC (water soluble organic carbon) mass concentrations are in units of μg C m^{-3}.

ganics, onto the BC particles, as discussed below. The R_{coat} (D_{BC}) was observed to be lower for the larger D_{BC}. For example, R_{coat} (250 nm) = 1.0% h^{-1} on average. R_{coat} (180 nm)/R_{coat} (250 nm) was observed to be 2.3. It is likely that this size dependence in R_{coat} (D_{BC}) can be explained by considering the size dependence of the rate of change in D_p (Seinfeld and Pandis, 2006).

Figure 26 shows the ratios of the mass concentrations of aerosol composition X (WSOC, non-sea salt (nss)-SO_4^{2-}, NH_4^+, and NO_3^-) to those of BC for three t_{age}-categories. The overall increase in each X/BC was Δ (WSOC/BC) = 0.9, Δ (nss-SO_4^{2-}/BC) = 2.1, and Δ (NH_4^+/BC) = 0.4. The inorganic ions NH_4^+, SO_4^{2-}, and NO_3^+ were in the form of ammonium sulfate ($(NH_4)_2SO_4$) and ammonium nitrate (NH_4NO_3) considering that the average ($\pm 1\sigma$) molar ratio of $NH_4^+/(2SO_4^{2-} + NO_3^-)$ for each t_{age}-category was 1.0 (±0.3), 1.0 (±0.3), and 0.9 (±0.1), respectively. From these results, it is likely that ammonium sulfate, and secondary organic compounds, formed during the transport should have mainly contributed to the increase in the coating on BC particles. In conclusion, these results give direct evidence that BC particles become internally mixed on a time scale of 12 h in urban plumes.

7.1.2 Ground-based observations Ground-based measurements provide continuous data suitable for more detailed investigations of aging processes. Ground-based measurements of aerosols and trace gases were performed from July 25 through August 14, 2004, in a Tokyo suburb (Kisai, 36.1°N, 139.6°E) located about 50 km north of Tokyo. Polluted air was transported there from Tokyo under southerly wind conditions (Takegawa *et al*., 2006). A dominant source of BC in Tokyo is diesel vehicle emissions (Kondo *et al*., 2006). The BC emissions were estimated to be greatest near the center of Tokyo (20 × 20 km^2), rapidly decreasing toward suburban areas (Kannari *et al*., 2004). Consequently, Kisai is an appropriate site to investigate the chemical evolution of aerosols transported from Tokyo.

BC measurements were made by an SP2. Measurements of the size-resolved chemical composition of the submicron aerosol were made using a quadrupole aerosol mass spectrometer (Q-AMS; Aerodyne) (Jayne *et al*., 2000). Hydrocarbons and alkyl nitrates were measured using a whole-air sampling technique (Simpson *et al*., 2003) with a 2–6 hour sampling interval. They were analyzed using gas chromatography (HP-6890) with flame ionization detection for hydrocarbons and electron capture detection for alkyl nitrates. The air mass ages were estimated from the 2-PeONO$_2$/n-C_5H_{12} ratios.

The BC particles were classified into two types: thinly- and thickly-coated BC. The fraction of thickly-coated BC with a core diameter (D_{BC}) of 180 nm increased at a rate of 1.9% h^{-1}. The increase rates were lower at larger D_{BC}, consistent with the PEACE-C aircraft observations (Moteki *et al*., 2007).

We applied Positive Matrix Factorization (PMF) (Paatero and Tapper, 1993; Paterson *et al*., 1999) to investigate the contribution to the coating on BC particles by sulfate, nitrate, and organics. PMF is a factor analysis that imposes a non-negativity constraint on the resulting factors. The ratio of the mass concentrations of sulfate, nitrate, and organics to those of BC with D_{BC} = 180 (±5) nm, and the number fraction of thickly-coated BC (D_{BC} = 180 (±5) nm) were applied to PMF. The parameters (sulfate/BC, nitrate/BC, organics/BC, and the number fraction of thickly-coated BC) predicted by the PMF model agree quite well with those observed, with r^2 values for the correlations between the observed and predicted values of 0.78, 0.91, 0.88, and 0.98, respectively.

The PMF analysis resulted in three physically interpretable factors, as shown in Fig. 27(a). On the y-axis is the explained variation (EV), which is a dimensionless number that shows a quantitative statement of how important each factor is in explaining each parameter (Paterson *et al*., 1999). The EV varies from 0 (no explanation) to 1 (complete explanation). Factor 1, which explains 62 (±10)% of sulfate/BC and 34 (±6)% of thickly-coated BC, means that sulfate is the principal contributor to the coating in this factor. Factor 2 explains 89 (±4)% of organics/BC and 49 (±6)% of thickly-coated BC, which means that organics is the main contributor in this factor. On the other hand, nitrate is the main contributor in Factor 3. The cumulative variance shows that the use of the three factors explains almost the entire variance (>96%) in every parameter. Figure 27(b) is the time series of the number fraction of thickly-coated BC (D_{BC} = 180 ± 5 nm, solid line) and the factor contribution for this BC particle type. Factors 1 and 2 mainly contribute over the entire period, especially in the daytime (90±7%), indicating that sulfate and organics were the major coating materials.

An evaluation of the diurnal variation shows an enhancement by 40% of Factor 3 from midnight to morning (2300 LT–0600 LT), when the RH was around 80%. Given that this RH was higher than the deliquescence RH of ammonium ni-

doi:10.5047/meep.2015.00301.0001

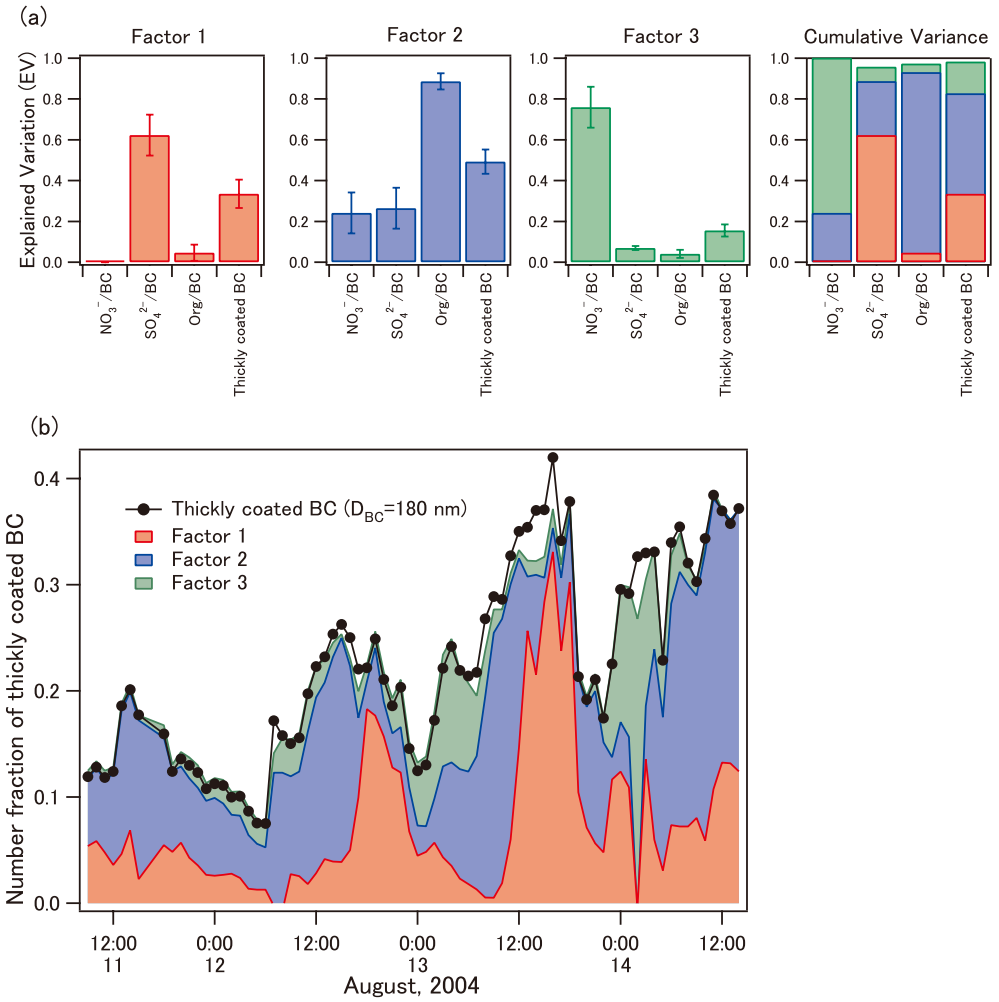

Fig. 27. (a) Explained variance of nitrate/BC, sulfate/BC, organics/BC, and thickly-coated BC (BC core diameter (D_{BC}) = 180 nm) in the three-factor PMF (positive matrix factorization) model. In addition to Factors 1, 2, and 3, the cumulative variance explained by the PMF analysis is also shown. (b) Time series of factor contributions for the number fraction of thickly-coated BC (D_{BC} = 180 nm). The figures are from Shiraiwa *et al.* (2007).

trate (DRH: 62% at 298 K), this inorganic compound would be found in the aqueous state (Morino *et al.*, 2006). The equilibrium of the nitric acid (HNO_3) reaction with ammonia (NH_3) to form ammonium (NH_4^+) and nitrate (NO_3^-) shifts toward the aerosol phase at high ambient RH. Therefore, nitrate likely contributed to the BC coating by dissolving in the liquid aerosol particles during periods of elevated RH around midnight. In summary, at D_{BC} = 180 nm, factors in which sulfate and organics dominated accounted for 90 (±7)% to the coating on BC during the daytime, while nitrate also contributed substantially to coating during the nighttime (2300 LT–0600 LT) under high-RH conditions.

7.2 Outflow from the Asian continent

Because of the high emission rates of aerosols and trace gases in East Asia (Bond *et al.*, 2013), their transport to the western Pacific affects the regional climate and air quality in this region. It is of great interest therefore to study the physicochemical properties of BC aerosols in the Asian outflow.

7.2.1 Surface observations Ground-based measurements of aerosols and trace gases were performed at a remote site in Japan (Fukue Island, 32.8°N, 128.7°E) during March 14–22 and April 5–16, 2007. The site is located about 600 km east of the coastline of the Asian continent, about 250 km south of the Korean peninsula, and about 100 km west of Kyushu Island (Japan), as shown in Fig. 28. The observatory house is located on the northwest side of Fukue Island (Takami *et al.*, 2005).

The SP2 was deployed to measure BC and light-scattering aerosols. Size-resolved PM_1 aerosol (particles with diameters smaller than 1 μm) chemical composition was analyzed using a quadruple aerosol mass spectrometer (Q-AMS; Aerodyne) (Jayne *et al.*, 2000). Hydrocarbons were measured using a whole air sampling technique (Simpson *et al.*, 2003). They were analyzed using gas chromatography (HP-6890) with flame ionization detection. The mixing ratio of carbon monoxide (CO) under ambient conditions was measured using a non-dispersive infrared absorption technique (Model48C, TECO, USA) (Takegawa *et al.*, 2006).

7.2.2 Classification of air masses and aerosol concentrations Four-day back trajectories were calculated to understand the observed variations associated with the differ-

doi:10.5047/meep.2015.00301.0001

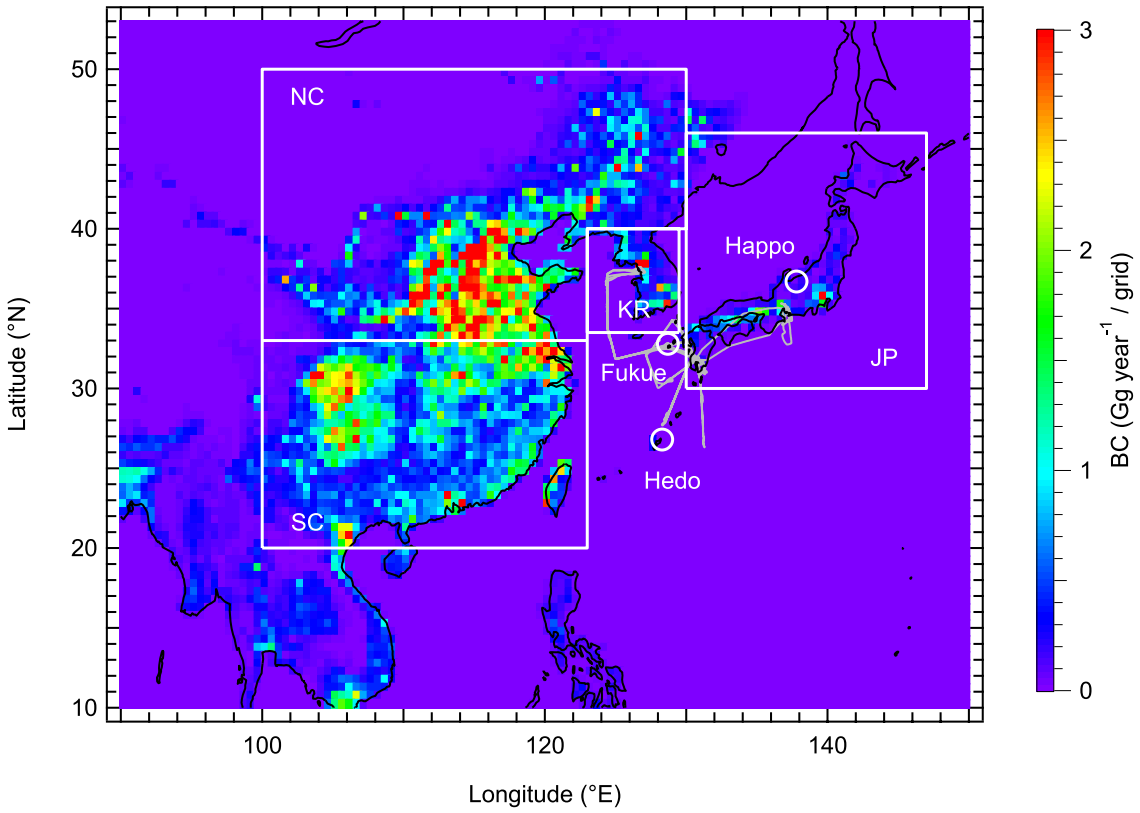

Fig. 28. Map of anthropogenic BC emissions over East Asia for the year 2006 with a spatial resolution of 0.5° × 0.5° (Zhang *et al.*, 2009). The regions of North China (NC), south China (SC), Korea (KR), and Japan (JP) defined in this study are shown with white boxes. The white circles are the locations of the measurement sites at Happo (36.7°N, 137.8°E), Hedo (26.9°N, 128.3°E), and Fukue (32.8°N, 128.7°E) in the western Pacific region. The gray lines show the flight tracks of the Aerosol Radiative Forcing in East Asia (A-FORCE) aircraft campaign (Oshima *et al.*, 2012), conducted over the East China Sea in spring 2009. This figure is from Liu *et al.* (2013b).

ent air mass origins. Observed air masses were distinctly classified into 5 types by region of origin and transport pathway: China (CH; 19%), Korea (KR; 17%), Japan (JP; 11%), Marine (MR; 10%), and Free Troposphere (FT; 20%). FT air masses were transported from the free troposphere (at altitudes greater than 2–3 km) over the Asian continent by northerly winds; these air masses then descended to the planetary boundary layer (PBL) over the eastern edge of the Korean peninsula (figure 4 of Shiraiwa *et al.* (2008)). The lowest values of ambient temperature and relative humidity among all the air masses confirm the free tropospheric origin of air masses. The fraction of each observed air mass type is also shown in parentheses, summing up to 77%. The remaining 23% of air masses were classified as transition periods and excluded in the analysis. The ambient temperature, relative humidity, and CO concentration have also been analyzed and are summarized in table 2 of Shiraiwa *et al.* (2008). Classifications of air masses were mainly based on back trajectories but also supported by trace gases and meteorological parameters.

The mass concentrations of BC and inorganic and organic aerosols are summarized in table 2 of Shiraiwa *et al.* (2008). The CH air masses had the highest concentration of BC, with a mass concentration of 0.50 (±0.14) μg m^{-3}, followed by the KR air masses: The MR air masses had the lowest value of 0.16 (±0.05) μg m^{-3}. The concentrations of aerosols essentially showed the highest values in the CH and KR air masses, because both are strongly influenced by anthropogenic emissions, and showed lower values in the JP, MR, and FT air masses. Sulfate and organics are the main constituents, while BC aerosol accounted for 1–4% in the mass of PM_1 aerosols in every air mass type (figure 5 of Shiraiwa *et al.* (2008)).

7.2.3 Size distribution Figure 29 shows the average BC mass and number size distributions for the air mass types measured using the SP2. To estimate the whole size distribution, a single, lognormal distribution was assumed, which has been observed in Asian outflow in the FT by Clarke *et al.* (2004). Mass median diameters (MMD) were 200–220 nm and count median diameters (CMD) were 120–140 nm in every air mass type. These MMDs were in a size range similar to those obtained by SP2 measurements in the FT (Schwarz *et al.*, 2006, 2008a, b) and the lower troposphere (Moteki *et al.*, 2007).

7.2.4 Mixing state The median values of the shell/core diameter ratio (R) with D_{BC} = 200 and 300 nm are summarized in table 3 of Shiraiwa *et al.* (2008). Average distributions of R with D_{BC} = 200 (±10) nm in each air mass type are shown in Fig. 30. In the CH and KR air masses, the median R with a diameter of 200 nm was ∼1.6, which indicates that most BC aerosols were thickly coated. It is likely that this resulted from the condensation

doi:10.5047/meep.2015.00301.0001

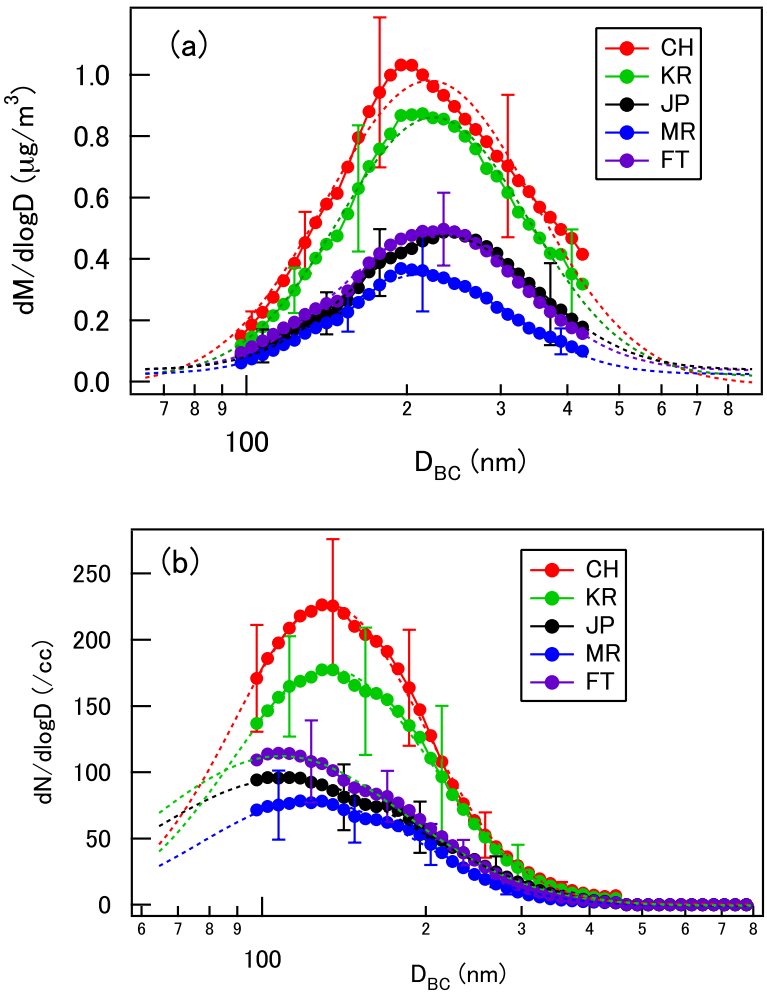

Fig. 29. Average (a) mass and (b) number size distributions of BC observed by the SP2 in air parcels of China (CH), Korea (KR), Japan (JP), marine (MR), and the free troposphere (FT) (from Shiraiwa *et al.*, 2008). Lognormal functions were fitted to the data for sizes of 98 nm $< D_{BC} <$ 430 nm. Bars show the 1σ values.

of organic and inorganic components and coagulation with co-existing aerosols during the transport from China and Korea. It is also possible that BC was coated to some extent already in China and Korea, depending on the time during which the air masses remain after BC emissions. Based on back trajectory analysis, the transport time from the Asian continent to the sampling site was long enough (2–3 days) for these processes to take place. The mass concentrations of organic and inorganic aerosols were much higher in the CH and KR air masses (table 2 of Shiraiwa *et al.* (2008)), which should result in thicker coatings on the BC aerosols. In the MR air masses, the BC was also thickly coated with a median R of $\sim$1.6.

In contrast, in the JP and FT air masses, the median values of R were 1.3–1.4, which indicates that large amounts of BC aerosols in these air masses were thinly-coated compared to other air mass types. The transport time from the Japanese main island to the sampling site was about 6 hours based on back trajectory analysis. BC is coated on a time scale of about 12 hours in urban polluted air (Moteki *et al.*, 2007; Shiraiwa *et al.*, 2007). Therefore, the transport time of about 6 hours is too short for full aging to take place in the JP air masses. Moreover, the mass loadings of organics and inorganic aerosol components, which possibly contributed to the coatings, were smaller in the JP air masses than those in the CH and KR air masses (table 2 of Shiraiwa *et al.* (2008)), suggesting that the aging time scale might have been longer than 12 hours.

7.2.5 Internally mixed compounds To investigate the contribution to the coating on BC aerosols by sulfate, organics, and nitrate measured by AMS, Positive Matrix Factorization (PMF) was applied (Shiraiwa *et al.*, 2007). The ratio of the mass concentrations of sulfate, organics, and nitrate to those of BC (X/BC, X = sulfate, organics, and nitrate) and the median value of R with $D_{BC} = 200$ ($\pm$10) nm were applied to the PMF analysis. We assumed that the coating composition matches the bulk aerosol composition. We used X/BC instead of absolute mass loadings, because it represents the relative amount of coating materials to BC aerosols (Moteki *et al.*, 2007). The parameters (sulfate/BC, organics/BC, nitrate/BC, and the median value of R) predicted by the PMF model agree quite well with those observed, with r^2 values for the correlations between the observed and predicted values of 0.97, 0.61, 0.95, and 0.98,

doi:10.5047/meep.2015.00301.0001

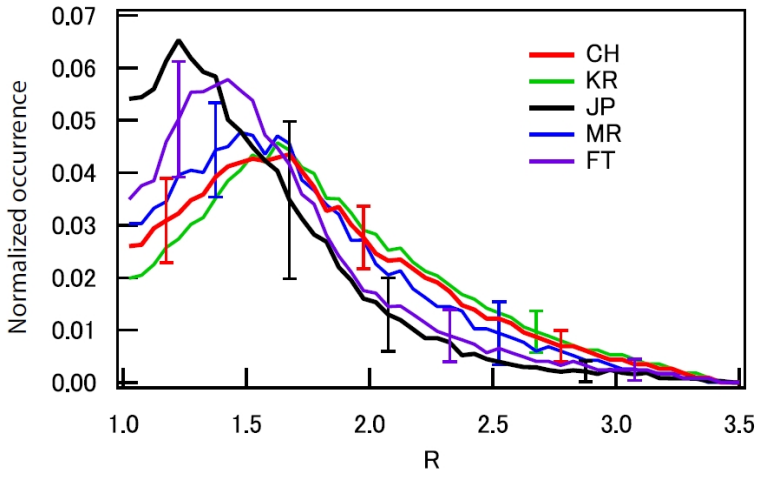

Fig. 30. Average normalized distributions of shell/core diameter ratio (R) with D_{BC} = 200 (±10) nm in the five air mass types shown in Fig. 29 (from Shiraiwa *et al.*, 2008).

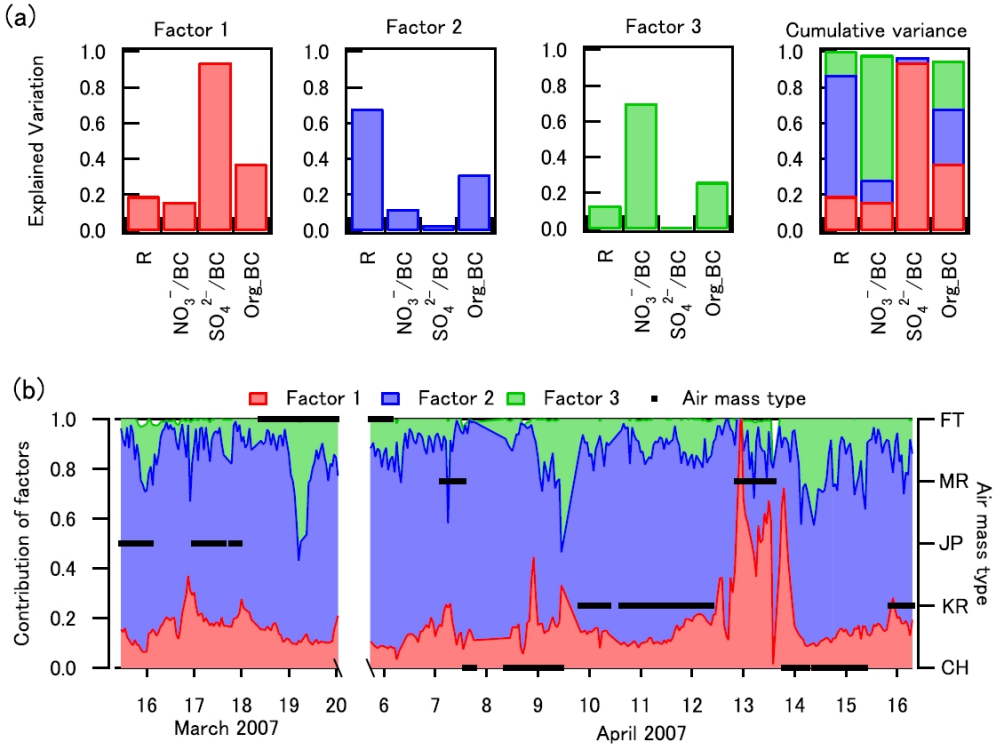

Fig. 31. Explained variation of the median values of R (D_{BC} = 200 nm), nitrate/BC, sulfate/BC, and organics/BC in the three-factor PMF (positive matrix factorization) model (from Shiraiwa *et al.*, 2008). In addition to factors 1, 2, and 3, the cumulative variance explained by the PMF analysis is also shown. (b) Time series of normalized factor contributions for the median value of R (D_{BC} = 200 nm) along with air parcel type.

respectively.

The three-factor PMF model resulted in physically interpretable factors (Fig. 31(a)). On the y-axis is the explained variation, which is a quantitative, dimensionless number of how important each factor is in explaining each parameter (Paterson *et al.*, 1999). Factor 1, which explains 94% of sulfate/BC and 19% of R, indicates that sulfate was the principal contributor to the coatings in this factor. Factor 2 explains 31% of organics/BC and 68% of R, which means that organics were the main contributor in this factor. On the other hand, nitrate was considered to be the main contributor to coatings in Factor 3. We note that Factors 1 and 3 also contain some contributions from organics/BC ratio. Therefore, organics are considered to be a sub-contributor to Factors 1 and 3. The cumulative variance shows that the use of the three factors explains almost the entire variance (>95%) in every parameter.

Figure 31(b) shows the time series of normalized factor contributions to the median value of R (D_{BC} = 200 nm) along with the air mass type. Factors 1 and 2 were the dom-

doi:10.5047/meep.2015.00301.0001

inant contributors over the entire period, indicating that organics and sulfate predominantly contributed to the coatings. These two factors accounted for 87% of the coating on BC aerosols according to the cumulative variance of R. At nighttime, the contribution of Factor 3 showed an enhancement of as high as 30%, for example on March 15 and 19, and April 14. In these periods, the relative humidity was around 80%. The equilibrium of the nitric acid (HNO_3) reaction with ammonia (NH_3) to form ammonium (NH_4^+) and nitrate (NO_3^-) shifts toward the aerosol phase at high ambient RH (Morino *et al*., 2006). This explains the larger contribution of nitrate to the coating under high relative humidity conditions, as also observed in the outflow from Tokyo (Shiraiwa *et al*., 2007). On April 14, the contribution of Factor 1 showed an enhancement as high as 70% in the MR air mass, which indicated the large contribution of sulfate to the coatings. The variability of the factor contributions reflects the different sources/mechanisms that can be associated with the different meteorological conditions and air mass types.

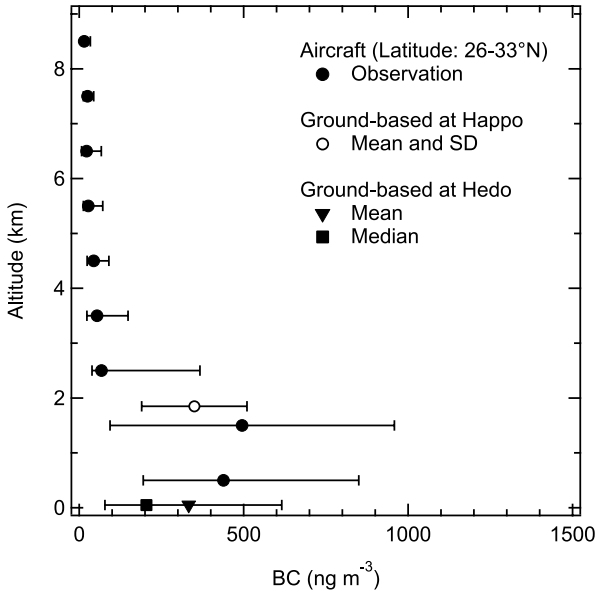

Fig. 32. Comparison of BC mass concentration (M_{BC}) values from ground-based observations at Hedo (∼60 m above sea level) and Happo (∼1800 m above sea level) in the western Pacific (from Liu *et al*., 2013b). The vertical profile of M_{BC} obtained during the Aerosol Radiative Forcing in East Asia (A-FORCE) (Oshima *et al*., 2012) aircraft campaign over the western Pacific is also shown for comparison.

8. Wet Deposition of BC

In this chapter, the results of aircraft measurements of the wet deposition of BC are presented based on Oshima *et al*. (2012) and Moteki *et al*. (2012). The former discussed the removal of the total BC mass concentration and the latter investigated its size dependence.

8.1 Total BC mass concentration

8.1.1 A-FORCE aircraft campaign BC particles emitted at the ground surface are transported from the planetary boundary layer (PBL) to the free troposphere (FT) by uplifting processes, including warm conveyor belts (WCBs) and cumulus convection, followed by efficient horizontal transport on a regional-to-hemispheric scale by the westerlies at midlatitudes. BC particles coated with sufficient water-soluble compounds are CCN active (e.g., Kuwata *et al*., 2009) and therefore can be efficiently removed from the atmosphere by precipitation during transport, while a small fraction of the remaining interstitial BC particles can be removed through the collection of cloud or rain droplets (Seinfeld and Pandis, 2006).

An understanding of the wet removal of BC is critically important because it directly controls the vertical profiles of BC and amounts of BC transported from source regions to receptor regions (i.e., long-range transport). Previous modeling studies showed that the direct radiative forcing by aerosols depends strongly on the vertical profile of BC (Hansen *et al*., 2005), and some fraction of BC particles uplifted from the PBL to the FT over source regions is transported over long distances to receptor regions (Koch and Hansen, 2005; Park *et al*., 2005; Stohl, 2006; Hadley *et al*., 2007; Koch *et al*., 2007; Liu *et al*., 2011), such as the Arctic troposphere, exerting a substantial impact on regional-to-global-scale radiative forcing (Hansen and Nazarenko, 2004). Despite the importance of the wet removal process of BC, a quantitative understanding of this process is still limited.

Over East Asia, several aircraft campaigns have been conducted, such as the Asian Aerosol Characterization Experiment (ACE Asia) in spring 2001 (Huebert *et al*., 2003) and the NASA Transport and Chemical Evolution over the Pacific (TRACE-P) in spring 2001 (Jacob *et al*., 2003). During these campaigns, Uno *et al*. (2003) discussed transport processes of BC within the PBL and Park *et al*. (2005) estimated the atmospheric lifetime of BC during TRACE-P. However, studies on the wet removal of BC over East Asia were quite limited, because there were only very small amounts of data available on BC obtained by aircraft in the FT. In fact, there have been no aircraft observations with high-accuracy BC measurements covering the entire altitude range of the FT over East Asia before the Aerosol Radiative Forcing in East Asia (A-FORCE) aircraft campaign conducted in 2009, although some aircraft BC measurements were conducted in the lower troposphere, such as the Cheju ABC Plume-Monsoon Experiment (CAMPEX) in summer 2008 (0–4 km in altitude) (Ramana *et al*., 2010).

The A-FORCE aircraft campaign was conducted over East Asia in March–April 2009 to investigate the transport and removal processes of aerosols, their physical and chemical properties, and cloud microphysical properties in Asian outflow. The flight tracks for A-FORCE are shown in Fig. 28. During the campaign, 120 vertical profiles of BC particles were obtained using an SP2, together with CO at 0–9 km in altitude. The mean profile of BC mass concentrations observed at 26–33°N is shown in Fig. 32 (Liu *et al*., 2013b), together with the data obtained by the ground-based observations.

8.1.2 Transport efficiency of BC during A-FORCE The TE (transport efficiency of BC) value for sampled air parcels transported from source regions can be estimated

doi:10.5047/meep.2015.00301.0001

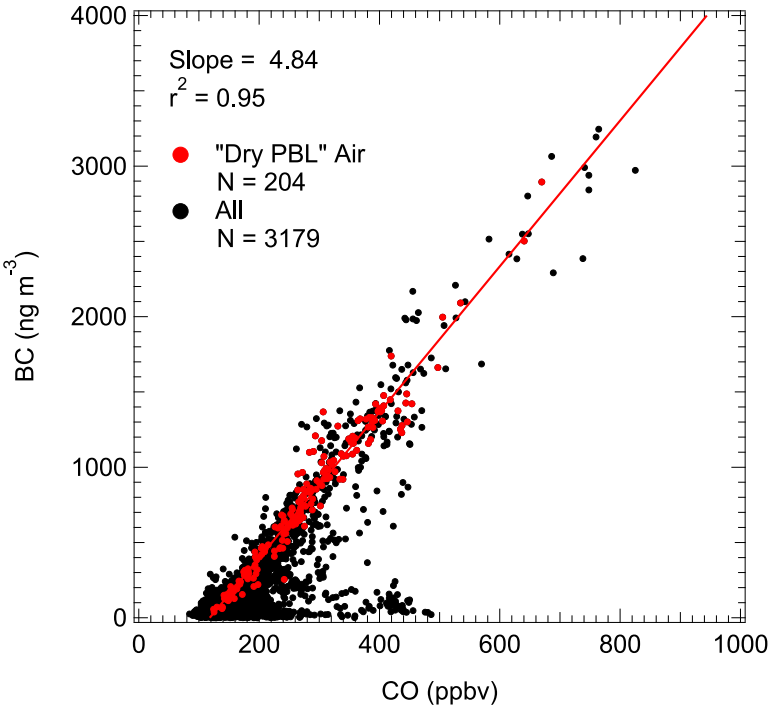

Fig. 33. Correlation between BC mass concentration and CO mixing ratio for the "dry PBL" air parcels (1-min average data that match the back trajectories) sampled by the aircraft below 2 km in altitude during A-FORCE (red circles) (from Oshima *et al.*, 2012). The red solid line is the linear regression line for the "dry PBL" air parcels. The unit of the slope is ng m^{-3} $ppbv^{-1}$. For comparison, BC mass concentrations and CO mixing ratios for all the air parcels (1-min average data that match the back trajectories) sampled during A-FORCE are denoted by black circles.

from changes in observed BC-to-CO ratios, because emission sources of BC and CO are generally similar (Streets *et al.*, 2003), and CO can be used as an inert combustion tracer within a time scale of a few weeks. The TE is defined for individual air parcels as follows:

$$\mathrm{TE} = \frac{\left(\dfrac{\Delta[\mathrm{BC}]}{\Delta[\mathrm{CO}]}\right)}{R_{\mathrm{BC\text{-}CO}}} \tag{28}$$

where Δ[BC] and Δ[CO] are the differences between the observed and background values of BC mass concentration and CO mixing ratio in individual air parcels, respectively, and $R_{\mathrm{BC\text{-}CO}}$ is the value of the Δ[BC]/Δ[CO] slope in air parcels that had not been influenced by wet processes during transport from the source regions (i.e., representing the emission ratio of BC to CO over the source regions). The definition of the "background value" of an air mass in this study is the concentration which the air mass would have had if it had not been influenced by emissions over the East Asian region.

The application of Eq. (28) requires the $R_{\mathrm{BC\text{-}CO}}$ value, which has been estimated from the slope of the correlation between BC mass concentrations and CO mixing ratios observed for "dry PBL" air parcels (1-min average data that match the back trajectories). The "dry PBL" air parcels are defined by the following criteria: (1) air parcels sampled below 2 km in altitude outside of clouds, (2) their trajectories found in the lower troposphere (between the surface and the 700-hPa level) over the Asian continent (the longitudinal sector between 90° and 122°E), and (3) the average RH of the highest 10% of RH values along the 5-day trajectory smaller than an RH value of 85%.

Figure 33 shows the resulting BC and CO correlation for the "dry PBL" air parcels (based on 1-min average data, indicated by red circles). The BC mass concentrations and CO mixing ratios for all air parcels sampled during A-FORCE are also shown for comparison (1-min average data, indicated by black circles). As indicated by the red line, the resulting $R_{\mathrm{BC\text{-}CO}}$ value is 4.84 ng m^{-3} (parts per billion by volume (ppbv))$^{-1}$ with 20% variability (i.e., the standard deviation of the Δ[BC]/Δ[CO] values over all the "dry PBL" air parcels). The high BC-CO correlation ($r^2 = 0.95$) supports the validity of the identification of dry air parcels within the PBL. The $R_{\mathrm{BC\text{-}CO}}$ value of 4.84 ng m^{-3} was within the range of the values of the Δ[BC]/Δ[CO] slopes (3.5–5.8 ng m^{-3}) observed in the Beijing area (Han *et al.*, 2009) that contributed dominantly to the BC emissions in northeastern China (Guinot *et al.*, 2007).

The background concentration of BC was assumed to be zero because the atmospheric lifetime of BC is estimated to be several days (e.g., Cooke *et al.*, 2002; Park *et al.*, 2005). The background value of CO was chosen to be 118 ppbv, which is the value of the x-intercept of the regression line at the bottom of Fig. 33. We only use air parcels in which Δ [CO] values are greater than 30 ppbv for estimates of TE following Koike *et al.* (2003), in order to select air parcels that are clearly influenced by emissions over East Asia.

8.1.3 Uplifted plumes As shown in Fig. 34, both BC mass concentrations and CO mixing ratios were enhanced in air parcels sampled at 3–6 km in altitude over the Yellow Sea

doi:10.5047/meep.2015.00301.0001

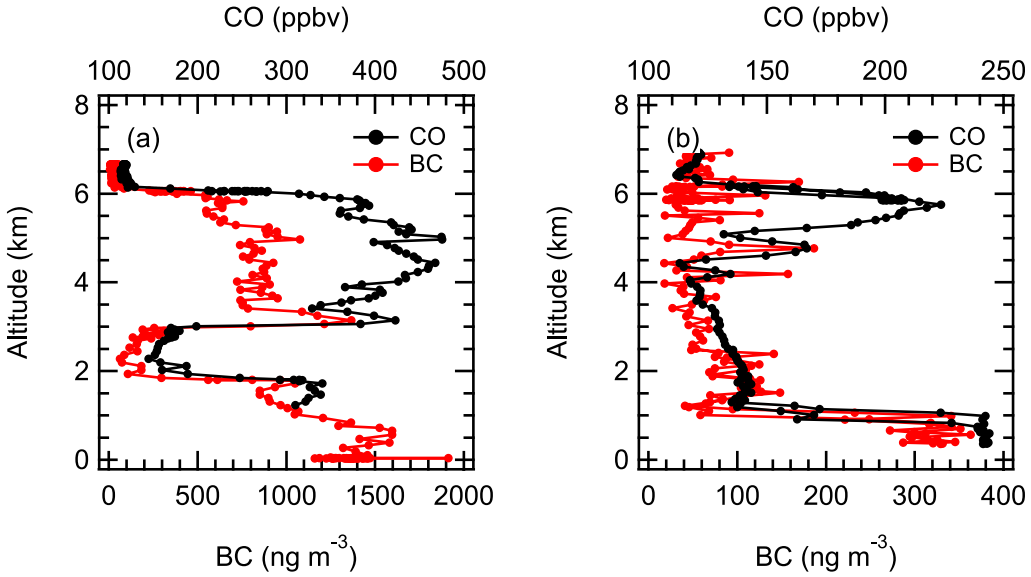

Fig. 34. Vertical profiles of 10-s mean CO mixing ratio (black circles) and BC mass concentration (red circles) measured over (a) the Yellow Sea around 37°N, 126°E during Flight 8 on March 30, 2009, and (b) the East China Sea around 33°N, 128°E during Flight 19 on April 23, 2009 (from Oshima *et al.*, 2012).

(around 37°N, 126°E) on March 30, 2009. These air parcels were uplifted due to a cyclone associated with modest precipitation (5.0 mm day^{-1} on average) over northern China, resulting in a 47% removal of BC on average. On the other hand, BC concentrations did not show a substantial increase despite high CO concentrations in air parcels sampled at 5–6 km in altitude over the East China Sea (around 33°N, 128°E) on April 23. These air parcels were uplifted due to cumulus convection associated with heavy precipitation (21 mm day^{-1} on average) over central China, resulting in large removals of BC (88% on average).

8.1.4 APT For our evaluation of the influence of precipitation on the air parcels sampled in the FT during transport, we utilized the results of the 5-day back trajectories of the "uplifted air parcels" in combination with the precipitation water content (i.e., sum of rain, snow and graupel content) available in the 3-D Weather Research Forecasting (WRF) model (Skamarock *et al.*, 2005) output and precipitation available in the WRF surface output. Specifically, we checked the precipitation water content in each WRF 3-D grid box along each of the trajectories at hourly intervals. The surface precipitation amount was then integrated in a Lagrangian sense along each trajectory when and where a trajectory had passed through the precipitation water content grid box anywhere from the "uplifted location" to the sampling point (the flight track). The amount of integrated precipitation is hereafter referred to as the "accumulated precipitation along a trajectory (APT)", which gives a measure of the influence of precipitation on the wet removal of aerosols from air parcels during transport. Knowing the WRF 3-D precipitation water content is necessary for identifying an air parcel influenced by precipitation during transport, while considering only surface precipitation data cannot identify the altitude relationship between air parcels along trajectories and the occurrence of precipitation (e.g., we cannot exclude the case that air parcels are above precipitating clouds). In addition, aerosol particles can be redistributed by the gravitational sedimentation of raindrops containing aerosol particles, followed by evaporation. The use of APT neglects this effect, assuming that re-distributed amounts of aerosols are generally smaller than net columnar losses.

8.1.5 Wet removal during upward transport We examined the dependence of wet removal of BC on precipitation for air parcels sampled in the FT using the entire A-FORCE data set. Figure 35 shows the relationship between the TE and the APT values for the "uplifted air parcels" sampled above 2 km (black circles). Although the negative correlation between TE and the logarithm of APT for the air parcels was modest ($r^2 = 0.43$), we found a good correspondence between their median values ($r^2 = 0.88$). This indicates that TE primarily depended on APT, namely the wet removal of BC from air parcels primarily depended on the amount of precipitation that the air parcels experienced during vertical transport from the PBL to the FT. The decreasing trend is also applicable for the case studies based on the flights 8 and 19 shown as Fig. 35, namely the mean TE and APT values for the flight 19 case were found to be smaller and greater than those for the flight 8 case, respectively.

Detailed discussion on the transport of BC from different parts of China, e.g. northern China (NC), north of 33°N, and southern China (SC), south of 33°N, is given in Oshima *et al.* (2012). The regions of NC and SC are shown in Fig. 28. An analysis is made to characterize the TE-APT correlation for air masses of different origins observed at different altitudes.

There remain large uncertainties in the representations of the wet removal process of BC in current 3-D models. A number of vertical profiles of BC over East Asia obtained by the A-FORCE aircraft campaign can be used for model

doi:10.5047/meep.2015.00301.0001

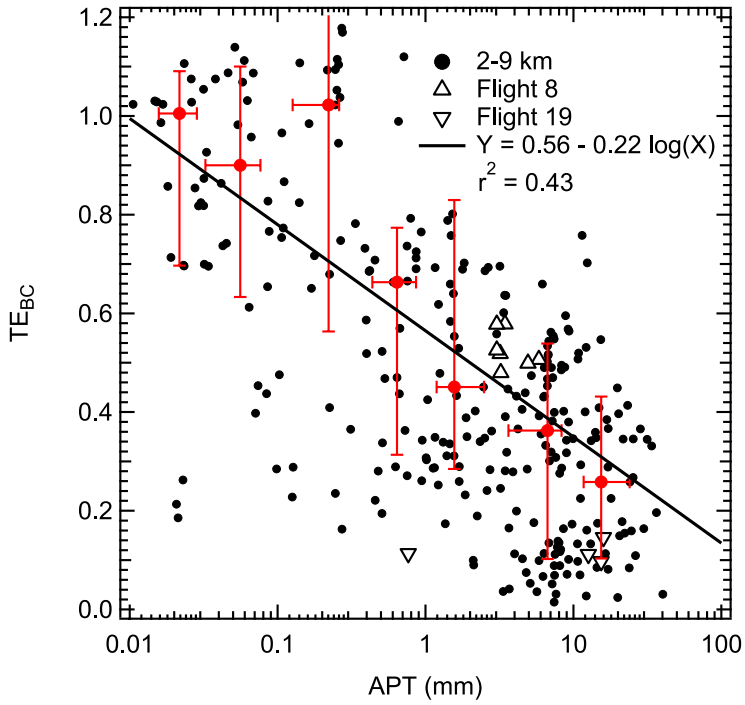

Fig. 35. Relationship between the TE (transport efficiency of BC) and the APT (accumulated precipitation along a trajectory) values for the "uplifted air parcels" sampled above 2 km in altitude during the entire A-FORCE period (black circles) (from Oshima *et al*., 2012). Open black triangles denote the Flight 8 case in which large enhancements of both BC mass concentration and CO mixing ratio were observed in air parcels sampled between 3 and 6 km in altitude on March 30, 2009. Open black upside-down triangles denote the Flight 19 case in which only enhancements of the CO mixing ratio were observed in air parcels sampled between 5 and 6 km in altitude on April 23, 2009. The black solid line is the regression line for the "uplifted air parcels" (black circles). The red circles denote the median values of TE and APT within each APT range (i.e., APT values were divided into eight even intervals between 0.01 mm and 100 mm based on a constant common ratio), and the red vertical and horizontal lines denote the central 67% ranges. Note that the air parcels with Δ[CO] values greater than 30 ppbv are shown.

validation of the spatial distribution of BC in this region. In particular, the observed TE values will provide a good constraint for accurate calculations of the wet removal of aerosols in 3-D models.

8.2 Size dependence of wet removal

8.2.1 Nucleation scavenging The analysis discussed above focused on the wet removal of BC mass concentration, which is a bulk property of BC. The size and mixing state of the BC were also obtained by an SP2 and these data were used for a more detailed analysis of the wet deposition of individual BC particles with different microphysical properties. The incorporation of aerosol mass into cloud water is due mainly to nucleation scavenging. The effect of impaction scavenging in a cloud is negligibly small compared to that of nucleation scavenging when mass is considered, whereas impaction scavenging can also be important when the number of aerosols is considered (Flossmann *et al*., 1985).

The critical supersaturation (SS_c) is a parameter characterizing the activity of aerosol particles as cloud condensation nuclei. The SS_c of an aerosol particle decreases as its size increases and as the amount of internally mixed hygroscopic compounds increases. Therefore, larger aerosol particles consisting of more internally mixed hygroscopic compounds will more likely be removed via nucleation scavenging. However, no observational evidence of the size dependence of the wet removal of aerosols has been reported due to difficulties in selectively extracting this effect. Namely, some major components (e.g., sulfates, nitrate, organics) of aerosols are produced in cloud droplets and then released as aerosols into the air as the clouds evaporate (Hegg and Hobbs, 1982; Flossmann *et al*., 1987). Also, new particles frequently form in the troposphere (Weber *et al*., 1999), especially near clouds (Perry and Hobbs, 1994). The production of new aerosols occurs at the same time and places as the wet removal of aerosols. Because BC is chemically inert and because its absolute mass can be detected for individual particles, BC particles are suited for investigating changes in the size distribution of aerosols in the atmosphere due solely to physical processes.

8.2.2 Characterization of air masses We defined three major groups of air parcel data to analyze the effects for this analysis, based on the analysis described in Section 8.1. First, the air parcels in "PBL-outflow" air were defined as those arriving directly from China in the PBL and sampled at altitudes below 1 km over the Yellow Sea. These air parcels were sampled at a relatively short distance (200–400 km) from China. The 45 PBL-outflow air parcels form a subset of the 231 "dry PBL" air parcels, which were sampled at altitudes below 2 km at distances up to ∼1000 km from China. We used the PBL-outflow samples to represent PBL air before its transport upward. The median value of the TE of PBL-outflow air parcels was 1.04 (the middle range of values within the 67th percentile was 0.93–1.15), which was

doi:10.5047/meep.2015.00301.0001

fairly consistent with the definition of $R_{\text{BC-CO}}$ as an emission ratio.

Based on trajectory analysis, we defined "uplifted air parcels" as those parcels sampled in the FT above an altitude of 2 km and which had been lifted from the PBL over China, then transported by the subtropical westerlies to the sampling locations. For this second group, we defined 227 parcels having CO higher than 180 ppbv as "FT-outflow" air parcels, a subset of the 361 "uplifted" air parcels.

For all "uplifted" air parcels, the TE was negatively correlated with APT (Fig. 35). For "uplifted" air parcels, the TE tended to be lower for higher sampling altitudes where greater APT values were estimated. At similar altitudes, the typical TE values were lower for air parcels uplifted over SC compared to those over NC, consistent with the spatial trend of greater APT in air parcels uplifted over the southern regions of China. The FT-outflow air parcels were divided into three subgroups by the TE value: TE < 0.3, $0.3 <$ TE < 0.8, and TE > 0.8.

Finally, for the third group we defined 963 "FT-clean" air parcels as those parcels sampled in the FT (above 2 km) with [BC] < 60 ng m^{-3}, at any latitude and longitude on the flight tracks. These parcels are assumed to represent clean FT air.

For the present analysis, we also introduce a useful parameter $\langle m \rangle$, the average of single-particle mass (m) of BC, as:

$$\langle m \rangle \equiv \frac{1}{n} \sum_{i=1}^{n} m_i . \tag{29}$$

m_i is the mass of BC in the i-th BC-containing particle, and n is the total number of BC-containing particles detected by the SP2 during a given time interval. We used the parameter $\langle m \rangle$ to quantify systematic changes in the size distribution of BC. The averaging time interval was fixed at 1 minute, and the corresponding n ranged from approximately 10^2 to 10^4 depending on the number concentration of BC.

8.2.3 Changes in BC size distribution The average number size distribution ($dN/d\log D$) of BC in five different types of air masses is shown in Fig. 36, with fitted lognormal functions. Each distribution is scaled differently in the vertical so as to adjust the peak of its curve at a fixed value. The geometric standard deviations (σ_g) of the lognormal functions were within a narrow range from 1.51 (for PBL-outflow air) to 1.64 (for FT-clean air). The count median diameters (CMDs) of the lognormal functions are markedly different in different types of air parcels: 128 nm (in PBL-outflow air), 127 nm (in FT-outflow air with TE $>$ 0.8), 107 nm (in FT-outflow air with $0.3 <$ TE < 0.8), 96.8 nm (in FT-outflow air with TE < 0.3), and 94.5 nm (in FT-clean air). The CMD decreased as TE decreased (Fig. 36). The size distribution of FT-outflow air with TE > 0.8 was very similar to that of PBL-outflow air. Note also that the size distribution of FT-outflow air with TE < 0.3 was very similar to that of FT-clean air. Schwarz *et al.* (2010) also measured the size distributions of BC over pristine remote Pacific sites with the SP2. The lognormal parameters of the size distributions of BC were stable for CMD values from 78 to 97 nm, with $\sigma_g = 1.64 \pm 0.06$. (These CMD values were calculated from the mass median diameter values given in Schwarz *et al.* (2010).) The CMD and σ_g values observed for the FT-clean air parcels in our study are within the reported ranges for pristine air over the remote Pacific.

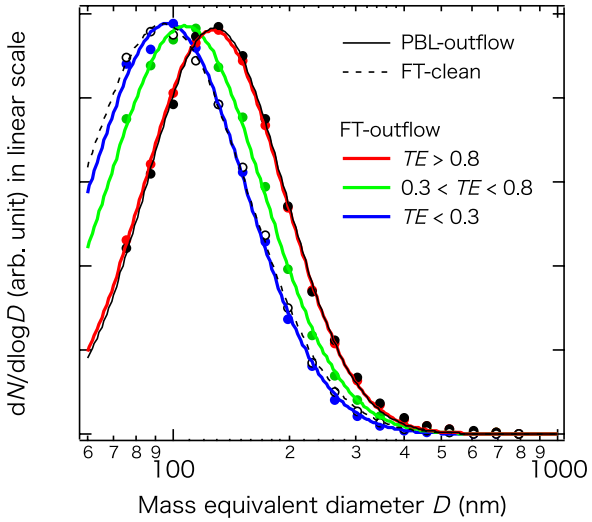

Fig. 36. The number size distribution of BC particles in five different types of air (from Moteki *et al.*, 2012). Each distribution is scaled differently in the vertical so as to adjust the peak of its curve to a fixed value.

Figure 37 shows a correlation plot of $\langle m \rangle$ versus TE in FT-outflow air. The $\langle m \rangle$ values decreased as TE decreased. The general trend of the correlation was very similar for air parcels uplifted over NC and over SC. For the FT-outflow air parcels, the correlation coefficient ($r^2 = 0.79$) between $\langle m \rangle$ and TE (Fig. 37) was greater than that between $\langle m \rangle$ and BC mass concentration ($r^2 = 0.57$). Therefore, the observed correlation between $\langle m \rangle$ and TE in FT-outflow air is very likely a consequence of an atmospheric process that strongly controls both $\langle m \rangle$ and TE. The median values for the $\langle m \rangle$ in PBL-outflow air and FT-clean air were 6.25 and 3.45 fg, which were close to the upper and lower limits of $\langle m \rangle$ in FT-outflow air. These results indicate that BC size distributions in air parcels tend to shift to lower sizes by wet removal processes during upward transport from the PBL to the FT. The BC size distribution underwent little change in less-processed air parcels (where TE > 0.8), even after vertical transport into the FT. In contrast, the size of BC in well-processed air parcels (where TE < 0.3) decreased to sizes typical of FT-clean air. This is the first demonstration of the size dependence of the wet removal of BC particles.

The mass of coating material monotonically increased with the mass of BC in the range from 5.5 to 45 fg, for BC-containing particles observed in PBL-outflow air (figure 3 of Moteki *et al.* (2012)). The coating mass was calculated from the coating thickness measured by the SP2, assuming 1 g cm^{-3} density. Wang *et al.* (2002) measured size-resolved mass fractions associated with the chemical composition of aerosols in Asian outflow air over the East China Sea in the spring (in a similar location and season as in this study) and observed that the mass fractions of NH_4^+, SO_4^{2-}, NO_3^-, organic carbon, and BC changed little with the particle size.

doi:10.5047/meep.2015.00301.0001

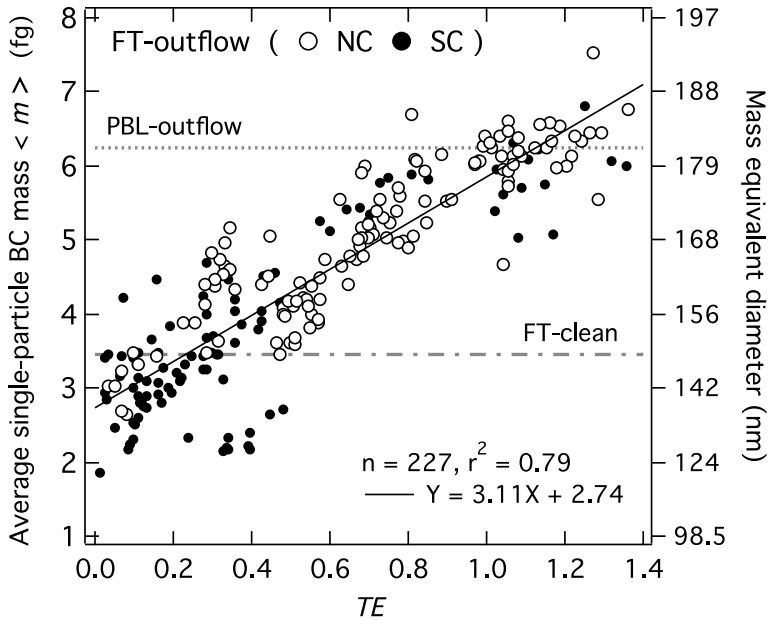

Fig. 37. Correlation between $\langle m \rangle$ (average of single-particle mass of BC) and TE (transport efficiencies of BC) for 227 FT (free tropospheric) outflow air parcels (from Moteki *et al*., 2012). Among these parcels, the 126 parcels uplifted over northern China (NC) and the 101 uplifted over southern China (SC) are shown by open and filled circles, respectively. The solid line gives the fitted linear correlation for all data points. The median values of $\langle m \rangle$ in PBL (planetary boundary layer)-outflow air and FT-clean air are also indicated by the dotted and dash-dotted lines, respectively. The right-side axis shows the mass equivalent diameters of BC that correspond to $\langle m \rangle$ values shown on the left-side axis.

If these aerosol chemical compositions are internally mixed, the results of Wang *et al*. are consistent with our finding that the mass of coating materials is linearly proportional to the mass of BC.

The SS_c of a BC-containing particle was calculated as a function of the mass of BC, assuming two coatings materials on BC: one is $NH_4(SO_4)_2$ (representing the upper limit of the solute effect) and the other is a water-insoluble material (neglecting the solute effect). The assumption that the chemical composition of a coating material is size-independent in the SS_c calculation may be reasonable, according to observations by Wang *et al*. (2002). The calculated SS_c was shown to decrease systematically with increasing BC mass (figure 3 of Moteki *et al*. (2012)). The correlation of $\langle m \rangle$ with TE is observed to be a tight one (Fig. 37), and may be due to the wet removal of BC-containing particles via nucleation scavenging becoming more efficient as the BC mass increases. Our calculated dependence of SS_c on BC mass for BC-containing particles in PBL-outflow air supports this hypothesis.

9. Size and BC Mixing State Resolved Bin Model

There is a strong need to develop 3-D models with appropriate representations of microphysical processes of aerosols, as discussed in Chapter 1. Matsui *et al*. (2013a, 2014) developed a size and BC mixing-state-resolved model (MS-resolved WRF-chem model) based on the WRF-chem model (Grell *et al*., 2005; Fast *et al*., 2006; Zaveri *et al*., 2008) for this purpose. Descriptions of the new model are given based on Matsui *et al*. (2013a, 2014).

9.1 Previous studies

The photo-absorption efficiency and CCN activity of BC-containing particles are enhanced with a coating of non-absorbing aerosols. The enhancement of photo-absorption efficiency largely impacts the optical properties of aerosols and radiative effects by aerosols (e.g., single scattering albedo (SSA), heating rate, and radiative forcing) (e.g., Jacobson, 2000, 2001; Bond *et al*., 2006; Shiraiwa *et al*., 2008; Oshima *et al*., 2009b; Zaveri *et al*., 2010). The enhancement of CCN activity could increase the wet scavenging efficiency of BC and modify cloud microphysical properties (e.g., Stier *et al*., 2006; Oshima *et al*., 2009b; Riemer *et al*., 2010; Zaveri *et al*., 2010; Park *et al*., 2011). For example, Jacobson (2000) showed that the treatment of the BC mixing state (MS) could considerably change global direct radiative forcing: the core-shell (internally mixed) treatment (+0.54 W m^{-2}) resulted in a BC forcing twice that obtained with externally mixed treatments (+0.27 W m^{-2}). Oshima *et al*. (2009b) showed the sensitivity of SSA and CCN activity to a representation of BC. They compared two box model simulations, with and without the detailed treatment of the BC mixing state, and found that the mixing state resolved simulations increased SSA (from 0.71–0.79 to 0.81–0.85) and decreased the hydrophilic BC mass fraction (from 0.74–0.90 to 0.55–0.83) in their case study. These studies indicate the necessity of resolving multiple BC mixing states in numerical models for estimating the BC impact on radiative effects and cloud microphysical properties properly. More concretely, at least three mixing states should be treated separately for estimating BC microphysical and radiative properties accurately: uncoated BC (hydrophobic BC), internally mixed BC (hydrophilic BC), and BC-free particles. An accurate representation of the hydrophobic to hydrophilic conversion rate is essential for the long-range transport of BC to the Arctic (Liu *et al*., 2011). The separation of BC-containing parti-

doi:10.5047/meep.2015.00301.0001

cles and BC-free particles is also important for evaluating BC photo-absorption (e.g., Oshima *et al*., 2009a, b). The internally mixed BC representation will underestimate BC concentrations over outflow regions but overestimate the lens effect of each BC particle.

There are many previous modeling studies considering pure BC, internally mixed BC, and BC-free particles separately. These models can be classified into zero-dimensional (box or parcel models) (e.g., Oshima *et al*., 2009a, b; Riemer *et al*., 2009, 2010; Lu and Bowman, 2010; Zaveri *et al*., 2010) and 3-D models (global or regional models) (e.g., Jacobson, 2002a; Riemer *et al*., 2003; Bauer *et al*., 2008; Kim *et al*., 2008; Seland *et al*., 2008; Aquila *et al*., 2011). Riemer *et al*. (2009) have developed a particle-resolved aerosol box model (PartMC-MOSAIC) and have applied it to study the evolution of the BC mixing state due to coagulation and condensation in an idealized urban plume. Oshima *et al*. (2009a) have made a box model with a two-dimensional (size and mixing state resolved) bin representation (MADRID-BC) and have applied it to simulate the condensational growth of BC particles for urban plumes in Japan. Since box models can treat detailed condensation/evaporation and coagulation processes with a number of BC mixing states, they are suitable for studies focused on physical and chemical processes in a plume (Riemer *et al*., 2010; Zaveri *et al*., 2010). However, these models are computationally too expensive to apply to three-dimensional calculations.

3-D models which consider pure BC, internally mixed BC, and BC-free particles are still limited. Even in these advanced models, relatively simple treatments of aerosol size representation (e.g., modal approach) and microphysical processes (e.g., assumption of equilibrium for inorganic species, single mixing state for internally mixed BC) are generally adopted to reduce computational cost. Therefore, there are few 3-D models that resolve both aerosol size and the BC mixing state with detailed microphysical processes and represent various coating fractions for internally mixed BC particles (Jacobson, 2001, 2002b; Bauer *et al*., 2008). In addition, few validation studies have been made previously using observed results of the BC mixing state (Bauer *et al*., 2013). This is because only limited advanced instruments, such as the SP2 and VTDMA can provide detailed information on the BC mixing state.

9.2 MS-resolved WRF-chem model

We developed an MS-resolved aerosol model based on the WRF-chem model (version 3.1.1), which has been used in our previous studies (Matsui *et al*., 2009, 2010, 2011a). In the original MOSAIC aerosol module, the mass concentrations of the following aerosol species and number concentrations are explicitly calculated for the size range between 40 nm and 10 μm with 8 size bins: sulfate, nitrate, ammonium, BC, primary organic aerosol (POA), other inorganics (non-reactive dust, OIN), sea salt (sodium and chloride), and aerosol water. The chemical processes considered in the WRF-chem model are emissions, gas-phase chemistry, aqueous-phase chemistry, binary homogeneous nucleation, dynamical gas-particle partitioning (condensation/evaporation), Brownian coagulation, and dry and wet deposition.

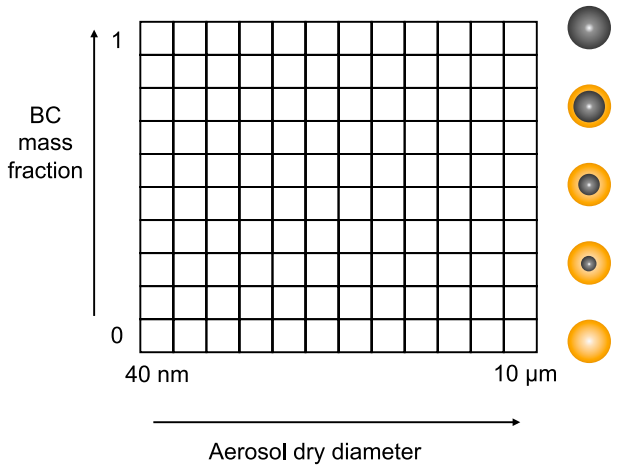

Fig. 38. Schematic of the 2-D aerosol bin representation adopted in the MS (mixing-sate)-resolved WRF-chem model (from Matsui *et al*., 2013a). One dimension is aerosol dry diameter and the other is BC mass fraction with respect to the total aerosol mass concentration under dry conditions. Aerosol dry diameters from 40 nm to 10 μm (same as the original WRF-chem model) were divided into 12 bins. BC mass fraction (between 0 and 1) was divided into 10 bins: one for externally mixed BC (BC mass fraction $>$ 0.99), one for BC-free particles (BC mass fraction $=$ 0), and the other 8 bins for internally mixed BC (BC mass fractions of 0–0.1, 0.1–0.2, 0.2–0.35, 0.35–0.5, 0.5–0.65, 0.65–0.8, 0.8–0.9, and 0.9–0.99).

The aerosol representation of the WRF-chem model was extended to resolve both aerosol size and BC mixing state. We adopted a 2-D aerosol bin representation, as shown in Fig. 38, for the first time. One dimension is the aerosol dry diameter and the other is the BC mass fraction of the total aerosol mass concentration under dry conditions. The aerosol size ranges between 40 nm and 10 μm (same as the original WRF-chem model) was divided into 12 bins. The BC mass fraction (between 0 and 1) was divided into 10 bins: one for pure BC (BC mass fraction $>$ 0.99), one for BC-free particles (BC mass fraction $=$ 0), and the other 8 bins for internally mixed BC (BC mass fractions of 0–0.1, 0.1–0.2, 0.2–0.35, 0.35–0.5, 0.5–0.65, 0.65–0.8, 0.8–0.9, and 0.9–0.99). Therefore, the MS-resolved WRF-chem model uses 120 aerosol bins (12 $\times$ 10 bins) in total.

To calculate aerosol microphysical processes with the 2-D representation, we made aerosol schemes for the following two processes: (1) the shift of size and mixing state bins resulting from condensation/evaporation and aqueous-phase chemistry, and (2) coagulation. The amount to be shifted along the aerosol size bin is calculated by a mass and number advection scheme (Simmel and Wurzler, 2006). The amount to be shifted along the BC mixing state bin is calculated using the moving center approach (Jacobson, 1997). The coagulation scheme developed in this study is a 2-D semi-implicit method (Matsui *et al*., 2013a), which is based on the 1-D semi-implicit coagulation algorithm (Jacobson *et al*., 1994). For wet removal processes, the volume averaged hygroscopicity and critical supersaturation are calculated for each of the 2-D aerosol bins. Using this information, aerosol activation to cloud droplets is calculated for each bin by applying a

doi:10.5047/meep.2015.00301.0001

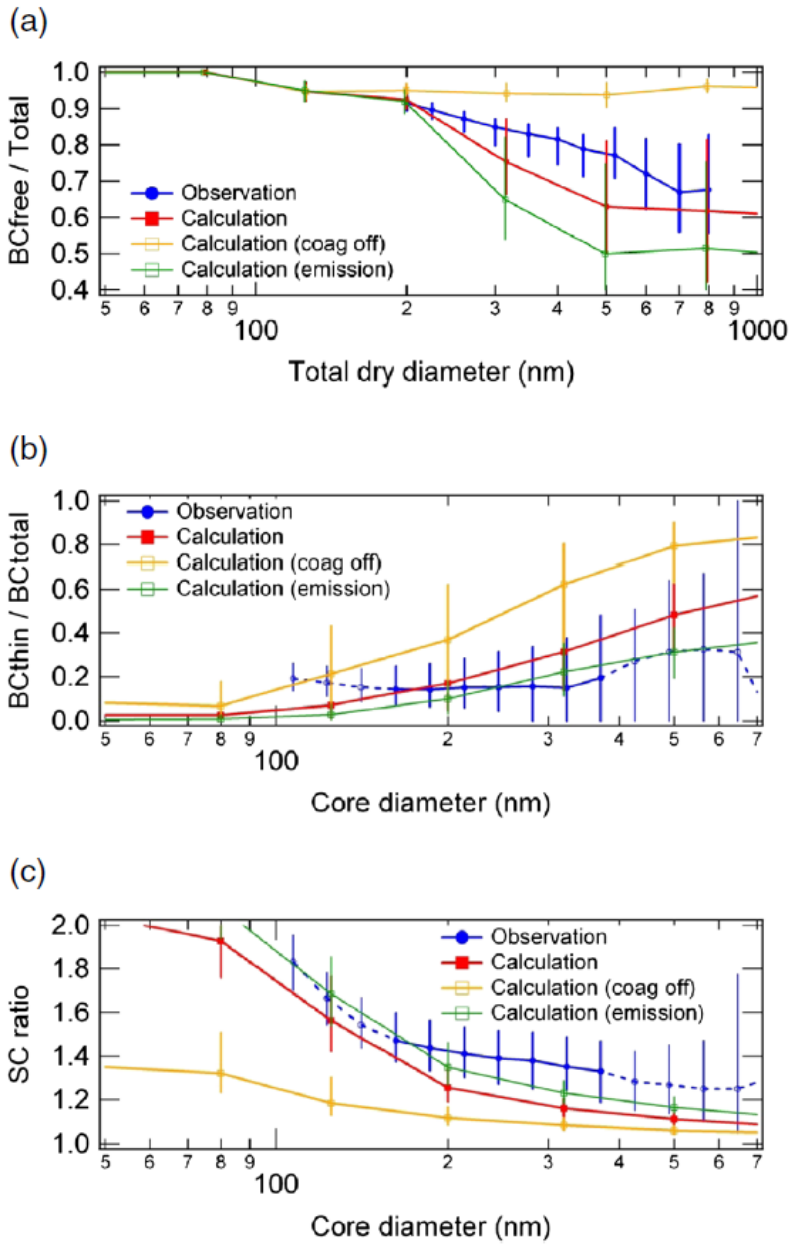

Fig. 39. (a) Dependence of the BC-free-to-total number concentration (BC-free/Total) ratio on the total dry (shell) diameter for both measurements (blue) and model simulations (red, orange, and green). Medians and 25th–75th percentiles during A-FORCE (all flights) are shown for individual bins. (b)–(c) Dependence of (b) the ratio of thinly-coated BC particles (SC (shell-to-BC core diameter) ratio < 1.1) and (c) mean SC ratio on BC core diameter. Closed circles and solid lines (open circles and dotted lines) show the diameters where the SP2 can measure all (a portion of) the internally mixed particles that have SC ratios between 1.0 and 2.0. The figures are from Matsui *et al*. (2013a).

maximum supersaturation determined from a Gaussian spectrum of updraft velocities (Abdul-Razzak and Ghan, 2000; Ghan *et al*., 2001; Gustafson *et al*., 2007; Chapman *et al*., 2009). Cloud-phase aerosols (activated as cloud particles under supersaturation of H_2O) and interstitial (unactivated) aerosols are tracked separately. Cloud-phase aerosols are removed by precipitation through cloud to rain water conversion rate, which is calculated in the cloud microphysical scheme of Lin *et al*. (1983).

The MS-resolved WRF-chem model was applied to the A-FORCE data. Model simulations were compared with the observed BC mixing state obtained by the SP2. Model simulations generally reproduced the observed features of the BC mixing state, such as the temporal variations and size dependencies of the following parameters: the number fraction of BC-containing, and BC-free, particles, the range and fraction of shell (total particle dry diameter)-to-BC core diameter ratio (SC ratio), and the mean SC ratio (Fig. 39). Both the observed and calculated mean SC ratios tended to be higher when aerosol mass concentrations were high, which was likely due to faster BC aging processes during transport from large sources (Fig. 40). This result shows that the model can simulate realistic BC mixing states in the atmosphere if microphysical processes, such as condensation

doi:10.5047/meep.2015.00301.0001

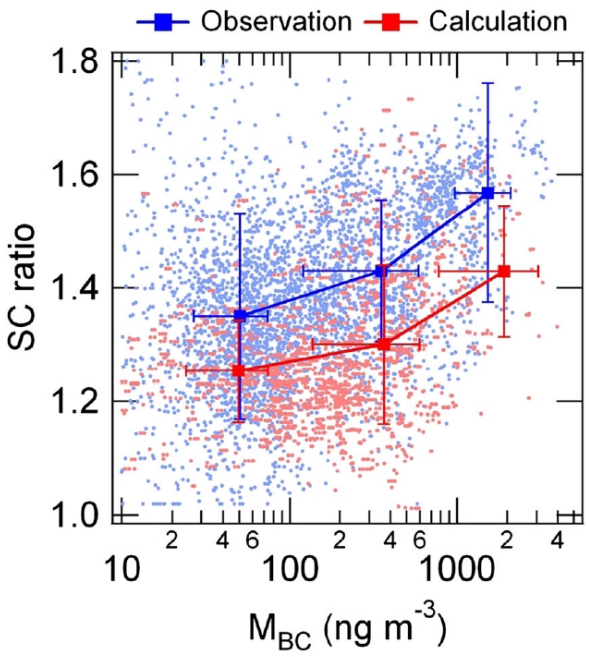

Fig. 40. Scatter plot of SC (shell-to-BC core diameter) ratio and BC mass concentrations during the A-FORCE campaign (all flights) (from Matsui *et al*., 2013a). Blue and red dots show observed and simulated 1-minute data, respectively.

and coagulation, are calculated explicitly with the detailed treatment of the BC mixing state.

We evaluated the impact of microphysical processes (condensation and coagulation) on the BC mixing state of atmospheric particles. Sensitivity simulations suggest that BC aging processes can be classified into two regimes because of competing effects between the condensation and coagulation processes. The condensation process is dominant for the growth of thinly-coated BC particles, while the coagulation process is necessary to produce thickly-coated BC particles. Therefore, in addition to the condensation process, the coagulation process is important in terms of the optical properties, radiative effects, and lifetime of BC. The orange lines in Fig. 39 show the BC mixing state (medians and 25th–75th percentiles) during A-FORCE when coagulation was switched off. The difference in the BC-free/total-number-concentration ratio between the coagulation-off and base simulations becomes larger with particle diameter, indicating the importance of coagulation processes for the growth to larger particles (Fig. 39(a)). Compared with the base simulation and measurements, the ratio of thinly-coated BC particles is larger and overestimated and the SC ratio is smaller and severely underestimated in the coagulation-off simulation (Figs. 39(b) and 39(c)).

We also conducted sensitivity simulations focused on the mixing state of emissions. We compared two simulations: (1) all the BC emissions were assumed to be externally mixed particles (base case simulation), and (2) 50% of the BC emissions were assumed to be internally mixed particles based on measurements at an urban site in Tokyo (sensitivity simulation). The results suggest that the mixing state of emissions significantly affects the BC mixing state in the atmosphere (green lines in Fig. 39), and therefore more observational studies are needed to evaluate the BC mixing state upon emission.

The spatial distributions of the BC mixing state were examined over East Asia during the simulation periods. Aged BC particles (low thinly-coated BC fraction and high SC ratio) were found at 30–40°N over China, the Yellow Sea, and the East China Sea. Model simulations suggest that the BC mixing state in East Asia is determined by synoptic-scale meteorological variations and most BC particles at 30–40°N have already experienced sufficient aging processes over the Asian continent.

10. Long-Term BC Observations at Hedo

Accurate long-term measurements of BC are necessary in assessing the transport of BC and the effects of BC on wide regions downstream of the large Asian sources. An evaluation of transport patterns and characterization of East Asian air masses for aerosols and trace gases have been made using aircraft (Hatakeyama *et al*., 2001, 2004; Carmichael *et al*., 2003; Verma *et al*., 2009) and surface measurements (Matsumoto *et al*., 2003; Li *et al*., 2007; Takami *et al*., 2007; Koga *et al*., 2008; Sahu *et al*., 2009). Other studies have discussed the transport patterns of CO and ozone for this region (Kajii *et al*., 1998; Narita *et al*., 1999; Pochanart *et al*., 1999; Kato *et al*., 2004). However, detailed studies of the transport of BC, including their seasonal variation, are limited, mainly due to the lack of long-term reliable BC measurements in Asian outflows. In order to overcome this difficulty, we made accurate measurements of the mass concentrations of BC (M_{BC}) using COSMOS at Hedo (26.9°N, 128.3°E) on Okinawa Island, Japan, for 15 months (March 2008–May 2009).

Measurements of M_{BC} from remote sites in the western Pacific are crucial to improving our understanding of the long-range transport of BC from continental Asia. Considering the large spatio-temporal variability in M_{BC} associated with the emission and transport of BC from the East Asian region, long-term BC measurements at high-altitude sites are important. We measured M_{BC} at Happo (36.7°N and 137.8°E) in Japan at 1.8 km asl for two consecutive years (August 2007–August 2009). In addition to the Hedo and Happo sites, M_{BC} was measured at Fukue (32.8°N and 128.7°E) using COSMOS since 2009 (Kanaya *et al*., 2013). Figure 28 shows the locations of these sites. The descriptions of the results at Hedo, given in this section, are based on Verma *et al*. (2011).

10.1 Observations of BC and CO

We made surface measurements of BC and CO at the Cape Hedo observatory (26.9°N, 128.3°E, 60 m ASL) on Okinawa Island, Japan, in the East China Sea from February 20, 2008 to May 31, 2009. The location of the site is shown in Fig. 28, together with the map of the BC emission rate estimated by Zhang *et al*. (2009). The Hedo site is 600 km distant from the main island of Japan, 1000 km from Korea, and 800 km from the coast of southern China. It is on a remote

doi:10.5047/meep.2015.00301.0001

island in Asian outflows, surrounded by ocean, typically within a few days of transport from the source region, thus allowing unambiguous identification of Asian BC sources. BC transported from China was clearly detected according to a detailed analysis of the temporal variations of BC and CO combined with trajectory calculations (Verma *et al*., 2011). More than 45% of air masses measured in winter and spring are estimated to have been influenced by BC emissions from China.

BC mass concentrations in the fine mode ($PM_{2.5}$, i.e., particles with aerodynamic diameters smaller than 2.5 μm) were measured using COSMOS. The BC was measured with an integration time of one minute. The estimated lower limit of detection (LOD) was about 0.047 μgC m^{-3}. We used one-hour average BC data for the present analysis.

CO was measured continuously using a commercial instrument, TECO Model 48C (Thermo Environmental Instruments, Inc.), based on a non-dispersive infrared absorption (NDIR) technique (Suthawaree *et al*., 2008). The instrument was calibrated at least once per calendar year using a 1.80 parts per million by volume (ppmv) CO standard gas (Nippon Sanso, Inc.). Changes in the calibration factor between each calibration did not exceed about 5%. Zero air generated by a TECO Model 96 was sampled for 20 minutes every hour to correct for the drift of the background signal of the instrument.

10.2 Variations of BC and CO

We carried out a detailed analysis of BC and CO data measured at Hedo for 15 months (March 2008–May 2009) in combination with a modified version of the Community Multiscale Air Quality (CMAQ) regional scale model. Detailed descriptions of the model are given in Kondo *et al*. (2011c) and Oshima *et al*. (2013). For the analysis of emissions and the removal of BC, we defined background levels of BC (BC_{BG}) and CO (CO_{BG}) for each month as the 5th percentile of the monthly observed data, similarly to the method for the A-FORCE data analysis. The average BC_{BG} and CO_{BG} values for spring 2008 and 2009 and winter 2009 were about 0.05 μg m^{-3} and 103 ppbv, respectively, and they are about half for summer and fall. We derived $\Delta BC = BC - BC_{BG}$ and $\Delta CO = CO - CO_{BG}$, where BC and CO denote their measured concentrations. We also calculated the transport efficiency (TE^{cal}) for the analysis of the wet deposition of BC:

$$TE^{cal} = [BC](CMAQ\text{-}Modified)/[BC](CMAQ\text{-}NoWetDep). \quad (30)$$

Here, [BC] (CMAQ-Modified) represents the BC mass concentration calculated by the CMAQ baseline simulation using the modified scheme of wet deposition of BC (Kondo *et al*., 2011c). [BC](CMAQ-NoWetDep) represents the BC mass concentration by another CMAQ simulation neglecting the effect of wet deposition.

To study the transport pattern influencing the measurement site, we analyzed 5-day back trajectories at hourly intervals, each starting from the Hedo site at a 950 hPa pressure height. Figure 41 shows the trajectories and relative humidities (RHs) from the NCEP FNL data along the trajectories for

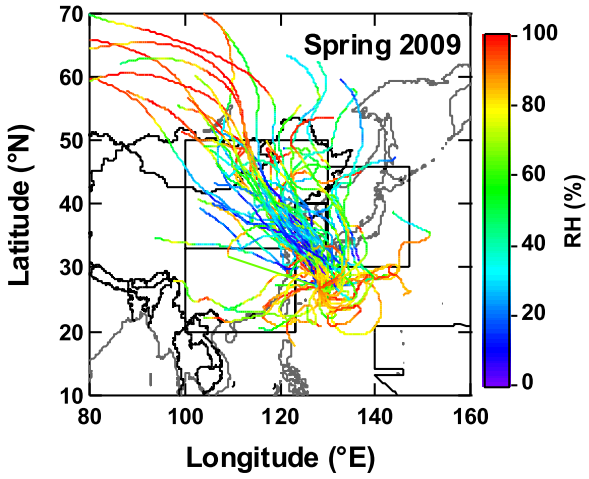

Fig. 41. Five-day back trajectories, each starting from the location of Hedo at 950 hPa pressure height (about 500 m in altitude) and 1200 LT or 0300 UTC (from Verma *et al*., 2011). Relative humidity (RH) along the trajectories is also shown. These trajectories were calculated using the trajectory model of the National Institute of Polar Research (NIPR, Japan), developed by Tomikawa and Sato (2005).

spring 2008. Irrespective of the seasons, the air masses arriving from the Chinese region were transported from higher altitudes (not shown) and were dry (Fig. 41). The origins of the observed air masses were determined by using 5-day back trajectories together with an analysis of the seasonally-averaged wind and precipitation fields: northern China (NC) (Fig. 28), southern China (SC) (Fig. 28), Korea (KR), Japan (JP), Marine (MA), and the free troposphere (FT). The seasonal variation of the transport of air masses over the East China Sea was controlled by alternating winter and summer monsoons. In spring and winter, the dominant source region air masses reaching Hedo was from China. During summer, most of the air masses were transported from the western Pacific. Due to the more frequent transport of Chinese air to Hedo in spring and winter, the average and background concentrations of BC and CO in these seasons were higher by about a factor of two than those of summer and fall, as discussed above.

Figure 42 shows the monthly mean and median values of BC and CO (first and second panels). The average concentrations of BC and CO in spring and winter were higher by about a factor 2 than those in summer and fall, reflecting the stronger influence of the continental outflows in winter and spring. In summer and early fall, Hedo was generally covered by relatively clean maritime air. These features are also clearly seen in Fig. 42 (first and second panels). Annual average concentrations of BC and CO were 0.29 μg m^{-3} and 150 ppbv, respectively.

10.3 ΔBC/ΔCO ratios

Irrespective of the season, higher concentrations of BC and CO were observed in the air masses arriving from NC and SC. For these air masses, the ΔBC/ΔCO ratios were generally correlated with the model-calculated transport efficiency of BC (TE^{cal}), suggesting the effect of wet removal in controlling BC transport. The validity of TE^{cal} has been

doi:10.5047/meep.2015.00301.0001

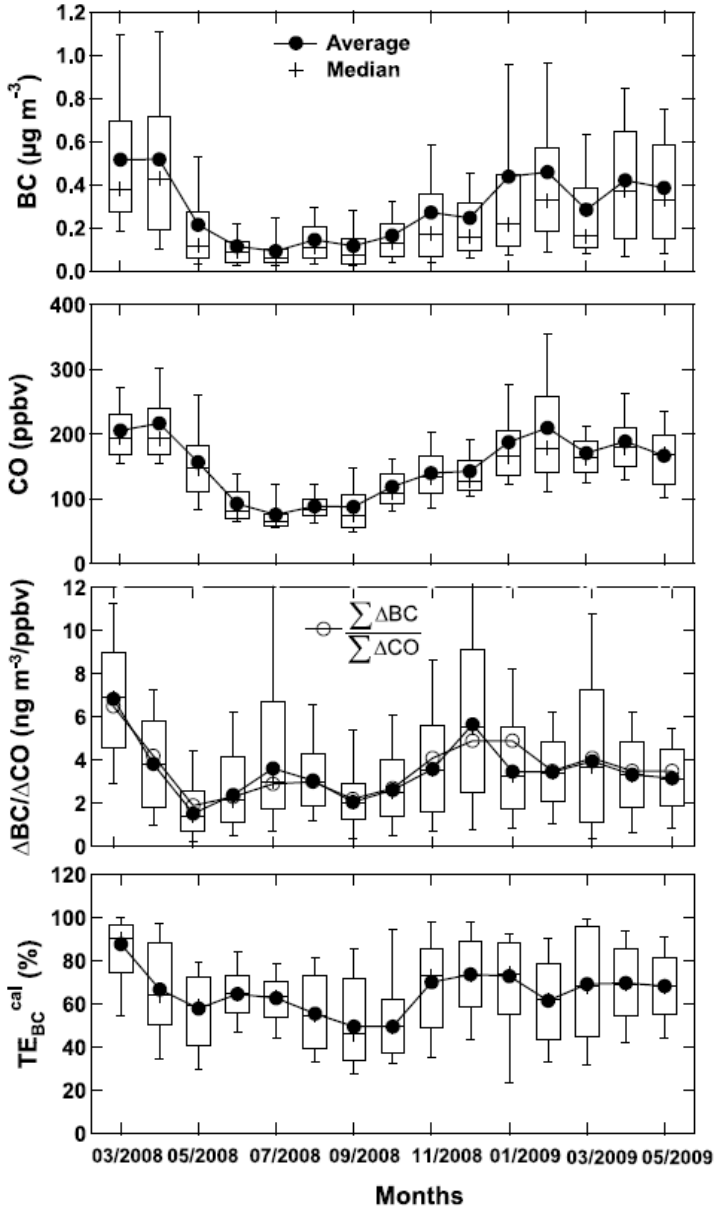

Fig. 42. Time series of the monthly values of BC, CO, $\Delta BC/\Delta CO$ ratios, and the model-calculated transport efficiency of BC (TE^{cal}) (from Verma *et al.*, 2011). Monthly mean $\Delta BC/\Delta CO$ ratios were derived using three methods: (1) the average, and (2) median, of the $(\Delta BC/\Delta CO)_i$ data points, shown with filled circles and pluses, respectively, and (3) the ratio of the sums of $(\Delta BC)_i$ and $(\Delta CO)_i$ (open circles). The lower and upper extent of the vertical bars represent the 10th and 90th percentiles of the values, respectively. The lower and upper limits of the boxes are the 25th and 75th percentiles, respectively.

partially supported by the agreement between the monthly average precipitation in East Asia predicted by the WRF simulation and the GPCP data. The average TE^{cal} for winter and spring was highest (72–81%) for NC air among all air mass categories, reflecting the lowest precipitation rates. This, together with the highest BC emission rate and frequency of transport, caused NC air to make the largest contributions to elevating BC levels at Hedo.

The $\Delta BC/\Delta CO$ ratios in air masses influenced by Chinese emissions showed significant correlations with TE^{cal}, clearly indicating that wet deposition is also an important controlling factor of the BC concentration at Hedo. We derived the $[\Delta BC/\Delta CO]_{ref}$ ratios least impacted by wet deposition by selecting data using TE_{cal} ($> 80\%$) as a meteorological parameter. The $[\Delta BC/\Delta CO]_{ref}$ ratios observed in the air masses of NC and SC were 7.0 and 7.5 ng m^{-3} ppbv, respectively. Further studies are needed for a systematic interpretation of these values.

Using the $[\Delta BC/\Delta CO]_{ref}$ ratios, the transport efficiencies of BC, TE^{obs}, was estimated as:

$$TE^{obs} = [\Delta BC/\Delta CO]_{all}/[\Delta BC/\Delta CO]_{ref}, \quad (31)$$

$$[\Delta BC/\Delta CO]_{all} = \Sigma_i(\Delta BC)_i/\Sigma_I(\Delta CO)_i, \quad (32)$$

doi:10.5047/meep.2015.00301.0001

where $(\Delta BC)_i$ and $(\Delta CO)_i$ represent the ith ΔBC and ΔCO values within individual groups of the data sets.

The derived TE^{obs} values were about 70% for NC and SC air. The TE^{obs} values were similar for winter and spring, despite the increase in precipitation over the outflow region in spring.

Evaluation of the CO emission inventory of Zhang *et al*. (2009) was made using ground-based and aircraft measurements. The $\Delta CO_{CMAQ}/\Delta CO_{Obs}$ ratios for ground-based and aircraft measurements were 0.49 (for NC at Hedo) and 0.52 in the PBL (aircraft), respectively. We also compared the $[\Delta BC/\Delta CO]_{ref}$ ratios with the BC/CO emission ratios derived from the emission inventories of Zhang *et al*. (2009). The derived BC/CO emission ratios were 1.8 and 1.6 times larger than the $[\Delta BC/\Delta CO]_{ref}$ ratios for NC and SC air, respectively. Since the overall BC emissions estimate by Kondo *et al*. (2011c) agreed well with those of the Zhang *et al*. (2009) inventory for China (Chapter 10), it is therefore likely that the emission rate of CO was underestimated by about a factor two by Zhang *et al*. (2009). An indication of the underestimation of CO was also shown by the comparison of the CMAQ model-calculated CO with that observed with ground-based and aircraft measurements.

11. Estimates of BC Emissions in East Asia

In this chapter, the methodology of estimating BC emissions from large sources using surface BC measurements at a remote downstream site is described based on Kondo *et al*. (2011c). We used the Hedo data to estimate BC emissions over the Asian continent.

11.1 Previous studies and new methodology

It is critically important to estimate or assess the emission rates from major source regions in Asia to improve our understanding of the effect of BC on climate, considering that Asia was the largest BC source region in 2000 according to recent emission inventories (Streets *et al*., 2003; Ohara *et al*., 2007; Zhang *et al*., 2009). The uncertainty of the most recent emission estimates for the year 2006 is still as large as 208% for China (Zhang *et al*., 2009), although the uncertainty was substantially improved as compared with that of 484% for an earlier inventory (Streets *et al*., 2003). Kondo *et al*. (2011c) made independent estimates of BC emissions by comparing BC mass concentrations calculated by three-dimensional (3-D) chemical transport models (CTMs) with those observed in the atmosphere, as detailed below. BC concentrations are influenced not only by BC emissions but also transport processes and removal during transport. Therefore the estimate of BC emissions using ambient BC data needs to include the uncertainties of predicting transport and the removal of BC in the models.

There have been attempts to evaluate BC emissions in Asia. Carmichael *et al*. (2003) compared the observed and model-calculated BC concentrations during the NASA Transport and Chemical Evolution over the Pacific (TRACE-P) aircraft campaign to find that the Sulfur Transport Eulerian Model 2001 (STEM-2K1) model underestimated the mean BC concentration by 20% for flight altitudes below 2 km. However, the period of the comparison was too short for assessing BC emissions from Asia with sufficient statistical significance. Uno *et al*. (2003) compared model BC values, predicted by the Regional Atmospheric Modeling System (RAMS)/Chemical Weather Forecast System (CFORS) model system with those measured at the surface on five remote islands in Japan during the Asian Aerosol Characterization Experiment (ACE Asia) campaign. These models predicted well the patterns of the temporal variations of the observed BC, leading to an improved understanding of the modes of transport of BC from the Asian continent. Hakami *et al*. (2005) utilized four-dimensional variational data assimilation (4D-Var) for the estimation of BC emissions from the observed BC values on the five islands and onboard a ship during ACE-Asia. However, the accuracies of the BC measured during ACE-Asia have not been fully quantified (e.g., Huebert and Charlson, 2000).

In addition to the uncertainties of the BC measurements, the effects of wet removal of BC from the atmosphere were not fully taken into account in these studies. In order to assess the bottom-up emission inventories accurately by comparison of the BC mass concentrations calculated by 3-D CTMs with those observed, the factors potentially leading to substantial uncertainties have to be evaluated and improved. They are (1) the accuracies of the observed BC values, and (2) the uncertainties in the model calculations, such as the horizontal and vertical diffusion and the microphysical properties of BC (size distribution and hygroscopicity), which affect the rate of wet removal of BC.

We have greatly reduced the uncertainties in the observed and model BC values to improve estimates of BC emissions in a more reliable way, compared with the previous studies. First, we used the BC and CO data obtained at Hedo, discussed in Chapter 10. Second, we excluded data substantially influenced by wet deposition by using carbon monoxide (CO) data as a water-insoluble tracer, combined with 3-D CTM calculations. We mainly used the modified version of the CMAQ model, which is described in Kondo *et al*. (2011c). We also used the Eulerian, Multiscale Tropospheric Aerosol Chemistry dynamics Simulator (EMTACS) model (Kajino and Kondo, 2011) for a comparison of the models. Third, we made inter-comparisons of the BC mass concentrations calculated by two CTMs with different formulations for atmospheric transport and aerosol processes to evaluate the uncertainties associated with the variability in transport and removal processes of BC. The vertical distributions of BC calculated by the models were also supported by the comparison of the BC vertical profiles obtained during A-FORCE. We show that improved BC measurements and models have enabled quantitative estimates of BC emissions in China.

11.2 Reference emission inventory

The estimates of BC emissions made for the East Asian region for the year 2000 with a spatial resolution of $1^\circ \times 1^\circ$ (Streets *et al*., 2003) were updated by Zhang *et al*. (2009) for the year 2006 with a spatial resolution of $0.5^\circ \times 0.5^\circ$. Figure 28 shows the spatial distribution of anthropogenic emissions of BC (Gg/year/grid) for the East Asian region (Zhang *et al*., 2009). In an estimate by Bond *et al*. (2004),

doi:10.5047/meep.2015.00301.0001

the amount of BC emitted from East Asia is about 30% of the total global anthropogenic BC emissions. According to Zhang *et al*. (2009), the total BC emissions from the East Asian region in 2006 are about 1.99 Tg. About 91% (1.81 Tg) of BC in East Asia is emitted from China (Zhang *et al*., 2009). Because of the dominance of China in the BC emissions, we focus on the estimate of the BC emissions from China, using this inventory as a reference. In China, a large fraction of BC is emitted from the residential (55%) and industrial (32%) sectors, while a smaller fraction is from transport (11%) and power (2%) (Zhang *et al*., 2009). These inventories are subject to an uncertainty of 208% for BC.

Ohara *et al*. (2007) estimated that BC emissions in Asia increased by 5% between 2000 and 2010. We estimate BC emissions based on the BC measurements made in 2008–2009. Our estimate should not depend on the reference BC inventory (in this case, Zhang *et al*. (2009)) as long as the pattern of spatial distribution and seasonal variation remain unchanged. In any case, the change in the BC emissions between 2006 (Zhang *et al*. (2009)) and 2008–2009 (this study) is estimated to be less than 2% by linear interpolation.

11.3 Emission rate of BC from China

The CMAQ-Modified simulation was used to calculate the mass concentrations of BC using annual mean emission inventories of Zhang *et al*. (2009) for the year of 2006. The model reproduced well the temporal variations of surface BC mass concentrations observed at Hedo during the whole observation period and the median BC vertical profile obtained by aircraft over the East China Sea in spring 2009.

In order to assess the model variability in the transport and removal processes of BC, we inter-compared CMAQ-Modified and EMTACS simulations, in which formulations of atmospheric dispersion and aerosol processes are different. The difference in the predicted BC mass concentrations between the models was small around Cape Hedo, with $r^2 = 0.6$–0.8, indicating the smaller uncertainty in the model predictions of BC at the location of Hedo.

We selected BC data strongly impacted by emissions from China ($f_{\mathrm{China}} > 0.8$) and least impacted by wet deposition during transport (TE > 0.8). Here, $f_{\mathrm{China}} >$ represents the relative contributions of BC emitted from the whole of China to the CMAQ-Modified simulation. The transport efficiency of BC (TE) is the mass fraction of BC transported to Hedo after emissions in East Asia. TE was estimated by comparing BC mass concentrations calculated by CMAQ-Modified with and without wet deposition of BC. After these selections, r^2 for the BC-CO correlation increased to 0.82, with a substantial amount of data ($N > 1000$) remaining for statistical analysis, as shown in Fig. 43.

We compared the median values of the selected observed (*Obs*. (med)) and modeled (*Model* (med)) BC values, as shown in Fig. 44. The *Model* (med)/*Obs*. (med) ratios were derived by taking into account the seasonal variations of BC emissions (table 7 of Kondo *et al*. (2011c)). The *Model* (med)/*Obs*. (med) ratio for the entire period was 1.06±0.03. The overall uncertainty of the ratio was estimated to be 40%. This means we estimate the annually averaged BC emission flux over all of China to be 1.71 Tg yr^{-1}, with an uncertainty

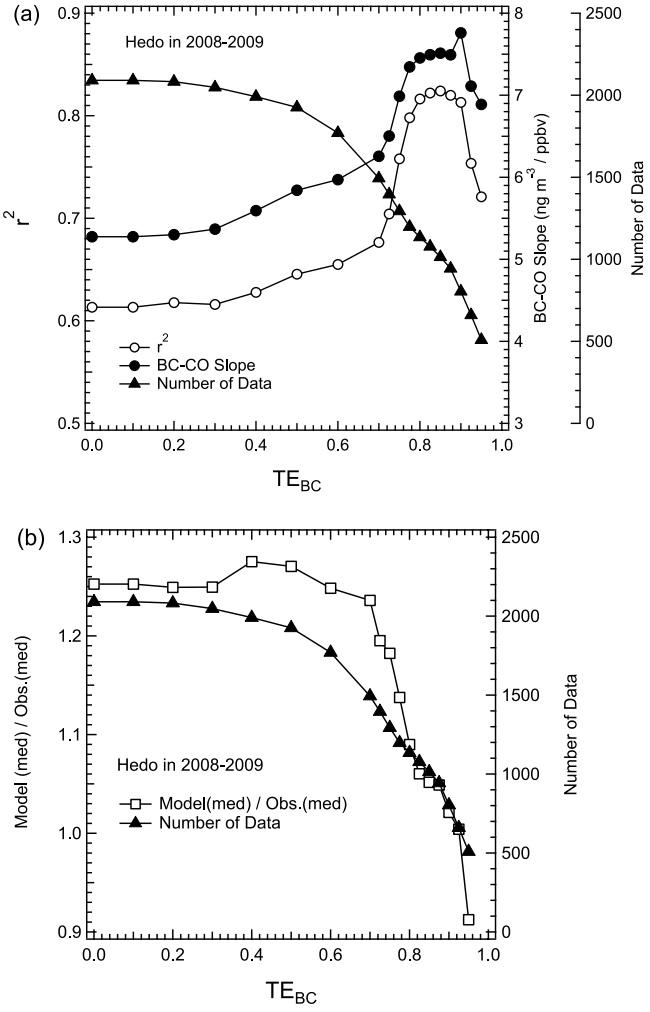

Fig. 43. (a) Changes in the slopes of the observed BC-CO correlations (solid circles), their correlation coefficients (open circles), and the number of remaining data points (solid triangles) with the changes in the threshold value of TE (transport efficiencies of BC). (b) Changes in the ratios of median values of modeled BC to those observed after the data selection with f_{China} (relative contributions of BC emitted from the whole of China) > 0.8 (open squares) and the number of remaining data points (solid triangles) with changes in the threshold value of TE. The figures are from Kondo *et al*. (2011c).

of about 40%. The value is very close to the value of 1.81 Tg yr^{-1} estimated by Zhang *et al*. (2009). Although the absolute values of the two estimates turned out to be very similar, partly by coincidence, the uncertainty of our estimate is much smaller than the 208% uncertainty given by Zhang *et al*. (2009).

12. Long-Term BC Observations at Happo

In this chapter, we discuss the transport of BC from different parts of Asia to the remote mountain site of Happo based on the descriptions by Liu *et al*. (2013b). The observed seasonal variation of BC is interpreted in terms of the temporal variations of the transport processes and sources of BC.

12.1 Observations

The M_{BC} measured at Hedo was found to be strongly influenced by BC transported from China throughout the year,

doi:10.5047/meep.2015.00301.0001

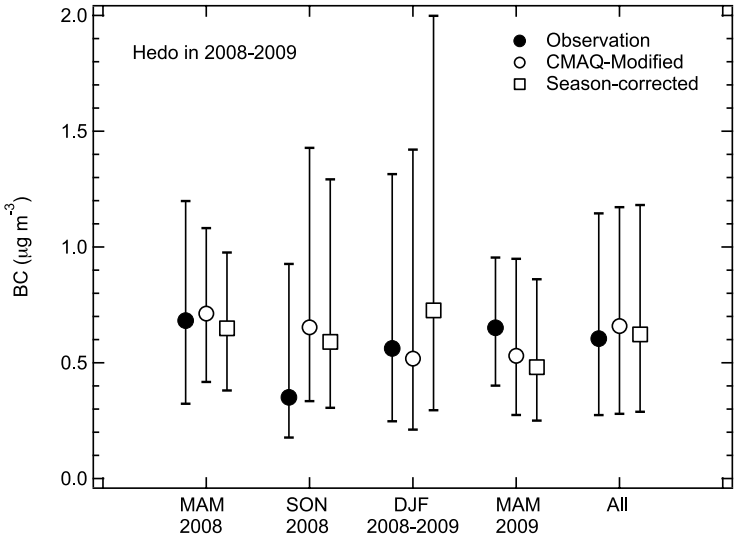

Fig. 44. Comparison of the median and the central 67% ranges of hourly BC mass concentrations observed at Hedo in winter, fall, spring, and the entire period (February 2008 to May 2009) (solid circles) and those calculated by the CMAQ-Modified simulation with (open squares) and without (open circles) taking into account the seasonal variation of BC emissions after data selection with $f_{\mathrm{China}} > 0.8$ and TE > 0.8 (from Kondo *et al.*, 2011c).

except in the summer (Chapter 10). Considering the large spatio-temporal variability in M_{BC} associated with the emission and transport of BC from the East Asian region, long-term BC measurements at high-altitude sites are important. We carried out measurements of M_{BC} using COSMOS at Happo (36.7°N and 137.8°E) in Japan at 1.8 km asl for two consecutive years (August 2007–August 2009). The Happo station is located in the Hakuba Mountains (northern Japanese Alps), in the center of the main island of Japan, about 200 km northwest of Tokyo and 25 km south of the Sea of Japan (Fig. 28). No significant effects of BC emissions in the vicinity of the sampling site were detected.

Earlier studies have suggested a seasonal variability in the CO concentration at this site and downstream of the Asian continent. In fact, the site was strongly influenced by the transport of anthropogenic emissions in China and Korea, and occasionally Siberian biomass burning events (Narita *et al.*, 1999; Kato *et al.*, 2002). However, reliable long-term measurements of M_{BC} are still limited at Happo and other locations in the western Pacific. For the first time, we present accurate measurements of M_{BC} for two years, 2007–2009, its seasonal and interannual variability, and the transport of BC aerosols from the Asian continent at this altitude in the western Pacific.

12.2 Origins of air masses

We classified the air mass types based on the residence time (RT) of an air mass in a given region as predicted by the trajectories. These regions are defined as NC, SC, KR, JP, marine (MA), and FT, in the same way as discussed in Chapter 10. The air masses were defined as NC, KR, SC, or JP, if their back trajectories originated in the PBL of NC, KR, SC, or JP. In this study, we defined the top level of the PBL over the Asian continent as the 700 hPa atmospheric pressure level (about 3.0 km). Air masses originating from NC often passed over the Korean region before reaching Happo. We defined mixed (MX) type of air masses if the air masses stayed in both regions long enough (Liu *et al.*, 2013b). Trajectories show that FT air passed predominantly over the Asian continent, especially China.

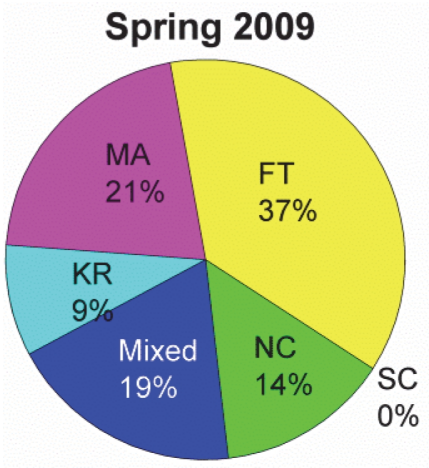

Fig. 45. Fractions of the air parcels of different categories arriving at Happo in different seasons for the entire measurement period (from Liu *et al.*, 2013b). For statistics, we included only air parcels that spent at least 24 h (i.e., RT > 24 h) in a specified region. NC: north China, SC: south China, KR: Korea, MA: marine, FT: free troposphere.

Figure 45 shows the percentage (%) contribution of different air mass types for spring 2009. Generally, the FT air masses dominated the total air masses reaching Happo, except during summer. The contribution of NC air was 9–14% during the study period and was a minimum during summer and fall 2008. If the air masses from KR and MX are considered to have been influenced by BC emissions in NC, the total fractions of air masses of NC origin increase to 35–55%. The fractions of the Chinese air (NC + SC + MX + KR) are similar to the values of 47–55% observed at Hedo (Verma *et al.*, 2011).

doi:10.5047/meep.2015.00301.0001

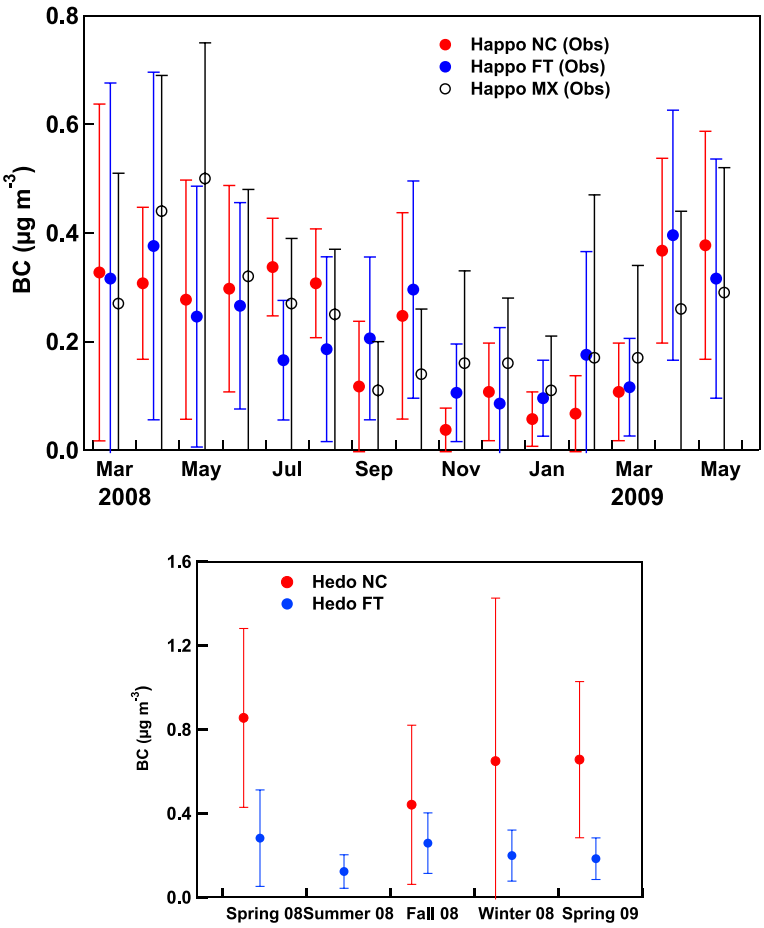

Fig. 46. Monthly mean ($\pm 1\sigma$) of the observed M_{BC} (BC mass concentration) values at Happo in FT, NC, and MX (mixed) air parcels during 2008–2009. (b) Seasonally averaged M_{BC} values observed at Hedo in NC and FT air masses. The 1σ values are those of the hourly M_{BC} values. The figures are from Liu *et al*. (2013b).

12.3 Effects of local emissions

Before analyzing the Happo data set in detail, we assessed the possible effects of local BC emission sources on the observed M_{BC}. The daytime/nighttime ratios of M_{BC} were 1.21 for July 2008 and 1.11 for January 2009. The ratios for other months were generally in this range (not shown). The seasonal variation of the ratio is mainly due to the variation of the heating rate of the mountain slopes. The diurnal variation of M_{BC} is not necessarily due to BC emitted locally. As discussed below, M_{BC} generally decreased with the increase in altitude from the BL to the FT over the western Pacific. The vertical gradient in M_{BC} can cause small diurnal variations in M_{BC} at Happo, coupled with diurnal variations of the upward and downward transport of ambient air. Because of this, we have used diurnally-averaged values of M_{BC} for the quantitative analysis without discarding the daytime data. The uncertainty in the interpretation of the M_{BC} data associated with the 24-hour averaging is estimated to be about 5% for winter and 10% for summer.

12.4 Seasonal variation of BC

Figure 46 (upper panel) shows the monthly averaged M_{BC} values for NC, FT, and MX air masses. The mean M_{BC} values in FT air masses are close to those of NC air masses, for which trajectories were located below 700 hPa. The mean pressure level of FT air near the eastern boundaries was about 570 hPa (about 4.5 km). This suggests that PBL air was well mixed up to at least about 700 hPa. It is also possible that FT air was mixed with NC air before reaching Happo at 1.8 km (~750 hPa). In this regard, the M_{BC} values in NC and FT air are interpreted to be the most representative M_{BC} values at 1.8 km height in the western Pacific, strongly influenced by BC emissions in NC. The M_{BC} values in FT and NC air were the lowest in the November–March period and they were similar for the other months. The M_{BC} values showed rather sharp increases from March to April. The lower M_{BC} values in late fall/early spring were also seen for MX air, although less pronounced, suggesting some differences in the characteristics of MX air.

Figure 46 (lower panel) shows seasonally averaged M_{BC} values for NC and FT air masses at Hedo. The observed M_{BC} values for NC and FT air masses at Hedo are very different from those at Happo. In contrast to the relatively similar M_{BC} values for NC and FT air masses at Happo, M_{BC} values were a factor of 2–3 higher for NC air masses at Hedo. However, the level of M_{BC} in FT air masses at Hedo is more or less similar to that at Happo. This suggests that the mixing and transport pathways of the NC air masses and the BC removal during the transport were somewhat different between Happo

doi:10.5047/meep.2015.00301.0001

and Hedo. The measurements of M_{BC} at Hedo represent values near the surface, whereas those at Happo were at an altitude of ∼1.8 km. In the case of Hedo, the NC air masses were transported at a lower altitude, well within the PBL.

The M_{BC} values for MX air in April and May 2008 were considerably higher than those for FT and NC air. They were also higher than those for MX air in 2009. This suggests additional sources of BC aerosols in Asia, especially in spring 2008. The possible cause of the high M_{BC} in MX air in spring is discussed in detail in Chapter 14.

M_{BC} values of ground-based observations at Hedo and Happo are also compared with the A-FORCE data in Fig. 32. The mean M_{BC} values were between 0.3 and 0.5 μg m^{-3} at altitudes below 2 km, strongly influenced by the transport of BC from China and decreasing sharply above 2 km altitude. The mean M_{BC} values at Happo are similar to the M_{BC} values obtained during the A-FORCE campaign, within the variability of M_{BC} shown as horizontal bars in Fig. 32. The small vertical gradient of M_{BC} from the surface up to 1.8 km is consistent with the similarity in the M_{BC} for FT and NC air at Happo, as discussed above.

12.5 Upward transport, wet deposition, and biomass burning

It is estimated that BC emissions and surface BC concentrations in China are relatively higher during winter compared with those during spring months (Streets *et al*., 2003; Zhang *et al*., 2009). However, the M_{BC} levels were significantly higher during the spring of both years than those in winter at Happo (Fig. 46, upper panel). The M_{BC} at Happo increased to 0.37 μg m^{-3} from an average value of 0.22 μg m^{-3}, in particular during the month of April of both years. There could be three reasons for the enhancement in the levels of M_{BC} at Happo during spring. First, the ambient temperature over NC is usually lower during winter than that in the spring season, resulting in shallower mixing layer heights over NC during winter as compared with the situation in spring. Therefore, the upward transport of BC-enriched air masses from the surface to the regions above the mixed layer could be lower during winter than those in spring. Second, in winter, BC can be removed efficiently by frequent snowfall before air parcels reach Happo, although no quantitative analysis has been made. Third, BC emissions from biomass burning during the spring season could also contribute to the winter-spring difference.

For a quantitative interpretation of the seasonal variations of BC, we used model-calculated values of the BC mass concentration $M_{BC\text{-model}}$ (AN), calculated by the CMAQ model combined with the source and process apportionment method (Matsui and Koike, 2012) including anthropogenic BC emissions. The $M_{BC\text{-model}}$ (AN) values at 1.8 and 2.8 km, at 130–140°E, were higher in April than in January (not shown). In contrast, the $M_{BC\text{-model}}$ (AN) in the PBL (∼0.2 km) over the Asian continent was much higher in January than April (not shown). These results suggest that the increase in the upward transport followed by northeastward horizontal transport partly caused the rapid increase in the M_{BC} values in April. However, we need to quantify the effect of the wet deposition of BC by the snowfall in winter, which often occurs near the coastal areas of the Japan Sea, upstream of the Happo site, in order to understand the relative contributions of the two processes to the winter minimum of M_{BC} at Happo.

We also extracted the M_{BC} values for FT, NC, and MX air, separately. $M_{BC\text{-model}}$ (AN) values for these air masses are compared with the observed M_{BC} values in Fig. 47.

The model calculations reproduced well the winter minimum for FT and NC air. Excellent agreement was obtained for FT air, which was least impacted by biomass burning (BB). It will be possible to estimate quantitatively the effects of the upward transport and wet deposition on the seasonal variations of the M_{BC} in FT air.

There could be additional BC emissions other than AN, such as those from biomass or agricultural waste burning in the Asian continent during the spring season. Earlier studies have suggested that the spring maximum of CO concentration at Happo results from BB events in East Asia, particularly from Siberia (Narita *et al*., 1999; Kato *et al*., 2002). Because BC and CO are produced simultaneously, as indicated by a strong correlation between their mass concentrations near source regions (Kondo *et al*., 2006; Limon-Sanchez *et al*., 2011; Pan *et al*., 2011), it is likely that Siberian biomass burning events had a strong influence on the M_{BC} at Happo during spring as well. The effect of BB is discussed in more detail in Chapter 14.

The long-term reliable measurements of M_{BC} at the remote sites Hedo and Happo are among the first, at least in East Asia. They are shown to be useful in a systematic understanding of the temporal variations of M_{BC} at different time scales throughout the PBL and lowest part of the FT.

13. Observations of Wet Deposition of BC at Hedo

Direct measurements of BC wet deposition on the ground will improve the understanding of the characteristics of BC wet deposition, in conjunction with measurements of BC loss in the atmosphere. Measurements of BC deposition flux are also useful to evaluate model performance in representing BC wet deposition if they are made accurately and with sufficient frequency. In this chapter, long-term observations of the BC wet deposition flux at Hedo are presented based on the descriptions by Mori *et al*. (2014).

13.1 Previous studies

Using the thermal optical transmittance (TOT) technique, BC mass concentrations in rainwater (C_{BC}) have been obtained at several locations in the United States and Europe, often together with BC mass concentrations in air (M_{BC}). Ogren *et al*. (1984) measured M_{BC}, C_{BC}, and BC wet deposition flux (F_{BC}) for 7 weeks in Seattle and for 5 months in Sweden. Ducret and Cachier (1992) measured M_{BC} and C_{BC} in Paris for 2 years and at a rural site in Ireland for about 2 months. They found that BC was removed more efficiently in Ireland than in Paris by comparing the C_{BC}/M_{BC} ratios measured at both sites. It was speculated that the difference in the C_{BC}/M_{BC} ratios might have been caused by the possible difference in hygroscopicity of BC at the two sites. Armalis (1999) measured F_{BC} at eight sites in rural Lithuania for 1–3 years. They found a maximum F_{BC} in winter in associa-

doi:10.5047/meep.2015.00301.0001

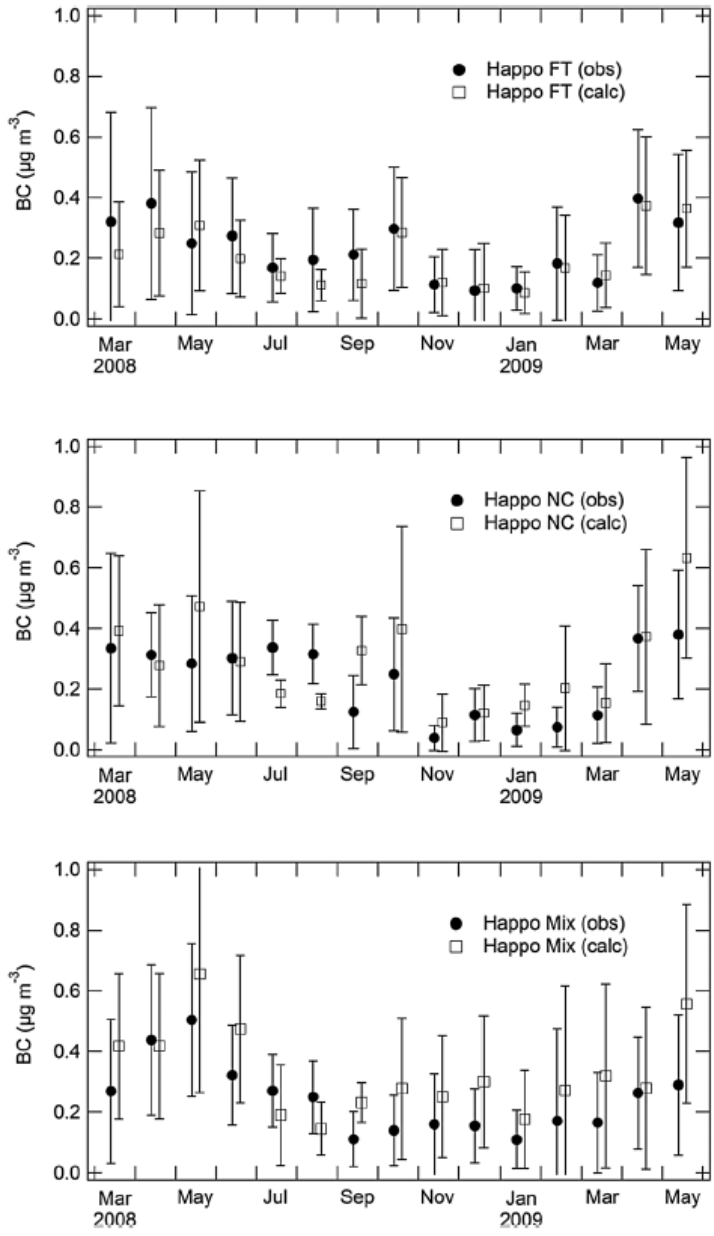

Fig. 47. Comparison of the model-calculated monthly mean M_{BC} (AN (fossil fuel combustion) + BB (biomass burning)) values with those observed for (top) FT, (middle) NC, and (bottom) MX air parcels (from Liu *et al*., 2013b).

tion with maxima in M_{BC} and C_{BC}. Cerqueira *et al*. (2010) obtained F_{BC} at five sampling sites in western and eastern Europe for a few years. However, these C_{BC} and F_{BC} observations were not analyzed with a consideration of transport of BC from major sources (e.g., East Asia).

13.2 Model estimate of BC wet deposition

To improve the understanding of the temporal and spatial variations of C_{BC} and F_{BC}, downstream of the Asian continent, we made measurements of BC in rainwater at Hedo, the first long-term measurements applying the validated technique described in Chapter 4.

In Fig. 48, we show maps of the BC emission rate, the column BC mass concentration, the precipitation rate, and the BC wet deposition flux in East Asia averaged from March to May 2010, as calculated by the CMAQ model with the Process, Age, and Source region Chasing Algorithm (PASCAL) regional scale model (Matsui and Koike, 2012; Matsui *et al*., 2013b), which is described in more detail in Chapter 14. During this period, BC emissions were highest in north China (NC) (33–50°N, 100–130°E) and are reflected in the high BC column mass concentrations in that region (Fig. 48(b)). However, the wet deposition flux of BC over the Asian continent was highest in south China (20–33°N, 100–123°E) (Fig. 48(d)) due to the much higher precipitation there (Fig. 48(c)). Figures 48(a) and 48(d) suggest that the majority of BC emitted in NC was removed downstream rather than locally. Figures 48(b) and 48(d) also show that the column BC mass concentrations and wet deposition

doi:10.5047/meep.2015.00301.0001

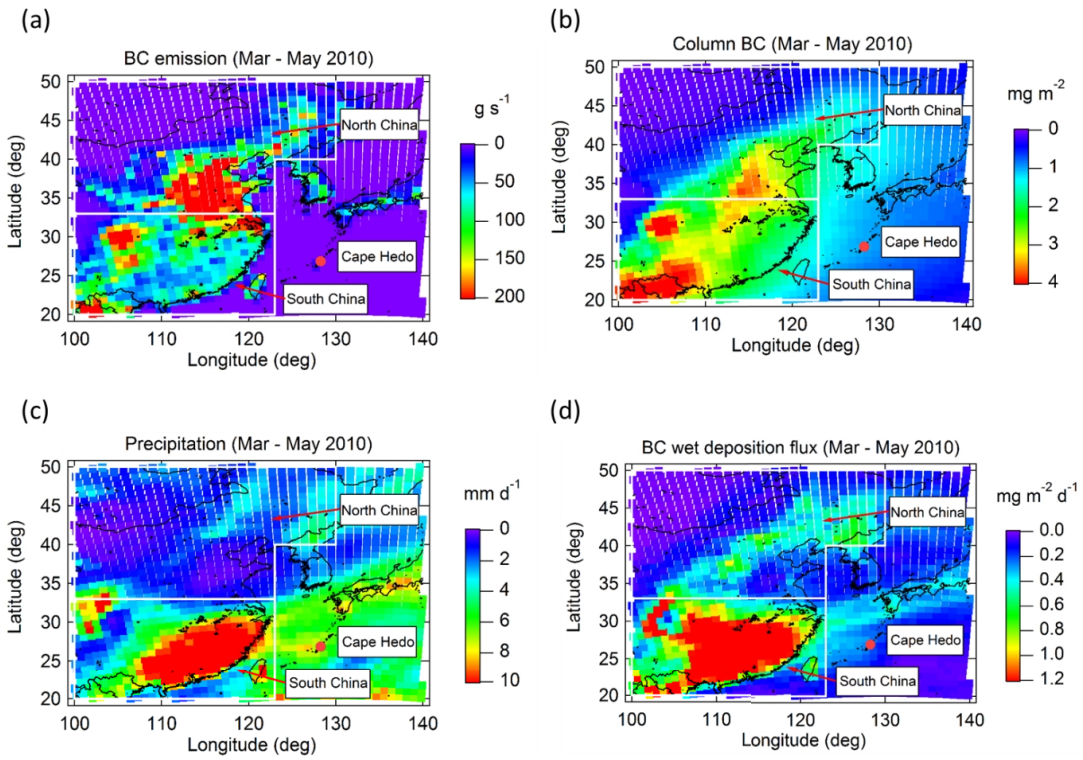

Fig. 48. Maps of (a) anthropogenic BC emissions, (b) column BC in the air, (c) precipitation, and (d) BC wet deposition flux over East Asia for March–May 2010, as calculated with the CMAQ-PASCAL model (Matsui *et al*., 2013b). The figures are from Mori *et al*. (2014).

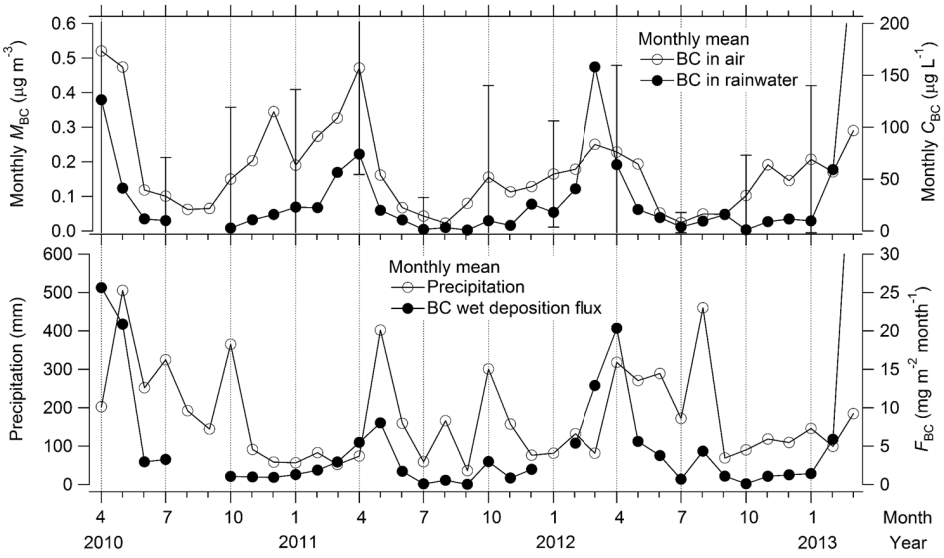

Fig. 49. Average monthly BC mass concentration in air (M_{BC}) and rainwater (C_{BC}), monthly precipitation, and monthly BC wet deposition flux (F_{BC}) from April 2010 to March 2013 (from Mori *et al*., 2014). Uncertainties ($\pm 1\sigma$) are shown for each 3-month season. A C_{BC} value of 270 μg L^{-1} month^{-1} and a F_{BC} value of 50 mg m^{-2} month^{-1} for March 2013 are not shown.

fluxes were rather uniform near Hedo, suggesting that the measurements of BC wet deposition at Hedo are representative of that region.

13.3 Seasonal variations of BC wet deposition

We measured M_{BC} and C_{BC} simultaneously at Hedo for three years (April 2010 to March 2013) with accuracies of about 10% and 25%, respectively. Figure 49 shows the average monthly M_{BC} and C_{BC}, monthly precipitation, and monthly F_{BC} from April 2010 to March 2013. The average seasonal values of these parameters are summarized in table 1of Mori *et al*. (2014). More detailed descriptions of the observations and meteorological analyses are given also in this paper. The monthly M_{BC} and C_{BC} values showed marked seasonal variations with the highest being in spring

doi:10.5047/meep.2015.00301.0001

(0.32 ± 0.13 μg m^{-3} and 92 ± 76 μg L^{-1}, respectively) and the lowest in summer (0.06 ± 0.03 μg m^{-3} and 8.0 ± 4.1 μg L^{-1}, respectively). The monthly average $M_{\rm BC}$ and $C_{\rm BC}$ were well correlated ($r^2 = 0.58$).

The high value of $C_{\rm BC}$ in spring was caused by $M_{\rm BC}$ transported from the Asian continent by monsoonal northwesterly winds. The wet deposition flux of BC ($F_{\rm BC}$), calculated as the product of $C_{\rm BC}$ and precipitation, also showed distinct seasonal variations. The annual averaged and springtime (March, April, and May) $F_{\rm BC}$ values were 5.5 ± 9.9 and 16.8 ± 6.7 mg m^{-2} month^{-1}, respectively. The total BC mass deposited per unit area in one year, denoted as $DEP_{\rm BC}$ (annual), was 66 mg m^{-2} (= 5.5 mg m^{-2} month^{-1} $\times$ 12) and that for spring ($DEP_{\rm BC}$ (spring)) was 50 mg m^{-2} (= 16.8 mg m^{-2} month^{-1} $\times$ 3) on average. From this,

$$DEP_{\rm BC}(\text{spring})/DEP_{\rm BC}(\text{annual}) = 0.76 \qquad (33)$$

meaning that about 76% of the annual BC deposition occurred in spring on average. The high seasonal $DEP_{\rm BC}$ of 50 mg m^{-2} in spring was the result of the highest $M_{\rm BC}$ (0.32 μg m^{-3}) and precipitation (about 700 mm), which is comparable to the value for summer.

It is noted that the observed $F_{\rm BC}$ value at Hedo was close to the net emission flux of BC in NC. The CMAQ-PASCAL predicts very low $F_{\rm BC}$ in NC as a result of low precipitation in spring. It is likely that a substantial fraction of BC emitted in this region is transported to latitudes south of 33°N, where precipitation is much higher. This analysis indicates the importance of precipitation along the Bai-u frontal system as an efficient removal mechanism for BC transported from NC in spring.

14. Comparison of Surface BC Data with Model Calculations

In this chapter, results of the regional scale model calculations are presented for comparison with the surface measurements, discussed in Chapters 10, 11, and 12, based on the descriptions by Matsui *et al*. (2013b). The comparison is useful for the quantitative interpretation of the observed spatial and temporal variations of BC. It also leads to the validation of the model in representing key parameters and processes that control BC mass concentrations.

14.1 Seasonal variations

For additional quantitative studies on BC transport, we have simulated the BC mass outflow from the Asian continent to the Pacific during the period 2008–2010, using the CMAQ-PASCAL (Matsui and Koike, 2012). We focused on the three largest BC sources over the Asian continent: AN emissions from China (China AN), BB emissions from Southeast Asia and SC (SEA BB), and BB emissions from Siberia and Kazakhstan (Siberia BB).

Figure 50 shows the temporal variations of $M_{\rm BC}$ at the Fukue, Hedo, and Happo stations for both measurements and model simulations. Simulated $M_{\rm BC}$ were chosen from a horizontal and vertical grid closest to each site. Model simulations reproduced both absolute concentrations and seasonal variations of the observed $M_{\rm BC}$ for other periods very well: normalized mean biases (NMB) and Pearson's correlation coefficients (R) for monthly mean concentrations were 0.7% and 0.91 at Fukue, -22% and 0.83 at Hedo, and -4% and 0.65 at Happo, respectively, during the simulation periods. The variability of $M_{\rm BC}$ (vertical bars in Fig. 50) was also reproduced well by the model simulations.

PASCAL can provide information on the source regions and types and TE of $M_{\rm BC}$ (Matsui *et al*., 2013b). The BC simulated at these three sites is transported mostly from AN sources on a three-year average (90–95%), while the simulated BB contribution becomes larger in spring (10–20%). For AN sources, the contribution from China is dominant in spring, fall, and winter (60–80% of the total BC), but the AN contribution from Japan becomes larger in summer (25–35% of the total BC). This is consistent with the wind fields controlled by the East Asian monsoon, as shown above. The contribution from Korea is slightly higher at Fukue (14% of the total BC on a three-year average) than at other sites, due to the close proximity of Fukue to Korea. For BB sources, the contribution from China is the largest in early spring (10% of the total BC) and Siberia BB contributes 20–30% (of the total BC) during the late spring in 2008 and 2009.

TE values have clear seasonal variations: 50–75% in spring, fall, and winter and 25–40% in summer at all three sites during the simulation periods. The lower TE values in summer are most likely due to moist air masses influenced by larger amounts of precipitation (resulting in efficient wet removal), during their transport from the south. In contrast, relatively dry air masses influenced by smaller amounts of precipitation are transported from the continent during other seasons. TE values are the highest at Fukue (64%) and lower at Hedo and Happo (45–50%). Since Hedo is the southernmost site influenced by moist air, and Happo is a mountain site, the air masses transported to both of these sites have higher likelihoods of being influenced by wet removal processes during transport. A detailed comparison of the observed and model-calculated TE is desirable.

14.2 Transport of biomass burning plumes

Figure 51 (upper panel) shows a time series plot of $M_{\rm BC}$ at Happo in May 2008. Model simulations (red line) reproduced observed $M_{\rm BC}$ and their temporal variations well. There are two high $M_{\rm BC}$ events with high TE values (> 80%) (Fig. 51 (lower panel)) during this month: the first is on May 6–10 when high BC was mostly transported from China AN sources and the other is on May 21–24 when BC was transported from Siberia BB sources (mixed with BC from China AN sources). We note that the latter event cannot be reproduced successfully without including the contribution from Siberia BB emissions in the model simulations.

Similar high-BC events influenced by BB sources in Siberia were simulated 3 times in April–May 2008 and 4 times in April–May 2009 at Happo (figures 10a and 10c of Matsui *et al*., 2013b). In some events, the model severely underestimated the observed $M_{\rm BC}$ when Siberia BB emissions were not considered, suggesting their importance during the high-BC events. Siberia BB contributions were also high at the Fukue and Hedo sites during most of the high-BC events influenced by BB sources (figures 10b and 10d of Matsui *et al*., 2013b). Therefore, the transport of high $M_{\rm BC}$ air from

doi:10.5047/meep.2015.00301.0001

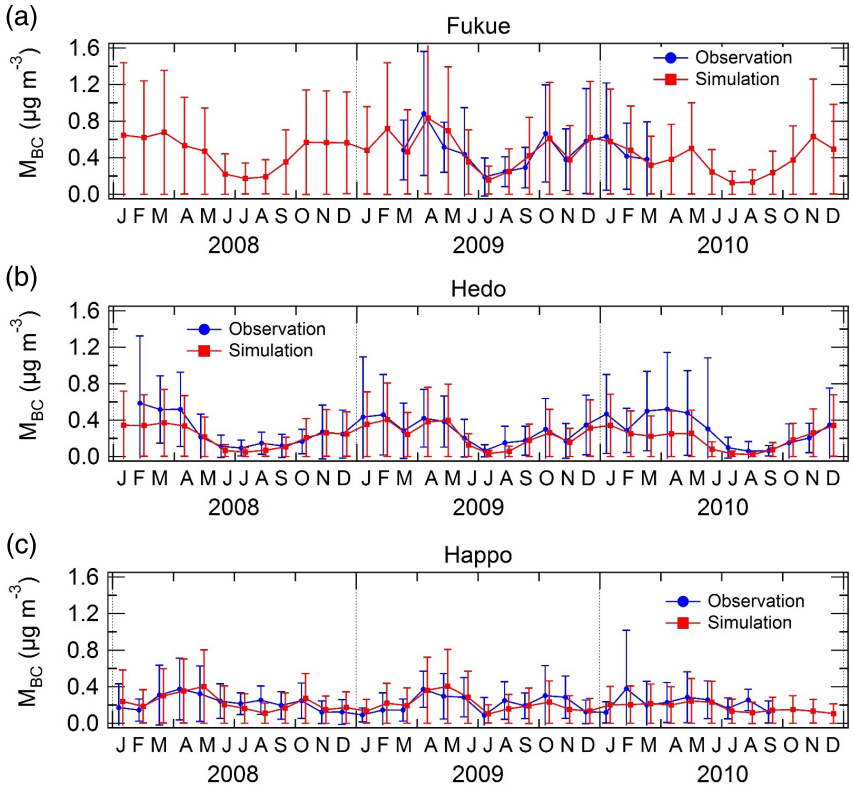

Fig. 50. Monthly mean BC mass concentrations at (a) Fukue, (b) Hedo, and (c) Happo sites for both measurements (blue) and model simulations (red) (from Matsui *et al*., 2013b). The vertical bars show the standard deviations of the BC mass concentrations.

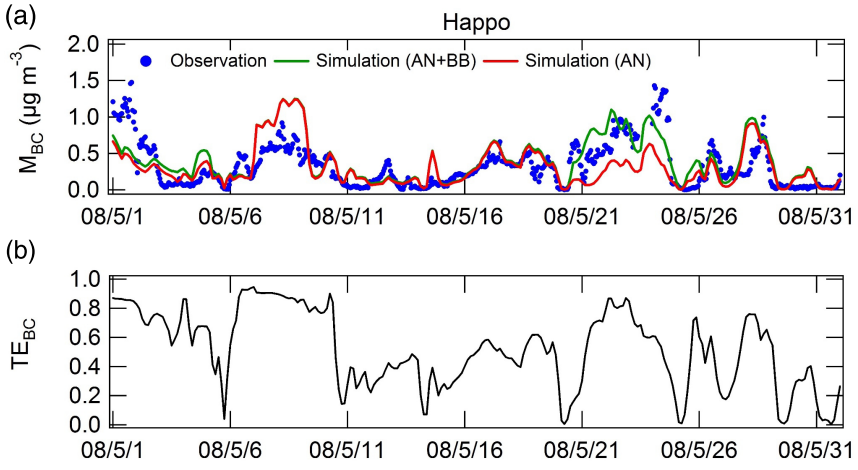

Fig. 51. Time series plots of (a) observed (blue) and simulated (red and green) BC mass concentrations (M_{BC}), and (b) the transport efficiency of BC (TE) at Happo in May 2008 (from Matsui *et al*., 2013b).

BB sources in Siberia (> 50°N) to the western Pacific was found to be a common phenomenon within the midlatitudes (25–50°N).

15. Vertical Transport Mechanisms of BC

In Chapter 8, the vertical transport of BC was discussed to some extent in connection with the wet deposition of BC. Here, a more detailed analysis of the vertical transport BC in East Asia is described based on Oshima *et al*. (2013).

15.1 Previous studies

The vertical transport processes of BC from the PBL to FT is critically important because these processes directly control the global- and regional-scale spatial distributions of BC and the amount of BC transported from source regions to receptor regions. Several recent studies have discussed the vertical transport of BC using high-altitude observations in the FT and the upper troposphere/lower stratosphere (UTLS) and model calculations in terms of the long-range transport of BC from source regions (e.g., Asia) to receptor regions

doi:10.5047/meep.2015.00301.0001

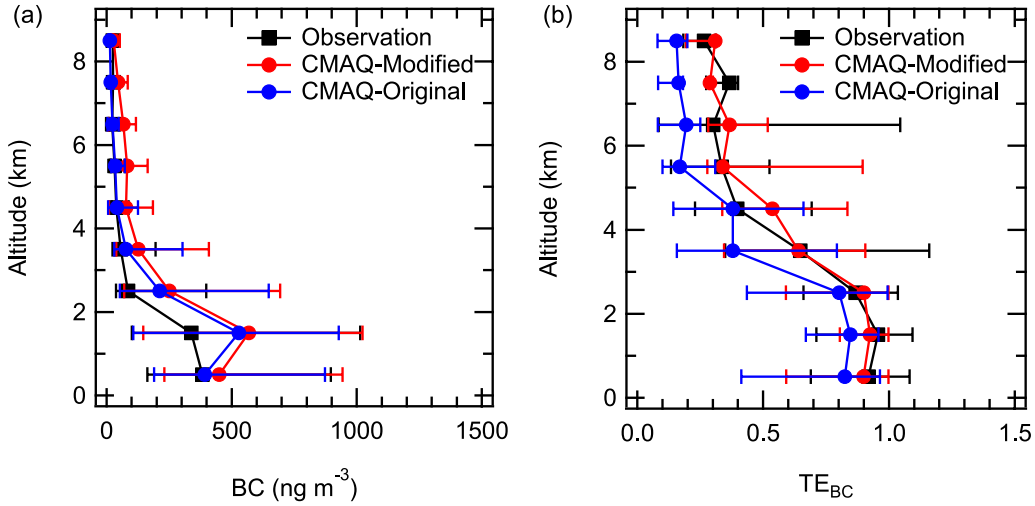

Fig. 52. Comparisons of the median values of (a) the mass concentration of BC (ng m^{-3}), and (b) the transport efficiency of BC (TE) observed by aircraft (black squares) with those in the CMAQ-Modified (red circles) and CMAQ-Original (blue circles) simulations for every 1-km-altitude interval for air parcels sampled in a latitude range of 26–38°N during the entire A-FORCE period. The horizontal lines denote the central 67% ranges.

(e.g., the Arctic and North America) (e.g., Koch and Hansen, 2005; Park *et al*., 2005; Stohl, 2006; Hadley *et al*., 2007, 2010; Koch *et al*., 2007, 2009; Schwarz *et al*., 2010; Spackman *et al*., 2010, 2011; Bourgeois and Bey, 2011; Brock *et al*., 2011; Liu *et al*., 2011; Matsui *et al*., 2011a). During the NASA Arctic Research of the Composition of the Troposphere from Aircraft and Satellites (ARCTAS) mission in the spring and summer of 2008 (Jacob *et al*., 2010), BC particles in air parcels that originated from anthropogenic sources in East Asia experienced a strong uplift associated with warm conveyor belts (WCBs) and were transported to the Arctic troposphere, although most BC particles were removed from the atmosphere by precipitation during transport (Matsui *et al*., 2011a). Spackman *et al*. (2011) used the BC observations from the Tropical Composition, Cloud, and Climate Coupling (TC4) experiment in August 2007 (Toon *et al*., 2010) to show that BC particles in air parcels that originated from anthropogenic sources in Asia were most likely transported to the tropical tropopause layer over Central America through cumulus convection associated with the Asian monsoon.

However, these studies focused on the receptor regions and might have limitations regarding the quantitative understanding of the vertical transport mechanisms of BC because uplifting processes (e.g., cyclones (WCBs) and cumulus convection) near the source regions are considered to largely control the amount of BC transported to the FT on regional to hemispheric scales. To improve our understanding of the vertical transport of BC, further studies covering large source regions (e.g., East Asia) are needed.

15.2 Vertical profiles of BC and TE

We studied the vertical transport mechanisms of BC particles and their transport pathways over East Asia in spring using the results from regional-scale 3-D chemical transport model calculations. For this purpose, a modified version of the WRF-CMAQ model was used to examine the vertical transport mechanisms of BC particles and their 3-D transport pathways during springtime in East Asia (20 March to 30 April 2009) through the simulations for the A-FORCE aircraft campaign.

Figure 52 shows the vertical profiles of the median values of the M_{BC} and TE for the aircraft observations and the CMAQ-Modified simulations at latitude ranges of 26–38°N during the entire A-FORCE period. The CMAQ-Modified simulation generally reproduced well the characteristics of the vertical profiles of the median M_{BC} despite the systematic overestimation in the FT (by a factor of 2.2 on average above 2 km). The good agreement in the TE values gives confidence in the validity of the treatment of the wet removal processes of BC in the CMAQ-Modified simulation. The correspondence between the TE values and the overestimates of the absolute value of the M_{BC} suggest that the anthropogenic BC emissions over East Asia may be overestimated to some extent and/or that the amount of BC transported from the PBL to the FT may be overestimated in the WRF-CMAQ model simulation. This is likely due to larger values of the vertical eddy diffusion coefficient in the offline WRF-CMAQ model than those in the online model, such as WRF-chem (e.g., Matsui *et al*., 2009).

15.3 Vertical transport

Figure 53(a) shows the spatial distribution of the upward BC mass fluxes at 700 hPa in the CMAQ-Modified simulation averaged over the A-FORCE period. Corresponding to the horizontal BC flux convergence regions within the PBL (figure 7a of Oshima *et al*. (2013)), two types of pronounced mean upward BC fluxes from the PBL to the FT were found over NC (35–45°N, 110–130°E) and inland-southern China (ISC) (25–35°N, 100–120°E). ISC defined here corresponds to the inland part of southern China, which is narrower than the region we referred to as SC in previous chapters.

To identify the mechanisms for the pronounced upward BC transport over NC and ISC, the BC mass concentration ([BC]) and the vertical velocity (w) are locally separated into their time means (with overbars) and instantaneous devia-

doi:10.5047/meep.2015.00301.0001

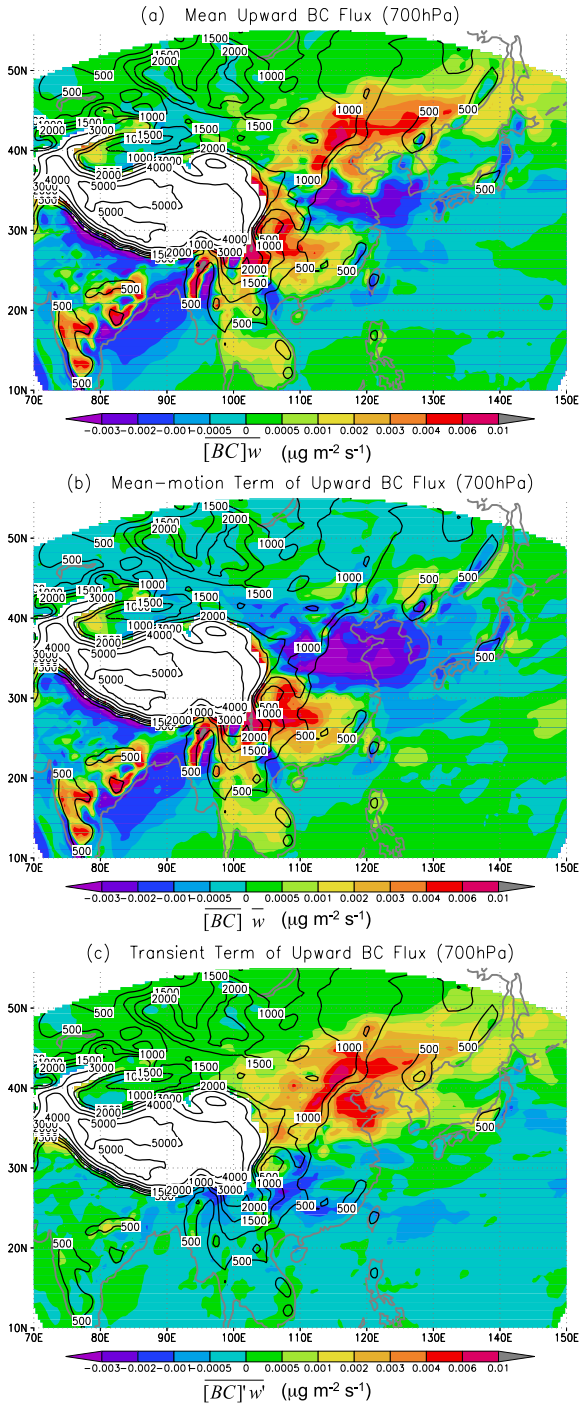

Fig. 53. (a) Time-averaged upward mass flux of BC ($\overline{[\mathrm{BC}]w}$) at the 700 hPa level during the A-FORCE period (March 20 to April 30, 2009) in the CMAQ-Modified simulation (μg m^{-2} s^{-1}), where the overbar denotes time averaging over the period. Positive fluxes are upward. The solid black lines denote the terrain elevations (m) used in the model simulation. Time averages of (b) the mean-motion term ($\overline{[\mathrm{BC}]}\,\overline{w}$), and (c) the transient term ($\overline{[\mathrm{BC}]'w'}$) ($\mu$g m^{-2} s^{-1}), where a prime denotes the instantaneous deviations from the respective mean at each grid point. These figures are from Oshima *et al*. (2013).

tions from the means (with primes) as follows:

$$[\mathrm{BC}] = \overline{[\mathrm{BC}]} + [\mathrm{BC}]', \tag{34}$$

$$w = \overline{w} + w'. \tag{35}$$

The time mean of the vertical BC mass flux can be locally expressed as follows:

$$\overline{[\mathrm{BC}]w} = \overline{[\mathrm{BC}]}\,\overline{w} + \overline{[\mathrm{BC}]'w'}. \tag{36}$$

The spatial distributions of the "mean-motion term" (the first term on the right-hand side of Eq. (36)) and the "transient term" (the second term of Eq. (36)) for the A-FORCE period are shown in Figs. 53(b) and 53(c), respectively, together with the spatial distribution of the total upward BC mass flux (the left-hand side of Eq. (36)) in Fig. 53(a). Each term on the right-hand side of Eq. (36) includes transport by sub-grid and grid scale vertical motions. Over NC, the transient term of the upward BC flux ($\overline{[\mathrm{BC}]'w'}$) (Fig. 53(c)) was dominant, which is consistent with large fluctuations in vertical motion associated with strong transient eddy activity (figure 5b and figure 6a of Oshima *et al*. (2013)). This collocation suggests the particular importance of migratory cyclones for the upward BC transport from the PBL to the FT. In contrast, the large values of the mean-motion term ($\overline{[\mathrm{BC}]}\,\overline{w}$) over ISC (Fig. 53(b)) are primarily attributed to the pronounced mean ascent. The mean ascent over this region was mainly caused by orographic uplifting along the slopes of the Tibetan Plateau and by active cumulus convection, with a modest additional contribution from migratory cyclones. The importance of orographic uplifting of pollutants (e.g., CO) to the FT along mountain slopes in East Asia has also been described in previous studies (e.g., Liu *et al*., 2003; Chen *et al*., 2009; Ding *et al*., 2009; Lin *et al*., 2010). We thus conclude that migratory cyclones played a major role in the BC uplifting from the PBL to the FT over NC, whereas orographic uplifting and cumulus convection were responsible for the upward BC transport over ISC.

Figures 54(a) and 54(b) show the average spatial distributions of the amounts of wet and dry depositions of BC, respectively. The contribution of the wet deposition of BC to the total deposition was estimated to be 90% in East Asia. The spatial distribution of the BC dry deposition amounts (Fig. 54(b)) was generally similar to BC emissions because the dry deposition flux of BC from the atmosphere to the surface is approximately proportional to the local BC concentration near the surface. In contrast, the spatial distribution of BC wet deposition (Fig. 54(a)) consisted generally of the combined effect of the upward BC flux (Fig. 53(a)) and the precipitation distribution (figure 5c of Oshima *et al*. (2013)) because the wet removal occurs in association with precipitation during the vertical transport of air parcels containing BC. The amount of BC wet deposition was largest over ISC, including the eastern slopes of the Tibetan Plateau, where both the upward BC flux and precipitation were pronounced. Figure 54(a) also shows fairly large amounts of BC wet deposition over NC, where the strong upward BC flux

doi:10.5047/meep.2015.00301.0001

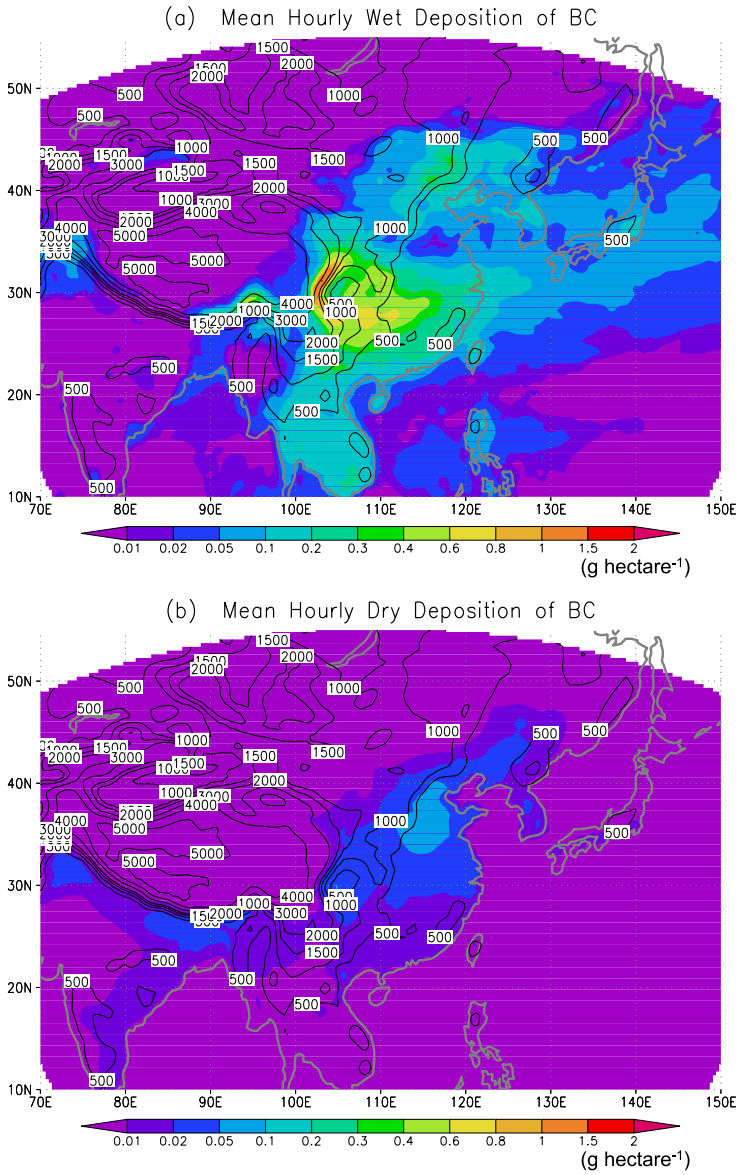

Fig. 54. Time-averaged hourly (a) wet deposition and (b) dry deposition amounts of BC during the A-FORCE period in the CMAQ-Modified simulation (g hectare^{-1}) (from Oshima *et al*., 2013). The solid black lines denote the terrain elevations (m) used in the model simulation.

was collocated with modest precipitation associated with cyclones. The region of modest amounts of BC wet deposition extended farther toward the east along the Pacific storm track.

To examine the intensity of the wet removal of BC from air parcels during their vertical transport over the two uplifting regions (i.e., NC and ISC), the TE values were evaluated for the mean BC mass concentrations. The mean TE values were 0.57 and 0.80 over ISC and NC, respectively, at 700 hPa. This indicates that the intensity of the wet removal of BC over ISC was approximately twice (i.e., a 43% decrease by wet removal) that over NC (a 20% decrease), which is nearly consistent with the geographical dependence of the amount of BC wet deposition (Fig. 54(a)).

15.4 Export of BC

The vertical distributions of the M_{BC} and TE values averaged longitudinally between 120°E and 140°E are shown in Figs. 55(a) and 55(b), respectively. Although the M_{BC} were greatest below the 700 hPa level over the midlatitude region, the high M_{BC} regions spread to the mid-troposphere (∼500 hPa level) extended to lower latitudes. In contrast, TE exhibits a more distinct dependency on latitude and altitude. Specifically, TE decreased with decreasing latitude and increasing altitude (Fig. 55(b)), reflecting the latitudinal distributions of moisture and precipitation.

Figure 56 shows the calculated meridional cross-section of the mean eastward mass flux of BC at 140°E. The eastward BC flux was largest in the PBL and the lower FT (600–900 hPa) at 35–45°N and the flux was also large in the middle FT (400–700 hPa) at 25–35°N. The cross section reflects the three major transport pathways for the export of BC. These pathways are schematically shown in Fig. 57. One pathway is the PBL outflow in the midlatitude region through which the BC, originating primarily from NC, was advected by the

doi:10.5047/meep.2015.00301.0001

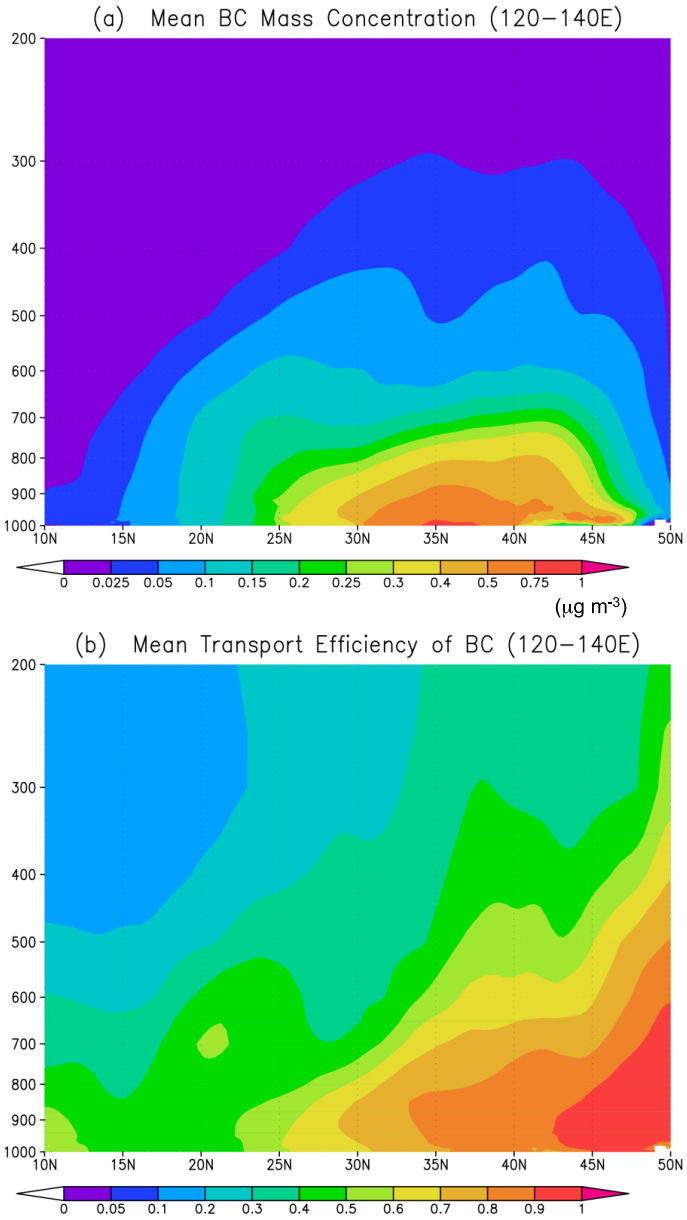

Fig. 55. Latitude-pressure cross sections of (a) the mean mass concentration of BC (μg m^{-3}) averaged longitudinally between 120°E and 140°E during the A-FORCE period in the CMAQ-Modified simulation, and (b) the corresponding transport efficiency of BC (TE) (from Oshima *et al*., 2013).

low-level westerlies without uplifting out of the PBL. The greater TE values for the PBL outflow (Fig. 55(b)) indicate that wet removal of BC was less efficient along this pathway.

The second pathway is through uplifting from the PBL to the FT by migratory cyclones over NC and the subsequent eastward transport in the lower FT over the midlatitude region. The BC originated mostly from NC (i.e., contributions of 58% and 20% from NC and SC, respectively), which is consistent with the strong divergence of the horizontal BC fluxes within the PBL over northern/central China (figure 7(a) of Oshima *et al*. (2013)). Along the second pathway, approximately half of the BC mass was removed from the atmosphere by precipitation prior to its arrival at 140°E.

The third pathway is orographic uplifting and/or convective upward transport from the PBL to the FT over ISC followed by westerly transport in the mid-FT over the subtropical region (25–35°N). The primary origins of the exported BC were SC and India (i.e., 43%, 30%, and 16% contributions from South Asia, SC, and NC, respectively). Despite the efficient wet removal of BC due to the large amount of precipitation, the eastward BC flux in the FT over the subtropical region was comparable in magnitude to that over the midlatitude region.

16. Transport of BC to the Arctic

All the field measurements shown in the previous chapters were made in Asia. In this and the next chapter, results of aircraft measurements of BC in the Arctic are used to discuss emissions and long-range transport BC to the Arctic based on the studies of Matsui *et al*. (2011a) and Kondo *et al*. (2011a).

doi:10.5047/meep.2015.00301.0001

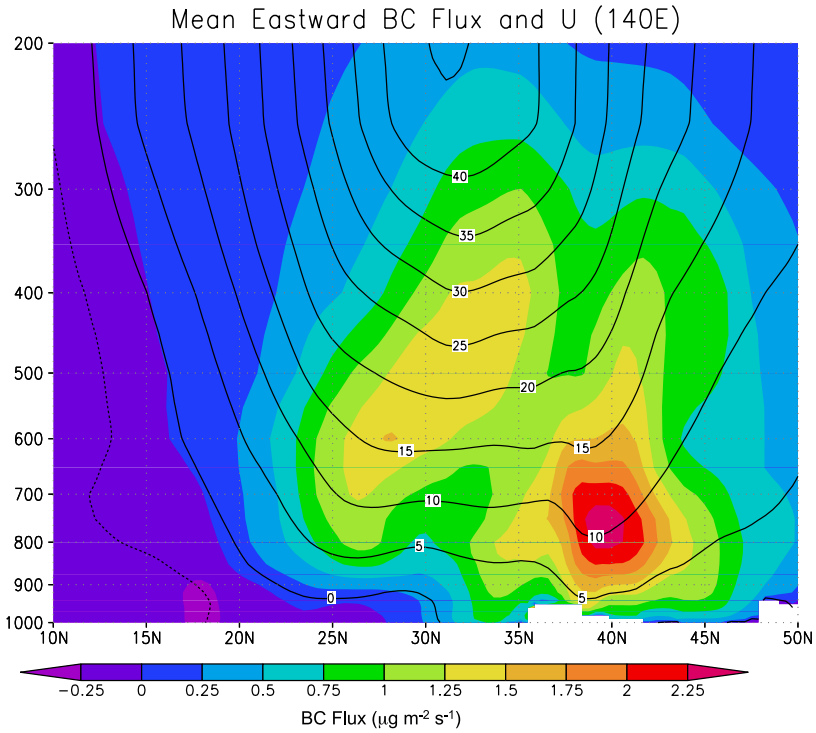

Fig. 56. Latitude-pressure cross section of the mean eastward mass flux of BC (μg m^{-2} s^{-1}, colored as indicated near the bottom) and the mean westerly velocity (m s^{-1}, black contours) at 140°E during the AFORCE period (March 20 to April 30, 2009) in the CMAQ-Modified and WRF simulations, respectively (from Oshima *et al.*, 2013).

16.1 Climate effects of aerosols in the Arctic

In the Arctic, high concentrations of aerosols and reactive gases, the so-called Arctic haze, occur in winter and spring because of the efficient transport of pollution from the midlatitudes and the slow removal processes in these seasons (Barrie, 1986; Shaw, 1995). Once these aerosols including BC deposit onto snow/ice surfaces, they lower the surface reflectance and promote faster melting of snow/ice sheets in the Arctic, which is tightly coupled to climate effects through the snow-albedo feedback (Clarke and Noone, 1985; Hansen and Nazarenko, 2004; Flanner *et al.*, 2007, 2009). In addition, high number concentrations of aerosol in the Arctic haze lead to the enhancement of cloud longwave emissivity (Lubin and Vogelmann, 2006; Garret and Zhao, 2006), contributing to surface warming and accelerating the melting of snow/ice. Shindell and Faluvegi (2009) estimated that decreasing concentrations of sulfate aerosols and increasing concentrations of BC in the Arctic have substantially contributed to rapid Arctic warming during the past three decades (1.1±0.8°C).

BC measurements have been conducted at various surface stations in the Arctic (e.g., Alert in Canada, Barrow in Alaska, and Janiskoski in Russia), and seasonal variations and long-term trends of aerosols including BC have been examined (e.g., Polissar *et al.*, 1999; Sirois and Barrie, 1999; Quinn *et al.*, 2002, 2007, 2008; Sharma *et al.*, 2002, 2004, 2006; Eleftheriadis *et al.*, 2009; Gong *et al.*, 2010; Huang *et al.*, 2010). However, because data from these studies are limited to the surface, the understanding of the sources, transport pathways and removal processes, and the distributions of BC in the entire troposphere is very limited. The NASA ARCTAS aircraft campaign was conducted in 2008 in the Arctic (Jacob *et al.*, 2010). As compared with previous aircraft campaigns in the Arctic (Shipham *et al.*, 1992; Baumgardner *et al.*, 2004; Yamanouchi *et al.*, 2005), much more accurate, extensive, and high-time resolution measurements of BC were collected during ARCTAS at various altitudes from the PBL to the upper troposphere (UT) in the Arctic in spring and summer. Here, we present our studies on BC in the Arctic based on Matsui *et al.* (2011b) and Kondo *et al.* (2011a). The former analyzed the transport of BC from source regions to the Arctic and the latter focused on the characterizations of emissions of BC from biomass burning.

16.2 ARCTAS observations

The measurements of BC and other related species were made on board the NASA DC-8 aircraft during the ARCTAS aircraft campaign conducted in April and June–July 2008. Figure 58 shows all the flight tracks of the DC-8 aircraft during the ARCTAS campaign. Flights were conducted mainly over Alaska in April (ARCTAS-A) and over western Canada in June–July (ARCTAS-B). Air masses impacted by forest fires that occurred in California were also sampled by the DC-8 ARCTAS instrument payload in June, 2008 for the California Air Resources Board (CARB) (Singh *et al.*, 2010). We used relevant data obtained during ARCTAS-CARB for comparison with the ARCTAS-B data.

The number and mass size distributions of BC were measured by an SP2. In addition to BC, we used the size distribution of light-scattering particles (LSP) measured by the SP2. LSP scatters laser light but does not incandesce. The

doi:10.5047/meep.2015.00301.0001

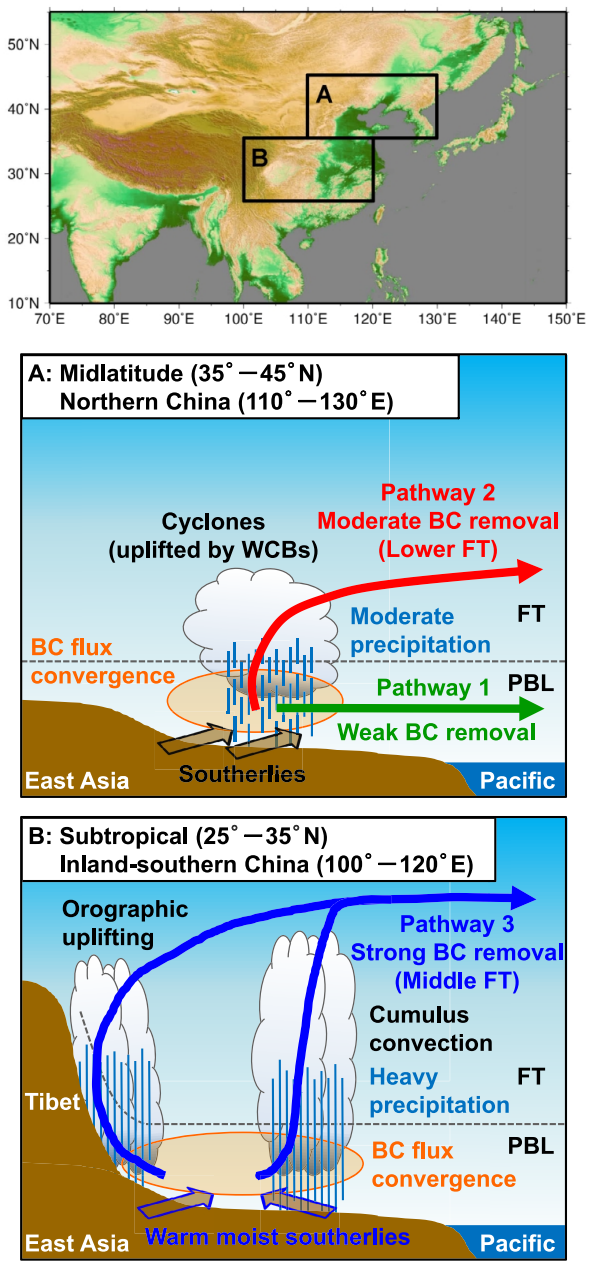

Fig. 57. Schematic of the three major transport pathways for BC export from continental East Asia to the Pacific in spring and its vertical transport mechanisms along each pathway (from Oshima *et al.*, 2013).

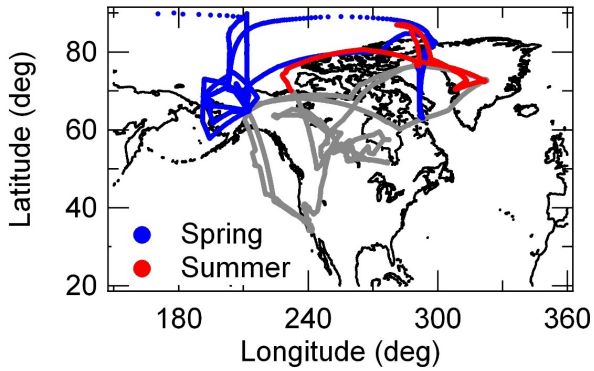

Fig. 58. All flight tracks during the ARCTAS aircraft campaign (gray, blue, and red lines). Blue (spring) and red (summer) lines show the flights in and near the Arctic mainly used in this study, and we refer to these data as "Arctic data" (from Matsui *et al.*, 2011b).

light-scattering signal was detected by two avalanche photodiodes. The peak scattering signal was converted to the scattering cross section of the particles. Calibration was made first by using polystyrene latex (PSL) particles with a refractive index of $1.59 + 0i$. Mie theory was then used to convert the calibration curve of PSL to that of $(NH_4)_2SO_4$ with a refractive index of $1.52 + 0i$. The diameters of LSP (D_p) were estimated from this curve with an uncertainty of about 10% in the size range of about 200–750 nm (Moteki and Kondo, 2008). The uncertainty in D_p due to possible changes in the refractive indices of LSP is estimated to be about 10%. The total mass concentrations of BC (M_{BC}) and the volume concentrations of LSP (V_{SC}) were derived by integrating the size distributions with respect to diameter. The values M_{BC} and V_{SC} are given in the units of mass and volume per unit volume of air at STP, respectively.

CO, CO_2, acetonitrile (CH_3CN) and dichloromethane (CH_2Cl_2) were also measured simultaneously (Sachse *et al.*, 1987; Wisthaler *et al.*, 2002; Blake *et al.*, 2003; Vay *et al.*, 2003). CH_3CN and CH_2Cl_2 have often been used as tracers of biomass burning (BB) and the combustion of anthropogenic fossil fuel (AN), respectively (e.g., Warneke *et al.*, 2006; Chen *et al.*, 2007).

The background concentrations of these species were defined as the lowest 5th percentiles of all ARCTAS data for every 10 K potential temperature range for each species and season, and they were linearly interpolated vertically (Koike *et al.*, 2003). Zero background concentration was assumed for the BC. We denote the short-term variability by the differences between the measured and background concentrations of these species as ΔCO, ΔCH_3CN, and ΔCH_2Cl_2.

16.3 Transport of BC from the Asian continent to the Arctic

16.3.1 Source regions Previous studies using trajectory (Stohl, 2006; Law and Stohl, 2007) and regional chemical transport models (Klonecki *et al.*, 2003) estimated that northern Eurasia (Europe and Siberia) is the major source of Arctic haze in the lower troposphere (LT). Aerosols and trace gases emitted from North America and Asia are uplifted during transport to the Arctic because of the large latitudinal gradient in the potential temperature. This distributes insoluble trace gases from North America and Asia at high altitudes in the Arctic. However, understanding the transport of water-soluble aerosols from midlatitudes to the Arctic has been poor and controversial.

For the present analysis, ten-day backward trajectories (Fuelberg *et al.*, 2010) were used to identify the source regions of pollutants in measured air parcels. The source regions were defined as the PBL from the surface to 700 hPa (about 3 km above ground level) over the four horizontal regions shown in Fig. 59: Europe, Russia, Asia (excluding Russia), and North America. The origins of the measured

doi:10.5047/meep.2015.00301.0001

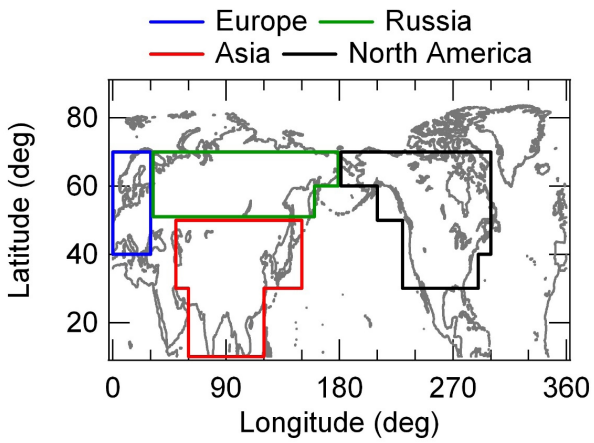

Fig. 59. Source regions (Europe, Russia, Asia, and North America) defined in this study (from Matsui *et al*., 2011b).

air parcels were classified into 7 categories: Europe, Russia, Asia, and North America, Russia + Asia (R + A), Russia + Europe (R + E), and other, based on the trajectory calculations. For trajectories passing over only a single source region within 10 days, the corresponding air parcels were classified as Europe, Russia, Asia, or North America. For trajectories passing two regions, e.g., Russia and Europe or Asia, air parcels were categorized as Russia + Europe or Russia + Asia. The types of combustion for polluted air parcels were classified into AN and BB according to the concentrations of CH_2Cl_2 and CH_3CN. We calculated the APT using the Global Precipitation Climatology Project (GPCP) global precipitation data (Huffman *et al*., 2001; Adler *et al*., 2003). The uncertainties in the estimates of the source regions and the APT are discussed in Matsui *et al*. (2011a).

16.3.2 Transport of BC in spring In the springtime, the median BC concentration in Asian AN air was 18 ng m^{-3}, which was much lower than the median concentration of 266 ng m^{-3} in Russian BB air. The higher BC in the Russian BB can be partly due to high BC emissions during this period. However, the efficiency of BC transport can have a great effect, as shown by the analysis detailed below.

Figure 60 shows the GPCP mean precipitation distribution and the trajectories of different types of air parcels, and the precipitation intensity. Most AN air parcels from Asia experienced a rapid ascent on WCBs associated with heavy precipitation near the source regions. Most Russian BB air parcels experienced a slower ascent and much less precipitation than the Asian AN air parcels.

Figure 61(a) shows BC/ΔCO-APT correlations for all Arctic data and those for individual source regions and fuel types. On average, the BC/ΔCO ratio decreased with increasing APT, indicating that BC removal by precipitation is one of the most important processes in controlling BC concentrations in the Arctic. The BC/ΔCO ratio was low and the APT was high for Asian AN air parcels. By contrast, the BC/ΔCO ratio was much higher for Russian BB air parcels with a low APT. The BC/ΔCO ratios of AN-impacted air (Asia, Europe and North America) with a higher APT were on average lower than those for BB-impacted air (Russia, Russia + Europe and Russia + Asia), on average.

The left panel of Fig. 61(a) also shows the median BC/ΔCO ratios for an APT < 5 mm for AN (Europe, Asia, Russia + Asia, and North America) and BB (Russia, Russia + Europe, and Russia + Asia) air parcels. They are considered representative of the BC/ΔCO ratios in the source regions (minimum impact of wet removal processes) and denoted $[BC/\Delta CO]_{source}$. A $[BC/\Delta CO]_{source}$ ratio of 3.3 for AN air parcels was derived mainly from North American air parcels, because there are few Asian and European air data with an APT < 5mm. The $[BC/\Delta CO]_{source}$ ratio of 7.6 for BB air was derived mostly from the Russian (Russia, Russia + Europe, and Russia + Asia) air data. The difference in the $[BC/\Delta CO]_{source}$ ratios between the AN and BB impacted air by a factor of 2.5 is consistent with previous studies (Warneke *et al*., 2009; Kondo *et al*., 2011a). For fossil fuel combustion, the BC/CO emission ratio was estimated to be 3.2±1.0 in California (Kondo *et al*., 2011a). For BB, the BC/CO emission ratio was estimated to be 8.7±3.7 for Russia (Kondo *et al*., 2011a) and 10±5 for Kazakhstan and 7±4 for Lake Baikal (Warneke *et al*., 2009).

We calculated TE using Eq. (37):

$$\mathrm{TE} = \frac{[\mathrm{BC}/\Delta\mathrm{CO}]}{[\mathrm{BC}/\Delta\mathrm{CO}]_{\mathrm{source}}}, \tag{37}$$

where [BC/ΔCO] is the observed BC/ΔCO ratio. Figure 61(b) shows the correlation of TE with APT. The median TE for Asian AN was as low as 13%, and TE for the Russian BB air was as high as 83%.

The altitude distributions of BC and ΔCO were substantially different between Asian AN and Russian BB air as shown in figure 10 of Matsui *et al*. (2011b). The Asian AN air parcels were typically measured in the UT and the Russian BB air parcels in the middle troposphere (MT). The median BC concentrations reached a maximum in the MT, while ΔCO remained high in the UT, uninfluenced by wet deposition.

Detailed analysis has shown that the contribution of BB air from Russia to BC in the North American Arctic (F_{BC}) was dominant (59%), and that of Asian AN air was only about 2% (Matsui *et al*., 2011b). The contributions of these sources to ΔCO were more comparable, i.e., 16% versus 43%, which were controlled by emissions and transport uninfluenced by wet deposition. No air parcels from south Asian sources (latitude < 30°N) reached the Arctic, leading to little contribution to BC in the North American Arctic during the ARCTAS-A campaign.

16.3.3 Seasonal variations of BC In summer, the median BC mass concentrations for all air parcels was 5.7 ng m^{-3}, which is 10 times lower than that in spring (55 ng m^{-3}), while the median ΔCO mixing ratio was somewhat higher than that in spring (23 ppbv versus 14 ppbv). The TE values for both Russian BB and Asian AN air were much lower in summer (4.0 and 0.76%, respectively) than those in spring (87 and 13%, respectively). Correspondingly, the median APT in summer was much higher (17 mm) than that in spring (3.2 mm) for all Arctic air parcels. This is mainly due to the

doi:10.5047/meep.2015.00301.0001

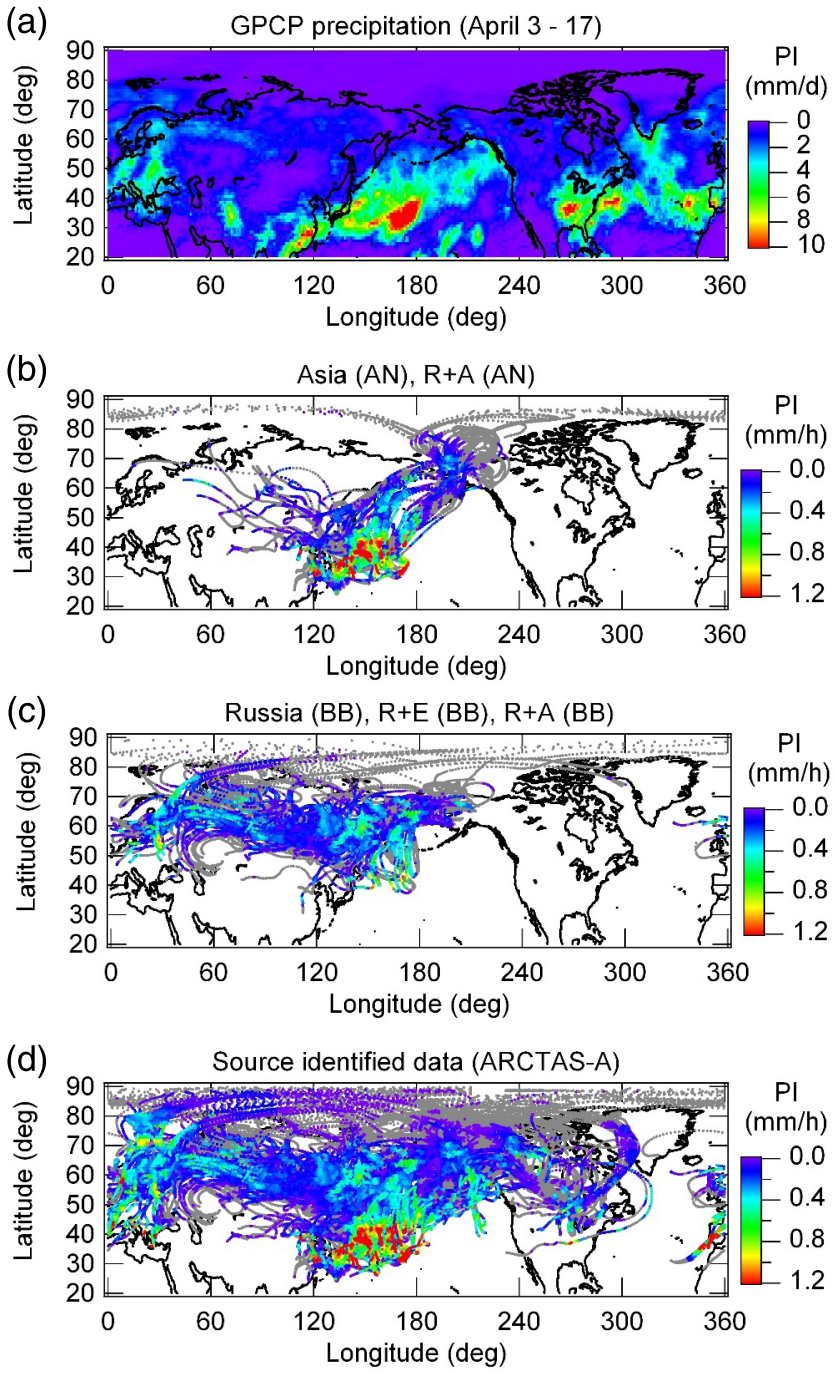

Fig. 60. (a) Average precipitation distribution before (April 3–7) and during the ARCTAS-A campaign (April 8–17). A period before the campaign was included considering the transport time from the sources to the locations of the measurement. Ten-day backward trajectories are shown for (b) anthropogenic air parcels from Asia (Asia and R + A (Russia + Asia)), (c) biomass burning air parcels from Russia (Russia, R + E (Russia + Europe), and R + A), and (d) all source-identified air parcels during the ARCTAS-A campaign. PI denotes precipitation intensity. The periods when PI < 0.01 mm/h are shown with gray dots. These figures are from Matsui *et al*. (2011b).

higher precipitation over the latitudes of 45–70°N in summer. The TE-APT correlation and the seasonal variations in the APT, as shown in figure 13 of Matsui *et al*. (2011b), indicate that the large seasonal variations in BC were caused mainly by those in the wet removal rates. The contribution of Russian BB in spring to North American Arctic BC concentrations was largest, because of the spring maximum in TE at higher latitudes with low relative humidity.

BB in Russia may increase in the future due to global warming (e.g., Stocks *et al*., 1998). The possible earlier onset of Russian BB could accelerate warming in the Arctic through the snow-albedo feedback and longwave indirect effect. The high efficiency of BC transport emitted from Russian BB indicates that this source has a large and realistic potential for this feedback to be effective, leading to an acceleration of the warming of the Arctic in the future.

doi:10.5047/meep.2015.00301.0001

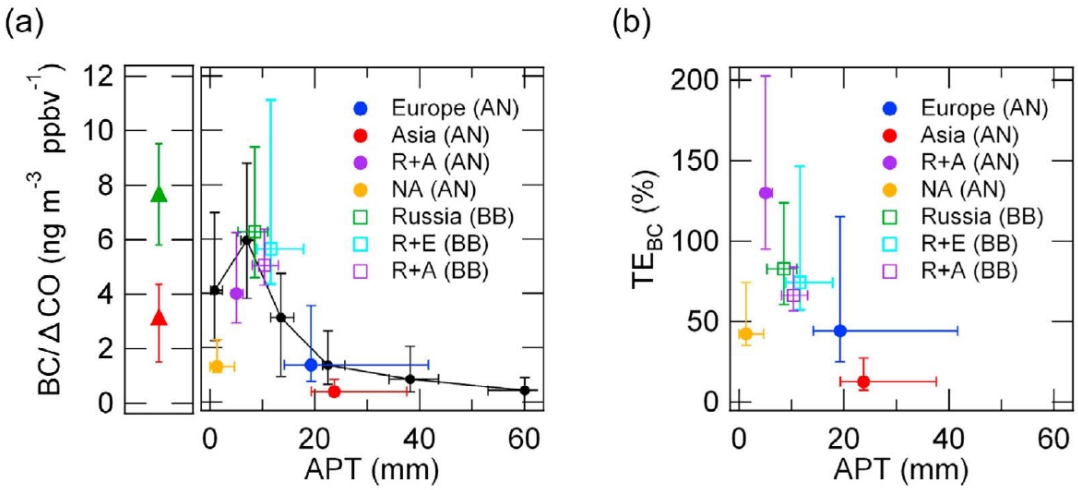

Fig. 61. Scatterplots of (a) BC/ΔCO ratio, and (b) transport efficiency of BC (TE), as a function of accumulated precipitation along trajectories (APT) during the ARCTAS-A campaign (from Matsui *et al*., 2011b). The medians (circles or squares with color) and the 25th to 75th percentiles (horizontal and vertical bars) are shown for different source regions and fuel types. The black line in the left panel shows the relationship between the BC/ΔCO ratio and APT for all the Arctic data in spring (Flights 6–10). The red and green triangles (left panel) and their bars show the medians and 25th to 75th percentiles of the BC/CO emission ratios for fossil fuel combustion (AN) and biomass burning (BB), respectively. These values were estimated using all source-identified air parcels with APT < 5 mm.

17. Biomass Burning as Sources of BC in the Arctic

17.1 Measurements of BB plumes

Boreal forest fires are one of the most important sources of aerosols transported to the Arctic (e.g., Stohl *et al*., 2006, 2007; Treffeisen *et al*., 2007; Eck *et al*., 2009). Large amounts of aerosols, predominantly in the form of carbonaceous aerosols, namely BC and organic aerosols (OA), are emitted from BB. Statistically, Russia and Canada have been the largest sources of BC emitted from boreal forest fires (Lavoué *et al*., 2000; Conrad *et al*., 2002; Stocks *et al*., 2002; Soja *et al*., 2004).

Reliable estimates of the effects of BC on the climate of the Arctic by global models necessitate a quantitative understanding of emissions of BC, aging and removal, and microphysical properties (e.g., Stier *et al*., 2006; Textor *et al*., 2006; Koch *et al*., 2009). As discussed in Chapter 1, calculations of the effects of light absorption by BC require photo-absorption cross sections and size distributions of BC. The cross section depends on diameter, and mixing state, together with the refractive index and shapes of BC (e.g., Moteki *et al*., 2010b; Moteki and Kondo, 2010; Shiraiwa *et al*., 2010). The size distributions of BC are controlled by emissions, aging during transport, and the deposition of BC.

Previous estimates of the emission factors of BC are considered to be highly uncertain, because they are based on measurements with large uncertainties (Reid *et al*., 2005). There is a critical need to characterize the emission ratios and microphysical properties of BC near BB sources before being transported over long distances. We also need to understand the evolution of the microphysical properties of BC after emission for an improved representation of these parameters and processes by models.

To fill in these gaps, we measured BC and LSP in the submicron range with an SP2 during ARCTAS and CARB. In Canada, aerosol measurements in large plumes were made in the vicinity of the burning areas 1–2 hours after the emissions. The air masses impacted by BB in Asia were sampled 2–3 days after the emissions. These observations have enabled detailed comparisons of the aerosol emission ratios and their microphysical properties in the two regions.

17.2 Modified combustion efficiency

The phase of BB has been shown to be represented by the modified combustion efficiency (MCE) (e.g., Ward *et al*., 1991; Delmas *et al*., 1995; Yokelson *et al*., 1999, 2008), estimated from the $\Delta CO/\Delta CO_2$ ratio:

$$MCE = \Delta CO_2/(\Delta CO_2 + \Delta CO) = 1/(1 + \Delta CO/\Delta CO_2). \quad (38)$$

MCE is useful in interpreting observed emission ratios as a function of MCE, irrespective of the relative amount of data in different combustion phases (Yokelson *et al*., 1999; Goode *et al*., 2000). The MCE value is sometimes used to distinguish air masses predominantly influenced by combustion in the flaming phase (MCE > 0.9) from emissions in the smoldering phase (MCE < 0.9) (Reid *et al*., 2005). MCE was used for the interpretation of the data impacted by BB.

17.3 Size distributions and mixing state

Figure 62 shows the average number and mass (or volume) size distributions of BC and LSP observed in layers impacted by wildfires over North America (ARCTAS-B) and those in plumes transported from Asia (Siberia and Kazakhstan) during ARCTAS-A. For the analysis of the North American and Asian data, we selected data with APT < 1 mm and APT < 10 mm, respectively, to minimize the effect of wet deposition. For North America, the count median diameters (CMDs) of the log-normal fitted BC size distributions were unvarying at 136±6 nm, with a geometric standard deviation (σ_{gc}) of 1.32, although the CMD slightly increased with the

doi:10.5047/meep.2015.00301.0001

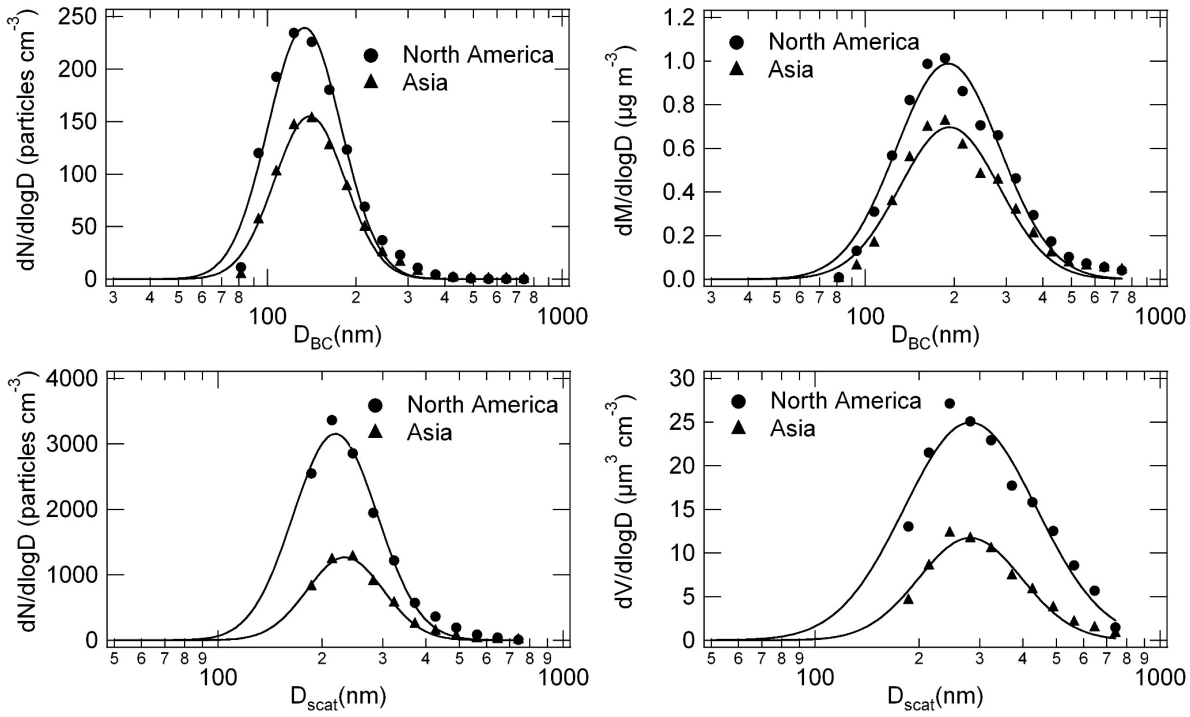

Fig. 62. Mean distributions for (top) BC in number and mass space and (bottom) LSP (light scattering particles) in number and volume space, averaged for eight major forest fire plumes encountered in Canada during ARCTAS-B and those in BB (biomass burning) fire plumes transported from Asia. Solid fitted lines are lognormal distribution functions (from Kondo *et al*., 2011a).

increase in MCE (figure 14 of Kondo *et al*. (2011a)). The size distributions of the LSP were also unvarying. The MMD of BC and volume median diameters (VMD) of LSP were 187±10 nm and 294±42 nm, respectively.

We also derived the median shell/core ratios (D_p/D_{BC}) of BC for $D_{BC} > 200$ nm. The median value of the D_p/D_{BC} was 1.48 (1.42 for the smoldering phase and 1.62 for the flaming phase. The estimated value using the above median of V_p/V_{BC} ($= {D_p}^3/{D_{BC}}^3$) is 3.24 (2.86 for the smoldering phase and 4.25 for the flaming phase), where V_p and V_{BC} are the volumes of BC-containing particles and BC cores, respectively. Thus, BC represents about 0.31 ($= 1/3.24$) of the volume (ranging from 0.23 to 0.35 for flaming and smoldering, respectively) of the particles that contain BC.

17.4 Chemical composition of aerosols

Figure 63 shows the average mass fractions of submicron non-refractory chemical components and BC in the extracted North American BB plumes as measured by the High-Resolution Time-of-Flight Aerosol Mass Spectrometer (HR-ToF-AMS) (DeCarlo *et al*., 2006; Dunlea *et al*., 2009) and an SP2. On average, OA constituted about 83% of the total mass concentration of BC and non-refractory aerosol with a D_{va} (vacuum aerodynamic diameter, see DeCarlo *et al*., 2004) smaller than about 1 μm (PM_1). We infer, therefore, that V_{SC} in the plumes approximately represents the volume concentration of OA. M_{BC} was converted to BC volume concentration (V_{BC}) assuming the density of BC to be 2 g cm^{-3}. The average volume fraction of BC was about 0.02. Together with the result above that the volume fraction of BC was 0.31 for particles containing BC, this indicates that the large majority of the scattering particles measured by the SP2 in the size range of 200 nm $< D_p <$ 750 nm did not contain BC with $D_{BC} > 80$ nm, which is consistent with the particle number observations with the SP2 (Fig. 62).

Figure 63 also shows the average mass fractions of non-refractory components of aerosol and BC in the Asian BB plumes. OA constituted the dominant fraction (about 60%) of the non-refractory components, similar to the Canadian BB plumes. However, the sulfate mass fraction was as large as about 30%, which is much larger than that for the North American plumes (3–8%). It is very likely that SO_2 emitted from biomass burning was oxidized to form sulfate during transport (Kondo *et al*., 2011a). The average V_{SC}/M_{BC} and V_{SC}/V_{BC} ratios in the Asian plumes, restricted to a low APT were about 2 times lower than those in the Canadian plumes. The conclusion that most of the light-scattering particles did not contain BC is still valid. In fact, LSP consisted of 89% and 97% of aerosol number and volume (LSP + BC), respectively during the ARCTAS-A period (Matsui *et al*., 2011c).

In all types of BB plumes, the BC mass (volume) factions of the total PM_1(LSP) were 1–5% (2–4%), while the BC volume fractions were about 30% for the particles containing BC, consistent with the fact that most particles did not contain BC. The $\Delta M_{BC}/\Delta V_{SC}$ ratios were much smaller than those for BC particles emitted from fossil fuel combustion.

17.5 Emission ratios

In general, BB plumes transported from Asia in spring experienced small amounts of APT. The observed $\Delta M_{BC}/\Delta$CO correlation tends to decrease with APT, especially for an APT $>$ 20 mm (figure 10 of Kondo *et al*.

doi:10.5047/meep.2015.00301.0001

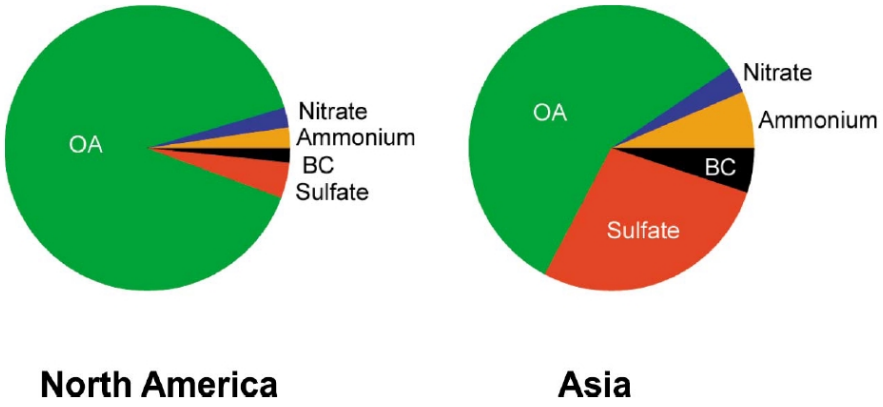

Fig. 63. Fractions of major chemical components of aerosols measured by HR-ToF-AMS (High-Resolution Time-of-Flight Aerosol Mass Spectrometer) in major forest fire plumes in (left) Canada and (right) Asia (from Kondo *et al*., 2011a).

(2011a)). We used the data with APT < 10 mm for the analysis of the emission ratios to minimize the possible effect of wet removal during transport. The slopes changed little by selecting data with APT < 5 mm, although the number of data points was greatly reduced.

Figure 64 shows the correlations between ΔCO_2, ΔCO, CH_3CN, ΔM_{BC}, and ΔV_{SC} of the plumes (with APT < 10 mm) transported from Siberia and Kazakhstan during the ARCTAS-A period. We defined mixed air masses as those in which the trajectories passed over both regions. The plumes from the different source regions in Asia were classified and are color coded in this figure. The correlations of air masses transported from Kazakhstan and Siberia did not show significant differences. The results were the same even if we used the data set without discrimination by APT. These data were used for the analysis of the emission ratios using these correlations. The practical method is described in detail by Kondo *et al*. (2011a).

We derived the average emission ratios of $M_{BC}/CO = 2.3 \pm 2.2$ ng m^{-3}/ppbv and $M_{BC}/CO_2 = 180 \pm 269$ ng m^{-3}/ppmv for BB in North America. For BB plumes from Asia, the average ratios were $M_{BC}/CO = 8.5 \pm 5.4$ ng m^{-3}/ppbv and $M_{BC}/CO_2 = 129 \pm 67$ ng m^{-3}/ppmv. The much higher M_{BC}/CO ratios for the Asian plumes were likely due to higher MCE. The M_{BC}/CO ratios in North America were lower than the values compiled by Andreae and Merlet (2001) by a factor of 2–4, although the ratios for the Asian plumes were similar. The M_{BC}/CO_2 emission ratios for North America and Asia were 4–5 times lower than their estimates.

We related the MCE to the emission ratios between ΔM_{BC}, ΔV_{SC}, ΔCO_2, and ΔCO for BB in North America and Asia. The $\Delta M_{BC}/\Delta CO_2$ ratios decreased with the increase in MCE, whereas the $\Delta M_{BC}/\Delta CO$ ratios increased with the increase in MCE. The dependence of the ratios on MCE is useful in improving the emissions estimate of aerosols from BB and estimating the transport efficiency of aerosols by using tracers, especially CO.

17.6 Evolution of the mixing state of BC

These BC particles were thickly coated by organics, with D_p/D_{BC} ratios of about 1.4 ($0.6 <$ MCE < 0.8) 1–2 hours after emission. In the smoldering phase, the D_p/D_{BC} ratios increased from 1.35 to 1.45 within about 12 hours, with a corresponding increase in the volume of non-refractory species on BC by 15–40%. In aged flaming phase plumes, the increase in D_p/D_{BC} ratios continued for a few days, leading to an increase of the volume of coating materials by a factor of 2. A potential explanation is that OA was being redistributed via the gas phase (e.g., Marcolli *et al*., 2004), by evaporating from particles that did not contain BC and recondensing on BC-containing particles.

We assessed the effect of the Brownian coagulation of LSP with BC on the evolution of the BC mixing state. For the observed conditions, coagulation can increase the D_p/D_{BC} ratios by factors of 1.2–1.5 in 1–2 days, depending on various parameters, influencing the rate of coagulation. Previous studies considered only condensation processes to explain the evolution of the BC mixing state. For the first time, we suggest that coagulation of LSP with BC can effectively increase the D_p/D_{BC} ratios, as well as condensation.

18. BC in Urban Regions

Large amounts of reactive gases and aerosol are emitted from urban areas, as reviewed by Kondo *et al*. (2010). Mega-cities, including the Tokyo Metropolitan Area (TMA), are very large, concentrated sources of these species, which affect aerosol and O_3 levels on local, regional, and global scales (e.g., Molina and Molina, 2004; Ramanathan *et al*., 2007). The uncertainties in the emission estimates of these species are generally large for Asia (Streets *et al*., 2006; Ohara *et al*., 2007) or are not assessed, depending on the areas.

The increased levels of pollutants have a large impact on regional air quality, nutrient deposition patterns, and climate. In order to assess the impacts of anthropogenic species emitted from these mega-cities on surrounding areas, we need to understand quantitatively the key processes involved in the chemical processing of aerosols near the source regions

doi:10.5047/meep.2015.00301.0001

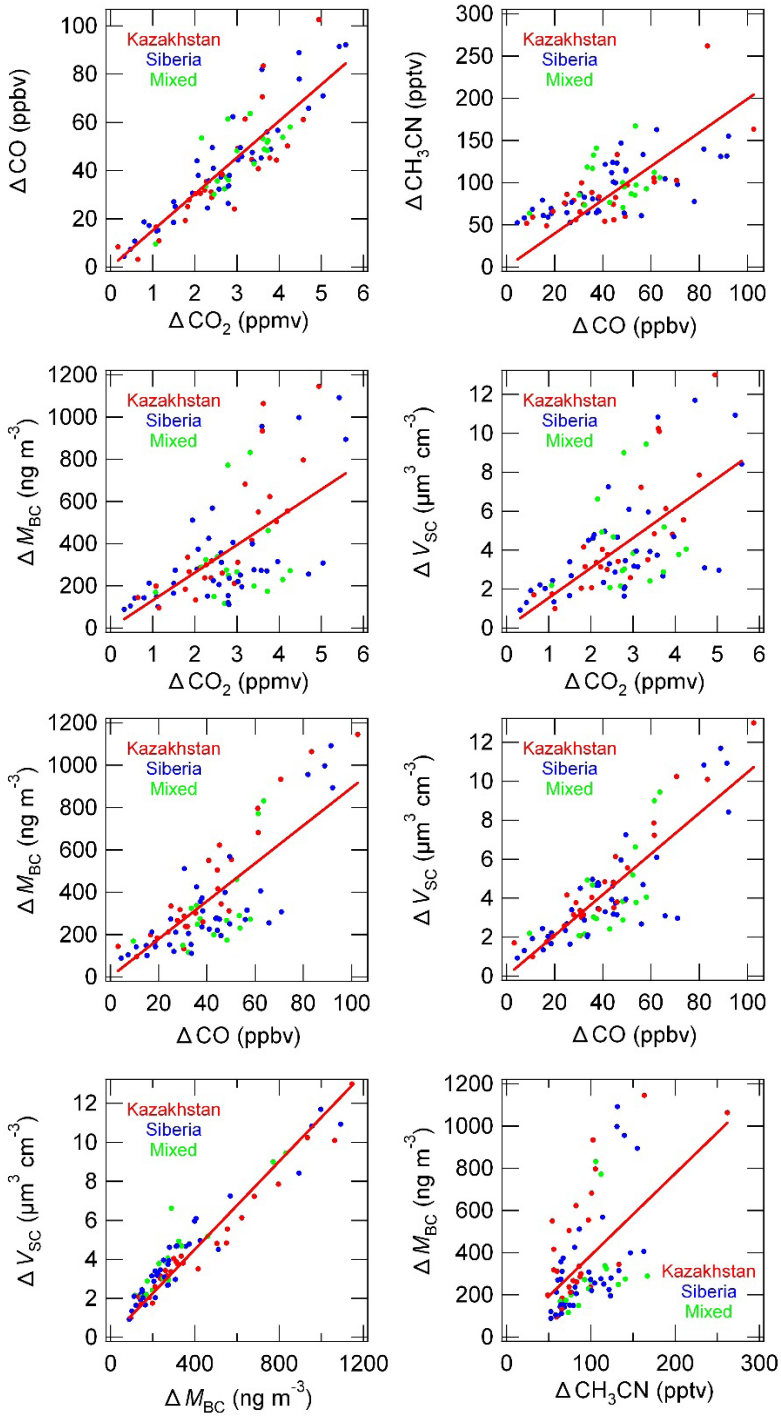

Fig. 64. Correlations between M_{BC}, V_{SC}, ΔCO_2, ΔCO, and CH_3CN in wildfire plumes over Canada (circles) and California (crosses) during ARCTAS-B with APT < 1 mm (from Kondo *et al.*, 2011a). The data points are color coded for the smoldering phase (MCE < 0.9; blue), the flaming phase (MCE > 0.95: red), and others (0.90 < MCE < 0.95; green).

(Fig. 65). In addition, clusters of mega-cities lead to an accumulation of O_3 and aerosol through large-scale mixing. Reactive species with elevated concentrations in urban outflows can also interact with species emitted from natural sources surrounding the mega-cities. It should be noted here that O_3 and aerosol are coupled due to similar sources, photochemical interactions (e.g., UV changes by aerosol), and transport.

Mass fractions of BC particles are about 2–10% of the total aerosol mass concentrations in the fine mode over urban areas (Cao *et al.*, 2003; Gelencsér *et al.*, 2007; Ram *et al.*, 2010). However, they contain carcinogenic poly-aromatic compounds and cause adverse health effects, including allergy, respiratory, and cancer-like diseases (Samet *et al.*, 2004; Somers *et al.*, 2004; Jansen *et al.*, 2005; Nel, 2005; Alessandrini *et al.*, 2006). Thus, there is growing interest in understanding BC emissions both for global climate and re-

doi:10.5047/meep.2015.00301.0001

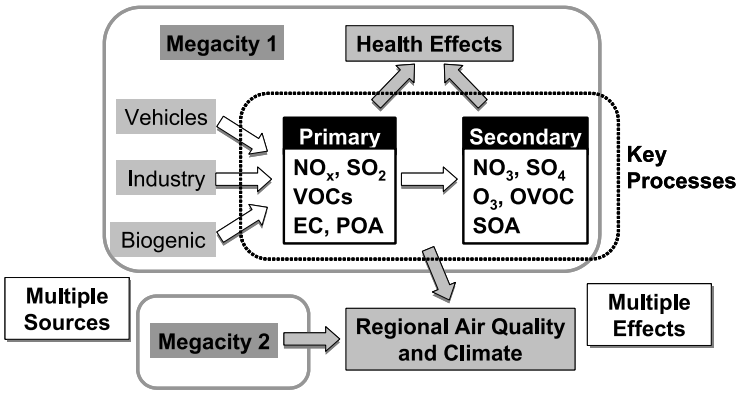

Fig. 65. Schematic of the key processes of ozone, aerosols, and their precursor gases near megacity regions (from Kondo *et al*., 2010).

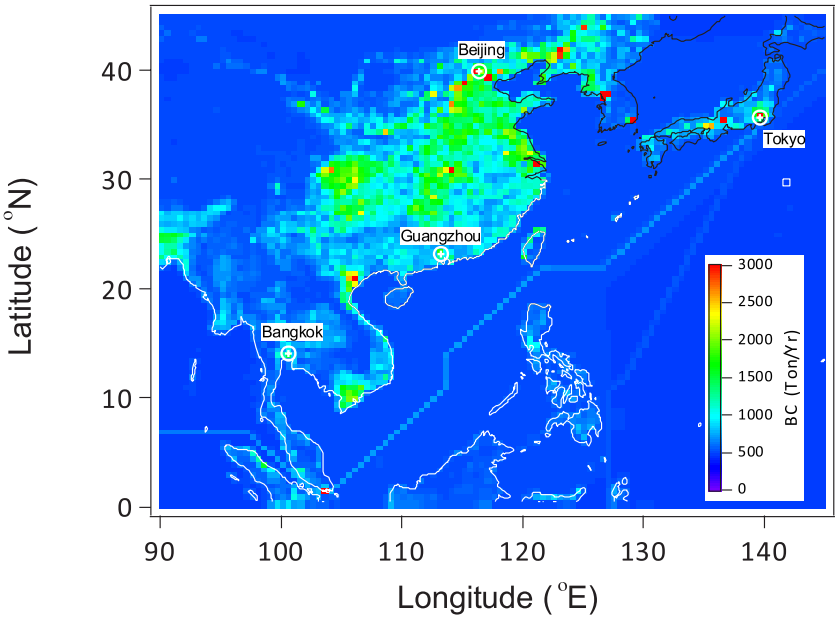

Fig. 66. Distribution of anthropogenic emissions of BC for the year 2000 at 0.5° × 0.5° resolution (Streets *et al*., 2003). The sites of BC measurements are also shown. The figure is from Sahu *et al*. (2011).

gional air quality (Hansen and Sato, 2001; Jacobson, 2002a; Yorifuji *et al*., 2011).

The growing emissions of carbonaceous species from the mega cities of Asia can impact local air quality and climate on regional and global scales. In most of the mega cities of the world, the emissions of carbonaceous aerosols are mainly due to the use of fossil fuels in automotive engines and industry. The annual emission map of BC from anthropogenic sources in parts of Asia for the year 2000 (Streets *et al*., 2003) is shown in Fig. 66. The major sources can be located mostly in the eastern part of China, South Korea and Japan where emissions from urban areas are highest. In the SEA region, however, the emissions of BC from anthropogenic sources are relatively less, and the emissions from biomass burning and forest fire sources make the major contributions.

Recent studies have suggested that emission control measures implemented in Beijing during the 2008 Olympics games significantly improved air quality (Wang *et al*., 2010; Okuda *et al*., 2011). Furthermore, emission control measures and the use of good quality fuels for transportation enhance not only air quality but also reduce the levels of ambient BC and carcinogenic hydrocarbons. The mitigation of BC aerosols will also help to improve air quality and, subsequently, its impact on the climate and hydrological cycles on a regional-to-global scale (Jacobson, 2010). In this chapter, the behavior BC in urban areas in Asia obtained from our previous measurements is presented based on the studies of Kondo *et al*. (2006, 2012) for Tokyo, Han *et al*. (2009) for Beijing, Verma *et al*. (2010) for Guangzhou, and Sahu *et al*. (2011) for Bangkok.

18.1 BC in Tokyo

18.1.1 Diurnal and seasonal variations PM_1 BC concentrations and CO were measured on an hourly basis near the urban center of Tokyo between May 2003 and February 2005. BC and CO were well correlated throughout the measurement period due to a similarity in sources. CO and CO_2 were also well correlated in autumn and winter, indicating that both CO and CO_2 are good tracers of BC. The

doi:10.5047/meep.2015.00301.0001

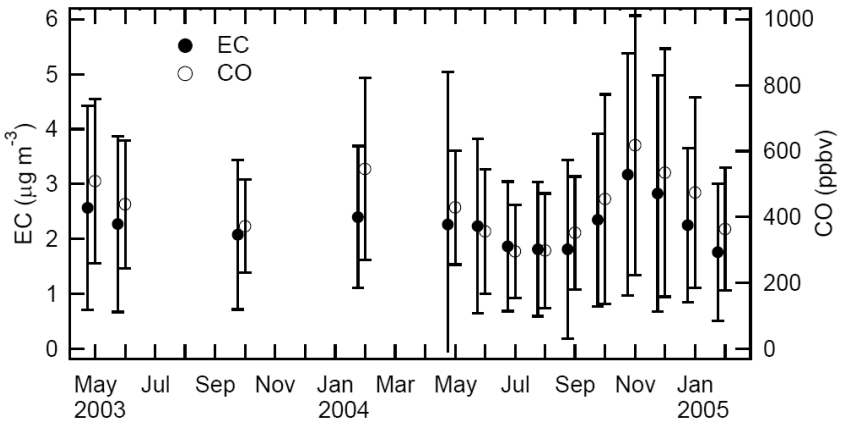

Fig. 67. Monthly median values of EC (elemental carbon = BC) (solid circles) and CO (open circles) for all the data obtained (from Kondo *et al*., 2006).

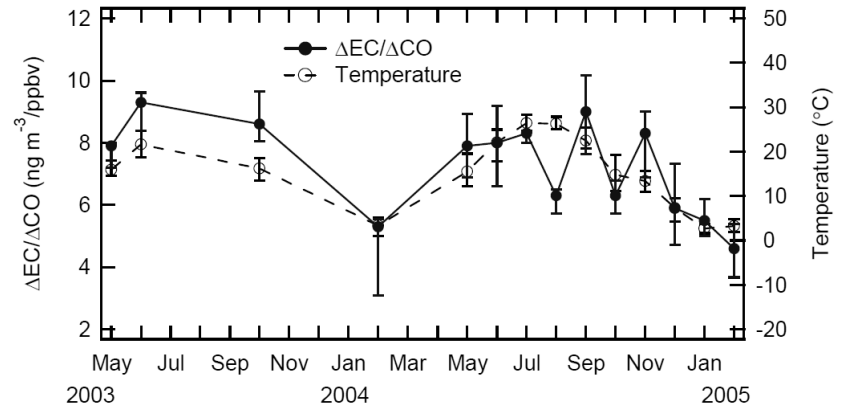

Fig. 68. Monthly median values of $\Delta EC/\Delta CO$ (= $\Delta BC/\Delta CO$) for the early morning (0400–0800 LT) (from Kondo *et al*., 2006).

BC generally decreased with increasing wind speed, indicating the importance of dilution by vertical mixing and horizontal transport in controlling their near surface concentrations. Because the $\Delta BC/\Delta CO$ ratio is not affected by dilution, it is a more suitable parameter for detecting changes in the strength of BC emissions than BC measurements alone.

BC and $\Delta BC/\Delta CO$ values showed a diurnal variation, peaking in the early morning (0400–0800 LT) and reaching minimum values around midnight. The peak BC and $\Delta BC/\Delta CO$ values were 2 times greater than the minimum values at midnight. This diurnal pattern is similar to that of the traffic density of diesel trucks. $\Delta BC/\Delta CO$ for Sundays was lower by about 50% than weekday values, in reasonable agreement with changes in truck traffic density. These results indicate that diesel trucks, especially heavy-duty trucks, are the dominant sources of BC in Tokyo.

The median BC and CO values of the whole data set obtained during the years 2003–2005 were 1.8 ± 1.8 μg m^{-3} and 368 ± 274 ppbv, respectively. Figure 67 shows the variations of monthly median BC and CO values. Because BC and CO were correlated, the average monthly $\Delta BC/\Delta CO$ ratio was stable at 7.2 ± 2.6 ng m^{-3}/ppbv for 0400–0800 LT. $\Delta BC/\Delta CO$ showed a seasonal variation, reaching broad maximum values in spring-autumn and reaching minimum values in midwinter, following the seasonal variation in temperature (Fig. 68). The overall dependence of $\Delta BC/\Delta CO$ on temperature was 0.17 ng m^{-3}/ppbv/°C for 2–25°C. The dependence of $\Delta BC/\Delta CO$ on temperature was also observed in Maryland, USA (Chen *et al*., 2001) and Beijing, China (Han *et al*., 2009). The possible cause of the temperature dependence is discussed in Section 18.2.

18.1.2 Long-term trend Vehicular emissions contribute to the majority of the BC loading in Tokyo, as mentioned above. Carbonaceous particulate matter (PM) in Tokyo is mainly emitted from diesel vehicles, and these emissions were first regulated in 1985 in Japan. Under the Automobile NO_x-PM law of the government of Japan, newly-produced vehicles were subject to a series of regulations, namely the Short-term Regulation in 1993, the Long-term Regulation in 1997–1998, the New Short-term Regulation in 2002–2003, and the New Long-term Regulation in 2005 in order to reduce PM emissions. As a result, emission factors of PM from heavy-duty diesel vehicles have decreased drastically since 1998. However, no clear evidence for a decrease in the ambient BC concentration has been reported so far, mainly due to the lack of time-resolved mea-

doi:10.5047/meep.2015.00301.0001

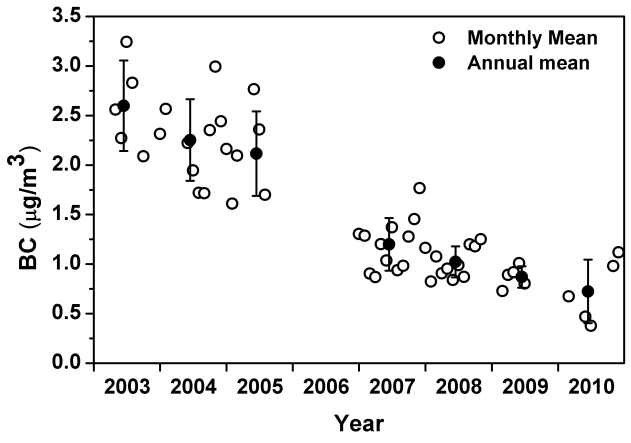

Fig. 69. Temporal variability of observed BC mass concentrations (monthly as well as the annual mean) at RCAST (Research Center of Advanced Science and Technology) of the University of Tokyo, Tokyo during 2003–2010 (Kondo *et al*., 2012). The vertical bars represent standard deviations of the BC mass concentrations. (Reprinted from *Atmos. Environ*., *54*, Kondo, Y., K. Ram, N. Takegawa, L. Sahu, Y. Morino, X. Liu, and T. Ohara, Reduction of black carbon aerosol in Tokyo: Comparison of real-time observations with emission estimates, 242–249, Copyright 2012, with permission from Elsevier.)

surements and/or emission estimates of BC aerosols. Considering this, we re-started BC measurements using COSMOS in Tokyo in 2007.

Figure 69 shows the measured M_{BC} in Tokyo from 2003–2005 and 2007–2010. We also estimated the total BC emissions in Tokyo for the decade (2000–2011). Results of real-time measurement as well as emission estimates indicate that M_{BC} decreased from 2.6 μg m^{-3} (in the year 2003) to 0.6 μg m^{-3} (in the year 2010) in Tokyo. Based on statistical estimates constructed using currently available data in Japan, vehicular emissions were shown to be the dominant source of BC. The reduction of M_{BC} is therefore mainly attributed to the continuous and stringent regulations by the government for PM emissions from diesel vehicles on a time-scale of several years to decades. The statistical estimate of the BC emissions for 2003–2010 is also supported from estimates using diurnal-weekly variations of M_{BC} in Tokyo by assuming that the measured holiday-to-weekday ratio of M_{BC} directly reflects the contributions of vehicles to total emissions.

The predicted decrease in BC (from emission estimates) explains the observed reduction (from real-time measurements) in 2003–2010 to within about 20%. The emission estimates suggest a decrease by a factor of ∼6 in total vehicular BC emission compared to that in the year 2000 whereas real-time measurements indicate a ∼80% reduction in M_{BC}. This is the first clear evidence of a dramatic reduction in BC emissions in Tokyo. However, it is noticeable that the total BC emission from all sources has decreased by only a factor of 3 (from 3.8 Gg in year 2000 to 1.3 Gg in year 2011). Furthermore, vehicular, off-road, and the remaining five emission sources (including large point sources, small combustion, incineration, field burning, ships, and aviation) contribute equally in the present scenario. Thus, it is suggested that precautionary measures should be taken, and that emission controls must be initiated to cut down off-road emissions in order to further reduce BC levels in Tokyo.

The present study also shows the importance of real-time measurements for longer periods to detect trends of BC and to validate the effects of regulations and emission estimates. High-quality measurements of BC by well-calibrated and stable instruments, such as COSMOS, are critical for such studies. This study also demonstrates that existing technologies and the implementation of stringent emission controls for vehicular emissions can greatly help in reducing the BC burden in mega-cities within a relatively shorter time because of the short residence time of BC in the atmosphere (days to weeks).

18.2 BC in Beijing

Among the Asian countries, China is the largest BC source, although uncertainties in the estimates are large. The Beijing area contributes dominantly to the BC emissions in northeastern China (Guinot *et al*., 2007). BC transported from this area strongly influences M_{BC} in Asian outflow over the western Pacific (Shiraiwa *et al*., 2008; Sahu *et al*., 2009; Verma *et al*., 2011; Oshima *et al*., 2012; Liu *et al*., 2013b). Reliable estimates of BC emissions in northeastern China are required for improved evaluations of the impacts of BC on air quality and climate in East Asia and regions downwind. A quantitative understanding of the temporal variations in Beijing is critically important for this purpose, because Beijing is located in a large source area in northeastern China.

Studies of BC in Tokyo have shown that highly-time-resolved BC measurements are very useful in interpreting temporal variations of BC emissions. In addition, CO and CO_2 have been shown to be key tracers for characterizing the sources of BC, because they are also produced by the combustion of fossil fuels and biofuels. In previous studies of BC in Beijing, the time resolutions of BC measurements were between one day and one week, as summarized in table 1 of Han *et al*. (2009). In addition, no simultaneous CO or CO_2 measurements were made in these studies. Because of the limitations of these measurements, the temporal variations of BC emissions in the Beijing area were not fully characterized. We measured BC in Beijing using a TOT analyzer with a 1-hour time resolution, together with CO and CO_2 for the first time. The major objective of this study was to establish statistically significant BC, CO, and CO_2 levels in Beijing during the four seasons.

M_{BC} in $PM_{2.5}$, CO, and CO_2 were measured every hour on the top of one of the buildings of Peking University (PKU) near the fourth ring road in Beijing between winter 2005 and fall 2006. The traffic of heavy-duty diesel trucks (HDDTs) measured on the fourth ring road during nighttime was about 20 times higher than that during daytime (figure 2 of Han *et al*., 2009). The same set of measurements were made at the Yufa site in the summer of 2006. The Yufa site is located in a rural area about 53 km south of the PKU site.

The temporal variations of these species at the PKU and Yufa sites were similar, indicating they were distributed uniformly over horizontal distances of about 50 km from the PKU site. The annual median M_{BC} was 5.9 μgC m^{-3} at the

doi:10.5047/meep.2015.00301.0001

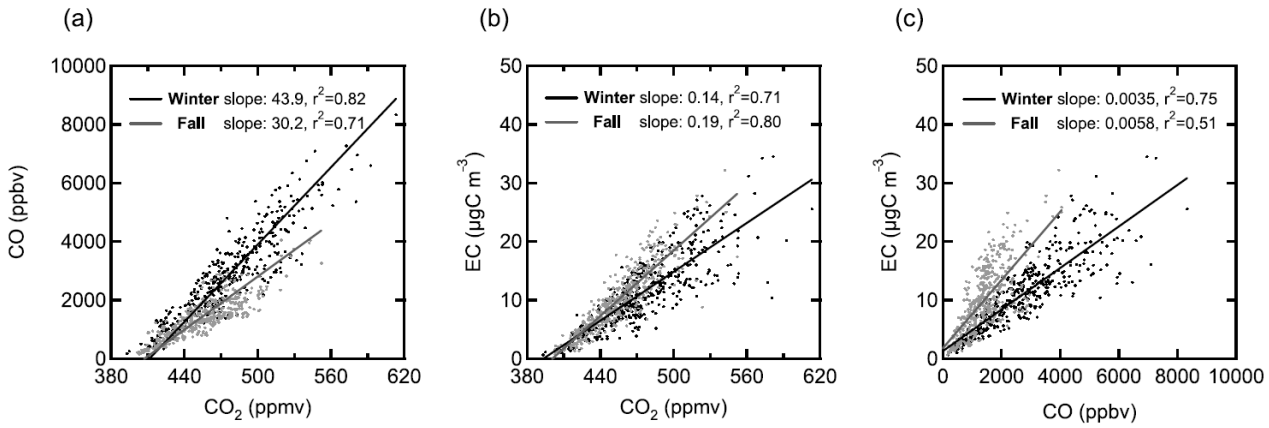

Fig. 70. Scatterplots of (a) CO versus CO_2, (b) EC (elemental carbon = BC) versus CO_2, and (c) EC versus CO for winter and fall under weak wind conditions (from Han *et al*., 2009). The solid line is the linear regression line determined by bivariate regression analysis.

PKU site. The M_{BC} decreased with near-surface wind speed (WS), similarly to Tokyo. The median M_{BC} was highest in the fall and lowest in winter due to the WS dependence.

The concentrations of CO_2, CO, and BC measured under strong-wind conditions (WS > 4.0 m s^{-1}) represented their background levels. The background levels were much higher for a southerly wind than those for a northerly wind, reflecting much higher emissions of these species in the regions south of Beijing (figure 9 of Han *et al*., 2009).

For weak-wind speed (WS ≤ 2.0 m s^{-1}) conditions, BC, CO, and CO_2 were well correlated throughout the measurement period due to the co-locations of sources, as shown in Fig. 70. In winter, CO and $\Delta CO/\Delta CO_2$ ratios during the night were largely higher than those in the other seasons. CO emissions associated with coal or biofuel combustion for domestic heating are not the main cause of the high CO in winter, considering the lack of predicted increases in BC in winter above the levels in the other seasons. Instead, the increase in the CO emissions from vehicles is more likely the dominant cause. The time required for catalysts to be heated to temperatures high enough for efficient CO removal is elongated at low temperatures, leading to higher CO emissions.

For further analysis, the $\Delta CO/\Delta CO_2$ ratios during the nighttime (2000–0600 LT) are plotted versus atmospheric temperature for winter, summer, and fall in Fig. 71(a). The $\Delta CO/\Delta CO_2$ ratio was highest at temperatures below 0°C. It decreased with increasing temperature. These results suggest that the CO emissions are temperature dependent. Figure 71(b) shows the increase in the $\Delta BC/\Delta CO$ ratios with ambient temperature. The similarity in the $\Delta BC/\Delta CO_2$ between winter and the other seasons indicates no significant additional BC sources in winter (Fig. 71(c)). It is shown that the changes in the $\Delta BC/\Delta CO$ ratios with temperatures are mainly driven by the changes in CO emissions. Similarly, it is likely that the temperature dependence of $\Delta BC/\Delta CO$ observed in Tokyo was also caused by the temperature dependence of CO emissions.

The M_{BC}, $\Delta BC/\Delta CO_2$ (except for summer), and $\Delta BC/\Delta CO$ (except for winter) showed similar diurnal patterns, increasing in the late evening and remaining high until early morning. These diurnal variations indicate regular sources of BC throughout the year. The variations of $\Delta BC/\Delta CO$ for vehicle exhaust ($[\Delta BC/\Delta CO]_{vehicle}$) were calculated using the measured fractions of heavy-duty diesel vehicles (HDVs) and light-duty gasoline vehicles (LDGVs) and their BC/CO emission ratios. $[\Delta BC/\Delta CO]_{vehicle}$ during nighttime was higher by about 0.004 μgC m^{-3}/ppbv than that during daytime, similar to the observed increase. The large increase in $\Delta BC/\Delta CO$ during the nighttime can be explained by the increase of the HDV fraction due to HDV inflow into the urban area during the nighttime.

The diurnal variations of BC, CO, and CO_2 concentrations and the $\Delta BC/\Delta CO$ ratios were similar for weekdays and weekends. This result indicates no significant weekend effects in Beijing.

The observed slopes of the CO-CO_2-BC correlations (Fig. 70) were used to evaluate the ratios of the emissions of these species from the all sources derived from the emission inventory of Streets *et al*. (2003) in the Beijing area. The comparison suggests that Streets *et al*. largely overestimated the contributions of the emissions from domestic sectors with high CO/CO_2 and BC/CO_2 emission ratios and/or underestimated those from non-domestic sectors, especially vehicle emissions, in the Beijing study area. These results indicate that the observed slopes are useful parameters in assessing the reliability of emission inventories.

18.3 BC in Bangkok

In the tropical regions of Asia, forest fires and biomass burning are widespread (Christopher *et al*., 1996; Folkins *et al*., 1997). The emissions from anthropogenic, forest fires and open biomass burning sources in Southeast Asia (SEA) contribute substantially to the inventories of carbonaceous aerosols in Asia (Streets *et al*., 2003; Bond *et al*., 2004). According to the estimates presented by Streets *et al*. (2003) for the year 2000, the total anthropogenic emissions of BC and OC aerosols in SEA were about 0.77 Tg and 3.68 Tg, respectively.

Thus far, detailed studies characterizing the variations of carbonaceous aerosols near the major source regions in SEA are rare mainly due to the lack of continuous observations

doi:10.5047/meep.2015.00301.0001

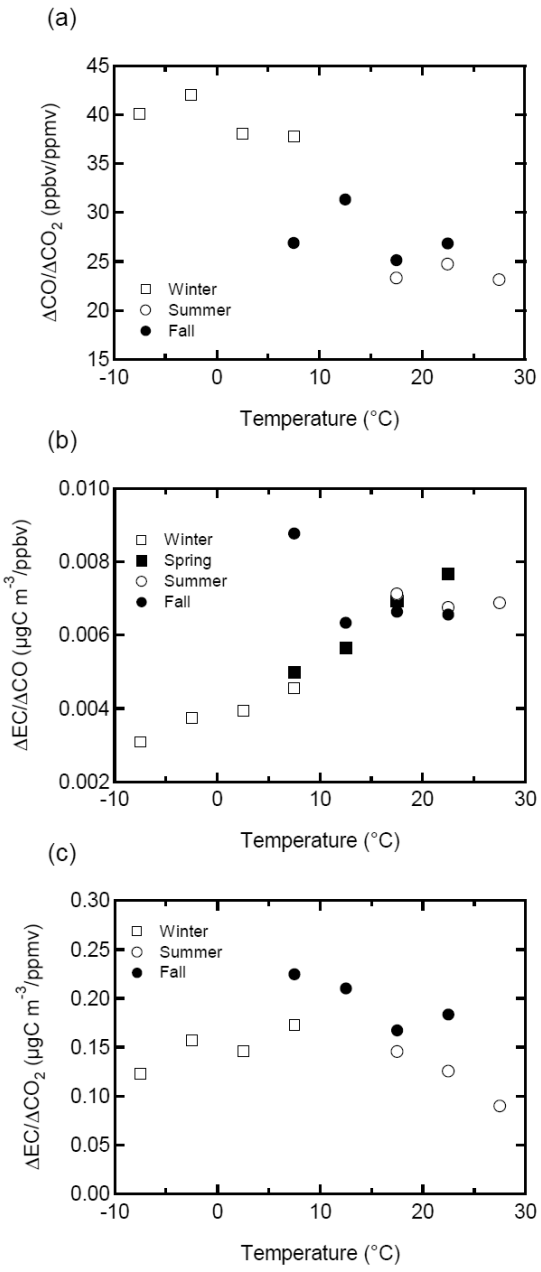

Fig. 71. (a) $\Delta CO/\Delta CO_2$ ratios, (b) $\Delta BC/\Delta CO$ ratios, and (c) $\Delta BC/\Delta CO_2$ ratios versus ambient temperature during nighttime (2000–0600 LT) (from Han *et al*., 2009).

(See *et al*., 2006, and references therein). The present study is based on continuous observations of $PM_{2.5}$ carbonaceous aerosols in Bangkok, Thailand, during the years 2007–2008. The characteristics of the temporal variations of BC and OC aerosols have been analyzed from the point of view of the short-term changes in local meteorology, the seasonality of the long-range transport, and the strength of local emissions. The observations of aerosols in Bangkok represent the activities of distinct emission sources rather than those in typical urban areas of Asia, for example, Beijing and Tokyo in East Asia (Kondo *et al*., 2006, 2012; Han *et al*., 2009).

18.3.1 Measurements and meteorological conditions Concentrations of BC and OC aerosols were measured by the TOT method, together with CO, in Bangkok during April 2007–March 2008. BC was measured also by COSMOS. There are three main seasons in Thailand, namely wet (May–October), dry (November–February), and hot (March–April) (Pochanart *et al*., 2003). The wet season prevails due to a southwesterly (SW) wind flow, and the dry season is due to a northeasterly (NE) wind flow. The SW wind flow is associated with the northward movement of the inter-tropical convergence zone (ITCZ) across Thailand which brings cleaner marine air from the southern Indian Ocean. During the dry season, the long-range transport of continental air from different regions of East Asia takes place due to the southward movement of the ITCZ. The observation site is influenced by mixed air masses (marine and continental) during the hot season.

Emission from automobile vehicles was a major anthropogenic source of aerosols throughout the year, while biomass burning contributed significantly during the hot season. The observation site was influenced by the flow of cleaner oceanic air during the wet season. On the other hand, the northeast flow transported the continental polluted air mainly from China passing through the SEA continent territory during the dry season.

18.3.2 Diurnal and seasonal variations The annual trends of both BC and OC aerosols showed a clear seasonality, with the lowest concentrations in the wet season and the highest in the dry season, as shown in Fig. 72. The average concentrations of BC were 3.0±1.2 μg m^{-3} and 4.3±1.3 μg m^{-3} in the wet and dry seasons, respectively. The concentrations of OC were 5.3±2.0 μg m^{-3} and 13.1±5.8 μg m^{-3} in the wet and dry seasons, respectively. In the wet season, the concentrations of aerosols emitted from local sources were diluted due to the flow of cleaner air from the Indian Ocean and wet removal. In the dry season, the long-range transport of pollutants, mainly from China, added to the local emissions, resulting in the highest concentrations of BC and OC aerosols. In spite of the highest activities of biomass burning in the hot season, moderate levels of BC of 3.8 μg m^{-3} and OC of 11 μg m^{-3} were due to the mixing with cleaner Pacific air masses. However, the highest average ratio of OC/BC of 3.8 μg μg^{-1} observed in the hot season confirms the predominant contributions from biomass burning sources.

The diurnal distributions of BC and OC showed elevated concentrations during evening-morning hours and the lowest in the afternoon hours. Concentrations of both BC and OC aerosols exhibited two prominent peaks during the rush hours, which also coincided with stagnant air flow (< 0.5 m s^{-1}). The minimum of the OC/BC ratio (for example ∼1.0 μg μg^{-1} in the wet season) also coincided with the peaks in BC, suggesting the influence of fresh emissions from vehicular exhausts during the rush hour. The diurnal variation in PBL depth controlled the diurnal patterns of both BC and OC, while the elevated level of the OC/BC ratio during the daytime suggests the secondary production of OC.

The concentrations of both BC and OC decreased with the increase in wind speed, as observed in Tokyo and Beijing.

doi:10.5047/meep.2015.00301.0001

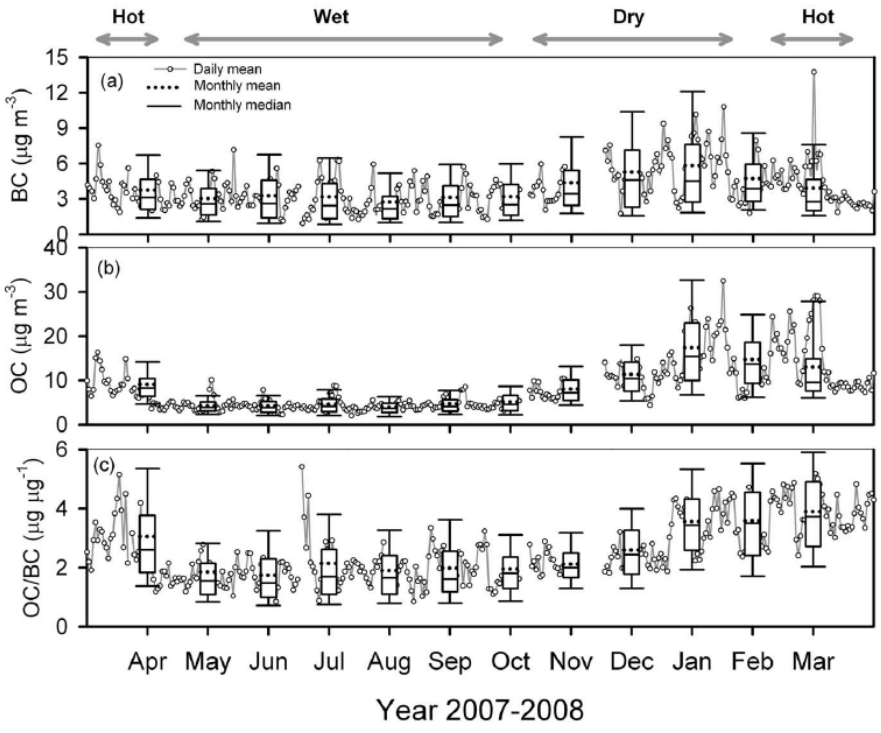

Fig. 72. The daily means and monthly variations of concentrations of (a) BC, (b) OC (organic carbon), and (c) OC/BC ratio measured at AIT (Asian Institute of Technology) in Bangkok (from Sahu *et al*., 2011). In the box-whisker plots the horizontal solid lines represent 10th, 25th, 50th, 75th, and 90th percentiles while dashed lines give the means obtained using hourly data.

The seasonality in the relationship between the concentrations of aerosols and wind speed could be due to the transport of air masses with different background levels of aerosols. The sharp declines in the concentrations of BC and OC were observed during rainfall in Bangkok due to the wet scavenging of aerosols in the wet season.

The $\Delta BC/\Delta CO$ ratio of $\sim$9.8 ng m^{-3} ppbv^{-1} estimated for the measurements in the wet season represents the emission ratio from local anthropogenic sources. In the dry season, a lower value of $\sim$7.9 ng m^{-3} ppbv^{-1} was due to the combined contributions of the long-range transport of continental air and the emissions from local sources. The $\Delta OC/\Delta BC$ ratio also shows a clear seasonality with lower values of 0.5–0.7 μg μg^{-1} in the wet season and higher values of 2.08–3.08 μg μg^{-1} in the hot season characterizing the emissions from fossil fuels and biomass burning, respectively.

The weekday-weekend differences in the distributions of BC and OC were significant. Overall, the decrease by $\sim$20–30% in the BC concentration was consistent with the reductions in traffic volume during the weekend. This study suggests that the implementation of stricter abatement rules in vehicular emissions could substantially reduce the levels of various anthropogenic pollutants in Bangkok.

18.3.3 Comparison with other urban areas in Asia

A comparison of the diurnal variations of BC in Bangkok with the measurements reported for major cities like Guangzhou (Verma *et al*., 2010), Beijing (Han *et al*., 2009), and Tokyo (Kondo *et al*., 2012), is shown in Fig. 73. The most remarkable point is that in the year 2007, BC concentrations were lowest in Tokyo. Clearly this was caused by the drastic reduction of BC emissions from vehicles.

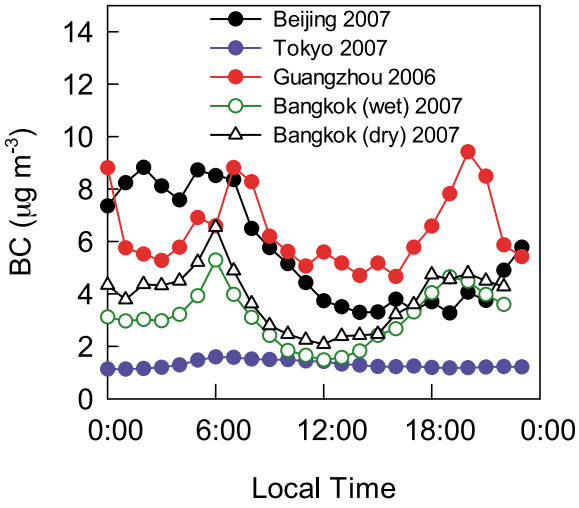

Fig. 73. Comparison of the diurnal variations of BC at AIT (Asian Institute of Technology) in Bangkok and observations reported for major urban areas of East Asia (from Sahu *et al*., 2011).

The level and pattern of the variability of BC differ between the cities. The peak of BC concentration during the morning rush hour in Bangkok was observed to be $\sim$2 hours earlier than those in urban sites of China. Although the concentration of BC shows weaker diurnal dependences in

doi:10.5047/meep.2015.00301.0001

Tokyo, however, it exhibits an opposite pattern compared to other cities. We can see a slightly higher level of BC during the daytime and lower during the night and early morning hours in Tokyo. The diurnal amplitudes of BC in Bangkok were significantly higher than the variations observed in Beijing, Guangzhou, and Tokyo. One of the reasons for such large variations in Bangkok could be the large diurnal variation in PBL depth due to the tropical climate, as other sites are located at higher latitudes. However, more quantitative studies are needed to investigate the roles of other factors, such as the local time dependence of emissions.

The concentrations of both BC and OC at Bangkok fall within the range of values for many urban locations, as shown in table 3 of Sahu *et al.* (2011). The OC/BC ratios in the wet season in Bangkok are close to the values reported for urban areas of North America, South Korea, and Japan where fossil fuel combustion is a major source of carbonaceous species. On the other hand, the higher values of OC/BC during the dry and hot seasons are close to the values reported for several urban areas of China (Novakov *et al.*, 2005). This similarity could be due to the emissions also from non-fossil fuel sources in urban regions of China and SEA (Verma *et al.*, 2010). Our observations showing the significant seasonality of the OC/BC ratio contradicts the suggestion that the OC/BC ratio does not change significantly with season for a given region (Novakov *et al.*, 2005). The OC/BC ratio of 7.13 derived from the inventory of biomass emissions in "other Asian countries" (Bond *et al.*, 2004) is higher by a factor of two or more than the values observed in Bangkok.

19. Absorption Aerosol Optical Depth (AAOD) Closure

In this chapter, column-integrated light absorption by BC is discussed based on the detailed analysis by Koike *et al.* (2014). This issue is closely related to the uncertainties in the estimate of BC DRF.

19.1 Previous studies

Absorption aerosol optical depth (AAOD) is a key parameter in the evaluation of radiative forcing and atmospheric heating by aerosols. AAOD is a measure of the column aerosol light absorption and expressed as (1 − SSA) AOD, where SSA and AOD are the column single scattering albedo and aerosol optical depth, respectively. In addition to BC, OA and dust particles also absorb solar radiation, especially in the ultraviolet region (e.g., Sokolik and Toon, 1999; Dinar *et al.*, 2008). Currently, the only way to measure AAOD routinely and globally is with ground-based radiation measurements, such as the sun-sky photometer measurements performed by the Aerosol Robotic Network (AERONET) (Dubovik *et al.*, 2002) and Sky Radiometer Network (SKYNET) (Nakajima *et al.*, 2007). In fact, these data are the only constraint available for estimates of the global radiative forcing of BC or carbonaceous (BC + OA) aerosols (Chung *et al.*, 2012; Bond *et al.*, 2013).

With regard to the sun-sky (or sun) photometer AOD measurements, validation studies have been made by conducting closure experiments with in situ aircraft aerosol extinction measurements (e.g., Redemann *et al.*, 2003; Shinozuka *et al.*, 2007; Esteve *et al.*, 2012). Generally, good agreement between the two measurements (about 10–50%) has been obtained. However, for AAOD or SSA measurements, only a very limited number of closure experiments have been conducted despite their great importance. During an aerosol intensive observation period of the Department of Energy's Atmospheric Radiation Measurement (ARM) in Oklahoma in May 2003, column SSAs derived from Cimel sun-sky photometer measurements (a part of the AERONET) were compared with in situ aircraft measurements (Ricchiazzi *et al.*, 2006). On board the aircraft, aerosol absorption and scattering coefficients were measured using a particle soot absorption photometer (PSAP) and TSI integrating nephelometers, respectively, and the column SSA was calculated using the following equation:

$$\mathrm{SSA_{column}} = 1 - \frac{\mathrm{AAOD}}{\mathrm{AOD}} = \frac{\int (1 - \mathrm{SSA}(z)) \cdot b_{\mathrm{ext}}(z) dz}{\int b_{\mathrm{ext}}(z) dz}, \tag{39}$$

where b_{ext} is the aerosol extinction coefficient. As a result, the column SSAs agree to within about 0.05; the sun photometer measurements were lower by 0–5% and higher by 2–15% at 676 and 440 nm, respectively. In terms of SSA, the agreement is good; however, AAOD errors were in fact about 100% because the average SSA was about 0.95. A portion of the differences could be due to errors in in situ aerosol absorption measurements made with PSAP, because these filter-based instruments without heated inlets are known to have uncertainties due to the scattering of aerosols and complicated radiative transfer within filters, as discussed in Chapter 3. Furthermore, PSAP is particularly unreliable in profiles because of its poor time resolution.

Much better AAOD agreement with a mean difference of 19% at 500 nm was obtained between absorption photometer measurements (Magee Scientific, AE-31 Aethalometer) on board aircraft and AERONET sun-sky photometer measurements at the Maldives (Corrigan *et al.*, 2008). However, aethalometer, like other filter-based measurements, is known to have uncertainties, as mentionrd above. Although instruments to measure aerosol absorption with greater accuracy have been developed in recent years, such as the photoacoustic spectrometer (PAS) (Arnott *et al.*, 2006) and photothermal interferometry (PTI) (Sedlacek and Lee, 2007), the accurate measurement of aerosol absorption on board aircraft is still a challenge. A more reliable method for comparing sun-sky photometer AAOD measurements with in situ measurements is to calculate the optical properties of local aerosols from the aerosol size distribution and the mixing state measured by an SP2.

One of the difficulties in estimating the BC contribution to AAOD at visible wavelengths is that uncertainties arise from dust. Previous studies in East Asia and other regions have reported that SSAs are typically lower (more absorbing) when atmospheric dust particle loading was higher (e.g., Kim *et al.*, 2005). Generally, when BC-rich air is transported from the Asian continent to the Pacific in winter and spring, dust particles, whose source regions are located upstream

doi:10.5047/meep.2015.00301.0001

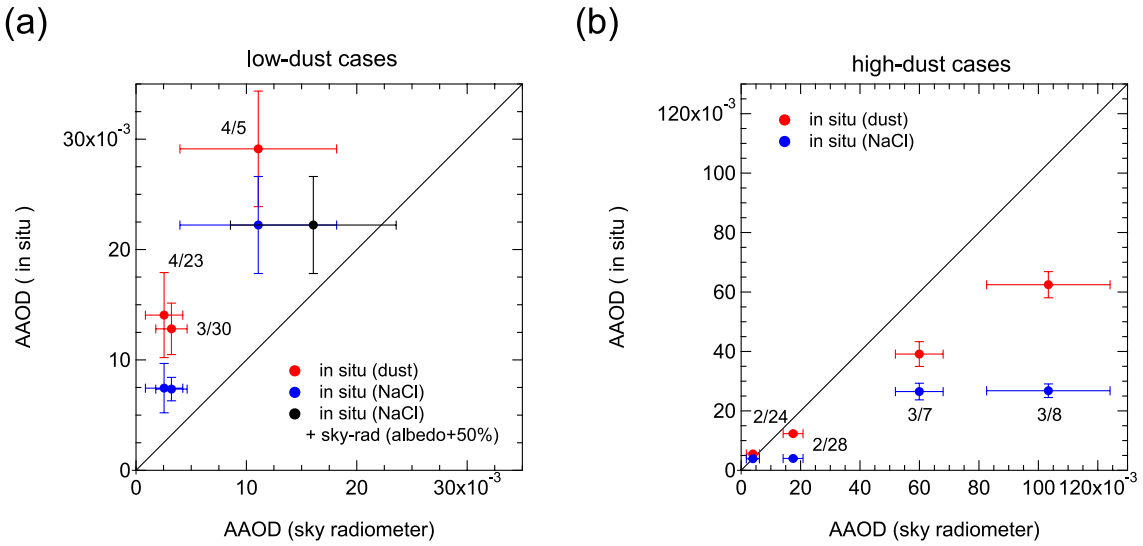

Fig. 74. Comparison of AAOD (absorption aerosol optical depth) and column SSA (single scattering albedo) between aircraft (in situ) and sky radiometer measurements (from Koike *et al*., 2014). The red and blue circles denote results obtained assuming all the coarse particles (in situ measurements) are dust and NaCl (+ water), respectively. Black circles denote values estimated from sky radiometer measurements assuming a 50% higher surface albedo indicating the uncertainty in the sky radiometer retrievals (values are shown only for April 5 case). Uncertainties (error bars) in in situ data were estimated from the contribution from altitudes below the aircraft soundings. The uncertainties in sky radiometers are the standard deviation of the data within each average time period. When compared with the in situ measurement-derived AAODs, the sky-radiometer-derived AAODs are systematically lower and higher in low-dust and high-dust cases, respectively. In accordance with this result, sky-radiometer-derived SSAs are, in general, systematically higher and lower in low-dust and high-dust cases, respectively.

from the BC sources, are potentially mixed.

19.2 A-FORCE comparison

During the A-FORCE experiments conducted in spring 2009 and winter to early-spring 2013 (denoted as the 2013W experiment), vertical profiles of size distributions and mixing states of BC were measured by an SP2 with other aerosol parameters onboard a research aircraft around the Fukue Observatory in the East China Sea (Fig. 28). Using this data set we calculated the optical properties of local aerosols using the core-shell model by taking aerosol water uptake effects into account. The calculated AOD and AAOD were compared with ground-based measurements made with a sun-sky photometer, called as sky radiometer (Prede Co., Ltd, Tokyo Japan), at the Fukue Observatory (part of SKYNET) to evaluate the AOD and AAOD closure.

The comparisons were made in 7 cases when the aircraft made vertical profile measurements near the Fukue Observatory. Aerosol extinction coefficients (b_{ext}) and SSA were calculated based on the total aerosol size distributions and detailed BC mixing state information for fine particles, assuming that all coarse particles are dust or NaCl (+ water). In these calculations, BC and dust are the only two light absorbers and an enhancement of BC light absorption by the lens effect is estimated using detailed information of the observed BC mixing state by adopting the core-shell optical calculation method. We classified 7 cases into groups using AOD values (AOD $>$ 0.4 or not) and the dust fraction (non-spherical contribution to the total AOD smaller than 0.2 or greater than 0.4). The criterion on AOD values is because, according to the data selection criteria of both AERONET (Dubovik *et al*., 2000) and SKYNET (Hashimoto *et al*., 2012), SSA retrieval is reliable only when AOD is greater than 0.4.

Good agreement was found for the calculated extinction coefficients and AOD with lidar and sky radiometer measurements, as shown in figures 2, 3, and 4 of Koike *et al*. (2014). In situ and sky radiometer measurements agreed within 12±18% and 2±8% for "high-AOD" and "low-dust" cases, respectively. The b_{ext} values of fine and coarse particles derived from in situ measurements generally agree with those of lidar-derived spherical and non-spherical particles, respectively, suggesting that most of the coarse particles observed on these days were dust.

Figures 74(a) and 74(b) show a comparison of the AAODs. Only one case (April 5) satisfies both the "high-AOD" and "low-dust" criteria. In this case, sky radiometer-derived AAOD values at 500 nm were found to be about a factor of two smaller than those calculated from in situ data even when all coarse particles were assumed to be NaCl, which does not absorb radiation at 500 nm. Although AOD values were lower than 0.4 (0.16 and 0.19), the other two "low-dust" cases (March 30 and April 23) show similar results. Because the mass absorption cross section (MAC = AAOD/column-BC-mass) estimated from sky radiometer-derived AAOD and in situ BC mass measurements is also systematically lower by a factor of two as compared with previous measurements, the result obtained in this study suggests a potential negative bias in the AAOD values in sky radiometer measurements. An accurate estimate of ground surface albedo used in the sky radiometer retrieval analyses is found to be critical. Because AAOD measurements made by sun-sky radiometers are currently the only constraint available for estimates of global radiative forcing of BC, more investigation should be made to validate these measurements.

doi:10.5047/meep.2015.00301.0001

On the other hand, under "high-dust" conditions, sky radiometer measurements provided systematically higher AAOD values for the two "high-AOD" cases (March 7 and 8). The AAOD valued derived from in situ measurements could be underestimated because of possible underestimation of dust contributions, uncertainty in the refractive index of dust, and possible surface coating of dust by BC.

The present study is the first attempt to assess the uncertainty of the AAOD derived from ground-based photometers by comparison with the SP2 measurements. The obtained results indicate that there are considerable uncertainties in AAOD data obtained by the ground-based sun-sky photometers. For an accurate estimate of the atmospheric heating effect of BC, it is especially essential to separate the dust contribution of aerosol light absorption.

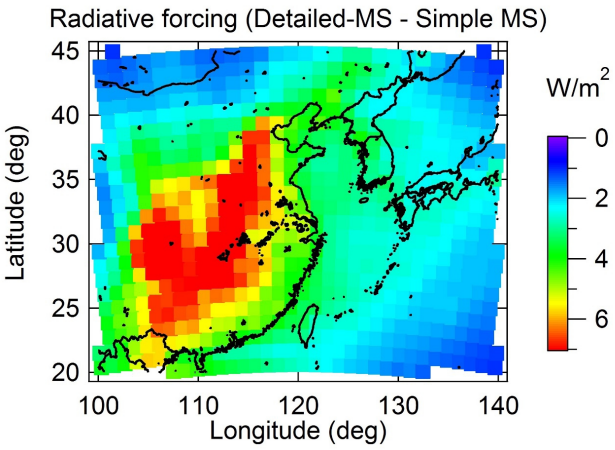

Fig. 75. Spatial distributions of the difference of the aerosol radiative forcing at the surface calculated by the Detailed-MS(mixing state) and Simple-MS calculations, namely Simple − Detailed.

20. Direct Radiative Forcing of BC

20.1 Global radiative forcing

A comprehensive assessment on the evaluation of the climate forcing of BC has been carried out by Bond *et al*. (2013). They have made systematic estimates of climate forcing terms consisting of direct solar absorption (BC DRF); the influence on liquid, mixed phase, and ice clouds; and deposition on snow and ice. The term most relevant to this monograph is BC DRF, which has been estimated to be +0.71 W m^{-2} with 90% uncertainty bounds of (+0.08, +1.27) W m^{-2}. Global-mean direct radiative forcing by BC (BC DRF), can be expressed symbolically as the product of four factors (Schulz *et al*., 2006):

$$\text{BC DRF} = E \times L \times \text{MAC} \times \text{AFE}, \qquad (40)$$

where E is the global mean BC emission rate, L is the global mean lifetime of BC governed by removal, MAC is the global-mean mass absorption cross section, and AFE is the global mean absorption forcing efficiency (forcing per AAOD). 3-D models simulate BC DRF, including many complex processes, and the derived BC DRF are decomposed only to first order into the factors in Eq. (40). The global mean AFE can be estimated from the ratio of the model-simulated BC DFR to the corresponding AAOD. The global mean AAOD is conceptually expressed as $E \times L \times$ MAC. BC AAOD is one of the most important diagnostics that can be compared with data derived from radiation measurements.

Comparison with remote sensing observations, i.e. AERONET AAOD data, indicated that the global AAOD is too low in many global aerosol models (Bond *et al*., 2013). Scaling model-calculated AAOD to match observations increases the modelled globally averaged AAOD by a factor of 2.9. Some of the model underestimate can be attributed to the models lacking treatment of enhanced absorption caused by the mixing of BC with other constituents. The remainder is attributed to underestimates of the amount of BC in the atmosphere. Namely, the emission rate is underestimated and/or deposition is overestimated by global models.

The validity of scaling the model-calculated AAOD by the observed AAOD depends also on the reliability of the observed AAOD. The uncertainties in AAOD are poorly estimated by previous studies. The analysis discussed in Chapter 19 indicates a large inconsistency between the BC-AAOD values derived from the sun-photometer and in situ BC measurements. Realizing a full understanding of the optical properties of BC still remains one of the critical problems for future studies.

20.2 Regional scale radiative forcing

Regional scale models can be used to represent more precisely the parameters and processes that influence the BC DRF. Evaluation of the aerosol schemes used for global models can be made in comparison with the calculations by regional scale models, which includes state-of-the art aerosol schemes. Such efforts have been made by Matsui *et al*. (2013a, 2014), as discussed in Chapter 9.

Matsui *et al*. (2013a) estimated the potential impact of the treatment of the BC mixing state on simulated optical properties of aerosols and radiative effects by aerosols using this model. The off-line optical and radiative calculations were conducted for both a detailed treatment of the BC mixing state (12 × 10 aerosol bins, Detailed-MS) and a single (average) BC mixing state (12 × 1 aerosol bins, Simple-MS) (the mass and number concentrations are the same for the two calculations). BC was assumed to be the center of particles for internally-mixed BC particles. The Detailed-MS calculation had higher SSA values than the Simple-MS calculation over the whole domain. The difference in SSA between the two calculations was 0.03 on period- and domain-average at noon, which corresponded to an overestimation of the absorption coefficient by 40% over East Asia when a single BC mixing state was assumed for aerosol optical calculations. Heating rates by BC reached more than 1.0 K/day over China for both the Detailed-MS and Simple-MS calculations. The difference between the two calculations was 0.1 K/day on period- and domain-average at noon. The heating rate by BC was overestimated by 30% in our calculations when a single BC mixing state was assumed for the radiation calculations. BC particles reduce the solar radiation reaching the surface by absorption and scattering (Fig. 1(a)).

doi:10.5047/meep.2015.00301.0001

Aerosol radiative forcing at the surface had average differences of 5–10 W m^{-2} over China and by 3 W m^{-2} on average over East Asia between the two calculations, as shown in Fig. 75. This difference is because a higher absorption coefficient in the Simple-MS calculation may have led to a decrease in the multiple scattering of radiation and, hence, underestimated the radiation reaching the surface (overestimated surface cooling). These results show that the treatment of the BC mixing state has a large impact on the optical properties of aerosols and radiative effects by aerosols.

The detailed MS-resolved model developed in this study has a large potential to reduce the uncertainties in the estimation of BC absorption and radiative effects because we calculate BC aging (i.e., condensation, coagulation) and optical/radiative (i.e., BC absorption enhancement) processes explicitly without parameterizations. Using this detailed aerosol model, we can evaluate the complicated and nonlinear climatic responses of BC processes to changes in the meteorological conditions (e.g., temperature, humidity, circulation) and the emissions of chemical species. This model can also be used as a benchmark model of global/climate aerosol models to understand the uncertainties in the simpler representation of BC processes in global/climate aerosol models.

21. Summary and Perspectives

21.1 Summary

We have studied the effects of BC on climate based on the new methodologies. First of all, we focused on a quantitative understanding of the physical and chemical processes that control the properties of individual BC particles, especially their numbers, sizes, and mixing states, not only their bulk properties. We developed new techniques for laboratory and field measurements and model calculations. Second, key processes represented by the models were validated one by one through comparison with field observations. The accumulated findings from the field data have been reflected in improving the schemes of the model calculations. The strength of our methodologies is demonstrated by the results of the individual studies. Their summaries are given below in the order that they were presented in the previous chapters.

We began our efforts by defining the "masses of individual BC particles", considering the confusion of the definition of BC which had existed for more than two decades. The intensity of laser induced incandescence (LII) caused by the photo-absorption of BC in a laser beam was shown to be uninfluenced by the internal mixing of BC, which provided a firm basis for the definition of the mass of BC. The dependence of LII intensity on refractive index and the shape of BC was measured and interpreted based on physical theory. A new algorithm to derive the coating thickness of BC (coated-type BC) was developed and was validated by laboratory experiments using BC particles coated by organic compounds. In addition, an algorithm was also developed to detect "attachment-type" BC, which is uncoated BC on the surface of non-BC particles.

A new method was introduced to measure the refractive index of small BC particles by using the relationship between the scattering cross section and the particle volume. The ranges of refractive indices of 8 different types of BC (fullerene soot, colloidal graphite, Aquadag, glassy carbon-100 nm, glassy carbon-50 nm, Aqua-black 001, Aqua-black 002, and ambient BC) were determined. The real and imaginary parts of the refractive index of ambient BC in Tokyo were found to be 2.26±0.13 and 1.26±0.13, respectively.

A filter-based absorption photometer with a heated inlet, COSMOS, was shown to provide reliable data for the total BC mass concentration through comparison with TOT and SP2 instruments at 6 locations in Asia. The dependence of the BC mass concentration measured by COSMOS on the BC size distribution is small, showing its usefulness for long-term BC measurements, especially at remote locations.

Techniques to measure the size distribution and mass concentration of BC (C_{BC}) suspended in water were developed. The measurement system consisted of an ultrasonic nebulizer and an SP2. Detailed evaluations were made for the size dependence of the nebulizer efficiency, the reproducibility of measurements, and the loss of BC to the walls of the container.

Laboratory experiments were conducted to measure the amplification of photo-absorption of BC coated by organics using an SP2 and the photoacoustic technique. The measured amplification was consistent with the prediction of Mie theory.

The dependence of CCN activity of BC on the mass of condensed compounds (Δm) on BC was measured in Tokyo. A volatility tandem aerosol particle analyzer was used to measure Δm. CCN activity was observed to increase with the increase in Δm.

Measurements of the mixing states of ambient BC in a remote area downstream of large BC sources showed a systematic increase in the coating thickness of BC particles with chemical aging. The chemical composition of the coating materials was estimated by simultaneous measurements of the compositions of inorganic and organic aerosols.

Large-scale transport efficiency (TE) of BC from the Asian continent to the western Pacific was studied by aircraft observations (A-FORCE) made in spring 2009. The TE of BC decreased from the PBL to the FT due to wet removal during upward transport. TE was shown to decrease with an increase in accumulated precipitation along the trajectory (APT).

Size distributions of BC measured during A-FORCE showed that the average single-particle BC mass decreased with decreasing transport efficiency. This suggests that aerosols containing a larger BC mass were removed more efficiently, which is qualitatively consistent with Köhler theory. It was shown that wet removal during upward transport is important in controlling the size distribution of BC in the FT.

A size and BC mixing-state-resolved model (MS-resolved WRF-chem model) was developed based on the WRF-chem model. Detailed aerosol microphysical processes, such as condensation/evaporation and coagulation, are simulated with these 12 × 10 aerosol bins. The mass concentrations of sulfate, nitrate, ammonium, BC, organic aerosol, dust, sea salt (sodium and chloride), and aerosol water and number

doi:10.5047/meep.2015.00301.0001

concentrations were explicitly calculated for individual size and mixing state bins in this model. Model simulations generally reproduced the features of the BC mixing state observed during A-FORCE, such as the temporal variations and size dependencies of the parameters representing the mixing state of BC.

Long-term surface BC and CO measurements were made using COSMOS and an NDIR instrument at Hedo, downstream of the Asian continent. BC and CO concentrations showed distinct seasonal variations, reaching their maximum values in winter and spring due to frequent transport of continental air associated with the winter monsoon. The TE of BC from China was estimated to be about 70%. The same data were used to validate the rate of BC emissions from China. The total BC emission rate from China was estimated to within an uncertainty of about 40%.

Long-term measurements of BC were made also at Happo at 1.8 km altitude. About 40% of the sampled air was of FT origin and 10% from North China (NC). The BC reached minimum values in winter, partly due to the suppressed upward transport of BC over the Asian continent. Wet deposition of BC by snowfall can also contribute to the winter minimum of BC.

We measured M_{BC} and C_{BC} simultaneously at Hedo for three years. The monthly M_{BC} and C_{BC} values showed marked seasonal variations being the highest in spring. The observed wet deposition flux of BC at Hedo was close to the net emission flux of BC in NC, indicating the importance of precipitation along the Bai-u frontal system as an efficient removal mechanism for BC transported from NC.

The observed BC in 3-D fields is controlled by all the processes involved: namely, emission, aging, vertical and horizontal transport, and deposition. A regional scale model (CMAQ-PSCAL) precisely representing these processes was developed. The model-calculated values of M_{BC} reproduced well those obtained by the ground-based and aircraft observations quite well. The results of the model calculations were used to identify source regions and types (anthropogenic or biomass burning) of the Asian BC outflow to the Pacific. An improved understanding was obtained of the processes and efficiency of the BC transport from each source region and type.

A detailed analysis was made to elucidate the mechanisms of transport of BC from the Asian continent. One pathway is PBL outflow in the midlatitude region through which BC from northern China was advected by the low-level westerlies. A second pathway is through uplifting from the PBL to the FT by migratory cyclones over northern China. The third pathway is orographic uplifting and/or convective upward transport from the PBL to the FT over inland-southern China.

BC measurements on board the NASA DC-8 were conducted in the Arctic in spring and summer in 2008 during ARCTAS. Emissions of BC and other aerosols from biomass burning (BB) were characterized as the ratios to the emission of CO and CO_2. BC particles from BB were observed to be thickly coated soon after emission. The contributions of BC from the combustion of biomass and fossil fuel in different regions were estimated using the tracer data and trajectories. BB in Russia is a major BC source in the Arctic, especially in spring. The long-range transport of BC mass concentrations was much lower in summer than in spring because of the higher precipitation and, thus, more efficient wet deposition in summer.

The average levels and temporal variations of BC mass concentrations in large cities in Asia (Tokyo, Beijing, Guangzhou, and Bangkok) were measured. The diurnal variations of BC emissions and dynamical processes in the PBL were the major drivers of the diurnal variation of BC at the surface. In Tokyo, BC mass concentrations decreased by a factor of 4 from 2003 to 2011, due to stringent regulations of particle emission from vehicles. As a result, BC concentrations in Tokyo were the lowest of the 4 cities compared.

AAOD values measured by a sky radiometer at Fukue were compared with those estimated by in situ aircraft measurements of the vertical profiles BC and non-BC particles. Although the two AAODs were generally correlated, the values derived from the radiometer were about half those estimated by the in situ data. This comparison strongly indicates the necessity of assessing the accuracy of AAOD of BC derived from ground-based radiometers.

The MS-resolved WRF-chem model was used to calculate the optical properties of aerosols. It was shown that the treatment of the BC mixing state has a large impact on the optical properties of aerosols and the radiative effects of aerosols. The model, with further improvements, will be very useful in improving the estimates of BC DRF.

21.2 Perspectives

An improved understanding of the role of BC in climate forcing is becoming increasingly important because of the potential effects of reducing emissions of short-lived climate pollutants (SLCPs) on mitigating near-term climate change (e.g., Shindell *et al*., 2011, 2012; Shoemaker *et al*., 2013). Tighter controls of vehicle emissions, especially BC, are estimated to lead to substantial cooling at northern mid and high latitudes (Shindell *et al*., 2011). However, it is likely that these estimates are associated with large uncertainties, as assessed by Bond *et al*. (2013). Reliable estimates of the direct and indirect effects of BC are critically important in the discussions and decision making processes for the reduction of BC emissions.

We have shown the results of our studies aimed at improving the estimates of BC DRF. Continued efforts based on the methodologies thus far used will result in further advances of the understanding of the effects of BC on climate. At this stage, it will be useful to list some of the unresolved issues that await further investigations in the near future.

We need to understand the causes of the discrepancy of the observed and model-calculated AAOD. Optical closure studies, especially for the absorption of aerosols, will contribute to a clarification of this issue. Namely, it is necessary to assess the consistency of directly measured absorption coefficients and those estimated from in situ measurements. However, careful preparations for experiments and theory are required to conduct this study in a meaningful way. We need to obtain means to better characterize the microphysical prop-

doi:10.5047/meep.2015.00301.0001

erties of BC by new instrumentation and theoretical frameworks.

Measurements of the hygroscopicity of BC are still limited, although there have been some studies in addition to ours. The hygroscopicity of BC influences light absorption which is related to the problem of AAOD. Hygroscopicity (or CCN activity) is also closely related to the wet deposition of BC. There are still substantial problems in the current measurement techniques to measure the hygroscopicity of BC in a satisfactory way. For example, the system used by Kuwata *et al*. (2009) is not optimized for field measurements because of the rather poor time resolution and difficulties in operating it at different locations. New systems using the SP2 have been in use for field measurements (McMeeking *et al*., 2011; Liu *et al*., 2013a). Further improvements of such systems will provide data for more detailed investigations of the hygroscopicity of BC.

Wet deposition plays a critical role in determining the distribution of BC. However, the wet deposition of BC is caused by a combination of a number of chemical and physical processes associated with cloud formation followed by precipitation and therefore is complex. One of the ways to constrain the overall effect of deposition is to characterize the wet deposition flux of BC by long-term ground-based observations at different locations downstream of the Asian continent and in other regions of the globe. It is desirable to make further improvements of the measurement technique, especially the size distributions of BC in water.

The detailed MS-resolved model discussed above has a great potential to reduce the uncertainties in the estimation of BC absorption and radiative effects, because BC aging and optical/radiative processes are calculated explicitly without parameterization. Using this detailed aerosol model, after having been fully validated, we can evaluate the complicated and nonlinear climatic responses of BC processes to changes in the meteorological conditions and the emissions of chemical species. This model can also be used as a benchmark model of global/climate aerosol models to understand the uncertainties in the simpler representation of BC processes in these models. We will then be able to construct climate models that incorporate important BC processes with realistic representations.

Our efforts on the indirect effects of BC have been very limited. It will be important to improve our understanding of the role of BC as ice nuclei (IN), especially for mixed phase clouds at northern high latitudes. New measurement techniques and modeling efforts are greatly needed for these studies.

Acknowledgments. I would like to thank all my colleagues who made important contributions to achieving the results described in this monograph. They are Makoto Koike, Nobuyuki Takegawa, Nobuhiro Moteki, Hitoshi Matsui, Yuzo Miyazaki, Naga Oshima, Kazuyuki Kita, Mikinori Kuwata, Manabu Shiraiwa, Mizuo Kajino, Yongjing Zhao, Lokesh Sahu, Akinori Takami, Sho Ohata, Tatsuhiro Mori, Hideaki Hashioka, Takuma Miyakawa, Irwin Martin, Ramlal L. Verma, Kirpa Ram, Sunghee Han, Xianyun Liu, Yugo Kanaya, Shuji Kawakami, and Tomoki Nakayama. There are a number of other colleagues, who made significant contributions to the achievements. Their dedicated efforts in all the phases of the studies culminated in these achievements.

I especially thank David W. Fahey, Ru-shan Gao, and Joshua Schwarz for their encouragements and collaboration in carrying out our BC studies. I thank Tami Bond for stimulating discussions during the preparations of "Bounding the role of black carbon aerosol in the climate system: A scientific assessment", which have been very encouraging and useful for our continued efforts.

I would like to thank Professor Atsuhiro Nishida, one of the chief editors of the Monographs on Environment, Earth and Planets (MEEP), for providing me a great opportunity to publish our BC studies in the form of the Monograph. He also made thorough comments by deeply reading the manuscript. I also thank David Fahey and Steven J. Ghan for making very constructive comments on the manuscript, which have been useful in greatly improving it.

Greg Kok of Droplet Measurement Technologies Inc. and Minoru Kano of Kanomax Inc. have been cooperative in developing and improving the SP2 and COSMOS instruments, respectively. We are indebted to the flight and ground crews of the King Air aircraft of the Diamond Air Service Inc. for the aircraft operation during A-FORCE. The ARCTAS mission was supported by NASA. We are indebted to all the ARCTAS participants for their cooperation and support. I deeply thank all the people who maintained ground-based BC measurements at Happo, Hedo, and Fukue.

This study was supported by the Ministry of Education, Culture, Sports, Science, and Technology (MEXT) in Japan, the GRENE Arctic Climate Change Research Project, the strategic international cooperative program of the Japan Science and Technology Agency (JST), and the global environment research fund of the Japanese Ministry of the Environment (A-1101 and 2-1403).

References

Abdul-Razzak, H., and S. J. Ghan (2000), A parameterization of aerosol activation: 2. Multiple aerosol types, *J. Geophys. Res.*, *105*, 6837–6844.

Ackerman, T. P., and O. B. Toon (1981), Absorption of visible radiation in atmosphere containing mixtures of absorbing and nonabsorbing particles, *Appl. Opt.*, *20*, 3661–3667, doi:10.1364/AO.20.003661.

Adler, R. F. *et al*. (2003), The Version 2 Global Precipitation Climatology Project (GPCP) monthly precipitation analysis (1979-Present), *J. Hydrometeor.*, *4*, 1147–1167.

Alessandrini, F., H. Schulz, S. Takenaka, B. Lentner, E. Karg, H. Behrendt, and T. Jakob (2006), Effects of ultrafine carbon particle inhalation on allergic inflammation of the lung, *J. Allergy. Clin. Immuno.*, *117*, 824–830.

Andreae, M. O., and P. Merlet (2001), Emission of trace gases and aerosols from biomass burning, *Global Biogeochem. Cycles*, *15*, 955–966, doi:10.1029/2000GB001382.

Aquila, V. *et al*. (2011), MADE-in: a new aerosol microphysics submodel for global simulation of insoluble particles and their mixing state, *Geosci. Model Dev.*, *4*, 325–355.

Armalis, S (1999), Wet deposition of elemental carbon in Lithuania, *Sci. Total. Environ.*, *239*, 89–93.

Arnott, W. P., H. Moosmuller, P. J. Sheridan, J. A. Ogren, R. Raspet, W. V. Slaton, J. L. Hand, S. M. Kreidenweis, and J. L. Collett (2003), Photoacoustic and filter-based ambient aerosol light absorption measurements: Instrument comparisons and the role of relative humidity, *J. Geophys. Res.*, *108*, 4034, doi:10.1029/2002jd002165.

Arnott, W. P., K. Hamasha, H. Moosmuller, P. J. Sheridan, and J. A. Ogren (2005), Towards aerosol light-absorption measurements with a 7-wavelength aethalometer: Evaluation with a photoacoustic instrument and 3-wavelength nephelometer, *Aerosol Sci. Technol.*, *39*, 17–29.

Arnott, W. P., J. W. Walker, H. Moosmuler, R. A. Elleman, H. H. Jonsson, G. Buzorius, W. C. Conant, R. C. Flagan, and J. H. Seinfeld (2006), Photoacoustic insight for aerosol light absorption aloft from meteorological aircraft and comparison with particle soot absorption photometer measurements: DOE Southern Great Plains climate research facility and the coastal stratocumulus imposed perturbation experiments, *J. Geophys. Res.*, *111*, D05S02, doi:10.1029/2005JD005964.

Barrie, L. A. (1986), Arctic air pollution: An overview of current knowledge, *Atmos. Environ.*, *20*, 643–663.

Bauer, S. E., D. L. Wright, D. Koch, E. R. Lewis, R. McGraw, L.-S. Chang,

S. E. Schwartz, and R. Ruedy (2008), MATRIX (Multiconfigulation Aerosol TRacker of mIXing state): and aerosol microphysical module for global atmospheric models, *Atmos. Chem. Phys.*, *8*, 6003–6035.

Bauer, S. E., A. Ault, and K.A. Prather (2013) Evaluation of aerosol mixing state classes in the GISS-modelE-MATRIX climate model using single particle mass spectrometry measurements, *J. Geophys. Res.*, *118*, 9834–9844, doi:10.1002/jgrd.50700.

Baumgardner, D., G. Kok, and G. Raga (2004), Warming of the Arctic lower stratosphere by light absorbing particles, *Geophys. Res. Lett.*, *31*, L06117, doi:10.1029/2003GL018883.

Baumgardner, D. *et al.* (2012), Soot reference materials for instrument calibration and intercomparisons: A workshop summary with recommendations, *Atmos. Meas. Tech.*, *5*, 1869–1887.

Blake, N. J. *et al.* (2003), NMHCs and halocarbons in Asian continental outflow during the Transport and Chemical Evolution over the Pacific (TRACE-P) Field Campaign: Comparison With PEM-West B, *J. Geophys. Res.*, *108*, 8806, doi:10.1029/2002JD003367.

Bohren, C. F., and D. R. Huffman (1983), *Absorption and Scattering of Light by Small Particles*, John Wiley & Sons, New York.

Bond, T. C., and R. W. Bergstrom (2006), Light absorption by carbonaceous particles: An investigative review, *Aerosol Sci. Technol.*, *40*, 27–67.

Bond, T. C., T. L. Anderson, and D. Campbell (1999), Calibration and intercomparison of filter-based measurements of visible light absorption by aerosols, *Aerosol Sci. Technol.*, *30*, 582–600.

Bond, T. C., D. G. Streets, K. F. Yarber, S. M. Nelson, J.-H. Woo, and Z. Klimont (2004), A technology-based global inventory of black and organic carbon emissions from combustion, *J. Geophys. Res.*, *109*, D14203, doi:10.1029/2003JD003697.

Bond, T. C., G. Habib, and R. W. Bergstrom (2006), Limitations in the enhancement of visible light absorption due to mixing state, *J. Geophys. Res.*, *111*, D20211, doi:10.1029/2006jd007315.

Bond, T. C., S. J. Doherty, D. W. Fahey, P. M. Forster, T. Berntsen, O. Boucher, B. J. DeAngelo, M. G. Flanner, S. Ghan, B. Kärcher, D. Koch, S. Kinne, Y. Kondo, P. K. Quinn, M. C. Sarofim, M. G. Schulz, M. Schulz, C. Venkataraman, H. Zhang, S. Zhang, N. Bellouin, S. Guttikunda, P. K. Hopke, M. J. Jacobson, J. Kaiser, Z. Klimont, U. Lohmann, J. P. Schwarz, D. Shindell, T. Storelvmo, S. G. Warren, and C. S. Zender (2013), Bounding the role of black carbon aerosol in the climate system: A scientific assessment, *J. Geophys. Res.*, *118*, doi:10.1002/jgrd.50171.

Bourgeois, Q., and I. Bey (2011), Pollution transport efficiency toward the Arctic: Sensitivity to aerosol scavenging and source regions, *J. Geophys. Res.*, *116*, D08213, doi:10.1029/2010JD015096.

Brock, C. A. *et al.* (2011), Characteristics, sources, and transport of aerosols measured in spring 2008 during the aerosol, radiation, and cloud processes affecting Arctic Climate (ARCPAC) Project, *Atmos. Chem. Phys.*, *11*, 2423–2453, doi:10.5194/acp-11-2423-2011.

Bueno, P. A., D. K. Havey, G. W. Mulholland, J. T. Hodges, K. A. Gillis, R. R. Dickerson, and M. R. Zachariah (2011), Photoacoustic measurements of amplification of the absorption cross section for coated soot aerosols, *Aerosol Sci. Technol.*, *45*, 1217–1230, doi:10.1080/02786826.2011.587477.

Cai, Y., D. C. Montague, W. Mooiweer-Bryan, and T. Deshler (2008), Performance characteristics of the Ultra High Sensitivity Aerosol Spectrometer for particles between 55 and 800 nm: Laboratory and field studies, *J. Aerosol Sci.*, *39*, 759–769.

Cao, J. J., S. C. Lee, K. F. Ho, X. Y. Zhang, S. C. Zou, K. Fung, J. C. Chow, and J. G. Watson (2003), Characteristics of carbonaceous aerosol in Pearl River Delta Region, China during 2001 winter period, *Atmos. Environ.*, *37*, 1451–1460.

Cappa, C. D., D. A. Lack, J. B. Burkholder, and A. R. Ravishankara (2008), Bias in filter-based aerosol light absorption measurements due to organic aerosol loading: Evidence from laboratory measurements, *Aerosol Sci. Technol.*, *42*, 1022–1032.

Cappa, C. D. *et al.* (2012), Radiative absorption enhancements due to the mixing state of atmospheric black carbon, *Science*, *337*, 1078–1081, doi:10.1126/science.1223447.

Carmichael, G. R. *et al.* (2003), Evaluating regional emission estimates using the TRACE-P observations, *J. Geophys. Res.*, *108*, 8810, doi:10.1029/2002JD003116.

Cerqueira, M., C. Pio, M. Legrand, H. Puxbaum, A. Kasper-Giebl, J. Afonso, S. Preunkert, A. Gelencsér, and P. Fialho (2010), Particulate carbon in precipitation at European background sites, *J. Aerosol Sci.*, *41*, 51–61.

Chapman, E. G., W. I. Gustafson Jr., R. C. Easter, J. C. Bernard, S. J. Ghan, M. S. Pekour, and J. D. Fast (2009), Coupling aerosol-cloud-radiative processes in the WRF-Chem model: Investigating the radiative impact of elevated point sources, *Atmos. Chem. Phys.*, *9*, 945–964.

Charalampopoulos, T. T., H. Chang, and B. Stagg (1989), The effects of temperature and composition on complex refractive index of flame soot, *Fuel*, *68*, 1173–1179.

Chen, L.-W. A., B. G. Doddridge, R. R. Dickerson, J. C. Chow, P. K. Mueller, J. Quinn, and W. A. Butler (2001), Seasonal variations in elemental carbon aerosol, carbon monoxide and sulfur dioxide: Implications for sources, *Geophys. Res. Lett.*, *28*, 1711–1714.

Chen, M., R. Talbot, H. Mao, B. Sive, J. Chen, and R. J. Griffin (2007), Air mass classification in coastal New England and its relationship to meteorological conditions, *J. Geophys. Res.*, *112*, D10S05, doi:10.1029/2006JD007687.

Chen, Y., C. Zhao, Q. Zhang, Z. Deng, M. Huang, and X. Ma (2009), Aircraft study of Mountain Chimney Effect of Beijing, China, *J. Geophys. Res.*, *114*, D08306, doi:10.1029/2008JD010610.

Christopher, S. A., D. V. Kliche, J. Chou, and R. M. Welch (1996), First estimates of the radiative forcing of aerosols generated from biomass burning using satellite data, *J. Geophys. Res.*, *101*, 21265–21273.

Chung, C. E., V. Ramanathan, and D. Decremer (2012), Observationally constrained estimates of carbonaceous aerosol radiative forcing, *Proc. Natl. Acad. Sci.*, *109*, 11624–11629.

Chylek, P., V. Ramaswamy, A. Ashkin, and J. M. Dziedzic (1983), Simultaneous determination of refractive index and size of spherical dielectric particles from light scattering data, *Appl. Opt.*, *22*, 2302–2307.

Clarke, A. D., and K. J. Noone (1985), Soot in the Arctic snowpack: A cause for perturbations in radiative transfer, *Atmos. Environ.*, *19*, 2045–2053.

Clarke, A. D. *et al.* (2004), Size distribution and mixtures of dust and black carbon aerosol in Asian outflow: Physicochemistry and optical properties, *J. Geophys. Res.*, *109*, D15S09, doi:10.1029/2003JD004378.

Colman, J. J. *et al.* (2001), Description of the analysis of a wide range of volatile organic compounds in whole air samples collected during PEM-Tropics A and B, *Anal. Chem.*, *73*, 3723–3731.

Conrad, S. G., A. I. Sukhinin, B. J. Stocks, D. R. Cahoon, E. P. Davidenko, and G. A. Ivanova (2002), Determining effects of area burned and fire severity on carbon cycling and emissions in Siberia, *Climatic Change*, *55*, 197–211.

Cooke, W. F., V. Ramaswamy, and P. Kasibhatla (2002), A general circulation model study of the global carbonaceous aerosol distribution, *J. Geophys. Res.*, *107*, 4279, doi:10.1029/2001JD001274.

Corrigan, C. E., G. C. Roberts, M. V. Ramana, D. Kim, and V. Ramanathan (2008), Capturing vertical profiles of aerosols and black carbon over the Indian Ocean using autonomous unmanned aerial vehicles, *Atmos. Chem. Phys.*, *8*, 737–747.

Cross, E. S. *et al.* (2010), Soot particle studies-Instrument inter-comparison-Project overview, *Aerosol Sci. Technol.*, *44*, 592–611.

Dahlkötter, F., M. Gysel, D. Sauer, A. Minikin, R. Baumann, P. Seifert, A. Ansmann, M. Fromm, C. Voigt, and B. Weinzierl (2013), The Pegami Creek smoke plume after long-range transport to the upper troposphere over Europe-aerosol properties and black carbon mixing state, *Atmos. Chem. Phys.*, *13*, 28751–28818.

DeCarlo, P., J. G. Slowik, D. R. Worsnop, P. Davidvits, and J. L. Jimenez (2004), Particle morphology and density characterization by combined mobility and aerodynamic diameter measurements. Part 1: Theory, *Aerosol Sci. Technol.*, *38*, 1185–1205.

DeCarlo, P. F., J. R. Kimmel, A. Trimborn, M. J. Northway, J. T. Jayne, A. C. Aiken, M. Gonin, K. Fuhrer, T. Horvath, K. Docherty, D. R. Worsnop, and J. L. Jimenez (2006), Field-deployable, high-resolution, time-of-flight aerosol mass spectrometer, *Anal. Chem.*, *78*, 8281–8289.

Delmas, R., J. P. Lacaux, and D. Brocard (1995), Determination of biomass burning emission factors: Method and results, *Environ. Monit. Assess.*, *38*, 181–204.

DeMott, P. J., A. J. Prenni, X. Liu, S. M. Kreidenweis, M. D. Petters, C. H. Twohy, M. S. Richardson, T. Eidhammer, and D. C. Rogers (2010), Predicting global atmospheric ice nuclei distributions and their impacts on climate, *Proc. Natl. Acad. Sci.*, *107*, 11217–11222.

Dinar, E., A. Abo Riziq, C. Spindler, C. Erlick, G. Kissc, and Y. Rudich (2008), The complex refractive index of atmospheric and model humic-like substances (HULIS) retrieved by a cavity ring down aerosol spectrometer (CRD-AS), *Faraday Discuss.*, *137*, 279–295.

Ding, A. *et al.* (2009), Transport of north China air pollution by midlati-

doi:10.5047/meep.2015.00301.0001

tude cyclones: Case study of aircraft measurements in summer 2007, *J. Geophys. Res.*, *114*, D08304, doi:10.1029/2008JD011023.

Doherty, S. J., S. G. Warren, T. C. Grenfell, A. D. Clarke, and R. E. Brandt (2010), Light-absorbing impurities in Arctic snow, *Atmos. Chem. Phys.*, *10*, 11647–11680, doi:10.5194/acp-10-11647-2010.

Dubovik, O., A. Smirnov, B. Holben, M. D. King, Y. J. Kaufman, T. F. Eck, and I. Slutsker (2000), Accuracy assessment of aerosol optical properties retrieval from Aerosol Robotic Network (AERONET) Sun and sky radiance measurements, *J. Geophys. Res.*, *105*, 9791–9806.

Dubovik, O., B. Holben, T. F. Eck, A. Smirnov, Y. J. Kaufman, M. D. King, D. Tanré, and I. Slutsker (2002), Variability of absorption and optical properties of key aerosol types observed in worldwide locations, *J. Atmos. Sci.*, *59*, 590–608.

Ducret, J., and H. Cachier (1992), Particulate carbon in rain at various temperate and tropical locations, *J. Atmos. Chem.*, *15*, 55–67.

Dunlea, E. J., P. F. DeCarlo, A. C. Aiken, J. R. Kimmel, R. E. Peltier, R. J. Weber, J. Tomlison, D. R. Collins, Y. Shinozuka, C. S. McNaughton, S. G. Howell, A. D. Clarke, L. K. Emmons, E. C. Apel, G. G. Pfister, A. van Donkelaar, R. V. Martin, D. B. Millet, C. L. Heald, and J. L. Jimenez (2009), Evolution of Asian aerosols during transpacific transport in INTEX-B, *Atmos. Chem. Phys.*, *9*, 7257–7287.

Dusek, U., G. P. Reischl, and R. Hitzenberger (2006), CCN activation of pure and coated carbon black particles, *Environ. Sci. Technol.*, *40*, 1223–1230.

Eck, T. F. *et al.* (2009), Optical properties of boreal region biomass burning aerosols in central Alaska and seasonal variation of aerosol optical depth at an Arctic coastal site, *J. Geophys. Res.*, *114*, D11201, doi:10.1029/2008JD010870.

Eleftheriadis, K., S. Vratolis, and S. Nyeki (2009), Aerosol black carbon in the European Arctic: Measurements at Zeppelin station, Ny-Ålesund, Svalbard from 1998-2007, *Geophys. Res. Lett.*, *36*, L02809, doi:10.1029/2008GL035741.

Esteve, A. R., J. A. Ogren, P. J. Sheridan, E. Andrews, B. N. Holben, and M. P. Utrillas (2012), Sources of discrepancy between aerosol optical depth obtained from AERONET and in-situ aircraft profiles, *Atmos. Chem. Phys.*, *12*, 2987–3003.

Fast, J. D., W. I. Gustafson Jr., R. C. Easter, R. A. Zaveri, J. C. Barnard, E. G. Chapman, G. A. Grell, and S. E. Peckham (2006), Evolution of ozone, particulates, and aerosol direct radiative forcing in the vicinity of Houston using a fully coupled meteorology-chemistry-aerosol model, *J. Geophys. Res.*, *111*, D21305, doi:10.1029/2005JD006721.

Flanner, M. G., C. S. Zender, J. T. Randerson, and P. J. Rasch (2007), Present-day climate forcing and response from black carbon in snow, *J. Geophys. Res.*, *112*, D11202, doi:10.1029/2006JD008003.

Flanner, M. G., C. S. Zender, P. G. Hess, N. M. Mahowald, T. H. Painter, V. Ramanathan, and P. J. Rasch (2009), Springtime warming and reduced snow cover from carbonaceous particles, *Atmos. Chem. Phys.*, *9*, 2481–2497.

Flossmann, A. I., W. D. Hall, and H. R. Pruppacher (1985), A theoretical study of the wet removal of atmospheric pollutants. Part I: The redistribution of aerosol particles captured through nucleation and impaction scavenging by growing cloud drops, *J. Atmos. Sci.*, *42*, 583–606.

Flossmann, A. I., H. R. Pruppacher, and J. H. Topalian (1987), A theoretical study of the wet removal of atmospheric pollutants. Part II: The uptake and redistribution of $(NH_4)_2SO_4$ particles and SO_2 gas simultaneously scavenged by growing cloud drops, *J. Atmos. Sci.*, *44*, 2912–2923.

Folkins, I., R. Chatfield, D. Baumgardner, and M. Proffitt (1997), Biomass burning and deep convection in southeastern Asia: Results from ASHOE/MAESA, *J. Geophys. Res.*, *102*, 13291–13299.

Fuelberg, H. E., D. L. Harrigan, and W. Sessions (2010), A meteorological overview of the ARCTAS 2008 mission, *Atmos. Chem. Phys.*, *10*, 817–842.

Gangl, M., M. Kocifaj, G. Videen, and H. Horvath (2008), Light absorption by coated nano-sized carbonaceous particles, *Atmos. Environ.*, *42*, 2571–2581.

Gao, R. S., J. P. Schwarz, K. K. Kelly, D. W. Fahey, L. A. Watts, T. L. Thompson, J. R. Spackman, J. G. Slowik, E. S. Cross, J.-H. Han, P. Davidovits, T. B. Onasch, and D. R. Worsnop (2007), A novel method for estimating light-scattering properties of soot aerosols using a modified single-particle soot photometer, *Aerosol Sci. Technol.*, *41*, 125–135.

Garrett, T. J., and C. Zhao (2006), Increased Arctic cloud longwave emissivity associated with pollution from mid-latitudes, *Nature*, *440*, 787–789.

Gelencsér, A., B. May, D. Simpson, A. Sánchez-Ochoa, A. Kasper-Giebl, H. Puxbaum, A. Caseiro, C. Pio, and M. Legrand (2007), Source apportionment of PM2.5 organic aerosol over Europe: Primary/secondary, natural/anthropogenic, and fossil/biogenic origin, *J. Geophys. Res.*, *112*, D23S04, doi:10.1029/2006JD008094.

Ghan, S., R. Easter, J. Hudson, and F. Bréon (2001), Evaluation of aerosol indirect radiative forcing in MIRAGE, *J. Geophys. Res.*, *106*, 5317–5334.

Ghazi, R., and S. Olfert (2013), Coating mass dependence of soot aggregate restructuring due to coatings of oleic acid and dioctyl sebacate, *Aerosol Sci. Technol.*, *47*, 192–200.

Gong, S. L., T. L. Zhao, S. Sharma, D. Toom-Sauntry, D. Lavoué, X. B. Zhang, W. R. Leaitch, and L. A. Barrie (2010), Identification of trends and interannual variability of sulfate and black carbon in the Canadian High Arctic: 1981–2007, *J. Geophys. Res.*, *115*, D07305, doi:10.1029/2009JD012943.

Goode, J. G., R. J. Yokelson, D. E. Ward, R. A. Susott, R. E. Babbitt, M. A. Davies, and W. M. Hao (2000), Measurements of excess O_3, CO_2, CO, CH_4, C_2H_4, C_2H_2, HCN, NO, NH_3, HCOOH, CH_3COOH, HCHO, and CH_3OH in 1997 Alaskan biomass burning plumes by airborne Fourier transform infrared spectroscopy (AFTIR), *J. Geophys. Res.*, *105*, 22147–22166.

Granfell, T. C., S. J. Doherty, A. D. Clarke, and S. G. Warren (2011), Light absorption from particulate impurities in snow and ice determined by spectrophotometric analysis of filters, *Appl. Opt.*, *50*, 2037–2048.

Grell, G. A., S. E. Peckham, R. Schmitz, S. A. McKeen, G. Frost, W. C. Skamarock, and B. Eder (2005), Fully coupled "online" chemistry within the WRF model, *Atmos. Environ.*, *39*, 6957–6975.

Guinot, B., H. Cachier, J. Sciare, Y. Tong, W. Xin, and Y. Jianhua (2007), Beijing aerosol: Atmospheric interactions and new trends, *J. Geophys. Res.*, *112*, D14314, doi:10.1029/2006JD008195.

Gustafson, W. I., Jr., E. G. Chapman, S. J. Ghan, R. C. Easter, and J. D. Fast (2007), Impact on modeled cloud characteristics due to simplified treatment of uniform cloud condensation nuclei during NEAQS 2004, *Geophys. Res. Lett.*, *34*, L19809, doi:10.1029/2007GL030021.

Gysel, M., M. Laborde, J. S. Olfert, R. Subramanian, and A. J. Gröhn (2011), Effective density of Aquadag and fullerene soot black carbon reference materials used for SP2 calibration, *Atmos. Meas. Tech.*, *4*, 2851–2858.

Hadley, O. L., V. Ramanathan, G. R. Carmichael, Y. Tang, C. E. Corrigan, G. C. Roberts, and G. S. Mauger (2007), Trans-Pacific transport of black carbon and fine aerosols (D $< 2.5\ \mu$m) into North America, *J. Geophys. Res.*, *112*, D05309, doi:10.1029/2006JD007632.

Hadley, O. L., C. E. Corrigan, and T.W. Kirchstetter (2008), Modified thermal-optical analysis using spectral absorption selectivity to distinguish black carbon from pyrolized organic carbon, *Environ. Sci. Technol.*, *42*, 8459–8464.

Hadley, O. L., C. E. Corrigan, T. W. Kirchstetter, S. S. Cliff, and V. Ramanathan (2010), Measured black carbon deposition on the Sierra Nevada snow pack and implication for snow pack retreat, *Atmos. Chem. Phys.*, *10*, 7505–7513.

Hakami, A., D. K. Henze, J. H. Seinfeld, T. Chai, Y. Tang, G. R. Carmichael, and A. Sandu (2005), Adjoint inverse modeling of black carbon during the Asian Pacific Regional Aerosol Characterization Experiment, *J. Geophys. Res.*, *110*, D14301, doi:10.1029/2004JD005671.

Han, S., Y. Kondo, N. Oshima, N. Takegawa, Y. Miyazaki, M. Hu, P. Lin, Z. Deng, Y. Zhao, N. Sugimoto, and Y. Wu (2009), Temporal variations of elemental carbon in Beijing, *J. Geophys. Res.*, *114*, D23202, doi:10.1029/2009jd012027.

Hansen, J., and L. Nazarenko (2004), Soot climate forcing via snow and ice albedos, *Proc. Natl. Acad. Sci.*, *101*, 423–428, doi:10.1073/pnas.2237157100.

Hansen, J. E., and M. Sato (2001), Trends of measured climate forcing agents, *Proc. Natl. Acad. Sci.*, *98*, 14778–14783.

Hansen, J. *et al.* (2005), Efficacy of climate forcings, *J. Geophys. Res.*, *110*, D18104, doi:10.1029/2005JD005776.

Hashimoto, M., T. Nakajima, O. Dubovik, M. Campanelli, H. Che, P. Khatri, T. Takamura, and G. Pandithurai (2012), Development of a new data-processing method for SKYNET sky radiometer observations, *Atmos. Meas. Tech.*, *5*, 2723–2737.

Hatakeyama, S., K. Murano, F. Sakamaki, H. Mukai, H. Bandow, and Y. Komazaki (2001), Transport of atmospheric pollutants from East Asia, *Water Air Soil Poll.*, *130*, 373–378.

Hatakeyama, S., A. Takami, F. Sakamaki, H. Mukai, N. Sugimoto, A. Shimizu, and H. Bandow (2004), Aerial measurement of air pollutants

doi:10.5047/meep.2015.00301.0001

and aerosols during 20–22 March 2001 over the East China Sea., *J. Geophys. Res.*, *109*, D13304, doi:10.1029/2003JD004271.

Hegg, D. A., and P. V. Hobbs (1982), Measurements of sulfate production in natural clouds, *Atmos. Environ.*, *16*, 2663–2668.

Hinds, W. C. (1999), *Aerosol Technoogy*, John Wiley & Sons, New York.

Huang, L., S. L. Gong, S. Sharma, D. Lavoué, and C. Q. Jia (2010), A trajectory analysis of atmospheric transport of black carbon aerosols to Canadian high Arctic in winter and spring (1990–2005), *Atmos. Chem. Phys.*, *10*, 5065–5073.

Huebert, B., and R. J. Charlson (2000), Uncertainties in data on organic aerosols, *Tellus*, *52B*, 1249–1255.

Huebert, B. J., T. Bates, P. B. Russell, G. Shi, Y. J. Kim, K. Kawamura, G. Carmichael, and T. Nakajima (2003), An overview of ACE-Asia: Strategies for quantifying the relationships between Asian aerosols and their climatic impacts, *J. Geophys. Res.*, *108*, 8633, doi:10.1029/2003JD003550.

Huffman, G. J., R. F. Adler, M. M. Morrissey, D. T. Bolvin, S. Curtis, R. Joyce, B. McGavock, and J. Susskind (2001), Global precipitation at one-degree daily resolution from multisatellite observations, *J. Hydrometeor.*, *2*, 36–50.

IPCC (2013), Climate Change 2013: The Physical Science Basis. Contribution of Working Group I to the Fifth Assessment Report of the Intergovernmental Panel on Climate Change, edited by Stocker, T.F., Qin, D, Plattner, G.-K., Tignor, M., Allen, S. K., Boschung, J., Nauels, A., Xia, Y., Bex, V., and Midgley, P. M., Cambridge University Press, Cambridge, United Kingdom and New York, NY, USA.

Irwin, M., Y. Kondo, N. Moteki, and T. Miyakawa (2013), Evaluation of a heated-inlet for calibration of the SP2, *Aerosol Sci. Technol.*, *47*, 895–905.

Irwin, M., Y. Kondo, and N. Moteki (2015), An empirical correction factor for filter-based photo-absorption black carbon measurements, *J. Aerosol Sci.*, *80*, 86–97.

Jacob, D. J., J. H. Crawford, M. M. Kleb, V. S. Connors, R. J. Bendura, J. L. Raper, G. W. Sachse, J. C. Gille, L. Emmons, and C. L. Heald (2003), Transport and Chemical Evolution over the Pacific (TRACE-P) aircraft mission: Design, execution, and first results, *J. Geophys. Res.*, *108*, 9000, doi:10.1029/2002JD003276.

Jacob, D. J. *et al.* (2010), The Arctic Research of the Composition of the Troposphere from Aircraft and Satellites (ARCTAS) mission: Design, execution, and first results, *Atmos. Chem. Phys.*, *10*, 5191–5212.

Jacobson, M. Z. (1997), Development and application of a new air pollution modeling system—II, Aerosol module structure and design, *Atmos. Environ.*, *31*, 131–144.

Jacobson, M. Z. (2000), A physically-based treatment of elemental carbon optics: Implications for global direct forcing of aerosols, *Geophys. Res. Lett.*, *27*(2), 217–220, doi:10.1029/1999GL010968.

Jacobson, M. Z. (2001), Strong radiative heating due to the mixing state of black carbon in atmospheric aerosols, *Nature*, *409*, 695–697.

Jacobson, M. Z. (2002a), Control of fossil-fuel particulate black carbon and organic matter, possibly the most effective method of slowing global warming, *J. Geophys. Res.*, *107*, 4410, doi:4410.1029/2001JD001376.

Jacobson, M. Z. (2002b), Analysis of aerosol interactions with numerical techniques for solving coagulation, nucleation, condensation, dissolution, and reversible chemistry among multiple size distributions, *J. Geophys. Res.*, *107*, 4366, doi:10.1029/2001JD002044.

Jacobson, M. Z. (2005), *Fundamentals of Atmospheric Modeling*, 2nd ed., Cambridge University Press, Cambridge.

Jacobson, M. Z. (2010), Short-term effects of controlling fossil-fuel soot, biofuel soot and gases, and methane on climate, Arctic ice, and air pollution health, *J. Geophys. Res.*, *115*, D14209, doi:10.1029/2009JD013795.

Jacobson, M. Z., R. P. Turco, E. J. Jensen, and O. B. Toon (1994), Modeling coagulation among particles of different composition and size, *Atmos. Environ.*, *28*, 1327–1338.

Jansen, K. L., T. V. Larson, J. Q. Koenig, T. F. Mar, C. Fields, J. Stewart, and M. Lippmann (2005), Associations between health effects and particulate matter and black carbon in subjects with respiratory disease, *Environ Health Perspect*, *113*, 1741–1746.

Janzen, J. (1979), The refractive index of carbon black, *J. Colloid Interface Sci.*, *69*, 436–447.

Japan Oil Chemist's Society (ed.) (2001), Lipid and surfactants, in *Handbook of Oil Chemistry (4th ed.)*, Maruzen, Tokyo, Japan.

Jayne, J. T. *et al.* (2000), Development of an aerosol mass spectrometer for size and composition analysis of submicron particles, *Aerosol Sci. Technol.*, *33*, 49–70.

Kajii, Y., K. Someno, H. Tanimoto, J. Hirokawa, and H. Akimoto (1998), Evidence for the seasonal variation of photochemical activity of tropospheric ozone: Continuous observation of ozone and CO at Happo, Japan, *Geophys. Res. Lett.*, *25*, 3505–3508.

Kajino, M., and Y. Kondo (2011), EMTACS: Development and regional-scale simulation of a size, chemical, mixing type, and soot shape resolved atmospheric particle model, *J. Geophys. Res.*, *116*, D02303, doi:10.1029/2010JD015030.

Kanaya, Y., F. Taketani, Y. Komazaki, X. Liu, Y. Kondo, L. K. Sahu, H. Irie, and H. Takashima (2013), Comparison of black carbon mass concentrations observed by Multi-Angle Absorption Photometer (MAAP) and Continuous Soot-Monitoring System (COSMOS) on Fukue Island and in Tokyo, Japan, *Aerosol Sci. Technol.*, *47*, 1–10.

Kannari, A. *et al.* (2004), Development of a grid database on atmospheric pollutants emissions in Japan, *J. Jpn. Soc. Atmos. Environ.*, *39*, 257–271 (in Japanese).

Kaspari, S. D., M. Schwikowsk, M. Gysel, M. G. Flanner, S. Kang, S. Hou, and P. A. Mayewski (2011), Recent increase in black carbon concentrations from a Mt. Everest ice core spanning 1860–2000 AD, *Geophys. Res. Lett.*, *38*, L04703, doi:10.1029/2010GL046096.

Kato, S., P. Pochanart, J. Hirokawa, Y. Kajii, H. Akimoto, Y. Ozaki, K. Obi, T. Katsuno, D. G. Streets, and N. P. Minko (2002), The influence of Siberian forest fires on carbon monoxide concentrations at Happo, Japan, *Atmos. Environ.*, *36*, 385–390, doi:10.1016/s1352-2310(01)00158-3.

Kato, S., Y. Kajii, R. Itokazu, J. Hirokawa, S. Koda, and Y. Kinjo (2004), Transport of atmospheric carbon monoxide, ozone, and hydrocarbons from Chinese coast to Okinawa island in the Western Pacific during winter, *Atmos. Envion.*, *38*, 2975–2981.

Khalizov, A. F., H. X. Xue, L. Wang, J. Zheng, and R. Y. Zhang (2009), Enhanced light absorption and scattering by carbon soot aerosol internally mixed with sulfuric acid, *J. Phys. Chem. A.*, *113*, 1066–1074, doi:10.1021/jp807531n.

Kim, D.-H., J. Sohn, T. Nakajima, and T. Takamura (2005), Aerosol radiative forcing over east Asia determined from ground-based solar radiation measurements, *J. Geophys. Res.*, *110*, D10S22, doi:10.1029/2004JD004678.

Kim, D., C. Wang, A. M. L. Ekman, M. C. Barth, and P. J. Rasch (2008), Distribution and direct radiative forcing of carbonaceous and sulfate aerosols in an interactive size-resolving aerosol-climate model, *J. Geophys. Res.*, *113*, D16309, doi:10.1029/2007JD009756.

Klonecki, A., P. Hess, L. Emmons, L. Smith, J. Orlando, and D. Blake (2003), Seasonal changes in the transport of pollutants into the Arctic troposphere-model study, *J. Geophys. Res.*, *108*, 8367, doi:10.1029/2002JD002199.

Knox, A., G. J. Evans, J. R. Brook, X. Yao, C. H. Jeong, K. J. Godri, K. Sabaliauskas, and J. G. Slowik (2009), Mass absorption cross-section of ambient black carbon aerosol in relation to chemical age, *Aerosol Sci. Technol.*, *43*, 522–532, doi:10.1080/02786820902777207.

Koch, D., and J. Hansen (2005), Distant origins of Arctic black carbon: A Goddard Institute for Space Studies ModelE experiment, *J. Geophys. Res.*, *110*, D04204, doi:10.1029/2004JD005296.

Koch, D., T. C. Bond, D. Streets, N. Unger, and G. R. van der Werf (2007), Global impacts of aerosols from particular source regions and sectors, *J. Geophys. Res.*, *112*, D02205, doi:10.1029/2005JD007024.

Koch, D., M. Schulz, S. Kinne, G. Schuster, T. C. Bond, A. Clarke, D. W. Fahey, S. Freitag, C. McNaughton, J. R. Spackman, Y. Kondo, N. Moteki, L. Sahu, H. Sakamoto, N. Takegawa, Y. Zhao, Y. Balkanski, Susanne Bauer, T. Berntsen, T. Berglen, O. Boucher, M. Chin, F. Dentener, T. Diehl, R. Easter, H. Feichter, D. Fillmore, S. Ghan, P. Ginoux, S. Gong, A. Grini, L. Horowitz, T. Iversen, A. Kirkevag, M. Krol, X. Liu, R. Miller, V. Montanaro, G. Myhre, J. Penner, J. Perlwitz, G. Pitari, S. Reddy, Ø. Seland, P. Stier, T. Takemura, C. Textor, Z. Klimont, and J. A. van Aardenne (2009), Evaluation of black carbon estimations in global aerosol models, *Atmos. Chem. Phys.*, *9*, 9001–9026.

Koga, S., T. Maeda, and N. Kaneyasu (2008), Source contributions to black carbon mass fractions in aerosol particles over the northwestern Pacific, *Atmos. Environ.*, *42*, 800–814.

Koike, M. *et al.* (2003), Export of anthropogenic reactive nitrogen and sulfur compounds from the East Asia region in spring, *J. Geophys. Res.*, *108*, 8789, doi:10.1029/2002JD003284.

Koike, M., N. Moteki, K. Pradeep, T. Takamura, N. Takegawa, Y. Kondo, H. Matsui, A. Shimizu, and N. Sugimoto (2014), Case study of absorption

doi:10.5047/meep.2015.00301.0001

aerosol optical depth closure over the East China Sea, *J. Geophys. Res.*, *119*, 122–136, doi:10.1002/2013JD020163.

Kondo, Y., Y. Komazaki, Y. Miyazaki, N. Moteki, N. Takegawa, D. Kodama, S. Deguchi, M. Nogami, M. Fukuda, T. Miyakawa, Y. Morino, M. Koike, H. Sakurai, and K. Ehara (2006), Temporal variations of elemental carbon in Tokyo, *J. Geophys. Res.*, *111*, doi:10.1029/2005JD006257.

Kondo, Y., L. Sahu, M. Kuwata, Y. Miyazaki, N. Takegawa, N. Moteki, J. Imaru, S. Han, T. Nakayama, M. Hu, Y. J. Kim, and K. Kita (2009), Stabilization of the mass absorption cross section of black carbon for filter-based absorption photometry by the use of a heated inlet, *Aerosol Sci. Technol.*, *43*, 741–756.

Kondo, Y., N. Takegawa, H. Matsui, T. Miyakawa, M. Koike, Y. Miyazaki, Y. Kanaya, M. Mochida, M. Kuwata, Y. Morino, and M. Shiraiwa (2010), Formation and transport of aerosols in Tokyo in relation to their physical and chemical properties—A review—, *J. Metorol. Soc. Jpn.*, *88*, 597–624.

Kondo, Y., H. Matsui, N. Moteki, L. Sahu, N. Takegawa, M. Kajino, Y. Zhao, M. J. Cubison, J. L. Jimenez, S. Vay, G. S. Diskin, B. Anderson, A. Wisthaler, T. Mikoviny, H. E. Fuelberg, D. R. Blake, G. Huey, A. J. Weinheimer, D. J. Knapp, and H. Brune (2011a), Emissions of black carbon, organic, and inorganic aerosols from biomass burning in North America and Asia in 2008, *J. Geophys. Res.*, *116*, D08204, doi:10.1029/2010JD015152.

Kondo, Y., L. Sahu, N. Moteki, F. Khan, N. Takegawa, X. Liu, M. Koike, and T. Miyakawa (2011b), Consistency and traceability of black carbon measurements made by laser-induced incandescence, thermal-optical transmittance, and filter-based photo-absorption techniques, *Aerosol Sci. Technol.*, *45*, 295–312, doi:10.1080/02786826.2010.533215.

Kondo, Y., N. Oshima, M. Kajino, R. Mikami, N. Moteki, N. Takegawa, R. L. Verma, Y. Kajii, S. Kato, and A. Takami (2011c), Emissions of black carbon in East Asia estimated from observations at a remote site in the East China Sea, *J. Geophys. Res.*, *116*, D16201, doi:10.1029/2011JD015637.

Kondo, Y., K. Ram, N. Takegawa, L. Sahu, Y. Morino, X. Liu, and T. Ohara (2012), Reduction of black carbon aerosol in Tokyo: Comparison of real-time observations with emission estimates, *Atmos. Environ.*, *54*, 242–249.

Kuwata, M., and Y. Kondo (2008), Dependence of size-resolved CCN spectra on the mixing state of nonvolatile cores observed in Tokyo, *J. Geophys. Res.*, *113*, D19202, doi:10.1029/2007JD009761.

Kuwata, M., Y. Kondo, M. Mochida, N. Takegawa, and K. Kawamura (2007), Dependence of CCN activity of less volatile particles on the amount of coating observed in Tokyo, *J. Geophys. Res.*, *112*, D11207, doi:10.1029/2006JD007758.

Kuwata, M., Y. Kondo, Y. Miyazaki, Y. Komazaki, J. H. Kim, S. S. Yum, H. Tanimoto, and H. Matsueda (2008), Cloud condensation nuclei activity at Jeju Island, Korea in spring 2005, *Atmos. Chem. Phys.*, *8*, 2933–2958.

Kuwata, M., Y. Kondo, and N. Takegawa (2009), Critical condensed mass for activation of black carbon as cloud condensation nuclei in Tokyo, *J. Geophys. Res.*, *114*, D20202, doi:10.1029/2009JD012086.

Laborde, M., P. Mertes, P. Zieger, J. Dommen, U. Baltensperger, and M. Gysel (2012), Sensitivity of the Single Particle Soot Photometer to different black carbon types, *Atmos. Meas. Tech.*, *5*, 1031–1043.

Laborde, M., M. Crippa, T. Tritscher, Z. Jurànyi, P. F. Decarlo, B. Temime-Roussel, N. Marchand, S. Eckhardt, A. Stohl, U. Baltensperger, A. S. H. Prévôt, E. Weingartner, and M. Gysel (2013), Black carbon physical properties and mixing state in the European megacity Paris, *Atmos. Chem. Phys.*, *13*, 5831–5856.

Lack, D. A., C. D. Cappa, E. S. Cross, P. Massoli, A. T. Ahern, P. Davidovit, and T. B. Onasch (2009), Absorption enhancement of coated absorbing aerosols: Validation of the photo-acoustic technique for measuring the enhancement, *Aerosol Sci. Technol.*, *43*, 1006–1012.

Lammel, G., and T. Novakov (1995), Water nucleation properties of carbon black and diesel soot particles, *Atmos. Environ.*, *29*, 813–823.

Lavoué, D., C. Liousse, H. Cachier, B. J. Stocks, and J. G. Goldammer (2000), Modeling of carbonaceous particles emitted by boreal and temperate wildfires at northern latitudes, *J. Geophys. Res.*, *105*, 26871–26890.

Law, K. S., and A. Stohl (2007), Arctic air pollution: Origins and impacts, *Science*, *315*, 1537–1540, doi:10.1126/science.1137695.

Li, C., L. T. Marufu, R. R. Dickerson, Z. Li, T. Wen, Y. Wang, P. Wang, H. Chen, and J. W. Stehr (2007), In situ measurements of trace gases and aerosol optical properties at a rural site in northern China during East Asian Study of Tropospheric Aerosols: An International Regional Experiment 2005, *J. Geophys. Res.*, *112*, D22S04, doi:10.1029/2006JD007592.

Limon-Sanchez, M. T., P. Carbajal-Romero, L. Hernandez-Mena, H. Saldarriaga-Norena, A. Lopez-Lopez, R. Cosio-Ramirez, J. L. Arriaga-Colina, and W. Smith (2011), Black carbon in PM2.5, data from two urban sites in Guadalajara, Mexico during 2008, *Atmos. Poll. Res.*, *2*, 358–365.

Lin, M., T. Holloway, G. R. Carmichael, and A. M. Fiore (2010), Quantifying pollution inflow and outflow over East Asia in spring with regional and global models, *Atmos. Chem. Phys.*, *10*, 4221–4239.

Lin, Y.-L., R. D. Farley, and H. D. Orville (1983), Bulk parameterization of the snow field in a cloud model, *J. Clim. Appl. Meteor.*, *22*, 1065–1092.

Liu, H., D. J. Jacob, I. Bey, R. M. Yantosca, B. N. Duncan, and G. W. Sachse (2003), Transport pathways for Asian combustion outflow over the Pacific: Interannual and seasonal variations, *J. Geophys. Res.*, *108*, 8786, doi:10.1029/2002JD003102.

Liu, J., S. Fan, L. W. Horowitz, and H. Levy II (2011), Evaluation of factors controlling long-range transport of black carbon to the Arctic, *J. Geophys. Res.*, *116*, D04307, doi:10.1029/2010JD015145.

Liu, D., J. Allan, J. Whitehead, D. Young, M. Flynn, H. Coe, G. McFiggans, Z. L. Fleming, and B. Bandy (2013a), Ambient black carbon particle hygroscopic properties controlled by mixing state and composition, *Atmos. Chem. Phys.*, *13*, 2015–2029.

Liu, X., Y. Kondo, K. Ram, H. Matsui, N. Oshima, K. Nakagomi, T. Ikeda, N. Oshima, R. L. Verma, N. Takegawa, M. Koike, and M. Kajino (2013b), Seasonal variations of black carbon observed at the remote mountain site Happo in Japan, *J. Geophys. Res.*, *118*, 3709–3722, doi:10.1002/jgrd.50317.

Lu, J., and F. M. Bowman (2010), A detailed aerosol mixing state model for investigating interactions between mixing state, semivolatile partitioning, and coagulation, *Atmos. Chem. Phys.*, *10*, 4033–4046.

Lubin, D., and A. M. Vogelmann (2006), A climatologically significant aerosol longwave indirect effect in the Arctic, *Nature*, *439*, 453–456, doi:10.1038/nature04449.

Marcolli, C., B. P. Luo, Th. Peter, and F. G. Wienhold (2004), Internal mixing of the organic aerosol by gas phase diffusion of semivolatile organic compounds, *Atmos. Chem. Phys.*, *4*, 2593–2599.

Matsui, H., and M. Koike (2012), New source and process apportionment method using a three-dimensional chemical transport model: Process, age, and source region chasing algorithm (PASCAL), *Atmos. Environ.*, doi:1016/j.atmosenv.2012.02.080.

Matsui, H. *et al.* (2009), Spatial and temporal variations of aerosols around Beijing in summer 2006: Model evaluation and source apportionment, *J. Geophys. Res.*, *114*, D00G13, doi:10.1029/2008JD010906.

Matsui, H. *et al.* (2010), Spatial and temporal variations of aerosols around Beijing in summer 2006: 2. Local and column aerosol optical properties, *J. Geophys. Res.*, *115*, D22207, doi:10.1029/2010JD013895.

Matsui, H., M. Koike, Y. Kondo, N. Takegawa, A. Wiedensohler, J. D. Fast, and R. A. Zaveri (2011a), Impact of new particle formation on the concentrations of aerosols and cloud condensation nuclei around Beijing, *J. Geophys. Res.*, *116*, D19208, doi:10.1029/2011JD016025.

Matsui, H, Y. Kondo, N. Moteki, N. Takegawa, L. K. Sahu, Y. Zhao, H. E. Fuelberg, W. R. Sessions, G. Diskin, D. R. Blake, A. Wisthaler, and M. Koike (2011b), Seasonal variation of the transport of black carbon aerosol from the Asian continent to the Arctic during the ARCTAS aircraft campaign, *J. Geophys. Res.*, *116*, D05202, doi:10.1029/2010JD015067.

Matsui, H., Y. Kondo, N. Moteki, N. Takegawa, L. K. Sahu, M. Koike, Y. Zhao, H. E. Fuelberg, W. R. Sessions, G. Diskin, B. E. Anderson, D. R. Blake, A. Wisthaler, M. J. Cubison, and J. L. Jimenez (2011c), Accumulation mode aerosol number concentrations in the Arctic during the ARCTAS aircraft campaign: Long-range transport of polluted and clean air from Asia, *J. Geophys. Res.*, *116*, D20217, doi:10.1029/2011JD016189.

Matsui, H., M. Koike, Y. Kondo, N. Moteki, J. D. Fast, and R. A. Zaveri (2013a), Development and validation of a black carbon mixing state resolved three-dimensional model: Aging processes and radiative impact, *J. Geophys. Res.*, *118*, 2304–2326, doi:10.1029/2012JD018446.

Matsui, H., M. Koike, Y. Kondo, N. Oshima, N. Moteki, Y. Kanaya, A. Takami, and M. Irwin (2013b), Seasonal variations of Asian black carbon outflow to the Pacific: Contribution from anthropogenic sources in China and biomass burning sources in Siberia and Southeast Asia, *J. Geophys. Res.*, *118*, 9947–9967, doi:10.1002/jgrd50702.

Matsui, H., M. Koike, Y. Kondo, J. D. Fast, and M. Takigawa (2014), Development of an aerosol microphysical module: Aerosol Two-dimensional bin module for foRmation and Aging Simulation (ATRAS), *Atmos.*

Chem. Phys., *14*, 10315–10331.

Matsumoto, K., Y. Uyama, T. Hayano, H. Tanimoto, I. Uno, and M. Uematsu (2003), Chemical properties and outflow patterns of anthropogenic and dust particles on Rishiri Island during the Asian Pacific Regional Aerosol Characterization Experiment (ACE-Asia), *J. Geophys. Res.*, *108*, 8666, doi:10.1029/2003JD003426.

McConnell, J. R., R. Edwards, G. L. Kok, M. G. Flanner, C. S. Zender, E. S. Saltzman, J. R. Banta, D. R. Pasteris, M. M. Carter, and J. D. W. Kahl (2007), 20th-century industrial black carbon emissions altered Arctic climate forcing, *Science*, *317*, 1381–1384.

McMeeking, G. R., T. Hamburger, D. Liu, M. Flynn, W. T. Morgan, M. Northway, E. J. Highwood, R. Krejci, J. D. Allan, A. Minikin, and H. Coe (2010), Black carbon measurements in the boundary layer over western and northern Europe, *Atmos. Chem. Phys.*, *10*, 9393–9414.

McMeeking, G. R., N. Good, M. D. Petters, G. McFiggans, and H. Coe (2011), Influences on the fraction of hydrophobic and hydrophilic black carbon in the atmosphere, *Atmos. Chem. Phys.*, *11*, 5099–5112.

McMurry, P. H., X. Wang, K. Park, and K. Ehara (2002), The relationship between mass and mobility for atmospheric particles: A new technique for measuring particle density, *Aerosol Sci. Technol.*, *36*, 227–238.

Michelsen, H. A. (2003), Understanding and predicting the temporal response of laser-induced incandescence from carbonaceous particles, *J. Chem. Phys.*, *118*, 7012–7045, doi:10.1063/1.1559483.

Mikhailov, E. F., S. S. Vlasenko, I. A. Podgorny, and V. Ramanathan (2006), Optical properties of soot-water drop agglomerates: An experimental study, *J. Geophys. Res.*, *111*, D07209, doi:10.1029/2005jd006389.

Miyazaki, Y., Y. Kondo, L. K. Sahu, J. Imaru, N. Fukushima, and A. Kanno (2008), Performance of a newly designed Continuous Soot Monitoring System (COSMOS), *J. Env. Monit.*, *10*, 1195–1201, doi:10.1039/b806957c.

Molina, M. J., and L. T. Molina (2004), Megacities and atmospheric pollution, *J. Air Waste Manage. Assoc.*, *54*, 644–680.

Mori, T., Y. Kondo, S. Ohata, N.Moteki, H. Matui, N. Oshima, and A. Iwasaki (2014), Wet deposition of black carbon at a remote site in the East China Sea, *J. Geophys. Res.*, *119*, doi:10.1002/2014JD022103.

Morino, Y. *et al.* (2006), Partitioning of HNO_3 and particulate nitrate over Tokyo: Effect of vertical mixing, *J. Geophys. Res.*, *111*, D15215, doi:10.1029/2005JD006887.

Moteki, N., and Y. Kondo (2007), Effects of mixing state on black carbon measurements by laser-induced incandescence, *Aerosol Sci. Technol.*, *41*, 398–417, doi:10.1080/02786820701199728.

Moteki, N., and Y. Kondo (2008), Method to measure time-dependent scattering cross-section of particles evaporating in a laser beam, *J. Aerosol Sci.*, *39*, 348–364.

Moteki, N., and Y. Kondo (2010), Dependence of laser-induced incandescence on physical properties of black carbon aerosols: Measurements and theoretical interpretation, *Aerosol Sci. Technol.*, *44*, 663–675.

Moteki, N., Y. Kondo, Y. Miyazaki, N. Takegawa, Y. Komazaki, G. Kurata, T. Shirai, D. R. Blake, T. Miyakawa, and M. Koike (2007), Evolution of mixing state of black carbon particles: Aircraft measurements over the western Pacific in March 2004, *Geophys. Res. Lett.*, *34*, L11803, doi:10.1029/2006gl028943.

Moteki, N., Y. Kondo, T. Nakayama, K. Kita, L. K. Sahu, T. Ishigai, T. Kinase, and Y. Matsumi (2010a), Radiative transfer modeling of filter-based measurements of light absorption by particles: Importance of particle size dependent penetration depth, *J. Aerosol Sci.*, *41*, 401–412.

Moteki, N., Y. Kondo, and S. Nakamura (2010b), Method to measure refractive indices of small nonspherical particles: Application to black carbon particles, *J. Aerosol Sci.*, *41*, 513–521.

Moteki, N., Y. Kondo, N. Oshima, N. Takegawa, M. Koike, K. Kita, H. Matsui, and M. Kajino (2012), Size dependence of wet removal of black carbon aerosols during transport from the boundary layer to the free troposphere, *Geophys. Res. Lett.*, *39*, doi:10.1029/2012GL052034.

Moteki, N., Y. Kondo, and K. Adachi (2014), Identification by single-particle soot photometer of black carbon particles attached to other particles: Laboratory experiments and ground observations in Tokyo, *J. Geophys. Res.*, *119*, doi:10.1002/2013JD020655.

Mullins, J., and A.Williams (1987), The optical properties of soot: a comparison between experimental and theoretical values, *Fuel*, *66*, 277–280.

Murray, B. J., D. O'Sullivan, J. D. Atkinson, and M. E. Webb (2012), Ice nucleation by particles immersed in supercooled cloud droplets, *Chem. Soc. Rev.*, *41*, 6519–6554.

Nakajima, T. *et al.* (2007), Overview of the Atmospheric Brown Cloud East Asian Regional Experiment 2005 and a study of the aerosol direct radiative forcing in east Asia, *J. Geophys. Res.*, *112*, D24S91, doi:10.1029/2007JD009009.

Nakayama, T., Y. Kondo, N. Moteki, L. K. Sahu, T. Kinase, K. Kita, and Y. Matsumi (2010), Size-dependent correction factors for absorption measurements using filter-based photometers: PSAP and COSMOS, *J. Aerosol Sci.*, *41*, 333–343.

Narita, D., P. Pochanart, J. Matsumoto, K. Someno, H. Tanimoto, J. Hirokawa, Y. Kajii, H. Akimoto, M. Nakao, T. Katsuno, and Y. Kinjo (1999), Seasonal variation of carbon monoxide at remote sites in Japan, *Chemosphere: Global Change Science*, *1*, 137–144.

Nel, A. (2005), Air pollution-related illness: Effects of particles, *Science*, *308*, 804–806.

Novakov, T., S. Menon, T. W. Kirchstetter, D. Koch, and J. E. Hansen (2005), Aerosol organic carbon to black carbon ratios: Analysis of published data and implications for climate forcing, *J. Geophys. Res.*, *110*, D21205, doi:10.1029/2005JD005977.

Ogren, J. A., R. J. Charlson, and P. J. Groblicki (1983), Determination of elemental carbon in rainwater, *Anal. Chem.*, *55*, 1569–1572.

Ogren, J. A., P. J. Groblicki, and R. J. Charlson (1984), Measurement of the removal rate of elemental carbon from the atmosphere, *Sci. Tot. Environ.*, *36*, 329–338.

Ohara, T., H. Akimoto, J. Kurokawa, N. Horii, K. Yamaji, X. Yan, and T. Hayasaka (2007), An Asian emission inventory of anthropogenic emission sources for the period 1980-2020, *Atmos. Chem. Phys.*, *7*, 4419–4444.

Ohata, S., N. Moteki, and Y. Kondo (2011), Evaluation of a method for measurement of the concentration and size distribution of black carbon particles suspended in rainwater, *Aerosol Sci. Technol.*, *45*, 1326–1336.

Ohata, S., N. Moteki, J. Schwarz, D. Fahey, and Y. Kondo (2013), Evaluation of a method to measure black carbon particles suspended in rainwater and snow samples, *Aerosol Sci. Technol.*, *47*, 1073–1082.

Okuda, T., S. Matsuura, D. Yamaguchi, T. Umemura, E. Hanada, H. Orihara, S. Tanaka, K. He, Y. Ma, Y. Cheng, and L. Liang (2011), The impact of the pollution control measures for the 2008 Beijing Olympic Games on the chemical composition of aerosols, *Atmos. Environ.*, *45*, 2789–2794.

Oshima, N., M. Koike, Y. Zhang, Y. Kondo, N. Moteki, N. Takegawa, and Y. Miyazaki (2009a), Aging of black carbon in outflow from anthropogenic sources using a mixing state resolved model: Model development and evaluation, *J. Geophys. Res.*, *114*, D06210, doi:10.1029/2008JD010680.

Oshima, N., M. Koike, Y. Zhang, and Y. Kondo (2009b), Aging of black carbon in outflow from anthropogenic sources using a mixing state resolved model: 2. Aerosol optical properties and cloud condensation nuclei activities, *J. Geophys. Res.*, *114*, D18202, doi:10.1029/2008JD011681.

Oshima, N., Y. Kondo, N. Moteki, N. Takegawa, M. Koike, K. Kita, H. Matsui, M. Kajino, H. Nakamura, J. S. Jung, and Y. J. Kim (2012), Wet removal of black carbon in Asian outflow: Aerosol Radiative Forcing in East Asia (A-FORCE) aircraft campaign, *J. Geophys. Res.*, *117*, D03204, doi:10.1029/2011JD016552.

Oshima, N., M. Koike, Y. Kondo, H. Nakamura, N. Moteki, H. Matsui, N. Takegawa, and K. Kita (2013), Vertical transport mechanisms of black carbon over East Asia in spring during the A-FORCE aircraft campaign, *J. Geophys. Res.*, *118*, 13175–13198, doi:10.1002/2013JD020262.

Paatero, P., and U. Tapper (1993), Analysis of different modes of factor analysis as least squares fit problems, *Chemom. Intell. Lab. Sys.*, *18*, 183–194.

Pan, X. L. *et al.* (2011), Correlation of black carbon aerosol and carbon monoxide in the high-altitude environment of Mt. Huang in Eastern China, *Atmos. Chem. Phys.*, *11*, 9735–9747, doi:10.5194/acp-11-9735-2011.

Park, K., D. B. Kittelson, and P. H. McMurry (2004a), Structural properties of diesel exhaust particles measured by transmission electron microscopy (TEM): Relationships to particle mass and mobility, *Aerosol Sci. Technol.*, *38*, 881–889.

Park, K., D. B. Kittelson, M. R. Zachariah, and P. H. McMurry (2004b), Measurement of inherent material density of nanoparticle agglomerates, *J. Nanoparticle Res.*, *6*, 267–272.

Park, R. J. *et al.* (2005), Export efficiency of black carbon aerosol in continental outflow: Global implications, *J. Geophys. Res.*, *110*, D11205, doi:10.1029/2004JD005432.

Park, S. H., S. L. Gong, V. S. Bouchet, W. Gong, P. A. Maker, M. D. Moran, C. A. Stroud, and J. Zhang (2011), Effects of black carbon aging on air quality predictions and direct radiative forcing estimation, *Tellus*, *63B*,

doi:10.5047/meep.2015.00301.0001

1026–1039.

Paterson, K. G. *et al.* (1999), Analysis of air quality data using Positive Matrix Factorization, *Environ. Sci. Technol.*, *33*, 635–641.

Perry, K. D., and P. V. Hobbs (1994), Further evidence for particle nucleation in clear air adjacent to marine cumulus clouds, *J. Geophys. Res.*, *99*, 22803–22818.

Petzold, A., and M. Schönlinner (2004), Multi-angle absorption photometry—A new method for the measurement of aerosol light absorption and atmospheric black carbon, *J. Aerosol Sci.*, *35*, 421–441.

Petzold, A., H. Kramer, and M. Schönlinner (2002), Continuous measurement of atmospheric black carbon using a multi-angle absorption photometer, *Environ. Sci. Poll. Res.*, *4*, 78–82.

Petzold, A., M. Gysel, X. Vancassel, R. Hitzenberger, H. Puxbaum, S. Vrochticky, E. Weingartner, U. Baltensperger, and P. Mirabel (2005a), On the effects of organic matter and sulphur-containing compounds on the CCN activation of combustion particles, *Atmos. Chem. Phys.*, *5*, 3187–3203.

Petzold, A., H., Schloesser, P. J. Sheridan, W. P. Arnott, J. A. Ogren, and A. Virkkula (2005b), Evaluation of multi-angle absorption photometry for measuring aerosol light absorption, *Aerosol Sci. Technol.*, *39*, 40–51.

Pinnick, R. G., J. D. Pendleton, G. Videen (2000), Response characteristics of the particle measuring systems active scattering aerosol spectrometer probes, *Aerosol Sci. Technol.*, *33*, 334–352.

Pochanart, P., J. Hirokawa, Y. Kajii, and H. Akimoto (1999), Influence of regional-scale anthropogenic activity in northeast Asia on seasonal variations of surface ozone and carbon monoxide observed at Oki, Japan, *J. Geophys. Res.*, *104*, 3621–3631.

Pochanart, P., H. Akimoto, Y. Kajii, and P. Sukasem (2003), Carbon monoxide, regional-scale transport, and biomass burning in tropical continental Southeast Asia: Observations in rural Thailand, *J. Geophys. Res.*, *108*, 4552, doi:10.1029/2002JD003360.

Polissar, A. V., P. K. Hopke, P. Paatero, Y. J. Kaufmann, D. K. Hall, B. A. Bodhaine, E. G. Dutton, and J. M. Harris (1999), The aerosol at Barrow, Alaska: Long-term trends and source locations, *Atmos. Environ.*, *33*, 2441–2458.

Quinn, P. K., T. L. Miller, T. S. Bates, J. A. Ogren, E. Andrews, and G. E. Shaw (2002), A 3-year record of simultaneously measured aerosol chemical and optical properties at Barrow, Alaska, *J. Geophys. Res.*, *107*, 4130, doi:10.1029/2001JD001248.

Quinn, P. K., G. Shaw, E. Andrews, E. G. Dutton, T. Ruoho-Airola, and S. L. Gong (2007), Arctic haze: Current trends and knowledge gaps, *Tellus B*, *59*, 99–114.

Quinn, P. K. *et al.* (2008), Short-lived pollutants in the Arctic: Their climate impact and possible mitigation strategies, *Atmos. Chem. Phys.*, *8*, 1723–1735.

Ram, K., M. M. Sarin, and S. N. Tripathi (2010), A 1 year record of carbonaceous aerosols from an urban location (Kanpur) in the Indo-Gangetic Plain: Characterization, sources and temporal variability, *J. Geophys. Res.*, *115*, D24313, doi:10.1029/2010JD014188.

Ramana, M. V., V. Ramanathan, Y. Feng, S.-C. Yoon, S.-W. Kim, G. R. Carmichael, and J. J. Schauer (2010), Warming influenced by the ratio of black carbon to sulphate and the black-carbon source, *Nature Geosci.*, *3*, 542–545.

Ramanathan, V., P. J. Crutzen, J. T. Kiehl, and D. Rosenfeld (2001), Aerosols, climate, and the hydrological cycle, *Science*, *294*, 2119–2124.

Ramanathan, V. *et al.* (2007), Atmospheric brownclouds: Hemispherical and regional variations in long-range transport, absorption, and radiative forcing, *J. Geophys. Res.*, *112*, D22S21, doi:10.1029/2006jd008124.

Redemann, J., S. J. Masonis, B. Schmid, T. L. Anderson, P. B. Russell, J. M. Livingston, O. Dubovik, and A. D. Clarke (2003), Clear-column closure studies of aerosols and water vapor aboard the NCAR C-130 during ACE-Asia, 2001, *J. Geophys. Res.*, *108*, 8655, doi:10.1029/2003JD003442.

Reid, J. S., R. Koppmann, T. F. Eck, and D. P. Eleuterio (2005), A review of biomass burning emissions part II: Intensive physical properties of biomass burning particles, *Atmos. Chem. Phys.*, *5*, 799–825.

Ricchiazzi, P., C. Gautier, J. A. Ogren, and B. Schmid (2006), A comparison of aerosol optical properties obtained from in situ measurements and retrieved from Sun and sky radiance observations during the May 2003 ARM Aerosol Intensive Observation Period, *J. Geophys. Res.*, *111*, D05S06, doi:10.1029/2005JD005863.

Riemer, N., H. Vogel, B. Vogel, and F. Fiedler (2003), Modeling aerosols on the mesoscale-γ: Treatment of soot aerosol and its radiative effects, *J. Geophys. Res.*, *108*, 4601, doi:10.1029/2003JD003448.

Riemer, N., H. Vogel, and B. Vogel (2004), Soot aging time scales in polluted regions during day and night, *Atmos. Chem. Phys.*, *4*, 1885–1893.

Riemer, N., M. West, R. A. Zaveri, and R. C. Easter (2009), Simulating the evolution of soot mixing state with a particle-resolved aerosol model, *J. Geophys. Res.*, *114*, D09202, doi:10.1029/2008JD011073.

Riemer, N., M. West, R. Zaveri, and R. Easter (2010), Estimating black carbon aging time-scales with a particle-resolved aerosol model, *Aerosol Sci.*, *41*, 143–158.

Roberts, G., and A. Nenes (2005), A continuous-flow streamwise thermal-gradient CCN chamber for atmospheric measurements, *Aerosol. Sci. Technol.*, *39*, 206–221.

Rose, D., B. Wehner, M. Ketzel, C. Engler, J. Voigtländer, T. Tuch, and A. Wiedensohler (2006), Atmospheric number size distributions of soot particles and estimation of emission factors, *Atmos. Chem. Phys.*, *6*, 1021–1031.

Rose, D. *et al.* (2011), Cloud condensation nuclei in polluted air and biomass burning smoke near the mega-city Guangzhou, China-Part 2: Size-resolved aerosol chemical composition, diurnal cycles, and externally mixed weakly CCN-active soot particles, *Atmos. Chem. Phys.*, *11*, 2817–2836, doi:10.5194/acp-11-2817-2011.

Saathoff, H., K. H. Naumann, M. Schnaiter, W. Schöck, O. Möhler, U. Schurath, E. Weingartner, M. Gysel, and U. Baltensperger (2003), Coating of soot and $(NH_4)_2SO_4$ particles by ozonolysis products of a-pinene, *J. Aerosol Sci.*, *34*, 1297–1321.

Sachse, G. W., G. F. Hill, L. O. Wade, and M. G. Perry (1987), Fast-response, high precision carbon monoxide sensor using a tunable diode laser absorption technique, *J. Geophys. Res.*, *92*, 2071–2081.

Sahu, L. K., Y. Kondo, Y. Miyazaki, M. Kuwata, M. Koike, N. Takegawa, H. Tanimoto, H. Matsueda, S. C. Yoon, and Y. J. Kim (2009), Anthropogenic aerosols observed in Asian continental outflow at Jeju Island, Korea, in spring 2005, *J. Geophys. Res.*, *114*, doi:10.1029/2008JD010306.

Sahu, L. K., Y. Kondo, Y. Miyazaki, P. Pongkiatkul, and N. T. Kim Oanh (2011), Seasonal and diurnal variations of black carbon and organic carbon aerosols in Bangkok, *J. Geophys. Res.*, D15302, doi:10.1029/2010JD015563.

Samet, J. M., D. M. DeMarini, and H. V. Malling (2004), Do airborne particles induce heritable mutations?, *Science*, *304*, 971–972.

Schnaiter, M., C. Linke, O. Möhler, K. H. Naumann, H. Saathoff, R. Wagner, U. Schurath, and B. Wehner (2005), Absorption amplification of black carbon internally mixed with secondary organic aerosol, *J. Geophys. Res.*, *110*, D19204, doi:10.1029/2005jd006046.

Schulz, M. *et al.* (2006), Radiative forcing by aerosols as derived from the AeroCom present-day and pre-industrial simulations, *Atmos. Chem. Phys.*, *6*, 5225–5246, doi:10.5194/acp-6-5225-2006.

Schwarz, J. P., R. S. Gao, D. W. Fahey, D. S. Thomson, L. A. Watts, J. C. Wilson, J. M. Reeves, D. G. Baumgerdner, G. L. Kok, S. H. Chung, M. Schluz, J. Hendricks, A. Lauer, B. Kärcher, J. G. Slowik, K. H. Rosenlof, T. L. Thompson, A. O. Langford, M. Lowenstein, and K. C. Aikin (2006), Single-particle measurement of mid latitude black carbon and light-scattering aerosols from the boundary layer to the lower stratosphere, *J. Geophys. Res.*, *111*, D16207, doi:10.1029/2006JD007076.

Schwarz, J. P., R. S. Gao, J. R. Spackman, L. A. Watts, D. S. Thomson, D. W. Fahey, T. B. Ryerson, J. Peischl, J. S. Holloway, M. Trainer, G. J. Frost, T. Baynard, D. A. Lack, J. A. de Gouw, C. Warnecke, and L. A. Del Negro (2008a), Measurement of the mixing state, mass, and optical size of individual black carbon particles in urban and biomass burning emissions, *Geophys. Res. Lett.*, *35*, L13810, doi:10.1029/2008GL033968.

Schwarz, J. P., J. R. Spackman, D. W. Fahey, R. S. Gao, U. Lohmann, P. Stier, L. A. Watts, D. S. Thomson, D. A. Lack, L. Pfister, M. J. Mahoney, D. Baumgardner, J. C. Wilson, and J. M. Reeves (2008b), Coatings and their enhancement of black carbon light absorption in the tropical atmosphere, *J. Geophys. Res.*, *113*, D03203, doi:10.1029/2007jd009042.

Schwarz, J. P., J. R. Spackman, R. S. Gao, L. A. Watts, P. Stier, M. Schulz, S. M. Davis, S. C. Wofsy, and D. W. Fahey (2010), Global-scale black carbon profiles observed in the remote atmosphere and compared to models, *Geophys. Res. Lett.*, *37*, L18812, doi:10.1029/2010GL044372.

Schwarz, J. P., S. J. Doherty, F. Li, S. T. Ruggiero, C. E. Tanner, A. E. Perring, R. S. Gao, and D. W. Fahey (2012), Assessing Single Particle Soot Photometer and Integrating Sphere/Integrating Sandwich Spectrophotometer measurement techniques for quantifying black carbon concentration in Snow, *Atmos. Meas. Tech.*, *5*, 2581–2592.

Schwarz, J. P., R. S. Gao, A. E. Perring, J. R. Spackman, and D. W. Fahey (2013), Black carbon aerosol size in snow, *Nature Sci. Rep.*, *3*, 1356,

doi:10.5047/meep.2015.00301.0001

doi:10.1038/srep01356.
Sedlacek, A., and J. Lee (2007), Photothermal interferometric aerosol absorption spectrometry, *Aerosol Sci. Technol.*, *41*, 1089–1101.
Sedlacek III, A. J., E. R. Lewis, L. Kleinman, J. Xu, and Q. Zhang (2012), Determination of and evidence for non-core-shell structure of particles containing black carbon using the Single-Particle Soot Photometer (SP2), *Geophys. Res. Lett.*, *39*, L06802, doi:10.1029/2012GL050905.
See, S. W., R. Balasubramanian, and W. Wang (2006), A study of the physical, chemical, and optical properties of ambient aerosol particles in Southeast Asia during hazy and nonhazy days, *J. Geophys. Res.*, *111*, D10S08, doi:10.1029/2005JD006180.
Seinfeld, J. H., and S. N. Pandis (2006), *Atmospheric Chemistry and Physics: From air Pollution to Climate Change*, Wiley-Interscience, pp-1203, New York.
Seland, O., T. Iversen, A. Kirkevåg, and T. Storelvmo (2008), Aerosol-climate interactions in the CAM-Oslo atmospheric GCM and investigation of associated basic shortcomings, *Tellus*, *60A*, 459–491.
Sellegri, K., P. Laj, R. Dupuy, M. Legrand, S. Preunkert, and J.-P. Putaud (2003), Size-dependent scavenging efficiencies of multicomponent atmospheric aerosols in clouds, *J. Geophys. Res.*, *108*, 4334, doi:10.1029/2002JD002749.
Sharma, S., J. R. Brook, H. Cachier, J. Chow, A. Gaudenzi, and G. Lu (2002), Light absorption and thermal measurements of black carbon in different regions of Canada, *J. Geophys. Res.*, *107*, 4771, doi:10.1029/2002JD002496.
Sharma, S., D. Lavoué, H. Cachier, L. A. Barrie, and S. L. Gong (2004), Long-term trends of the black carbon concentrations in the Canadian Arctic, *J. Geophys. Res.*, *109*, D15203, doi:10.1029/2003JD004331.
Sharma, S., E. Andrews, L. A. Barrie, J. A. Ogren, and D. Lavoué (2006), Variations and sources of the equivalent black carbon in the high Arctic revealed by long-term observations at Alert and Barrow: 1989–2003, *J. Geophys. Res.*, *111*, D14208, doi:10.1029/2005JD006581.
Shaw, G. E. (1995), The Arctic haze phenomenon, *Bull. Amer. Meteorol. Soc.*, *76*, 2403–2413.
Sheridan, P. J., W. P. Arnott, J. A. Ogren, E. Andrews, D. B. Atkinson, D. S. Covert, H. Mosssmüller, A. Petzold, B. Schmid, A. W. Strawa, R. Varma, and A. Virkkula (2005), The Reno Aerosol Optics Study: An evaluation of aerosol absorption measurement methods, *Aerosol Sci. Technol.*, *39*, 1–16.
Shindell, D., and G. Faluvegi (2009), Climate response to regional radiative forcing during the twentieth century, *Nature Geosci.*, *2*, 294–300, doi:10.1038/ngeo473.
Shindell, D., G. Faluvegi, M. Walsh, S. C. Anenberg, R. V. Dingenen, N. Z. Muller, J. Austin, D. Koch, and G. Milley (2011), Climate, health, agricultural and economic impacts of tighter vehicle-emission standards, *Nature Clim. Change*, *1*, 59–66, doi:10.1038/nclimate1066.
Shindell, D. *et al.* (2012), Simultaneously mitigating near-term climate change and improving human health and food security, *Science*, *335*, 183–189, doi:10.1126/science.1210026.
Shinozuka, Y., A. D. Clarke, S. G. Howell, V. N. Kapustin, C. S. McNaughton, J. Zhou, and B. E. Anderson (2007), Aircraft profiles of aerosol microphysics and optical properties over North America: Aerosol optical depth and its association with PM2.5 and water uptake, *J. Geophys. Res.*, *112*, D12S20, doi:10.1029/2006JD007918.
Shipham, M. C., A. S. Bachmeier, D. R. Cahoon, Jr., and E. V. Browell (1992), Meteorological overview of the Arctic Boundary Layer Expedition (ABLE 3A) flight series, *J. Geophys. Res.*, *97*, 16395–16419.
Shiraiwa, M., Y. Kondo, N. Moteki, N. Takegawa, Y. Miyazaki, and D. R. Blake (2007), Evolution of mixing state of black carbon in polluted air from Tokyo, *Geophys. Res. Lett.*, *34*, L16803, doi:10.1029/2007GL029819.
Shiraiwa, M., Y. Kondo, N. Moteki, N. Takegawa, L. K. Sahu, A. Takami, S. Hatakeyama, S. Yonemura, and D. R. Blake (2008), Radiative impact of mixing state of black carbon aerosol in Asian outflow, *J. Geophys. Res.*, *113*, D24210, doi:10.1029/2008JD010546.
Shiraiwa, M., Y. Kondo, T. Iwamoto, and K. Kita (2010), Amplification of light absorption of black carbon by organic coating, *Aerosol Sci. Technol.*, *44*, 46–54.
Shoemaker, J. K., D. P. Schrag, M. J. Molina, and V. Ramanathan (2013), What role for short-lived climate pollutants in mitigation policy, *Science*, *342*, 1323–1324, doi:10.1126/science.1240162.
Simmel, M., and S. Wurzler (2006), Condensation and activation in sectional cloud microphysical models, *Atmos. Res.*, *80*, 218–236.
Simpson, I. J. *et al.* (2003), Photochemical production and evolution of selected C_2-C_5 alkyl nitrates in tropospheric air influenced by Asian outflow, *J. Geophys. Res.*, *108*, 8808, doi:10.1029/2002JD002830.
Singh, H. B. *et al.* (2010), Pollution influences on atmospheric composition and chemistry at high northern latitudes: Boreal and California forest fire emissions, *Atmos. Environ.*, *44*, 4553–4564.
Sirois, A., and L. A. Barrie (1999), Arctic lower tropospheric aerosol trends and composition at Alert, Canada: 1980–1995, *J. Geophys. Res.*, *104*, 11599–11618.
Skamarock, W. C., J. B. Klemp, J. Dudhia, D. O. Gill, D. M. Barker, W. Wang, and J. G. Powers (2005), A description of the advanced research WRF version 2, Tech. Note NCAR/TN-468+STR, Natl. Cent. for Atmos. Res., Boulder, Colo. (Available at http://wrf-model.org/wrfadmin/publications.php).
Slinn, W. G. N. (1983), *Precipitation Scavenging, in Atmospheric Sciences and Power Production—1979*, Division of Biomedical Environmental Research, US Department of Energy, Washington DC, Chapter 11, 466–532.
Slowik, J. G., E. S. Cross, J. H. Han, P. Davidovits, T. B. Onasch, J. T. Jayne, L. R. Williams, M. R. Canagaratna, D. R. Worsnop, R. K. Chakrabarty, H. Moosmuller, W. P. Arnott, J. P. Schwarz, R. S. Gao, D. W. Fahey, G. L. Kok, and A. Petzold (2007), An inter-comparison of instruments measuring black carbon content of soot particles, *Aerosol Sci. Technol.*, *41*, 295–314, doi:10.1080/02786820701197078.
Soja, A. J., W. R. Cofer, H. H. Shugart, A. I. Sukhinin, P. W. Stackhouse Jr., D. J. McRae, and S. D. Conard (2004), Estimating fire emissions and disparities in boreal Siberia (1998-2002), *J. Geophys. Res.*, *109*, D14S06, doi:10.1029/2004JD004570.
Sokolik, I. N., and O. B. Toon (1999), Incorporation of mineralogical composition into models of the radiative properties of mineral aerosol from UV to IR wavelengths, *J. Geophys. Res.*, *104*, 9423–9444.
Somers, C. M., B. E. McCarry, F. Malek, and J. S. Quinn (2004), Reduction of particulate air pollution lowers the risk of heritable mutations in mice, *Science*, *304*, 1008–1010.
Spackman, J. R., R. S. Gao, W. D. Neff, J. P. Schwarz, L. A. Watts, D. W. Fahey, J. S. Holloway, T. B. Ryerson, J. Peischl, and C. A. Brock (2010), Aircraft observations of enhancement and depletion of black carbon mass in the springtime Arctic, *Atmos. Chem. Phys.*, *10*, 9667–9680, doi:10.5194/acp-10-9667-2010.
Spackman, J. R., R. S. Gao, J. P. Schwarz, L. A. Watts, D. W. Fahey, L. Pfister, and T. P. Bui (2011), Seasonal variability of black carbon mass in the tropical tropopause layer, *Geophys. Res. Lett.*, *38*, L09803, doi:10.1029/2010GL046343.
Stagg, B. J., and T. T. Charalampopoulos (1993), Refractive-indexes of pyrolitic-graphite, amorphous-carbon, and flame soot in the temperature-range 25°C to 600°C, *Combust. Flame*, *94*, 381–396.
Stephens, M., N. Turner, and J. Sandberg (2003), Particle identification by laser-induced incandescence in a solid-state laser cavity, *Appl. Opt.*, *42*, 3726–3736.
Stier, P., J. H. Seinfeld, S. Kinne, J. Feichter, and O. Boucher (2006), Impact of nonabsorbing anthropogenic aerosols on clear-sky atmospheric absorption, *J. Geophys. Res.*, *111*, D18201, doi:10.1029/2006JD007147.
Stocks, B. J. *et al.* (1998), Climate change and forest fire potential in Russian and Canadian boreal forests, *Climate Change*, *38*, 1–13.
Stocks, B. J. *et al.* (2002), Large forest fires in Canada, 1959-1997, *J. Geophys. Res.*, *107*, 8149, doi:10.1029/2001JD000484.
Stohl, A. (2006), Characteristics of atmospheric transport into the Arctic troposphere, *J. Geophys. Res.*, *111*, D11306, doi:10.1029/2005JD006888.
Stohl, A. *et al.* (2006), Pan-Arctic enhancements of light absorbing aerosol concentrations due to North American boreal forest fires during summer 2004, *J. Geophys. Res.*, *111*, D22214, doi:10.1029/2006JD007216.
Stohl, A. *et al.* (2007), Arctic smoke-record high air pollution levels in the European Arctic due to agricultural fires in Eastern Europe in spring 2006, *Atmos. Chem. Phys.*, *7*, 511–534.
Streets, D. G. *et al.* (2003), An inventory of gaseous and primary aerosol emissions in Asia in the year 2000, *J. Geophys. Res.*, *108*, 8809, doi:10.1029/2002JD003093.
Streets, D. G., Q. Zhang, L. Wang, K. He, J. Hao, Y. Wu, Y. Tang, and G. R. Carmichael (2006), Revisiting China's emissions after the Transport and Chemical Evolution over the Pacific (TRACE-P) mission: Synthesis of inventories, atmospheric modeling, and observation, *J. Geophys. Res.*, *111*, doi:10.1029/2006JD007118.
Sugimoto, N., Y. Hara, A. Shimizu, K. Yumimoto, I. Uno, and M. Nishikawa

doi:10.5047/meep.2015.00301.0001

(2011), Comparison of surface observations and a regional dust transport model assimilated with lidar network data in Asian dust event of March 29 to April 2, 2007, *SOLA*, *7A*, 13–16.

Sullivan, A. P. *et al.* (2004), A method for on-line measurement of water-soluble organic carbon in ambient aerosol particles: Results from an urban site, *Geophys. Res. Lett.*, *31*, L13105, doi:10.1029/2004GL019681.

Suthawaree, J., S. Kato, A. Takami, H. Kadena, M. Toguchi, K. Yogi, S. Hatakeyama, and Y. Kajii (2008), Observation of ozone and carbon monoxide at Cape Hedo, Japan: Seasonal variation and influence of long-range transport, *Atmos. Environ.*, *42*, 2971–2981.

Takami, A. *et al.* (2005), Chemical composition of fine aerosol measured by AMS at Fukue Island, Japan during APEX period, *Atmos. Environ.*, *39*, 4913–4924.

Takami, A., T. Miyoshi, A. Shimono, N. Kaneyasu, S. Kato, Y. Kajii, and S. Hatakeyama (2007), Transport of anthropogenic aerosols from Asia and subsequent chemical transformation, *J. Geophys. Res.*, *112*, D22S31, doi:10.1029/2006JD008120.

Takegawa, N., T. Miyakawa, Y. Kondo, D. R. Blake, Y. Kanaya, M. Koike, M. Fukuda, Y. Komazaki, Y. Miyazaki,1 A. Shimono, and T. Takeuchi (2006), Evolution of submicron organic aerosol in polluted air exported from Tokyo, *Geophys. Res. Lett.*, *33*, L151814, doi:10.1029/2006GL025815.

Textor, C. *et al.* (2006), Analysis and quantification of the diversities of aerosol life cycles within AeroCom, *Atmos. Chem. Phys.*, *6*, 1777–1813.

The Chemical Society of Japan (Ed.) (1993), *Handbook of Chemistry (Basic 4th ed.)*, Maruzen, Tokyo, Japan.

Tomikawa, Y., and K. Sato (2005), Design of the NIPR trajectory model, *Polar Meteorol. Glaciol.*, *19*, 120–137.

Toon, O. B. *et al.* (2010), Planning, implementation, and first results of the Tropical Composition, Cloud and Climate Coupling Experiment (TC4), *J. Geophys. Res.*, *115*, D00J04, doi:10.1029/2009JD013073.

Treffeisen, R. *et al.* (2007), Arctic smoke-aerosol characteristics during a record smoke event in the European Arctic and its radiative impact, *Atmos. Chem. Phys.*, *7*, 3035–3053.

Uno, I., G. R. Carmichael, D. G. Streets, S. Satake, T. Takemura, J.-H. Woo, M. Uematsu, and S. Ohata (2003), Analysis of surface black carbon distributions during ACE-Asia using a regional-scale aerosol model, *J. Geophys. Res.*, *108*, 8636, doi:10.1029/2002JD003252.

Van-Hulle, P., M. Talbaut, M. Weill, and A. Coppalle (2002), Inversion method and experiment to determine the soot refractive index: application to turbulent diffusion flames, *Meas. Sci. Technol.*, *13*, 375–382.

Vay *et al.* (2003), Influence of regional-scale anthropogenic emissions on CO_2 distributions over the western North Pacific, *J. Geophys. Res.*, *108*, 8801, doi:10.1029/2002JD003094.

Verma, R. L. *et al.* (2010), Temporal variations of black carbon in Guangzhou, China, in summer 2006, *Atmos. Chem. Phys.*, *10*, 6471–6485, doi:10.5194/acp-10-6471-2010.

Verma, R. L., Y. Kondo, N. Oshima, H. Matsui, K. Kita, L. K. Sahu, S. Kato, Y. Kajii, A. Takami, and T. Miyakawa (2011), Seasonal variations of the transport of black carbon and carbon monoxide from the Asian continent to the western Pacific in the boundary layer, *J. Geophys. Res.*, *116*, D21307, doi:10.1029/2011JD015830.

Verma, S., J. Worden, S. Payra, L. Jourdain, and C. Shim (2009), Characterizing the long-range transport of black carbon aerosols during Transport and Chemical Evolution over the Pacific (TRACE-P) experiment, *Environ. Monit. Assess.*, *15*, 85–92, doi:10.1007/s10661-008-0379-2.

Virkkula, A., N. C. Ahlquist, D. S. Covert, W. P. Arnott, P. J. Sheridan, P. K. Quinn, and D. J. Coffman (2005), Modification, calibration and a field test of an instrument for measuring light absorption by particles, *Aerosol Sci. Technol.*, *39*, 68–83.

Wang, J. *et al.* (2002), Clear-column radiative closure during ACE-Asia: Comparison of multiwavelength extinction derived from particle size and composition with results from Sun photometry, *J. Geophys. Res.*, *107*, 4688, doi:10.1029/2002JD002465.

Wang, M., B. Xu, H. Zhao, J. Cao, D. Joswiak, G. Wu, and S. Lin (2011), The influence of dust on quantitative measurements of black carbon in ice and snow when using a thermal optical method, *Aerosol Sci. Technol.*, *46*, 60–69.

Wang, S., M. Zhao, J. Xing, Y. Wu, Y. Zhou, Y. Lei, K. He, L. Fu, and J. Hao (2010), Quantifying the air pollutants emission reduction during the 2008 Olympic games in Beijing, *Environ. Sci. Technol.*, *44*, 2490–2496.

Ward, D. E., A. Setzer, Y. J. Kaufman, and R. A. Rasmussen (1991), Characteristics of smoke emissions from biomass fires of the Amazon region-Base-A experiment, in *Global Biomass Burning*, edited by Levine, J. S., MIT Press, Cambridge, MA, 394–402.

Warneke, C. *et al.* (2006), Biomass burning and anthropogenic sources of CO over New England in the summer 2004, *J. Geophys. Res.*, *111*, D23S15, doi:10.1029/2005JD006878.

Warneke, C. *et al.* (2009), Biomass burning in Siberia and Kazakhstan as an important source for haze over the Alaskan Arctic in April 2008, *Geophys. Res. Lett.*, *36*, L02813, doi:10.1029/2008GL036194.

Warren, S. G., and W. J. Wiscombe (1980), A model for the spectral albedo of snow, II, snow containing atmospheric aerosols, *J. Atmos. Sci.*, *37*, 2734–2745.

Weber, R. J., P. H. McMurry, R. L. Mauldin III, D. J. Tanner, F. L. Eisele, A. D. Clarke, and V. N. Kapustin (1999), New particle formation in the remote troposphere: A comparison of observations at various sites, *Geophy. Res. Lett.*, *26*, 307–310.

Weber, R. J. *et al.* (2001), A particle-into-liquid collector for rapid measurement of aerosol bulk chemical composition, *Aerosol Sci. Technol.*, *35*, 718–727.

Weingartner, E., H. Saathoff, M. Schnaiter, N. Streit, B. Bitnar, and U. Baltensperger (2003), Absorption of light by soot particles: Determination of the absorption coefficient by means of aethalometers, *J. Aerosol Sci.*, *34*, 1445–1463.

Wisthaler, A., A. Hansel, R. R. Dickerson, and P. J. Crutzen (2002), Organic trace gas measurements by PTR-MS during INDOEX 1999, *J. Geophys. Res.*, *107*, 8024, doi:10.1029/2001JD000576.

Yamanouchi, T. *et al.* (2005), Arctic Study of Tropospheric Aerosol and Radiation (ASTAR) 2000: Arctic haze case study, *Tellus B*, *57*, 141–152.

Yokelson, R. J., J. G. Goode, D. E. Ward, R. A. Susott, R. E. Babbitt, D. D. Wade, I. Bertschi, D. W. T. Griffith, and W. M. Hao (1999), Emissions of formaldehyde, acetic acid, methanol, and other trace gases from biomass fires in North Carolina measured by airborne Fourier transform infrared spectroscopy, *J. Geophys. Res.*, *104*, 30,109–30,125.

Yokelson, R. J., T. J. Christian, T. G. Karl, and A. Guenther (2008), The tropical forest and fire emissions experiment: Laboratory fire measurements and synthesis of campaign data, *Atmos. Chem. Phys.*, *8*, 3509–3527.

Yorifuji, T., I. Kawachi, M. Kaneda, S. Takao, S. Kashima, and H. Doi (2011), Diesel vehicle emission and death rates in Tokyo, Japan: a natural experiment, *Sci. Tot. Environ.*, *409*, 3620–3627.

Yumimoto, H., I. Uno, N. Sugimoto, A. Shimizu, Z. Liu, and D. M. Winker (2008), Adjoint inversion modeling of Asian dust emission using lidar observations, *Atmos. Chem. Phys.*, *8*, 2869–2884.

Zaveri, R. A., R. C. Easter, J. D. Fast, and L. K. Peters (2008), Model for Simulating Aerosol Interactions and Chemistry (MOSAIC), *J. Geophys. Res.*, *113*, D13204, doi:10.1029/2007JD008782.

Zaveri, R. A., J. C. Barnard, R. C. Easter, N. Riemer, and M. West (2010), Particle-resolved simulation of aerosol size, composition, mixing state, and the associated optical and cloud condensation nuclei activation properties in an evolving urban plume, *J. Geophys. Res.*, *115*, D17210, doi:10.1029/2009JD013616.

Zhang, Q., D. G. Streets, G. R. Carmichael, K. B. He, H. Huo, A. Kannari, Z. Klimont, I. S. Park, S. Reddy, J. S. Fu, D. Chen, L. Duan, Y. Lei, L. T. Wang, and Z. L. Yao (2009), Asian emissions in 2006 for the NASA INTEX-B mission, *Atmos. Chem. Phys.*, *9*, 5131–5153.

Zhang, R. Y., A. F. Khalizov, J. Pagels, D. Zhang, H. X. Xue, and P. H. McMurry (2008), Variability in morphology, hygroscopicity, and optical properties of soot aerosols during atmospheric processing, *Proc. Natl. Acad. Sci.*, *105*, 10291–10296, doi:10.1073/pnas.0804860105.

Zhang, Z., and B. Y. H. Liu (1991), Performance of TSI 3760 condensation nuclei counter at reduced pressures and flow rates, *Aerosol. Sci. Technol.*, *15*, 228–238.

Zuberi, B., K. S. Johnson, G. K. Aleks, L. T. Molina, M. J. Molina, and A. Laskin (2005), Hydrophilic properties of aged soot, *Geophys. Res. Lett.*, *32*, L01807, doi:10.1029/2004GL021496.

doi:10.5047/meep.2015.00301.0001